

Dissertation

Evaluation of thermophysical properties for thermal energy storage materials - determining factors, prospects and limitations

carried out for the purpose of obtaining the degree of Doctor technicae (Dr. techn.),
submitted at TU Wien, Faculty of Mechanical and Industrial Engineering, by

Daniel Lager

Mat.Nr.: 00127134

Schubertgasse 3, 2491 Steinbrunn, Austria

under the supervision of

Ao.Univ.Prof. Dipl.-Ing. Dr.techn. Andreas Werner

Institute for Energy Systems and Thermodynamics, E302

Privatdoz. Dipl.-Ing. Dr.techn. Peter Weinberger

Institute of Applied Synthetic Chemistry, E163

reviewed by

Ao.Univ.Prof. Dipl.-Ing. Dr.techn.

Heimo Walter

TU Wien, Institute for Energy

Systems and Thermodynamics

Univ.Prof. Dipl.-Ing. Dr.techn.

Dr.h.c.mult. Herbert Dannerer

TU Wien, Institute of Chemical

Technologies and Analytics

This work was funded by the “Climate and Energy Fund” and the “Austrian research funding association (FFG)” under the scope of the energy research program (contract #848876).

I confirm that going to press of this thesis needs the confirmation of the examination committee.

Affidavit

I declare in lieu of oath, that I wrote this thesis and performed the associated research myself, using only literature cited in this volume. If text passages from sources are used literally, they are marked as such.

I confirm, that this work is original and has not been submitted elsewhere for any examination, nor is it currently under consideration for a thesis elsewhere.

Vienna, December, 2017

Signature

TECHNISCHE UNIVERSITÄT WIEN

Abstract

Faculty of Mechanical and Industrial Engineering
Institute for Energy Systems and Thermodynamics, E302

Doctor technicae (Dr. techn.)

Evaluation of thermophysical properties for thermal energy storage materials - determining factors, prospects and limitations

by Daniel LAGER

Thermal Energy Storage (TES) is representing a promising technology for energy conservation and utilizing fluctuating renewable energy sources and waste heat. While Sensible Thermal Energy Storage (STES) systems make use of the enthalpy change due to differences of heat capacity and temperature, Latent Thermal Energy Storage (LTES) systems utilize phase change enthalpies of different phase transitions and Thermochemical Energy Storage (TCES) systems use the heat of chemical reactions or sorption of the storage material. LTES and TCES promise higher energy densities based on higher enthalpy changes during phase transitions or chemical reactions at different temperature levels compared to STES. Due to that, a detailed knowledge of the thermophysical properties is needed, in order to identify the actual energy density but also thermal transport properties of the observed storage material.

In this thesis, a literature review on already published TES materials and their thermophysical properties is done. Furthermore the state-of-the art in measurement methodologies for thermophysical properties is shown and applied to different Phase Change Material (PCM) and Thermochemical Material (TCM) candidates. Focusing on specific heat capacity $c_p(T)$, phase transition enthalpy Δh_t , reaction enthalpy Δh_r , thermal diffusivity $a(T)$, thermal conductivity $\lambda(T)$ and characteristic temperatures, different already standardized but also new measurement methodologies were conducted, compared and evaluated.

In the end, this thesis should serve as a handbook for engineers and scientists who are working with thermal analysis and thermophysical measurements of heat storage materials and demonstrate the determining factors, prospects and limitations of the different measurement methodologies.

Acknowledgements

Diese Danksagung widme ich allen Personen, die mich dazu ermutigt haben, diese Arbeit fertigzustellen.

Besonders möchte ich mich bei meinen beiden Betreuern Andreas Werner und Peter Weinberger bedanken, die mir immer ein offenes Ohr als auch die notwendige Freiheit gegeben haben, um diese Dissertation nach meinen Vorstellungen durchführen zu können. Darüber hinaus bedanke ich mich bei Heimo Walter und Herbert Danninger für den Aufwand der Begutachtung dieser Arbeit.

Des Weiteren bedanke ich mich bei Markus Deutsch, Stylianos Flegkas, Christian Knoll, Danny Müller, Christian Jordan, Christian Gierl und Michael Harasek die während der Projekttreffen immer wertvolle Diskussionspartner waren.

Ganz besonders möchte ich mich bei meinem Kollegen Wolfgang Hohenauer bedanken, der mir vor 10 Jahren die Chance gegeben hat, in der Thermophysik Fuß zu fassen und in dieser Zeit als Mentor und Diskussionspartner immer zur Verfügung stand.

Der größte Dank richtet sich an meine Frau Patricia und meine beiden Kinder Roman und Iris, die immer Verständnis für die vielen Stunden, die in diese Arbeit geflossen sind, gezeigt haben.

Daniel Lager

Contents

Abstract	i
Acknowledgements	iii
Glossaries	ix
Acronyms	ix
Symbols	x
Subscripts	xii
Superscripts	xii
1 Introduction	1
2 Thermal Energy Storage Materials and Thermophysical Properties	3
2.1 Introduction	3
2.2 Sensible Thermal Energy Storage - STES	4
2.2.1 Principles	4
2.2.2 Applications	4
2.2.3 Sensible Heat Storage Materials - SHSM	5
2.3 Latent Thermal Energy Storage - LTES	7
2.3.1 Principles	7
2.3.2 Applications	8
2.3.3 Phase Change Materials - PCM	9
2.4 Thermochemical Energy Storage - TCES	12
2.4.1 Principles	12
2.4.2 Applications	14
2.4.3 Thermochemical materials - TCM	15
3 Thermodynamic Quantities and Measurement Methods	19
3.1 Introduction	19
3.2 Enthalpy	20
3.2.1 Specific heat capacity	20
3.2.2 Phase transition enthalpy	21
3.2.3 Reaction enthalpy	22
3.3 Kinetics	23
3.4 Thermal conductivity	24
3.5 Thermal expansion	24
3.6 Differential Scanning Calorimetry - DSC	25

3.6.1	Measurement principle	25
3.6.2	Calibration	26
3.6.3	Specific heat capacity measurements	28
3.6.4	Phase transition and chemical reaction temperatures and enthalpies	30
3.7	Thermogravimetric Analysis - TGA	31
3.7.1	Measurement principle	31
3.7.2	Calibration	32
3.7.3	Mass change and temperature	33
3.8	Laser Flash Apparatus - LFA	34
3.8.1	Measurement principle	34
3.8.2	Calibration	34
3.8.3	Thermal diffusivity measurements	35
3.8.4	Specific heat capacity measurements	36
3.9	Transient Hot Bridge - THB	37
3.9.1	Measurement principle	37
3.9.2	Calibration	38
3.9.3	Thermal conductivity measurements	38
3.10	Heat Flow Meter - HFM	40
3.10.1	Measurement principle	40
3.10.2	Calibration	41
3.10.3	Thermal conductivity measurements	41
3.11	Push rod dilatometry	42
3.11.1	Measurement principle	42
3.11.2	Calibration	42
3.11.3	Linear thermal expansion	43
4	PCM measurement methods and evaluated thermophysical properties	45
4.1	Introduction	45
4.2	PCM measurements via DSC	47
4.2.1	DSC equipment and setup	47
4.2.2	Calibration experiments	47
4.2.3	Enthalpy curve measurement of organic PCMs	52
4.2.4	Specific heat capacity measurements	54
4.2.5	Cycling tests	58
4.3	Thermal Conductivity and thermal diffusivity measurements	59
4.3.1	LFA experiments	59
4.3.2	THB experiments on PCM	62
4.3.3	Comparison of the THB and LFA thermal conductivity results	63
4.4	Applicability of LFA liquid sample holder systems	66
4.4.1	FE Modell	66
4.4.2	LFA measurements with water	69
4.4.3	FE results and comparison to laser flash measurements	70

4.5	Conclusion	72
5	TCM measurement methods and evaluated thermophysical properties	73
5.1	Introduction	73
5.2	Sorption and composite measurements via STA	75
5.2.1	Equipment and setup	75
5.2.2	Gas conditions	76
5.2.3	Characterization of clinoptilolite and salt-based composites	76
5.2.4	Characterization of a synthetic zeolite	80
5.3	Characterization of TCMs based on chemical reactions	84
5.3.1	STA measurements	84
5.3.2	DSC protocol and data analysis for specific heat capacity evaluation	86
5.3.3	LFA experiments on compacted TCM	90
5.3.4	THB experiments on powdery TCM	94
5.4	Thermophysical properties of promising TCM candidates	96
5.4.1	Calcium oxalate monohydrate $\text{CaC}_2\text{O}_4 \cdot \text{H}_2\text{O}$	96
5.4.2	Boric acid H_3BO_3	102
5.4.3	Calcium hydroxide $\text{Ca}(\text{OH})_2$	107
5.4.4	Magnesium hydroxide $\text{Mg}(\text{OH})_2$	112
5.5	Effective thermal conductivity measurements of packed beds	116
5.5.1	Reference material	116
5.5.2	Thermal conductivity of the solid Yttria-Stabilized Zirconia (YSZ)	117
5.5.3	Effective thermal conductivity measurements of YSZ packed beds	119
5.5.4	Comparison of the results	124
5.6	Conclusion	126
6	Discussion	127
A	Thermophysical data from literature	129
A.1	Sensible heat storage materials - SHSM	130
A.2	Phase Change Materials - PCM	131
A.3	Thermochemical materials - TCM	132
	Bibliography	139

Glossaries

Acronyms

CFD Computational Fluid Dynamics	LVDT Linear Variable Displacement Trans- former
DIN German Institute for Standardization	MCT Mercury Cadmium Telluride
DSC Differential Scanning Calorimetry	MFC Mass Flow Controller
DTA Differential Thermal Analysis	MS Mass Spectrometry
ECES Energy Conservation through Energy Storage	MSU Model Specific Uncertainty
ECTP European Conference on Thermo- physical Properties	NBS National Bureau of Standards
EGA Evolved Gas Analysis	NIST National Institute of Standards and Technology
EN European Standard	NIST-JANAF National Institute of Stan- dards and Technology - Joint Army- Navy-NASA-Air Force
EPS Expanded Polystyrene	PCM Phase Change Material
ESU Equipment Specific Uncertainty	PEEK Polyether Ether Ketone
FCC Face-Centered Cubic	PEG Polyethylene Glycol
FEM Finite Element Method	PMMA Polymethyl Methacrylate
FTIR Fourier-Transform Infrared Spec- troscopy	PTB Physikalisch-Technische Bundesanstalt
HDPE High Density Polyethylene	SHC Solar Heating and Cooling
HFM Heat Flow Meter	SHSM Sensible Heat Storage Material
HTF Heat Transfer Fluid	SNR Signal-to-Noise Ratio
IEA International Energy Agency	SRM Standard Reference Material
IR Infrared Radiation	SSU Sample Specific Uncertainty
IRMM Institute for Reference Materials and Measurements	STA Simultaneous Thermal Analysis
ISO International Organization for Stan- dardization	STES Sensible Thermal Energy Storage
ITCC International Thermal Conductivity Conference	TCES Thermochemical Energy Storage
ITS-90 International Temperature Scale of 1990	TCM Thermochemical Material
LFA Laser Flash Analysis	TES Thermal Energy Storage
LTES Latent Thermal Energy Storage	TGA Thermogravimetric Analysis
	THB Transient Hot Bridge
	THS Transient Hot Strip
	YSZ Yttria-Stabilized Zirconia

Symbols

Symbol	Description	Unit
A	area	m^2
A_0	pre-exponential factor	s^{-1}
a	thermal diffusivity	$\text{m}^2 \text{s}^{-1}$
C	heat capacity	J K^{-1}
c	specific heat capacity	$\text{J kg}^{-1} \text{K}^{-1}$
d	diameter	m
E_a	activation energy	J mol^{-1}
E_{kin}	kinetic energy	J
F	force	N
f	degrees of freedom	1
G	gibbs energy	J
H	enthalpy	J
h	specific enthalpy	J kg^{-1}
I	electrical current	A
K	calibration factor	V W^{-1}
k	rate constant	J K^{-1}
k_B	Boltzmann constant	$1.380\,648\,52 \times 10^{-23} \text{J K}^{-1}$
l	length, distance	m
M	molar mass	kg mol^{-1}
m	mass	kg
N	calibration factor for heat flow meter	$\text{W V}^{-1} \text{m}^{-2}$
p	pressure	Pa
Q	quantity of heat	J
\dot{q}	heat flux density	W m^{-2}
R	electrical resistance	Ω
R_{th}	thermal resistance	$\text{m}^2 \text{K}^{-1} \text{W}^{-1}$
R_U	universal gas constant	$8.314\,459\,8 \text{J K}^{-1} \text{mol}^{-1}$
r	reaction rate	$\text{mol m}^{-3} \text{s}^{-1}$
S	entropy	J K^{-1}
S_{DSC}	sensitivity	V W^{-1}
T	temperature	$^{\circ}\text{C}$
t	time	s
U	electrical voltage	V
U_i	internal energy	J
u	uncertainty	1
V	volume	m^3
\dot{V}	volume flow rate	$\text{m}^3 \text{s}^{-1}$
v	velocity	m s^{-1}

Symbol	Description	Unit
α	coefficient of thermal expansion, temperature coefficient	K^{-1}
β	heating rate	K s^{-1}
Γ	concentration	mol m^{-3}
Δ	difference	1
δ	thickness	m
ϵ	hemispherical emissivity	1
Θ	absolute temperature	K
λ	thermal conductivity	$\text{W m}^{-1} \text{K}^{-1}$
ν	stoichiometric number	1
ρ	density	kg m^{-3}
σ	uncorrected sample standard deviation	1
σ_B	Stefan–Boltzmann constant	$5.670\,367 \times 10^{-8} \text{W m}^{-2} \text{K}^{-4}$
τ	characteristic time	s
ϕ	heat flow rate	W

Subscripts

<i>0</i>	zero line	<i>i</i>	initial
<i>acq</i>	acquisition	<i>lit</i>	literature
<i>amb</i>	ambient	<i>m</i>	melting
<i>B</i>	bulk	<i>max</i>	maximum
<i>BL</i>	baseline	<i>mean</i>	mean
<i>bind</i>	binding	<i>min</i>	minimum
<i>c</i>	combined	<i>mol</i>	molar
<i>char</i>	charging	<i>p</i>	at constant pressure
<i>cond</i>	condensation	<i>pk</i>	peak
<i>cont</i>	contact	<i>R</i>	reference
<i>cr</i>	crystallization	<i>Ref</i>	calibration reference
<i>DSC</i>	DSC signal	<i>r</i>	reaction
<i>e</i>	extrapolated	<i>S</i>	sample
<i>eff</i>	effective	<i>sens</i>	sensible
<i>F</i>	furnace	<i>t</i>	transition
<i>f</i>	final	<i>V</i>	volume

Superscripts

app apparent

Chapter 1

Introduction

Decarbonization is an important keyword which is related to the climate change and global warming. As shown by [1], sustainable energy systems lead to a decrease of the production of carbon dioxide and other greenhouse gases. Thermal energy storage (TES) allows energy conservation which is needed to bridge the time gap between energy production and energy demand. This could be used to store heat due to overproduced energy coming from sustainable energy sources but also to re-utilize waste heat from different processes.

According to the study of [2] there are three core technologies for TES. The sensible thermal energy storage (STES) is currently the most common way to store heat by utilizing the heat capacity of the used storage material due to a prevailing temperature difference. Recent technologies are the latent thermal energy storage (LTES), using the heat of a phase change of a material as well as the thermochemical energy storage (TCES), which is based on the heat consumed or released by chemical reactions.

For all three technologies it is essential to have a detailed knowledge of the thermophysical properties of the investigated storage materials to predict possible storage capacities, energy densities and thermal power on material scale. In this work, already standardized but also new measurement methodologies to evaluate these needed thermophysical properties were developed, compared and evaluated.

In the first part of the thesis, a literature review on already published materials and reaction pairs for TES applications is done, followed by the fundamentals of the thermodynamic quantities and the principles of the applied measurement methods.

The second part is focusing on different measurement methods to analyze enthalpy changes and thermal transport properties of organic phase change materials (PCM) while the third and last part concentrates on gravimetric, caloric and transport properties of thermochemical materials (TCM) based on sorption effects and chemical reactions.

Chapter 2

Thermal Energy Storage Materials and Thermophysical Properties

2.1 Introduction

The following chapter describes materials and reaction pairs for Thermal Energy Storage (TES) applications based on a literature review. Some of these materials are still in research state, others are already commercially available. To distinguish between the different technologies, a classification based on the physical or chemical phenomena is done and are defined as follows:

- Sensible Thermal Energy Storage (STES): Enthalpy change ΔH due to heat capacity C and temperature gradient ΔT of a Sensible Heat Storage Material (SHSM)
- Latent Thermal Energy Storage (LTES): Enthalpy change in solid-solid or solid-liquid phase transitions ΔH_t of a PCM
- Thermochemical Energy Storage (TCES): Enthalpy change due to physical sorption or a chemical reaction ΔH_r , respectively, of a TCM

In the next sections physical and chemical fundamentals of the different heat storage technologies, available thermodynamic data of the used storage materials as well as a state-of-the-art description of TES applications is done.

A comparison of relevant thermodynamic material properties (specific heat capacity c_p , phase transition enthalpies ΔH_t , reaction enthalpies ΔH_r , characteristic temperatures T and thermal conductivity λ) should show the prospects and limitations of the storage materials as a heat storage candidate in the different TES technologies.

2.2 Sensible Thermal Energy Storage - STES

2.2.1 Principles

The current most common way to store heat is the use of sensible heat. Fig. 2.1 shows a simplified representation of the stored heat ΔQ of two materials with different specific heat capacities c_p at a defined temperature difference ΔT . It is assumed that there is no phase transition in the range of examination and that c_p is a temperature independent constant. Different quantities of heat ΔQ can be stored at the same temperature difference ΔT due to different c_p values of different materials. A detailed description about the specific heat capacity can be found in 3.2.1.

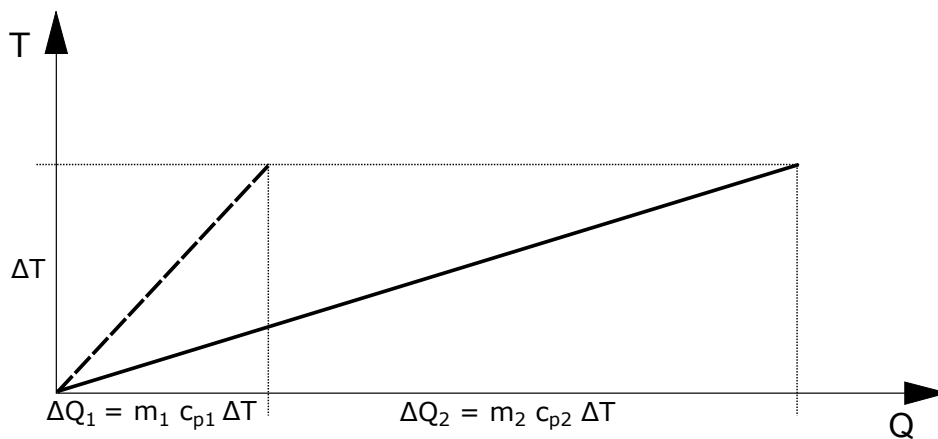


FIGURE 2.1: Temperature difference ΔT and stored heat difference ΔQ of two materials with different specific heat capacities c_p

2.2.2 Applications

Based on research and development of new materials, which are not only resulting from thermal energy storage investigations or other energy research activities, a multitude of possible storage candidates exists. Based on [2] the selection of a sensible heat storage material complies with the demand as a long-time or short-time storage material in the application. Applied materials on the one hand are liquids like water, oils or organic liquids on the other hand solids like metals, polymers, natural products and building materials.

Solids

Sensible heat storage based on solids is already in use in combination with heating of buildings and high temperature solar applications. The main advantages are the possible application at high temperatures and to avoid leakage problems. Restrictions are e.g. low energy densities compared to liquids or stratification of the storage unit.

Liquids

Liquids as storage material or used as heat transfer fluids are widespread. A multitude of applications for solar heat storage use water as storage liquid. The main advantages of water are a high specific heat capacity, availability and costs. The stored energy or specific enthalpy change Δh of water, using the averaged specific heat capacity from [3] between 0 to 100 °C with $\bar{c}_p = 4.193 \text{ kJ kg}^{-1} \text{ K}^{-1}$ at ambient pressure conditions $p = 101.3 \text{ kPa}$ and a temperature difference of $\Delta T = 70 \text{ °C}$ results in $\Delta h = 293.49 \text{ kJ kg}^{-1}$.

2.2.3 Sensible Heat Storage Materials - SHSM

Requirements

In the study of [4] the following reasonable requirements regarding thermophysical properties of sensible heat storage materials are identified:

- high specific heat capacity c_p
- good thermal conductivity λ
- high density ρ
- small thermal expansion coefficient α

Thermophysical properties

In a recent study [5], the authors investigated a method to select a sensible material candidate between 100 to 150 °C for long-time or short-time storage. Based on commercial material databases and analysis software, specific heat capacity, thermal conductivity, thermal expansion, fracture toughness and price are compared. In the study of [4] a similar method was applied for the temperature range from 500 to 750 °C using the same methodology as in [5].

Figure 2.2 depicts an analysis of the specific heat capacity c_p and volumetric energy density Q/V for $\Delta T = 1 \text{ °C}$ versus the thermal conductivity λ of different sensible heat storage candidates. For a thermal conductivity $\lambda < 10 \text{ W m}^{-1} \text{ K}^{-1}$ water has the highest specific heat capacity compared to the other candidates as shown in figure 2.2. It is followed by organic fluids with $\bar{c}_p = 2.48 \text{ J g}^{-1} \text{ K}^{-1}$, building materials with $\bar{c}_p = 1.05 \text{ J g}^{-1} \text{ K}^{-1}$, stones with $\bar{c}_p = 0.80 \text{ J g}^{-1} \text{ K}^{-1}$ and polymers with $\bar{c}_p = 0.72 \text{ J g}^{-1} \text{ K}^{-1}$. Materials with a thermal conductivity $\lambda > 10 \text{ W m}^{-1} \text{ K}^{-1}$ are silicon carbide $c_p = 1.04 \text{ J g}^{-1} \text{ K}^{-1}$, metal oxides with $\bar{c}_p = 0.86 \text{ J g}^{-1} \text{ K}^{-1}$, pure graphite with $c_p = 0.71 \text{ J g}^{-1} \text{ K}^{-1}$ and metals with $\bar{c}_p = 0.60 \text{ J g}^{-1} \text{ K}^{-1}$. Focusing on the volumetric energy density Q/V with $\Delta T = 1 \text{ °C}$ in figure 2.2, metals show not only high values for energy density but also high thermal conductivities. By contrast, building materials and polymers indicate low energy densities and thermal conductivities, respectively. Corresponding data can be found in table A.1 in appendix A on page 130.

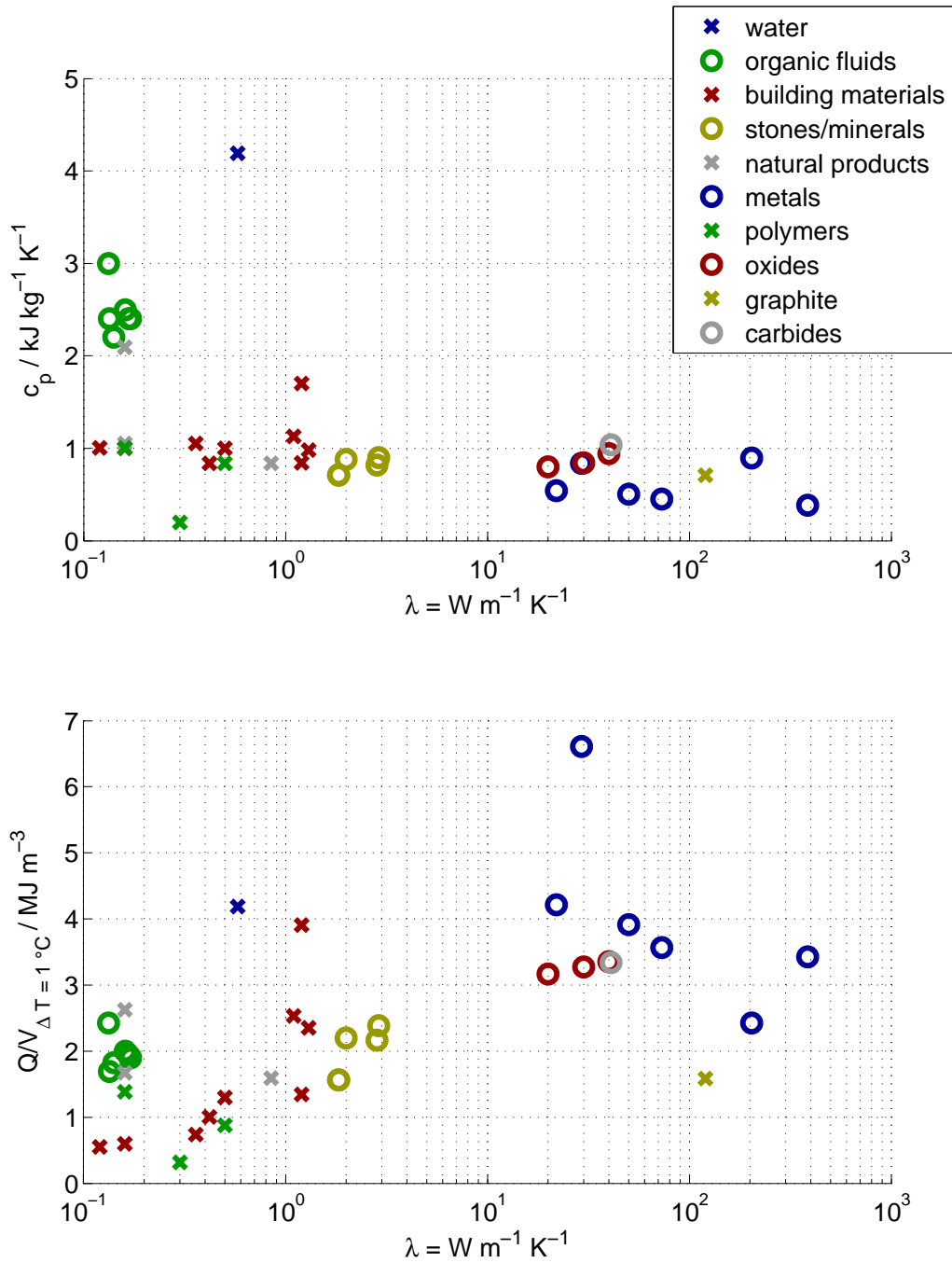


FIGURE 2.2: Comparison of the specific heat capacity c_p and energy density Q/V for a temperature difference of $\Delta T = 1^\circ\text{C}$ versus thermal conductivity λ of different sensible heat storage candidates from [5] and [4]

2.3 Latent Thermal Energy Storage - LTES

2.3.1 Principles

A short introduction to transition enthalpy ΔH_t can be found in section 3.2.2 on page 21. In this work, the transition enthalpy ΔH_t is defined as the heat which a material needs to perform a phase change. In case of PCM these are mainly solid-liquid and liquid-gas transitions.

Latent heat of liquid-gas phase transitions

LTES are utilizing the heat of a phase transition by using a PCM. According to [2, 6, 7, 8] mainly solid-solid or solid-liquid transitions are termed in relationship to LTES and PCM. Although evaporation and condensation are connected to high phase transition enthalpies following boundary conditions according to [6] are crucial:

- In a closed system with constant volume ($V = \text{const.}$) evaporation or condensation would lead to pressure changes in the system. Due to that, the phase transition temperatures T_t would also change.
- In a closed system with constant pressure ($p = \text{const.}$) evaporation or condensation would lead to a volume change of the storage system.
- In an opened system at ambient pressure conditions, the gas phase would escape into the ambient during evaporation. To re-utilize the heat, the gas phase must be retrieved from the surroundings for condensation. This principle is used for sorption TES as described in subsection 2.4.1 on page 12.

Latent heat of solid-liquid phase transitions

According to [2] the main difference between STES and LTES is the utilization of the stored heat in a small temperature interval or the temperature stability in the phase change region. Figure 2.3 represents the difference of temperature ΔT versus the difference of the stored heat ΔQ before, during and after the phase change region.

The sensible part of the heat ΔQ before the transition temperature T_t depends on the mass m , the specific heat capacity $c_p(T)$ and the temperature difference ΔT . In the phase transition area the phase transition enthalpy H_t is needed to transform the material from the original phase into the new phase. In that region there is no temperature change, the entire applied heat is needed for the phase transition. The heat needed to change the temperature of the new phase is again depending on the mass m , $c_p(T)$ of the new phase and ΔT .

Supercooling

Supercooling is a phenomenon, which can also arise with PCM. It occurs when a liquid phase of a substance can be cooled down to a crystallization temperature T_{cr} below the

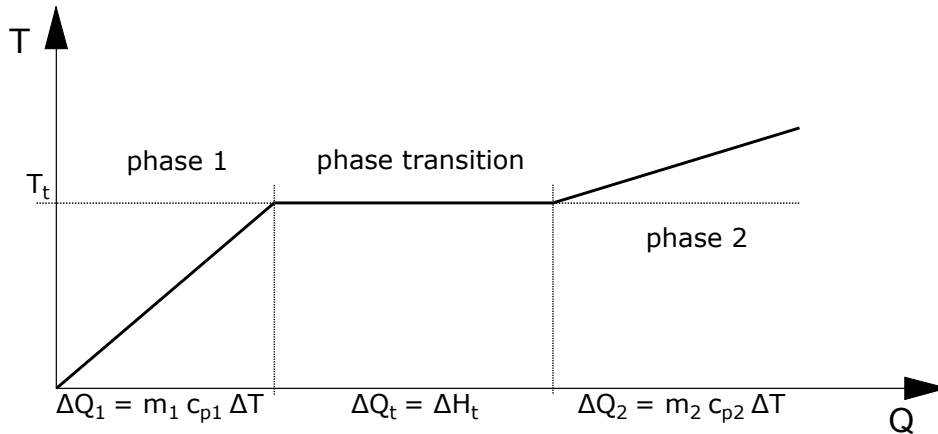


FIGURE 2.3: Temperature ΔT versus stored heat ΔQ characteristics before, during and after a phase change region

melting temperature T_m . In [9] the supercooling behavior of pure water was studied extensively. It is described, that T_{cr} of water is depending on the available nucleation sites which could be dissolved gases or aggregates. Furthermore, it is distinguished between homogeneous and heterogeneous nucleation, where the first one is caused by electrostatic attraction between the pure water molecules and the second one by an extrinsic substance, which is acting as nucleating agent.

2.3.2 Applications

Figure 2.3 represents the ideal case of a fusion or freezing process which is only valid for a first-order phase transition of a pure substance according to the the *Ehrenfest* classification [10]. In reality, supercooling effects or coexistence of different phases would show a different behavior than depicted in Figure 2.3 but it is still a first-order phase transition.

PCM in a LTES have a defined volume and geometry, so thermal transport properties of the used materials play an important role. PCMs with high thermal conductivity (e.g. monoatomic metals) lead to faster heat transport in the PCM increasing the thermal power of the LTES system. PCMs with low thermal conductivity (e.g. organic substances) lead to slower heat transport in the PCM, which needs a more sophisticated design of the LTES to increase the thermal power.

The complexity of a phase change is increasing if a solid substance has different structural properties. As shown in [11, 12], in case of thermoplastics the melting curves show a broad melting temperature range due to different thickness distribution of the lamellas, which are structured regions of the polymer molecular chains. This distribution, the melting temperature T_m , the melting enthalpy H_m and the specific heat capacity c_p is, therefore, depending on the thermal history of the thermoplastic. Two-component systems [13, 10] can also show broad melting temperature ranges depending on the concentration of the contributing elements.

In [6] commercial applications for PCM are listed. Paraffin wax in building materials or ice for cold drinks are two examples where PCMs are used for temperature stabilization. Heat or cold storage systems for buildings, cooling systems for food transport or medical applications are examples for utilizing the high phase change enthalpy in a narrow temperature range. Water, as an attractive material with regard to price and availability, is used as PCM in commercially available ice storage applications for heating and cooling in buildings.

2.3.3 Phase Change Materials - PCM

Requirements

According to [2] the following requirements regarding thermophysical properties are necessary for PCMs:

- Suitable phase change temperature T_t for stored and delivered heat in the application
- High phase change enthalpy ΔH_t to reach high storage densities
- Reproducibility and cycling stability
- No or only slight supercooling to ensure melting and solidification in a narrow temperature range
- High thermal conductivity for short charging and discharging times or high thermal power, respectively

PCM classification

In recent decades a multitude of pure substances or mixtures were investigated as potential PCM. Due to that an overview of material classes and associated thermophysical properties is necessary. A detailed information about current known PCMs could be found in [7, 6, 2]. Usually the PCMs are classified as

1. Organic (paraffin, fatty acids, sugar alcohols, polyethylene glycol, polymers)
2. Inorganic (water, salt hydrates, metals, nitrates, fluorides, etc.)
3. Mixtures (aqueous salt solutions, etc.)

Thermophysical properties

Figure 2.4 is an overview of available thermophysical literature data from [7, 6]. The upper diagram represents the specific phase change enthalpy Δh_t for different PCM classes. For $T_t < 0^\circ\text{C}$ there are water salt solutions, for $T_t = 0^\circ\text{C}$ water, between $0^\circ\text{C} < T_t < 100^\circ\text{C}$ mainly organic candidates like paraffin, fatty acids, Polyethylene Glycol (PEG) and salt hydrates and for $T_t > 100^\circ\text{C}$ there are a multitude of sugar alcohols, salts and metals.

Focusing on the phase change enthalpies related to mass Δh_t it is evident that water has much higher values compared to paraffin, PEG and fatty acids at transition temperatures

$T_t < 150\text{ }^\circ\text{C}$. Sugar alcohols indicate high enthalpies between $150\text{ }^\circ\text{C} < T_t < 200\text{ }^\circ\text{C}$. Above this temperature mainly salts and metals can be found.

According to figure 2.4 the phase change temperature T_t may be attributed to the phase change enthalpy Δh_t or the volumetric specific enthalpy $\Delta H/V$. In [6] a theoretical model named as *Rule of Richardson* allows to calculate the latent heat of melting and solidification processes of different materials. Equation 2.1 shows an example which is valid for metals.

$$1 \cdot R_U \cdot T_t < \Delta Q_{mol} < 1.5 \cdot R_U \cdot T_t \quad (2.1)$$

where R_U is the gas constant, T_t the phase transition temperature and ΔQ_{mol} the molar heat difference. The underlying principle behind this rule is again the relationship between ΔS_t , ΔH_t and T_t as shown in equation 3.8. If the entropy change ΔS_t after the phase transition is comparable between the substances and melting occurs at higher transition temperatures T_t also the transition enthalpy ΔH_t has to increase.

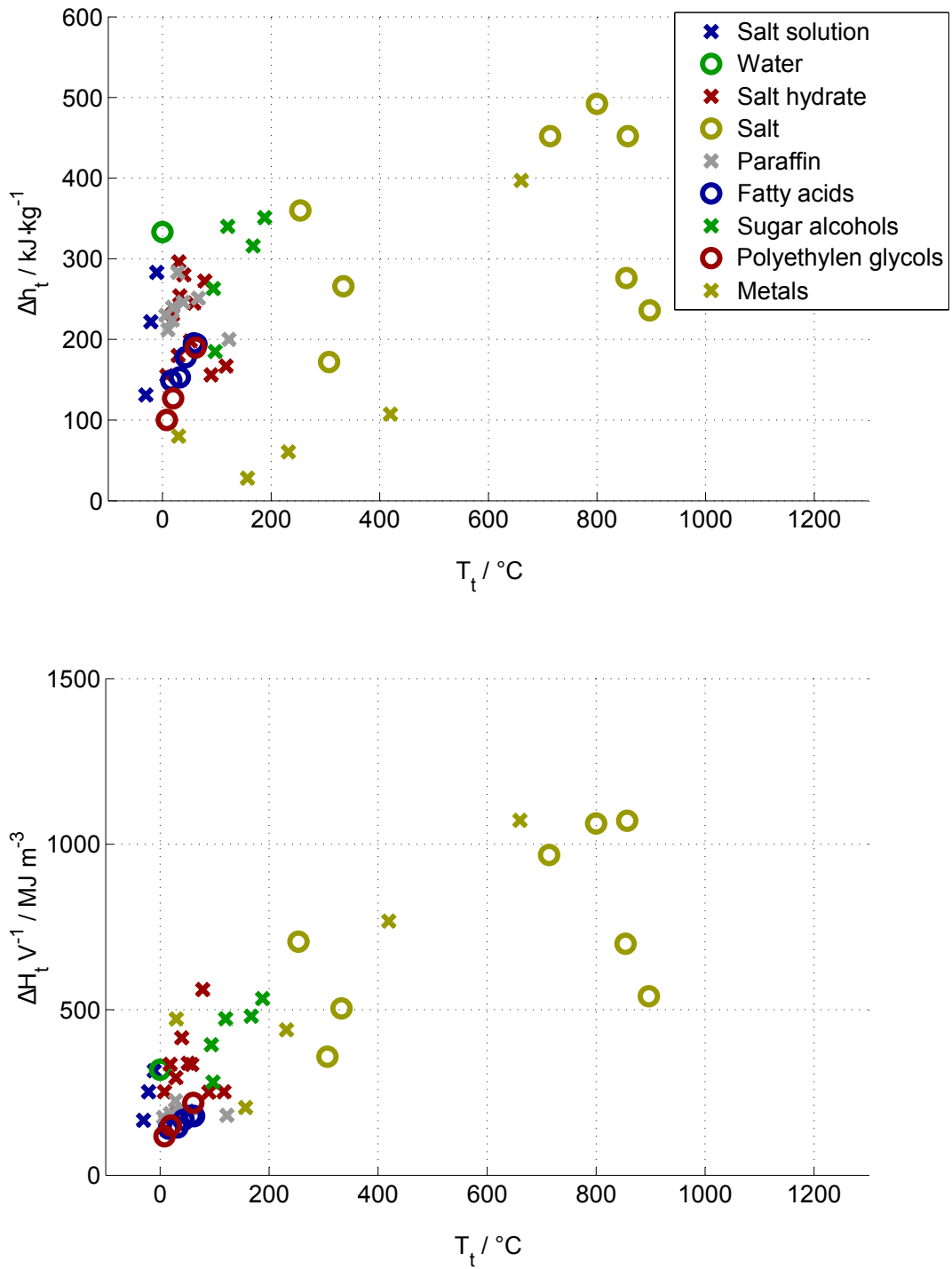


FIGURE 2.4: Phase change enthalpy Δh_t related to mass and volume $\Delta H V^{-1}$ versus T_t of different PCM classes

2.4 Thermochemical Energy Storage - TCES

2.4.1 Principles

According to [14] thermochemical heat storage is based on the reaction enthalpy of reversible chemical reactions or heat which is consumed or released due to sorption effects. For chemical reactions, the storage material remains charged as long as the reacting components are separated from each other. As soon as they are brought together the reaction starts, a product is formed and the heat of the reaction is released.



Equation 2.2 shows a simplified reaction equation for a solid-gas or liquid-gas reaction. The assets in comparison to STES and TCES technologies are:

- No thermal losses to the environment as long as both reactants are separated
- High reaction enthalpies and energy densities due to higher binding energies

Sorption

We propose to define TCES even to be related on sorption effects like adsorption or absorption phenomena. According to [14] the term adsorption is generally taken to mean a weak interaction between a solid surface and a fluid phase. The term absorption tends to be used to refer to an interaction between atoms or molecules which are penetrating the surface of a solid or liquid substance into the structure.

Focusing on the adsorption phenomenon there are two possibilities of an interaction between a fluid and the surface of a solid or substrate respectively - physical or chemical adsorption. In this work, the fluid substance which interacts with the solid surface is defined as adsorptive, the solid substance which is able to adsorb is defined as adsorbent and the condensed phase at the surface after adsorption is defined as adsorbate.

Physical adsorption - Physisorption

According to [10] physical adsorption, also known as physisorption, is a *Van der Waals* interaction between the surface of a substrate and the adsorbate. The heat which is released by the adsorbed atom or molecule is in the same order of magnitude, compared to condensation enthalpy, in a range of 20 kJ mol^{-1} and yields in an increase of temperature. The small amount of energy is not sufficient to change or break bonds of the substrate and the adsorbed particles maintain their chemical structure.

Chemical Adsorption - Chemisorption

As [10] has noted, during a chemisorption process, chemical bonding (usually covalent bonding) occurs between the surface of a substrate and the adjacent fluid phase. The resulting reaction enthalpy is in range of 200 kJ mol^{-1} which is one order of magnitude higher

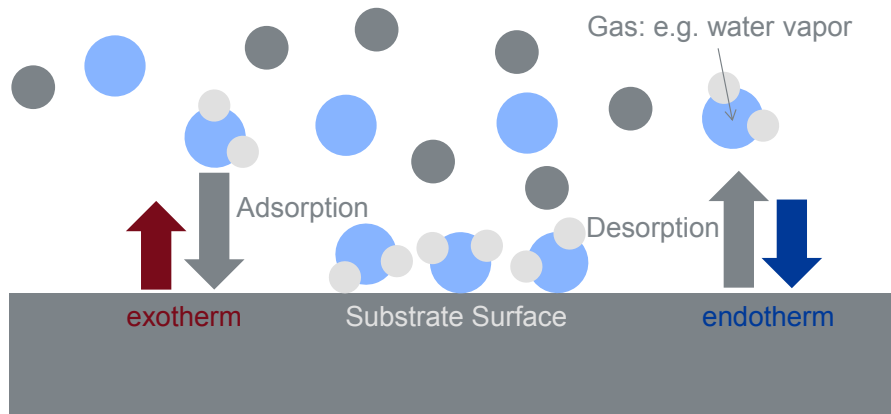


FIGURE 2.5: Simplified representation of a physical adsorption process. As shown in [14], the adsorptiv (water vapor) is adsorbed by a solid substrate surface and builds the adsorbate. Heat is released (exotherm) during the adsorption process while heat is consumed (endotherm) during desorption, which is the reverse process

compared to physisorption. Unsaturated valences of the surface atoms of the substrate can disrupt the chemisorbed particles and resulting molecular fragments on the surface can lead to catalytic reactions.

Absorption

As described in [14] absorption takes place when atoms or molecules penetrate through the surface layer of a substance and lead to a changes in structure and composition of one or both bulk phases. As shown in this literature review regarding TCES, mainly liquid-gas absorption processes are mentioned. Several absorption material pairs from different technologies in the field of heat pumps and chillers were already investigated and evaluated. In this work, absorption processes are not handled in detail so the reader is referred to further reading [2, 15, 16, 14].

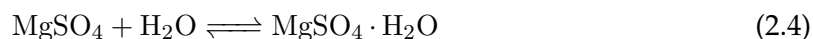
Chemical reactions

A literatur review on chemical reactions which are used in relation to TCES [17, 18, 19] are usually solid-gas reactions. Due to availability and ease of use H_2O , CO_2 or O_2 are the most common used gaseous phase reactants. Further possible gaseous candidates are SO_2 , NH_3 or H_2 . The following list should give an overview of already used chemical reactions in TCES applications:

Hydration of metal oxides [17]:



Hydration reaction of salts [18]:



Carbonization of metal oxides with CO_2 [19]:



Hydrogenation reaction of metals [19]:



Redox reaction [19]:



2.4.2 Applications

TCES systems based on physisorption are already in commercial use as shown in [20]. The described dishwasher system uses the preheating program step to dry the integrated zeolite packed bed. The resulting water vapor of the dried zeolite bed is condensing and warming up the dishes. After the rinsing process, the humid air is dried by the zeolite bed and the resulting adsorption heat is used to dry the dishes.

In the extensive literature review [21] about current research projects in the field of sorption TCES it is described, that the necessary technical level for a commercialization is not reached at that time. The authors describe the following crucial factors:

- Design of the reactor: Improvement of heat and mass transport
- Materials: Development of new and cheap materials with high energy density, cycling stability and reduced regeneration temperature
- Humidification: New humidification systems with low energy consumption for water sorption systems

- Regeneration process: Solar systems on their own deliver too low temperatures for the regeneration process of sorption materials with high energy density

In the literature review on high temperature TCES of [19] the authors concentrate on chemical reactions. The represented labor or pilot systems are still far away from commercialization. The authors summarize, that upscaling of the different TCES technologies is necessary to investigate the feasibility as long or short time TES. Additionally it is described, that the whole TCES system should be considered in a technical and economical evaluation, including the TCM, the reactor, the control strategy as well as the application.

2.4.3 Thermochemical materials - TCM

Requirements

In the recent study of [19] the following requirements regarding TCM were discussed:

- High reaction enthalpies at small molar product volume
- Reversible forth and back reaction without side reactions
- High reaction rates
- Reactants are inert at environmental conditions
- Low costs and ease of use

TCM classification

The next figure represents the TCM classifications according to the studies [14, 21, 19]. The different classes shown are separated according the actual physical or chemical phenomena.

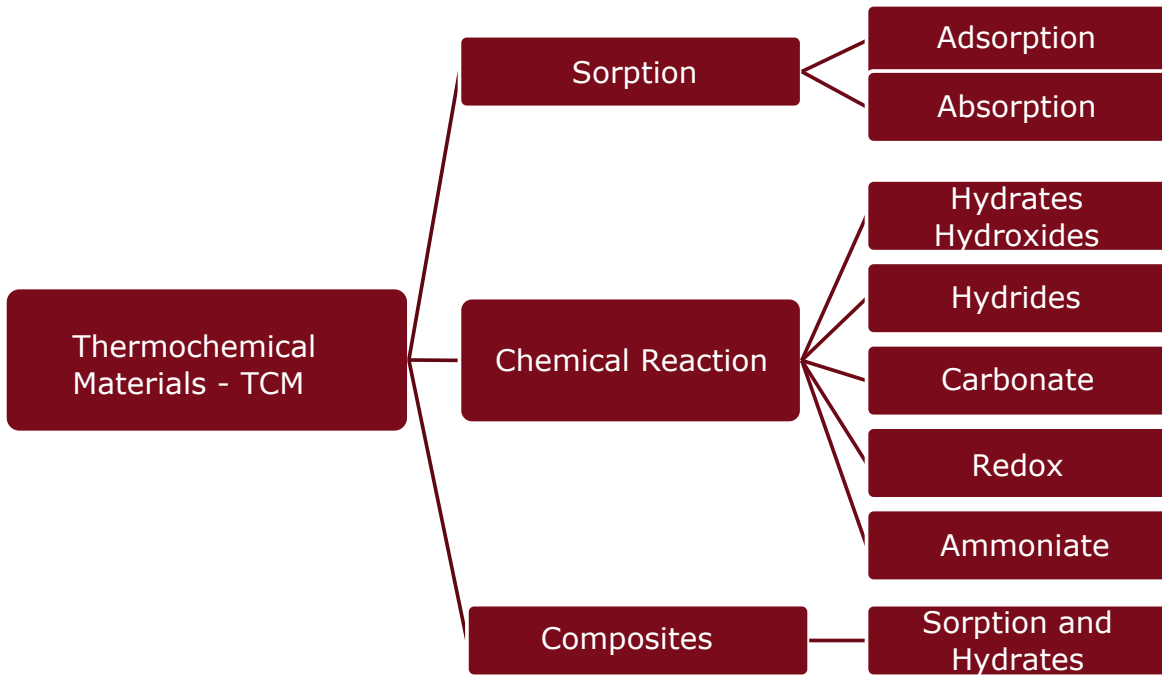


FIGURE 2.6: TCM classification based on [14, 21, 19]

Thermophysical properties

Based on the study of [14] for TCM, a superposition of the different energy terms based on different phenomena is valid. If we consider TCES based on physisorption as example, equation 2.8 for the needed charging heat Q_{char} of the sorption material can be written as:

$$Q_{char} = Q_{sens} + Q_{cond} + Q_{bind} \quad (2.8)$$

The sensible part Q_{sens} results from the specific heat capacity $c_p(T)$, the mass m and the investigated temperature interval ΔT and can be calculated with equation 3.5. Q_{cond} corresponds to the heat of condensation due to the gas-liquid phase change on the surface of the substrate. Q_{bind} is defined as the heat needed to overcome the *Van der Waals* forces as described in section 2.4.1. In [14] it is also stated, that in case of physisorption the actual stored heat ΔQ depends on the desorption temperature T and the partial pressure p of the adsorptive.

For chemical reactions, literature usually specifies the reaction enthalpy ΔH_r as shown in figure 3.1. For comparing ΔH_r for different TCMs a detailed specification about the temperature and pressure conditions is needed. In case of a given equilibrium temperature T also the equilibrium pressure of the gas phase is needed.

Results of the literature review on TCMs regarding the reaction enthalpy of different TCM candidates are shown in figure 2.7. Associated data can be found in table A.3 in Appendix A

on page 132. Sorption materials, based on physisorption and composites can be found at $T < 200\text{ }^\circ\text{C}$. These materials show lower reaction enthalpies in comparison to pure hydrate reactions. Also the liquid absorption reactions are in this temperature range but due to their low density, the volume related reaction enthalpies $\Delta H_r / V$ are significant below the hydrate reactions. For the temperature range $T > 200\text{ }^\circ\text{C}$ hydroxides, carbonate, ammonia and hydride reactions show up with volume related reaction enthalpies of $\Delta H_r / V > 2\text{ GJ m}^{-3}$.

The challenging point in comparing the enthalpy data is the dependency on system conditions and the thermal history of the different TCMs. If we take physisorption materials as an example, the enthalpy of adsorption strongly depends on the previously applied temperatures and gas conditions during desorption. Also the partial pressure of the adsorptive and temperature of the adsorbent are influencing the enthalpy change.

Focusing on chemical reactions, the reaction temperatures can be changed by varying the applied pressure of the reacting gas phase. This fact allows to adapt the reaction procedure according to the needed application. A comparison of the reaction enthalpy ΔH_r is only meaningful at the same temperature and pressure conditions.

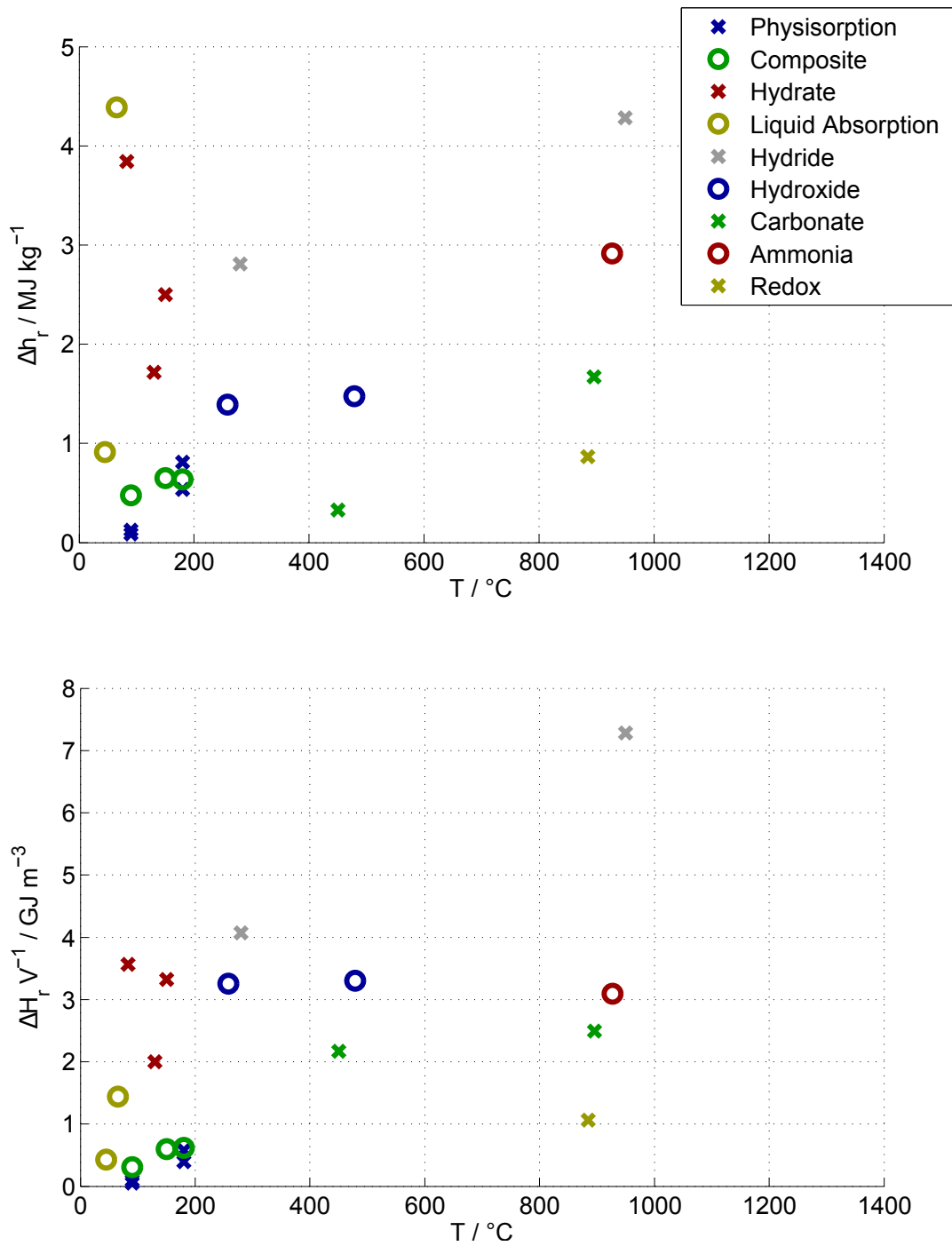


FIGURE 2.7: Comparison of the reaction enthalpy related to mass Δh_r and related to volume $\Delta H_r V^{-1}$ versus the charging or equilibrium temperature T over several TCM classes. Associated data can be found in table A.3 in Appendix A on page 132.

Chapter 3

Thermodynamic Quantities and Measurement Methods

3.1 Introduction

In this chapter, the fundamentals of the thermodynamic quantities to evaluate the performance of TES materials based on energy density, thermal transport capabilities and thermal expansion are explained. Additionally, the principles of applied measurement methods to measure these quantities are described.

In the first part, the actual stored heat in a material is specified by the enthalpy change ΔH in a defined temperature interval ΔT . In a TES material, this enthalpy change ΔH can be based on different physical or chemical phenomena. The transition enthalpy ΔH_t defines the energy consumed or released by a phase change of a PCM, whereas in case of a chemical reaction of a TCM the reaction enthalpy ΔH_r is used. If there is no phase change or chemical reaction, the sensible part of the heat can be described by the specific heat capacity $c_p(T)$. These different contributions can be measured by calorimetric experiments like the Differential Scanning Calorimetry (DSC) or Simultaneous Thermal Analysis (STA). The principles of this methods are explained within the end of the first part.

In the second part of this chapter, theoretical backgrounds to thermal transport quantities as thermal diffusivity $a(T)$ and thermal conductivity $\lambda(T)$ are given. These quantities are necessary to define the thermal power of a TES material. Subsequently, the principles of Laser Flash Analysis (LFA) experiments to evaluate $a(T)$ and Transient Hot Bridge (THB) and Heat Flow Meter (HFM) to evaluate $\lambda(T)$ are shown.

Finally, the principle of thermal expansion $\alpha(T)$ and the push rod dilatometry experiment to evaluate $\alpha(T)$ is explained. This quantity allows to identify the volumetric expansion or density change of a TES material.

3.2 Enthalpy

According to [10] and the first law of thermodynamics, the energy of a system is its capacity to do work. In case of TES the energy has been transferred to heat. Assuming a STES, heat is transferred due to a temperature difference between the material and e.g. a heat exchanger with a Heat Transfer Fluid (HTF). After the heat has been transferred, it is stored by isolating the STES to its surroundings.

Enthalpy is defined by the sum of the internal energy U_i , which represents the total kinetic and potential energy of the molecules in the system, and the product of system pressure p and volume V .

$$H = U_i + pV \quad (3.1)$$

$$\Delta H = Q_p \quad (3.2)$$

Equation 3.2 clarifies, that the supplied heat at constant pressure Q_p is changing the internal energy U_i but can also change the volume V at constant pressure p . As stated by [10], if the system provides no additional work, the change in enthalpy ΔH is equal to the supplied heat Q_p at constant pressure.

Enthalpy H is a function of state, so there is no information about how the system arrived in this state. On the contrary, the quantity of heat Q is a process function which describes the path between the reached equilibrium states.

3.2.1 Specific heat capacity

As [10] has noted, the enthalpy of a substance increases with increasing temperature. It can be described as an enthalpy change ΔH which is defined by the product of the temperature difference ΔT and the heat capacity C_p of the material as long as the heat capacity is constant over the range of temperatures of interest. The specific heat capacity is defined as the heat capacity related to mass m .

$$\Delta H = C_p \cdot \Delta T \quad (3.3)$$

$$c_p = \frac{C_p}{m} \quad (3.4)$$

The heat capacity of a material is specified through the substance type, mass and temperature itself. Equation 3.4 is only valid for a constant heat capacity. The temperature dependency of the specific heat capacity $c_p(T)$ becomes more important for larger temperature differences.

$$\Delta H(T) = m \int_{T_1}^{T_2} c_p(T) dT \quad (3.5)$$

According to [22], heat capacity can be defined at constant pressure $C_p(T)$ or constant volume $C_V(T)$ with the physical unit JK^{-1} . The relationship between these two heat capacities for a perfect gas were defined in [10] as shown in equation 3.6.

$$C_p - C_V = n \cdot R \quad (3.6)$$

For incompressible or only slightly compressible substances like liquids or solids, $C_p(T)$ and $C_V(T)$ have comparable data.

As [23] has noted, the specific heat capacity can be approximately calculated for simple substances like monoatomic metals. For monoatomic metals or element crystals, respectively, three translational and three rotational degrees of freedom exist. Connecting with the Boltzmann constant k_B the following equation can be obtained:

$$c_p = \frac{\Delta E_{kin}}{M \Delta T} = \frac{f \cdot k_B}{2 \cdot m} \quad (3.7)$$

where ΔE_{kin} is the kinetic energy, M the molar mass, f the degrees of freedom, m the mass and k_B the Boltzmann constant.

To measure the specific heat capacity $c_p(T)$ of a solid or a liquid, DSC offers a well-established procedure. This comparative method uses a reference material with known $c_p(T)$ to evaluate the $c_p(T)$ of an unknown solid or liquid sample. A detailed description of the measurement principle of DSC is given in section 3.6.

3.2.2 Phase transition enthalpy

According to [10] a phase is defined by stable physical state and chemical composition. A phase transition or phase change is defined by a conversion between two phases at a characteristic temperature and pressure. During the phase transition, the particles of the matter i.e. atoms or molecules are rearranged sterically. Consideration of a solid-liquid phase change with the structured solid melting to a dispersed liquid leads to an increase of entropy according equation 3.8.

$$\Delta S_t = \frac{\Delta H_t}{T_t} \quad (3.8)$$

ΔH_t corresponds to the difference of the phase transition enthalpy, ΔS_t is the difference of phase transition entropy and ΔT_t the phase change temperature. If it is an exothermic transition $\Delta H_t < 0$ the entropy change is negative, as it occurs for condensation or crystallization. If it is an endothermic transition $\Delta H_t > 0$ the entropy change is positive, as it occurs for melting or evaporation.

Phase transition enthalpies ΔH_t can be evaluated by applying calorimetry. The DSC offers the possibility to measure heat to or from the sample at a phase transition process. A detailed description to DSC can be found in section 3.6 on page 25.

3.2.3 Reaction enthalpy

As shown in [10, 24], *Hess's law* of constant heat summation describes, that a reaction enthalpy ΔH_r at the reference state can be defined as the difference of the standard enthalpy of formation ΔH_f^0 of the products and reactants of a chemical reaction.

$$\Delta H_r^0 = \sum_{\text{Products}} \nu \Delta H_f^0 - \sum_{\text{Reactants}} \nu \Delta H_f^0 \quad (3.9)$$

According equation 3.9, the reaction enthalpy ΔH_r only depends on the initial and final state of a system, not on the reaction path. The standard enthalpy of formation ΔH_f^0 is defined as the needed reaction enthalpy for the formation of a molecule from its elements in the reference state. The reference state is defined as the most stable state at the specified temperature and pressure.

Chemical equilibrium and equilibrium temperature

According to the second law of thermodynamics, chemical reactions tend to equilibrate with respect to temperature, pressure, composition or concentration. According to [24] a chemical equilibrium describes, that forward and backward reaction take place with the same reaction rate. From the outside it appears that the reaction came to a standstill - but it is a dynamic equilibrium, not a static equilibrium.

$$\Delta G_r = \Delta H_r - \Theta \cdot \Delta S_r \quad (3.10)$$

Equation 3.10 represents the Gibbs-Helmholtz equation where G_r is the Gibbs energy, H_r the reaction enthalpy, Θ the temperature (in Kelvin) and S_r the reaction entropy. Considering this equation for a chemical equilibrium, there is no change of the reaction entropy $\Delta S_r = 0$ and the reaction enthalpy $\Delta H_r = 0$. The Gibbs energy becomes $\Delta G_r = 0$ at the equilibrium temperature Θ .

3.3 Kinetics

Kinetics in association to chemical reactions informs about the reaction rate r and reaction mechanism. According [24] the reaction rate r is proportional to the change of concentration of the reactants at constant reaction volume, or unchanged density of the reaction medium over time respectively.

$$r_j = \frac{1}{\nu_j} \cdot \frac{d\Gamma_j}{dt} \quad (3.11)$$

Γ_j corresponds to the concentration of the component j , ν_j is the stoichiometric coefficient of the component j , t is the time and r_j is the reaction rate of the component j . The reaction rate r depends on the temperature T and the composition of the reaction mixture or concentration of the components, respectively ($\Gamma = \Gamma_1, \Gamma_2, \dots, \Gamma_n$). A temperature and concentration dependent term can be inserted into equation 3.12 to evaluate the reaction rate.

$$r = r(T, \Gamma) = k(T) \cdot g(\Gamma) \quad (3.12)$$

In literature, the temperature dependent function or rate constant $k(T)$ is usually described with the *Arrhenius* equation as shown in equation 3.13.

$$k(T) = A_0 \cdot e^{-\frac{E_a}{R \cdot \Theta}} \quad (3.13)$$

The pre-exponential factor A_0 defines the frequency of collisions of the reacting particles. A_0 corresponds to the maximum reaction rate which can be reached, it would imply that every collision would lead to a reaction. The activation energy E_a is the minimum amount of energy needed that a collision of educt particles would lead to a successful reaction. The universal gas constant R_U and the absolute temperature Θ in the exponential term specify, which ratio of reacting particles exceed the needed activation energy E_a according to the *Maxwell-Boltzmann* distribution.

Figure 3.1 clarifies the connection between the activation energy E_a and the reaction enthalpy ΔH_r and illustrates, that the forward reaction needs less activation energy than the backward reaction. The difference between these two energy levels corresponds to the reaction enthalpy ΔH_r .

Furthermore, the reaction rate depends on the concentration of the different species (s. 3.12). For a detailed description the reader is referred to further reading [24].

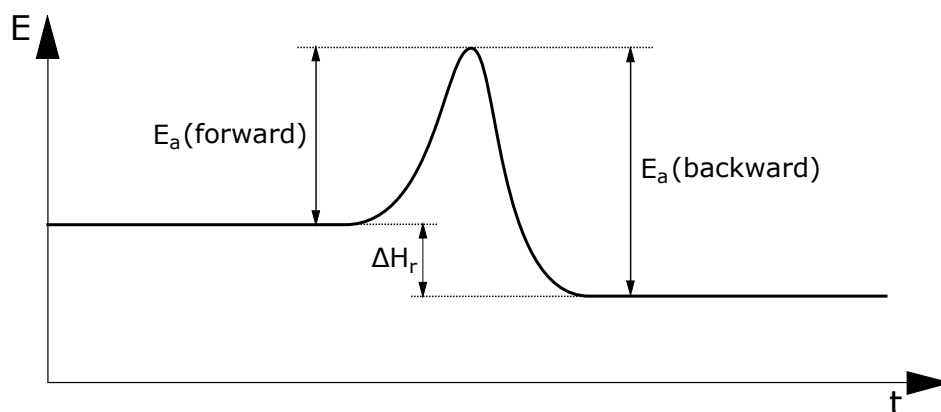


FIGURE 3.1: Activation energy of a forth and back reaction

3.4 Thermal conductivity

As described in [24] heat transport between two places in a medium with different temperatures occurs through heat conduction, convection or heat radiation. Heat conduction needs no transport of matter, two adjacent particles transport heat through kinetic energy of the atoms or molecules due to the prevailing temperature gradient. In the simplified case of one-dimensional heat conduction in a solid body with two parallel wall areas it is described through *Fourier's law*.

$$\dot{q} = \frac{\phi}{A} = -\lambda \frac{dT}{dz} = -\lambda \frac{\Delta T}{\delta} \quad (3.14)$$

\dot{q} corresponds to the heat flux density, ϕ is the heat flux, A the cross-sectional area, λ the thermal conductivity and δ the observed layer thickness. More information about the theory of thermal conductivity can be found in [25]. An extensive summary of available steady-state and dynamic thermal conductivity measurement methods are shown in [26].

3.5 Thermal expansion

As shown in [27], most substances increase their volume when they are heated at constant pressure. Some substances also contract during heating as it can be seen for water below 4 °C. This thermal expansion can be negative or positive and also anisotropic depending on the observed substance.

Figure 3.2 shows an explanation of the thermal expansion of isolated diatomic molecules based on the *Morse potential* as described in [27]. This assumption is based on central forces between the observed atoms and the *Morse potential* shows an increase of the mean distance l due to the atomic vibrations and anharmonicity in comparison to harmonic oscillations. One weakness of this model is that only longitudinal vibrational modes are considered and transverse effects are neglected. Furthermore, negative expansions cannot be explained by this model. For a more detailed description on thermal expansion theory, the reader is referred to further reading [27, 28, 29].

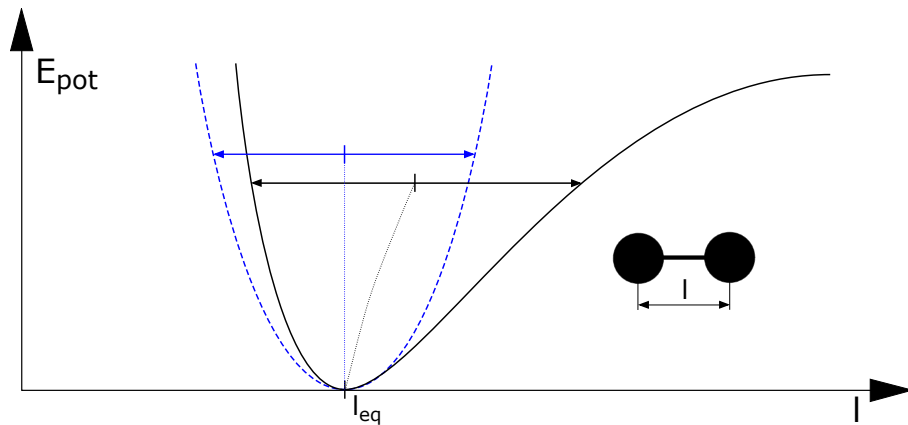


FIGURE 3.2: Morse potential (solid) and harmonic oscillator (dashed)

3.6 Differential Scanning Calorimetry - DSC

3.6.1 Measurement principle

Nowadays, the DSC is one of the most common types of calorimeters used in many fields of research, development and quality assurance. The main purpose of a calorimeter is the measurement of an exchange of heat. In the case of TES, calorimetry is an important tool to measure the specific heat capacity, physical phase transitions enthalpy but also chemical reaction enthalpy. According [30] the following definition applies for DSC:

"Differential Scanning Calorimetry means the measurement of the change of the difference in the heat flow rate to the sample and to a reference sample while they are subjected to a controlled temperature program"

There are two different basic types of DSC, the heat flux and the power compensated DSC. In this work, the heat flux DSC with disk type sensor is described, which was also used for the further experiments. If the reader is interested on other calorimetry instrumentations please refer to [31, 30].

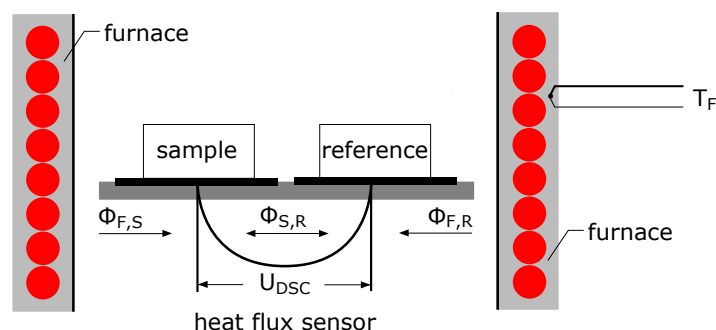


FIGURE 3.3: Schematics of a heat flow DSC with a disk type sensor - heat flow paths

In figure 3.3 a typical heat flow DSC with a disk type sensor is depicted. On the sample

and reference side of the heat flux sensor there are two crucibles shown, which can be filled with a solid or a liquid substance. If reference and sample have the same thermal behavior (e.g. both crucibles are identical without any substance inside) during the heating or cooling segment of the furnace and a full symmetry of furnace and sensor construction is given, the heat flow from the furnace to the sample $\phi_{F,S}$ and from the furnace to the reference $\phi_{F,R}$ is equal. From this it follows that the temperature gradient $\Delta T = 0$.

In case of a filled sample crucible and an empty reference crucible, different heat flows $\phi_{F,S} \neq \phi_{F,R}$ during a heating or cooling segment of the furnace occur. Due to a thermal resistance between sample and reference side, a temperature gradient ΔT develops. This temperature gradient is proportional to the electrical voltage U_{DSC} which is measured by the attached thermocouples.

Due to that, any difference of the heat flow would lead to $U_{DSC} \neq 0$ and the differential arrangement allows to compensate influences which applies to both sides at the same time.

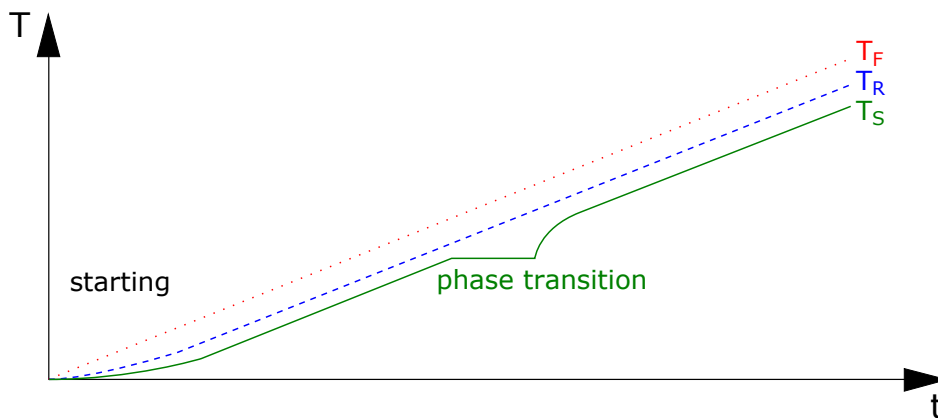


FIGURE 3.4: Furnace temperature T_F , reference temperature T_R and sample temperature T_S of a heat flow DSC versus time of a sample material with a first-order phase transition

In figure 3.4 the available temperatures during a heat flow DSC experiment are shown. Assuming a temperature segment with linear heating rate β , T_F increases constantly while T_R and T_S lag behind T_F . T_S lag behind T_R , assuming an empty crucible on the reference side and a filled sample crucible with the same crucible properties on the sample side.

A first-order phase transition, as it is the case for the latent heat of a PCM, would show no temperature change of T_S during the phase transition.

3.6.2 Calibration

According to [32], which is entitled "International vocabulary of metrology" and written by the leading metrology institutes worldwide, calibration is defined as "operation that, under specified conditions, in a first step, establishes a relation between the quantity values with measurement uncertainties provided by measurement standards and corresponding indications with associated measurement uncertainties and, in a second step, uses this information to establish a relation for obtaining a measurement result from an indication."

In case of DSC calibration, this would mean that measurement standards or certified reference materials are needed for the measured quantities temperature T , heat Q and heat flow ϕ . In the standard document [33] several points are listed, which are influencing the calibration result. Some of these points are:

- heating and cooling rates
- type and size of the used crucibles
- position of the sample in the sample crucible
- mass and size of the sample
- thermal contact between crucible and sensor

Temperature calibration

Temperature calibration in the heating segment of a DSC is done by melting calibration substances in a crucible on the sample side of the DSC sensor. As recommended by [30] at least 3 fixed points of the calibration materials defined in the International Temperature Scale of 1990 (ITS-90) [34] should be used to calibrate temperature in the desired temperature range.

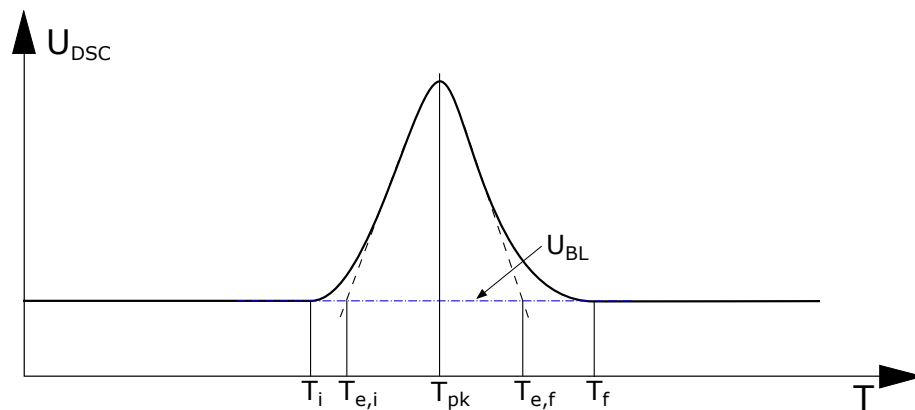


FIGURE 3.5: U_{DSC} versus T during a transition with the characteristic temperatures

Due to the fact that a DSC experiment is no static method, a phase transition measurement results in a peak as shown in figure 3.5. The shape of the measured peak is changing with different system setup, measurement or sample parameters. For temperature calibrations, the extrapolated initial temperature $T_{e,i}$ is used to compare the measured temperature to the fixed temperature point of the calibration standard.

Heat calibration

Heat calibration is done by a comparative method, where pure substances with known transition enthalpy ΔH_t are compared to the measured transition peak area. As shown in figure 3.5, the output signal of a not calibrated heat flow DSC is the voltage U_{DSC} of the differential thermocouple setup versus temperature T or time t . To identify the actual heat flow ϕ from the U_{DSC} signal, a sensitivity S_{DSC} with the unit VW^{-1} is needed.

$$S_{DSC}(T_t) = \frac{\int_{t_1}^{t_2} (U_{DSC}(t) - U_{BL}(t)) dt}{\Delta H_t} \quad (3.15)$$

As shown in equation 3.15 a peak baseline U_{BL} has to be subtracted from the U_{DSC} signal to compare only the heat which is consumed by the phase transition and to exclude offsets which are related to the specific heat capacity $c_p(T)$ of the substance or other influences like different crucible mass or asymmetric sensor position. Additionally, it has to be noted, that the evaluated calibration factor $S_{DSC}(T_t)$ is only valid for the transition temperature T_t of the measured calibration material.

Heat flow calibration

A heat flow calibration identifies the relation between the measured voltage U_{DSC} and true heat flow ϕ by measuring a reference material with known specific heat capacity $c_p(T)$. To do a heat flow calibration at least two measurement runs are necessary:

1. a zero line measurement U_0 with empty crucibles to eliminate system related influences (e.g. asymmetric sensor, different crucible masses)
2. a standard reference measurement U_{Ref} with a known $c_p(T)$ in the temperature range of interest

$$S_{DSC}(T) = \frac{U_{Ref}(T) - U_0(T)}{m_{Ref} \cdot c_{p,Ref}(T) \cdot \beta} \quad (3.16)$$

In case of the heat flow calibration, the sensitivity $S_{DSC}(T)$ is valid for the measured temperature range in the temperature resolution of $c_p(T)$ of the standard reference material.

3.6.3 Specific heat capacity measurements

According to [35, 36] $C_p(T)$ is the amount of heat required to raise the temperature of a substance by 1 K at constant pressure without a first-order phase transition. To evaluate $c_p(T)$ from an already calibrated and zero line corrected heat flow ϕ of a DSC, the mass m and the heating rate β are needed.

$$c_p(T) = \frac{C_p(T)}{m} = \frac{\phi(T)}{m \cdot \beta} \quad (3.17)$$

As described by [30], $c_p(T)$ capacity is only valid in the absence of transitions or reactions (peaks) and it describes the amount of heat needed, to raise the temperature of a substance.

In case of transitions or reactions, it is a so called apparent specific heat capacity $c_p^{app}(T)$, which could be a superposition of several effects.

According to the German Institute for Standardization (DIN) 51007 standard [36], at least three measurement runs are needed to evaluate $c_p(T)$ of a substance: a zero line measurement with empty crucibles, a standard reference measurement (e.g. $\alpha\text{-Al}_2\text{O}_3$ Sapphire standard) and a sample measurement. The temperature program starts with an isothermal segment followed by a dynamic heating segment and ends again with an isothermal segment at the maximum temperature as shown in figure 3.6. The recommended heating rate is $\beta = 10 \text{ K min}^{-1}$.

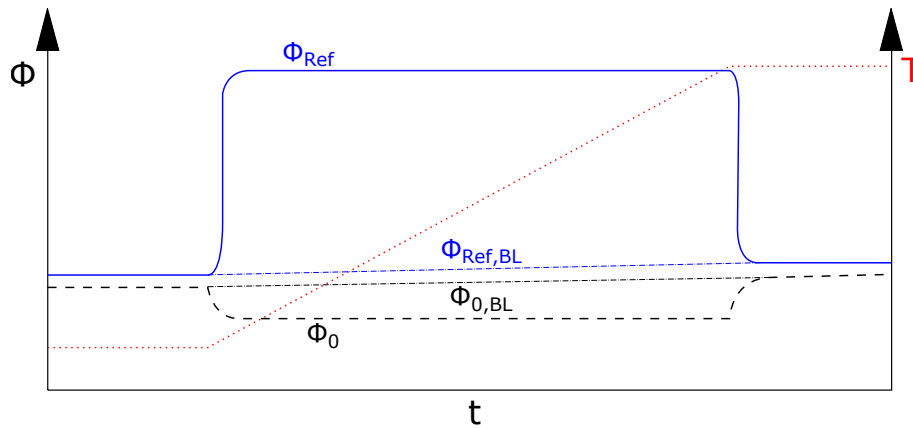


FIGURE 3.6: DSC signals for ϕ_R and ϕ_0 to evaluate the calibration factor $K(T)$ for $c_p(T)$ measurements according [36]

A dimensionless calibration factor $K(T)$ is used to calibrate the heat flow and also to subtract a baseline construction between the isothermal segments of $\phi_0(T)$ and $\phi_{Ref}(T)$. This baseline construction allows a correction if there is an offset of the heat flow ϕ between the isothermal segments.

$$K(T) = \frac{C_{p,Ref}(T) \cdot \beta}{(\Phi_{Ref}(T) - \Phi_{Ref,BL}(T)) - (\Phi_0(T) - \Phi_{0,BL}(T))} \quad (3.18)$$

$$c_{p,S}(T) = \frac{K(T) \cdot (\Phi_S(T) - \Phi_0(T))}{\beta \cdot m_S} \quad (3.19)$$

In the standard DIN European Standard (EN) International Organization for Standardization (ISO) 11357-4 [35] another procedure for the evaluation of $c_p(T)$ is mentioned. As described before, again three measurements are needed to evaluate $c_{p,S}(T)$.

$$c_{p,S}(T) = c_{p,Ref}(T) \cdot \frac{m_{Ref}}{m_S} \cdot \frac{\Phi_S(T) - \Phi_0(T)}{\Phi_{Ref}(T) - \Phi_0(T)} \quad (3.20)$$

$$c_{p,S}(T) = c_{p,Ref}(T) \cdot \frac{m_{Ref}}{m_S} \cdot \frac{U_S(T) - U_0(T)}{U_{Ref}(T) - U_0(T)} \quad (3.21)$$

The main difference between these two standards is that in DIN EN ISO 11357-4 no additional baseline construction between the isothermal segments is needed. Additionally, a starting temperature 30 K below the first evaluated $c_{p,S}(T)$ is recommended. This is due to the time needed to reach a constant heating rate starting from an isothermal segment. Figure 3.4 indicates, that in the beginning of a heating segment, time is needed to reach a constant heating rate on the reference and sample side of the sensor.

3.6.4 Phase transition and chemical reaction temperatures and enthalpies

Transition or reaction enthalpy measurements in a DSC are comparable to the temperature and heat calibration as already described in the section 3.6.2. As already shown in figure 3.5, a phase transition as well as a chemical reaction of a substance leads to a peak with characteristic temperatures. To identify the enthalpy change ΔH , a baseline between the T_i and T_f of the peak is constructed and the peak area between the baseline and the peak is calculated. Assuming a temperature and heat calibrated device, the enthalpy change ΔH of the sample can be calculated according equation 3.22.

$$\Delta H = \int_{t_1}^{t_2} \phi_S(t) - \phi_{BL} dt \quad (3.22)$$

A detailed description of the evaluation of the characteristic temperatures and enthalpies of phase transitions or chemical reactions can be found in literature [31, 30, 11, 37].

3.7 Thermogravimetric Analysis - TGA

3.7.1 Measurement principle

The Thermogravimetric Analysis (TGA) is a measurement method to evaluate the mass change Δm of a substance versus temperature T or time t . This method is useful to investigate the mass change of a sample due to the current temperature (e.g. thermal indicated decomposition, dehydration, etc.) or a gas phase which interacts with the sample (e.g. sorption, oxidation, etc.).

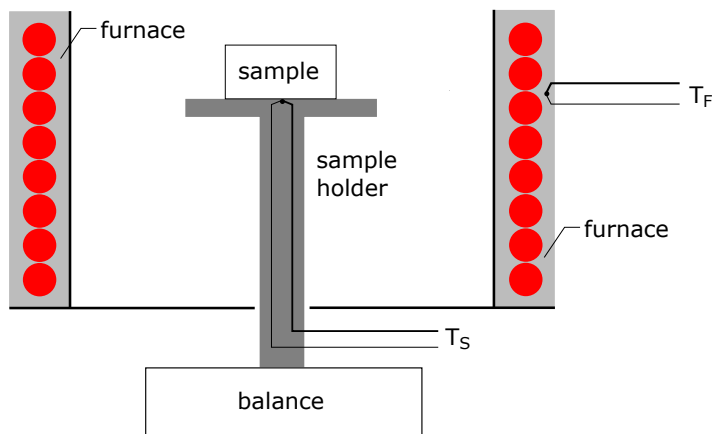


FIGURE 3.7: Schematics of a TGA with a thermocouple at the sample bottom

Figure 3.7 represents a typical setup for a TGA system. The sample is on a plate or inside a crucible on the top of the sample holder system. The sample is fully enclosed by the furnace in comparison to the sample holder, which is partly outside the furnace and connected to the balance. In that case, the furnace temperature T_F and the sample temperature T_S is measured during the whole measurement run. In different setups, the balance is temperature-controlled by a separate thermostat and a defined gas flow can be applied in the sample chamber. There are also hanging constructions available, where the balance is on top of the system. A detailed description on different TGA systems can be found in [38, 37].

The sample holder system can also be replaced by a DSC sensor, as shown in figure 3.3. The DSC sensor is additionally connected to the balance system, leading to a simultaneous measurement of the mass change $\Delta m(T)$ and the heat flow $\phi(T)$. This simultaneous measurement is known as TGA-DSC or STA measurement system. With a STA setup, a distinction between mass changing effects (e.g. sorption effects) and phase transitions, which have no influence on the sample mass (e.g. melting) can be drawn.

In figure 3.8 a typical measurement result of a TGA measurement is depicted. The mass change $\Delta m(T)$ is defined as shown in equation 3.23.

$$\Delta m_S(T) = m_S(T) - m_i \quad (3.23)$$

Mass and heat transport in the sample are influencing the measured result of a TGA measurement. As stated by [37] there are several negative influences on the measured TGA signal:

- A temperature difference ΔT between sample and thermocouple temperature leads to a systematic temperature deviation
- An inhomogeneous spatial and time dependent temperature field in the sample due to a low thermal conductivity or big sample volume
- Different intensity of the sample-gas interaction due to different surface areas, gas pressure or gas flow rate
- Sample independent influences as buoyancy and gas flow effects or temperature drifts in the balance

To overcome the temperature difference between the measured temperature at the thermocouple and the current temperature on the surface of the sample, a temperature calibration as described in section 3.7.2 can be used. Sample independent influences (e.g. buoyancy, gas flow) can be corrected by measuring a zero line before measuring the mass loss of the actual sample. This zero line is measured using the same measurement parameters ($T(t)$, gas conditions, gas flow, crucible type) as the following sample measurement. This zero line is subtracted from the following sample measurement.

$$\Delta m_{S,corr}(T) = [m_S(T) - m_0(T)] - m_i \quad (3.24)$$

3.7.2 Calibration

Mass calibration

According to [38, 37], the mass calibration at room temperature is done by using standard calibrated weights. The linearity of the mass measurement over temperature can be tested using the calcium oxalate monohydrate $\text{CaC}_2\text{O}_4 \cdot \text{H}_2\text{O}$ as a reference material [39]. $\text{CaC}_2\text{O}_4 \cdot \text{H}_2\text{O}$ dehydrates to the anhydrate CaC_2O_4 with a theoretical mass loss of $\Delta m/m_i = 12.33\%$ followed by transformation into calcium carbonate CaCO_3 and losing CO (under inert gas atmosphere) with $\Delta m/m_i = 19.17\%$ and finally transforms to calcium oxide CaO losing CO_2 with $\Delta m/m_i = 30.12\%$. The theoretical mass loss steps are calculated using the molar masses $M = 146.11 \text{ g mol}^{-1}$ for $\text{CaC}_2\text{O}_4 \cdot \text{H}_2\text{O}$, $M = 18.02 \text{ g mol}^{-1}$ for H_2O , $M = 28.01 \text{ g mol}^{-1}$ for CO and $M = 44.01 \text{ g mol}^{-1}$ for CO_2 .

Temperature calibration

As described by [37], TGA systems which have no temperature measurement information near the sample use magnetic substances which are changing their magnetic properties at a specified temperature. By measuring a ferromagnetic substance in a magnetic field inside the TGA, a different mass, due to the magnetic force on the sample, is measured. At

the specified temperature (*Curie* temperature), the calibration substance is losing its ferromagnetic properties and the real mass of the sample is indicated. This indicated transition temperature is related to the known *Curie* temperature of the standard reference material. As already shown for DSC measurements in figure 3.4, the temperature stays constant during first-order phase transition. This effect can also be used for the TGA temperature calibration as long as the sample temperature T_S is known.

3.7.3 Mass change and temperature

According to DIN 51006 [40] for the evaluation of mass change and temperature a zero line measurement is mandatory to eliminate sample independent influences. The beginning of a physical or chemical process is recognized by a deviation of the tangent to the TGA curve before the mass change step. The end of the process is defined by the converge of the tangent after the step. The mass change Δm of the step is then evaluated between m_i at T_i and m_f at T_f .

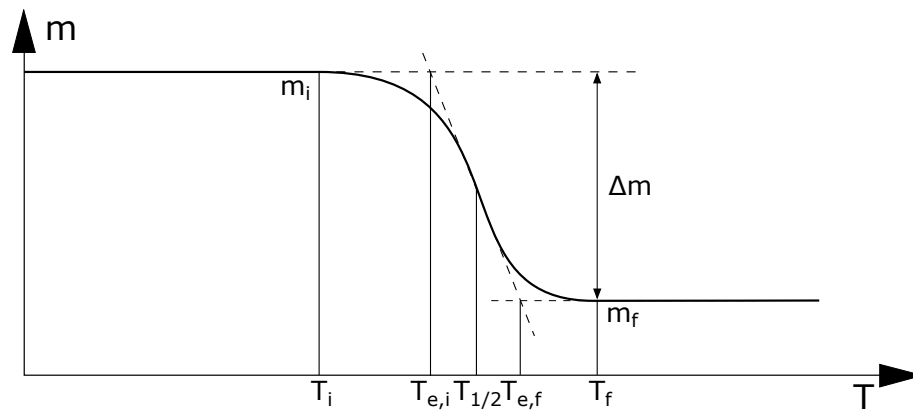


FIGURE 3.8: Characteristic temperatures and mass change evaluation based on the standard DIN 51006 [40]

3.8 Laser Flash Apparatus - LFA

3.8.1 Measurement principle

The measurement principle of the LFA method was introduced in 1960 by W. J. Parker [41]. At this time, the main motivation was, to have a reliable and fast measurement device for evaluating thermal diffusivity of solids with small sample sizes and also high temperatures.

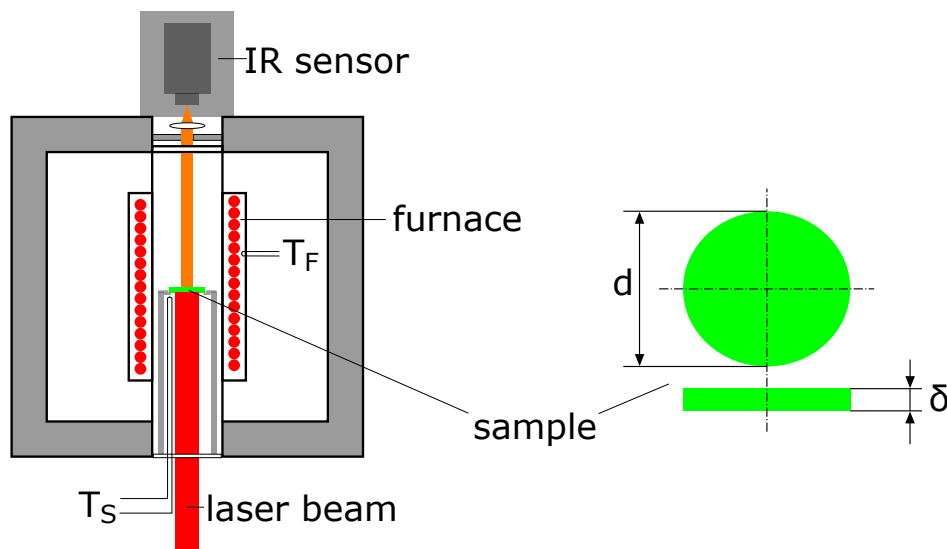


FIGURE 3.9: Principle of a LFA for thermal diffusivity measurements

Figure 3.9 shows a possible measurement setup for a LFA. A short laser or light pulse is heating up the front side of the sample while an Infrared Radiation (IR) sensor is detecting a temperature raise due to the short laser pulse on the back side of the sample. The temperature field inside the sample depends on the thermal transport properties of the sample as long as there are no heat sources or sinks (e.g. phase transitions or chemical reactions) during the measurement. The LFA method eliminates thermal contact resistance problems, furthermore, surface heat losses can be minimized due to fast measurements.

The sample can be heated inside a furnace as shown in figure 3.9. In the depicted case, the temperature is measured near the furnace T_F and near the sample T_S to enable controlled temperature programs $T(t)$. In comparison to DSC and TGA measurements, isothermal conditions at the sample are necessary for a reliable measurements in the LFA.

Technically mature LFA systems have a high sensitive IR detector, time and energy controlled laser or light beam, gas inlets with Mass Flow Controller (MFC), controlled vacuum conditions in the sample chamber and different furnaces for a broad temperature range.

3.8.2 Calibration

Temperature calibration

In one of the latest standards regarding LFA measurements on plastics [42] it is recommended to do a separate calibration on the temperature measurement device to measure

the sample temperature. As depicted in 3.9 this could be only done by detaching the sample thermocouple and calibrate it externally using ITS-90 reference standards.

Another possibility without detaching the thermocouple was mentioned in the conference paper *A New Method for the Temperature calibration of Laser Flash Systems* by J. Blumm et al., published in [43]. In this study, transition temperatures (*Curie* temperatures) of various ferromagnetic metals are used to calibrate the sample thermocouple in the LFA. It could be shown, that a sharp minimum in the thermal diffusivity occurs at the magnetic transition temperature which could be used to calibrate the sample thermocouple temperature.

Verification experiments

As shown in [42], a certified reference material from the Institute for Reference Materials and Measurements (IRMM) is available to compare the measured $a_S(T)$ of a sample to the $a_R(T)$ of the standard reference *Pyroceram 9606*. If there are significant differences ($\Delta a > 5\%$), the method for the determination of the thickness of the sample, the temperature calibration, time base and voltage of the data acquisition system and the IR detector have to be inspected.

3.8.3 Thermal diffusivity measurements

The model proposed by [41] assumes an insulated solid (adiabatic conditions) of uniform thickness. Under the defined boundary conditions the following equation can be derived for the evaluation of the thermal diffusivity $a(T)$:

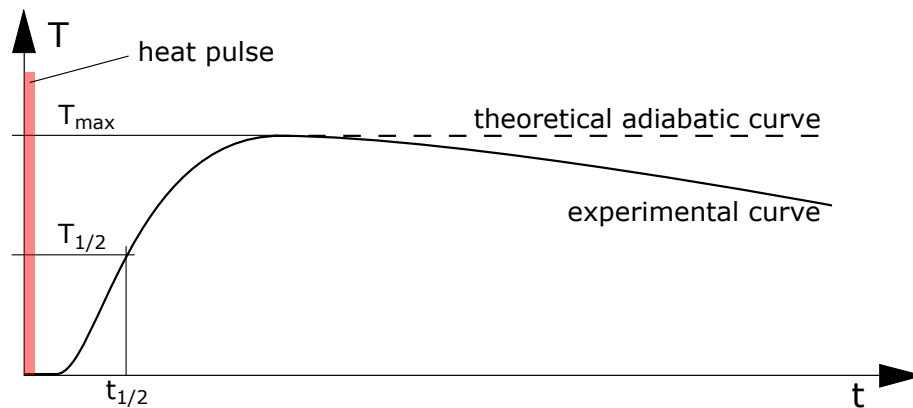


FIGURE 3.10: Heat pulse, theoretical adiabatic trend and IR experimental detector response of the sample back side temperature of a LFA experiment

$$a(T) = 1.38 \cdot \frac{\delta^2}{\pi^2 \cdot t_{1/2}} \quad (3.25)$$

The time $t_{1/2}$ is the time required to reach the half of the maximum of the measured IR detector signal from the back side of the sample. Equation 3.25 indicates, that for theoretical adiabatic conditions, the thickness δ as well as the measured half time $t_{1/2}$ are sufficient to calculate the thermal diffusivity $a(T)$ of a solid sample.

As shown in figure 3.10, the theoretical adiabatic case shows a deviation in comparison to experimental curves. This is due to heat losses by radiation or convection which are not considered in the *Parker* model. Furthermore, it has been seen, that pulse-durations near the $t_{1/2}$ of the sample could lead to wrong $a(T)$ values. Several models for the evaluation of the measured $a(T)$ were already developed and can be applied on the experimental detector signal to handle heat losses and pulse width corrections [44, 45, 46, 47]. Also models to overcome semitransparent samples were proposed by [48].

3.8.4 Specific heat capacity measurements

According to [49] LFA can also be used to measure $c_p(T)$ of a sample by a comparative method. It requires a uniform laser beam irradiation which leads to the same heat flux density \dot{q} on the irradiated face of sample and reference. Furthermore, both samples have to have the same absorptivity of the irradiated face.

$$\Delta T_{Ref} = \frac{A_{Ref}}{m_{Ref} \cdot c_{p,Ref}} \cdot \dot{q} \quad (3.26)$$

$$\Delta T_S = \frac{A_S}{m_S \cdot c_{p,S}} \cdot \dot{q} \quad (3.27)$$

$$c_{p,S} = \frac{A_S \cdot m_S \cdot \Delta T_S}{A_{Ref} \cdot m_{Ref} \cdot \Delta T_{Ref}} \quad (3.28)$$

The measured $c_p(T)$ values of [49] on different materials like molybdenum, glassy carbon, tungsten and zirconia showed a deviation within 6 % of the reference values derived by this method.

3.9 Transient Hot Bridge - THB

The THB method is a transient method to measure thermal conductivity λ based on a thermoelectric sensor. The sensor technology was developed by the Physikalisch-Technische Bundesanstalt in Germany and published 2006 in [50].

3.9.1 Measurement principle

The THB sensor is an enhancement of the Transient Hot Strip (THS) method, first published in 1979 in [51], based on electrical conducting strips which can act as Joule heaters and resistance thermometers. A current source delivers a constant heating current, leading to a heating of its surroundings (e.g. a solid specimen) and the sensor itself. The measured voltage over time $U(t)$ due to the changing electrical resistance of the strip is used for the evaluation of λ , a and c_V . One major drawback of the THS method is a small electrical resistance leading to small $U(t)$ signals and a low Signal-to-Noise Ratio (SNR).

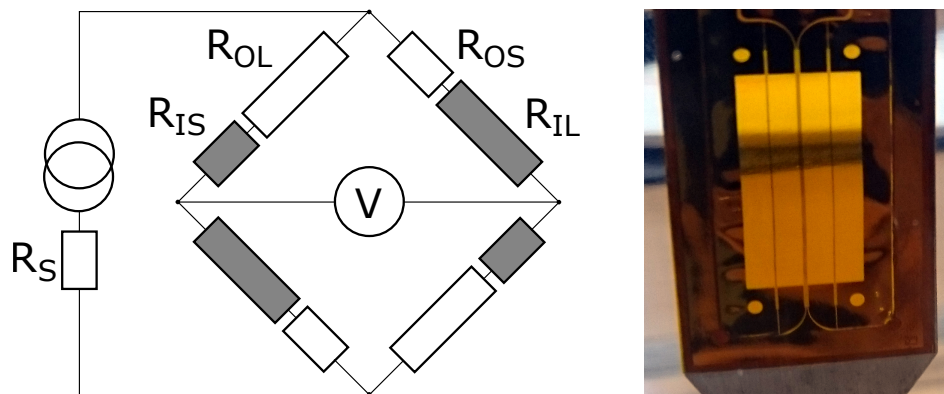


FIGURE 3.11: Equivalent circuit diagram and THB foil sensor

The THB sensor design is based on a printed circuit foil of nickel between two polyimide sheets as shown in figure 3.11. The sensor consists of meander formed strips, where two strips form one tandem strip. Each meander consists of a short strip (R_{OS} or R_{IS}) and a long strip (R_{OL} or R_{IL}). In sum, four tandem strips are configured as *Wheatstone* bridge as shown in the equivalent circuit diagram in figure 3.11. The direct current source delivers the heating current and a shunt resistance R_S is needed for the actual current measurement.

This setup allows to increase the electrical resistance due to longer current paths and a higher sensitivity of the measured $U(t)$ due to the symmetric bridge. At isothermal conditions the bridge is balanced. Applying a constant current leads to an inhomogeneous temperature field around the THB sensor due to the spatial arrangement of the strips. While the outer strips (R_{OS} , R_{OL}) are on the border area of the sensor, the inner strips (R_{IS} , R_{IL}) are going through the center of the sensor area. This leads to an unsymmetrical bridge and

a voltage change over time $U(t)$, which is recorded and used for further evaluation of the thermophysical properties.

3.9.2 Calibration

In the study of [50] two reference materials were used to compare the measured $\lambda_S(T)$ to available literature data. The first reference used was Polymethyl Methacrylate (PMMA) which was already measured in a round robin test as shown in [52] with $\lambda_{Ref}(20\text{ }^\circ\text{C}) = 0.1934\text{ W m}^{-1}\text{ K}^{-1}$. The second reference is a borosilicate crown glass which was evaluated by [50, 53] with $\lambda_{Ref}(20\text{ }^\circ\text{C}) = 1.09\text{ W m}^{-1}\text{ K}^{-1}$.

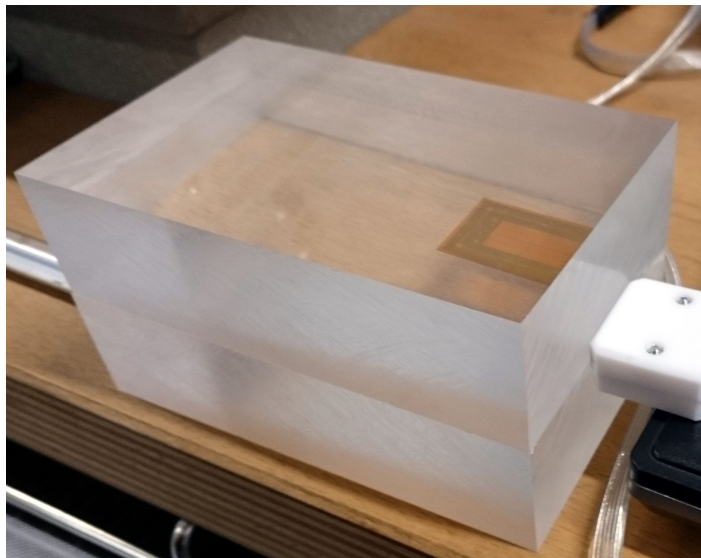


FIGURE 3.12: THB sensor calibration setup with PMMA

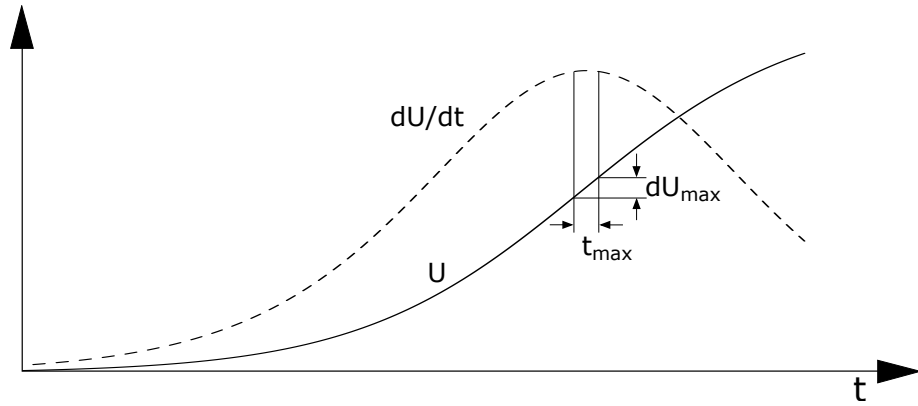
The foil sensor is placed between two blocks of the reference material. For the calibration experiment, the current temperature T_S as well as the thermal conductivity λ_{Ref} of the reference sample have to be known. Furthermore, the heating current of the current source I as well as the measurement time t have to be defined.

The calibration experiment is an iterative process where the measured $\lambda_S(T)$ is compared to $\lambda_{Ref}(T)$ and a sensor specific calibration factor is calculated. This process ends when a specified allowed deviation between $\lambda_S(T)$ and $\lambda_{Ref}(T)$ is reached.

3.9.3 Thermal conductivity measurements

As shown in figure 3.11 a voltmeter is used to measure $U(t)$ caused by a change of the electrical resistances due to the inhomogeneous temperature field on the sensor area.

As described in [50], the maximum slope of the measured $U(t)$ curve is proportional to the thermal conductivity $\lambda_S(T)$. The relation between the measured THB signal $U(t)$ and the measured $\lambda_S(T)$ is described in equation 3.29.

FIGURE 3.13: Sketch of a possible THB signal $U(t)$ and its first derivative

$$\lambda_S = \frac{\alpha \cdot R_{eff}^2 \cdot \ln(t_{max})}{4 \cdot \pi \cdot l_{eff} \cdot dU_{max}} \cdot \left(\frac{I}{2}\right)^3 \cdot m \quad (3.29)$$

The temperature coefficient of the specific electrical resistance of the nickel foil is described by α , l_{eff} is the thermal effective length and R_{eff} corresponds to the effective electrical resistance, dU_{max} and $\ln(t_{max})$ describe the maximum slope of the measured $U(t)$ curve as shown in figure 3.13, I is the current from the current source and m is a dimensional factor for the distances of the inner and outer strip of the sensor. For a more detailed description on the electrical and thermal model of the THB sensor the reader is referred to [50].

3.10 Heat Flow Meter - HFM

The HFM technique is a steady-state method to measure the thermal conductivity $\lambda(T)$ of solid materials by applying a defined temperature difference ΔT across the sample and measure the heat flow ϕ over a defined area resulting in the heat flux density \dot{q} .

3.10.1 Measurement principle

The explained measurement principle is based on a HFM with two temperature controlled plates and a slab sample between them (symmetrical arrangement with one sample).

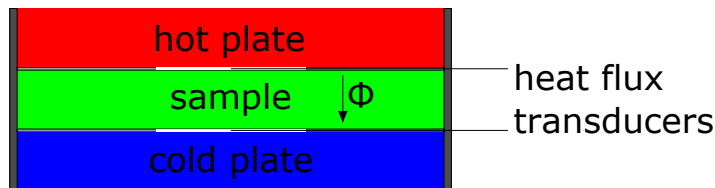


FIGURE 3.14: Sketch of a HFM with a symmetrical arrangement and one slab sample

The depicted arrangement is one of several possible arrangements which are described in the according standards [54, 55, 56]. These standards are mainly focused on building materials and products with an upper limit of $\lambda_{max}(T) = 2 \text{ W m}^{-1} \text{ K}^{-1}$.

As already mentioned before, it is a steady-state measurement, which needs an equilibrium regarding T and ϕ . When this equilibrium is reached, the indicated values are used for the determination of $\lambda(T)$. For accurate results of the constant one directional heat flow ϕ , it is necessary to have plane-parallel, homogeneous samples between the plates. Additionally, a thermal insulation or a guarded ring, which is reproducing the thermal gradient ΔT of the sample, are used to reduce heat flows to the margin area of the sample. Another tactic to overcome the margin area effects is to place the heat flux transducers in the center of the HFM system, as shown in figure 3.14.

To measure materials with high thermal conductivity $\lambda(T)$ it is recommended [54] to prepare thicker samples to increase the overall thermal resistance $R_{th}(T)$. Furthermore, it is stated that the influence of the thermal contact resistance $R_{th}(T)$ between the plates and the sample increases with a low R_{th} of the sample.

New commercial available HFM devices can measure the current thickness $\delta(T)$ and the applied pressure $p(T)$ during the measurement run. Also a new approach to measure $c_p(T)$ by applying a HFM device has been shown by [57].

3.10.2 Calibration

According [54] calibration is achieved by comparing the thermal resistance $R_{th,S}$ of a sample to the thermal resistance $R_{th,R}$ of a standard reference material. Under the assumption of a constant \dot{q} , ΔT and T_{mean} , a relation between ϕ_S , ϕ_R , $R_{th,R}$ and $R_{th,S}$ according 3.30 can be drawn.

$$\frac{R_{th,S}}{R_{th,Ref}} = \frac{\phi_{Ref}}{\phi_{Sam}} \quad (3.30)$$

This relation is a function of T_{mean} and is only valid in the measured temperature range.

Standard reference materials are provided by several metrology institutes. A prominent standard reference used for HFM is the Standard Reference Material (SRM) 1450d, a fibrous-glass board for thermal conductivity measurements between 7 to 65 °C provided by the National Institute of Standards and Technology (NIST). The SRM 1450d is an insulating material with $\lambda(293 \text{ K}) = 0.032 \text{ W m}^{-1} \text{ K}^{-1}$.

3.10.3 Thermal conductivity measurements

The heat flux transducers shown in 3.14 are usually several thermocouples measuring an electrical voltage U proportional to the heat flux density \dot{q} . This principle is similar to the measurement principle of a DSC sensor as already shown in section 3.6. The measured \dot{q} is influenced by the thermal conductivity of the sample λ_S , the thickness of the sample δ_S , the temperature difference ΔT and the area A .

$$\dot{q} = \frac{\phi}{A} = \lambda \frac{\Delta T}{\delta} \quad (3.31)$$

To ensure that the measured \dot{q} is accurate, a calibration with a standard reference has to be done. The calibration delivers the relation between the measured U , caused by the thermocouples in the heat flux transducer, and the actual heat flow density \dot{q} through a calibration function.

$$\dot{q}(T_{mean}) = N(T_{mean}) \cdot U(T_{mean}) \quad (3.32)$$

$$\lambda(T_{mean}) = N(T_{mean}) \cdot U(T_{mean}) \cdot \frac{\delta}{\Delta T} \quad (3.33)$$

3.11 Push rod dilatometry

Push rod dilatometry is a specific method of dilatometry to determine the linear thermal expansion of a solid as a function of temperature $\alpha(T)$.

3.11.1 Measurement principle

According to [37] a typical push rod dilatometer consists of a furnace, a displacement transducer, a sample carrier and a push rod.

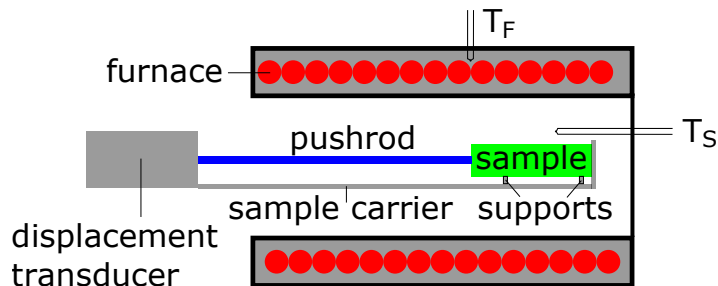


FIGURE 3.15: Sketch of a horizontal push rod dilatometer

The sample is placed on supports which are typically made from the same material as the sample carrier and the push rod (e.g. Al_2O_3). When the sample is heated, the thermal expansion of the sample leads to a displacement of the push rod, which is recorded by the displacement transducer. Common displacement transducers used are Linear Variable Displacement Transformer (LVDT) based on electromagnetic induction. Furthermore, the temperature at the sample T_S is recorded during the whole measurement run.

It has to be noticed that all built-in components (sample carrier, push rod, supports) expand during the heating segment of the furnace. Due to that, a correction function is necessary to separate both expansion behaviors. Additionally, the push rod has to "push" the sample with a minimal force to ensure a contact between sample and push rod.

There are several different configurations of push rod dilatometers used depending on the application and needed accuracy. Special types are quenching dilatometers as shown in [58] and differential dilatometers as shown in [59].

3.11.2 Calibration

Temperature calibration

As described in [60] for the sample temperature T_S an accuracy of thermocouples according [61] is required. This can be fulfilled by external calibration of the used thermocouple according ITS-90.

Another possibility is the use of the ITS-90 standard reference materials in the dilatometer measurement. Measuring the melting process of an ITS-90 standard would lead to a sharp

response of the displacement transducer. This indication could be used for the relation to the actual melting temperature of the reference standard.

Correction function

As shown in [60] it is necessary to determine a correction function based on standard reference materials with known thermal expansion. The used standard reference material should have the same geometrical dimensions as well as related thermal properties (α , λ , c_p) as the following sample body. Typical standard reference materials are sapphire (α -Al₂O₃), platinum or fused silica. Both, the standard reference material and the sample body have to be measured under identical conditions.

3.11.3 Linear thermal expansion

The linear thermal expansion coefficient can be defined as shown in equation 3.34.

$$\alpha(T) = \frac{1}{l_0} \cdot \frac{l(T) - l_0}{T - T_0} = \frac{\Delta l}{l_0 \cdot \Delta T} \quad (3.34)$$

The length l_0 is the sample body length at T_0 . The definition of $\alpha(T)$ refers to an initial temperature $T_0 = 20^\circ\text{C}$. Due to mathematical reasons α shows a singularity at the reference temperature T_0 which has no physical background. As shown before, a correction function is needed to eliminate the expansion behavior of the built-in components. Upon measurement of a sample and a reference under identical conditions, a correction according 3.36 can be calculated.

$$\left. \frac{\Delta l_S}{l_{0,S}} \right|_{corr} = \left. \frac{\Delta l_S}{l_{0,S}} \right|_{ind} + \left(\left. \frac{\Delta l_{Ref}}{l_{0,Ref}} \right|_{lit} - \left. \frac{\Delta l_{Ref}}{l_{0,Ref}} \right|_{ind} \right) \quad (3.35)$$

$$\alpha_S(T) = \frac{1}{\Delta T} \cdot \left. \frac{\Delta l_S}{l_{0,S}} \right|_{corr} \quad (3.36)$$

For further information on dilatometry and different applied standards, the reader is referred to [60, 37].

Chapter 4

PCM measurement methods and evaluated thermophysical properties

4.1 Introduction

This chapter represents the assets and drawbacks of several measurement methods to analyze enthalpy changes and thermal transport properties of organic PCM based on DSC, LFA and THB experiments. While the first part addresses the challenges in measuring characteristic temperatures T , phase transition enthalpies Δh_t and specific heat capacity $c_p(T)$ applying the DSC, the second part concentrates on evaluation of thermal diffusivity $a(T)$ and thermal conductivity $\lambda(T)$ measurements of organic PCM based on LFA and THB experiments.

The developed measurement protocols as well as experimental results of different organic PCM were already reported in different journals or conference proceedings. Contributions to the developed DSC measurement protocols were presented at "Die 21. Kalorimetrietage" at the Physikalisch-Technische Bundesanstalt (PTB) in Braunschweig, Germany [62] and a detailed description of the developed protocols as well as the results of a round robin test on octadecane paraffin wax are documented in [63]. Content about DSC calibration, specific heat capacity evaluation $c_p(T)$ and thermal conductivity $\lambda(T)$ of organic PCM are published with the title "Thermal Analysis on Organic Phase Change Materials for Heat Storage Applications" in [64]. The application of the developed measurement protocols on High Density Polyethylene (HDPE) as well as sugar alcohols and synthetic derivatives are contributed to [65, 66] and [67], respectively.

As participant in the work of the *International Energy Agency (IEA) Solar Heating and Cooling (SHC) Task 42* joint with the *Energy Conservation through Energy Storage (ECES) Annex 29* about compact TES systems, the described experiments and results on different organic PCMs were contributed to the subtask "Test and Characterization". The analyzed materials were provided by the participants and the measured results were used for round robin tests, comparing the measured data of several different heat flow DSCs. Based on this work, a measurement protocol was developed by all participants in this *IEA SHC Task 42*. This

procedure was published in a conference paper with the title "Standardization of PCM Characterization via DSC" [63] and was presented at the *IEA ECES Greenstock 2015* conference in Beijing. Additionally, this paper was honored with the "*Best PCM Paper Award*" for the most innovative PCM contribution to the conference.

4.2 PCM measurements via DSC

As already described in section 2.3.3, there are several requirements on a suitable PCM for a LTES application. The DSC is a recognized measurement technique to analyze the required material parameters such as phase transition temperatures T_t or phase transition enthalpies Δh_t as well as reproducibility and cycling stability of these quantities. Before a PCM can be measured in a DSC, following prerequisites have to be ensured:

- The measured DSC sample is representative for the bulk PCM
- No interaction between the PCM sample and its surroundings (crucible material, gas conditions)
- No decomposition or irreversible changes of the PCM in the measured temperature range

In this section, the application of the DSC method on different PCMs is shown. At first, the different approaches of temperature, heat and heat flow calibration are discussed and compared. After that, the challenges and possible solutions to measure the enthalpy change Δh_t , including the specific heat capacity $c_p(T)$ of the solid and the liquid phase as well as the phase transition enthalpy Δh_t are demonstrated on two different possible organic PCMs. Subsequently, the evaluation of specific heat capacity $c_p(T)$ and corresponding uncertainties are discussed and, finally, DSC cycling tests on a HDPE material are presented.

4.2.1 DSC equipment and setup

The following DSC experiments were conducted on a disc type heat flux DSC from NETZSCH, the DSC 204 F1 Phoenix. A detailed description on the measurement principle can be found in section 3.6.

The integrated furnace block covers a temperature range $T = -180$ to 700°C using a silver furnace for heating and liquid or gaseous nitrogen as cooling fluid. The implemented DSC sensor is based on Type E thermocouples and placed in the center of the furnace chamber. Two separate silver lids are used to close the furnace block after placement of the crucibles. To adjust the gas conditions during the measurement inside and outside the furnace block, two different gas inlets are available. A purge gas flow directly in contact with the DSC sensor and the crucibles and a protective gas flow on the outside of the furnace block for protecting the system components from gaseous products from the sample. Both gas flows are controlled by separate MFCs.

4.2.2 Calibration experiments

Due to the fact, that temperature and heat calibration in the heat flow DSC is based on phase changes of different substances (s. section 3.6.2) it is important to understand the influence of the heating rate β on the evaluated extrapolated initial temperature $T_{e,i}$ of the phase transition and the evaluated phase transition enthalpy Δh_t .

Temperature, heat and heat flow calibrations were performed according to DIN 11357 [33]. For temperature and heat calibration, pure substances like adamantane ($C_{10}H_{16}$), indium, tin, bismuth and zinc were applied. For heat flow calibration, a sapphire ($\alpha\text{-Al}_2\text{O}_3$) with known $c_p(T)$ was used as reference standard. In the calibration measurements different heating rates ($\beta = 2\text{ K min}^{-1}$, 5 K min^{-1} and 10 K min^{-1}) are used to analyze deviations in the determined temperatures $T_{e,i}$ and sensitivities $S_{DSC}(T)$ of the DSC sensor. Aluminum crucibles with $V = 25\text{ }\mu\text{l}$ volume and cold welded lids were filled with the different calibration substances. All measurements were done in a nitrogen gas atmosphere with a gas flow of 40 ml min^{-1} .

Temperature calibration results

The results of the measured temperature difference ΔT between the evaluated $T_{e,i}$ of the phase transition processes and the corresponding literature values T_{lit} (s. [33]) are compared.

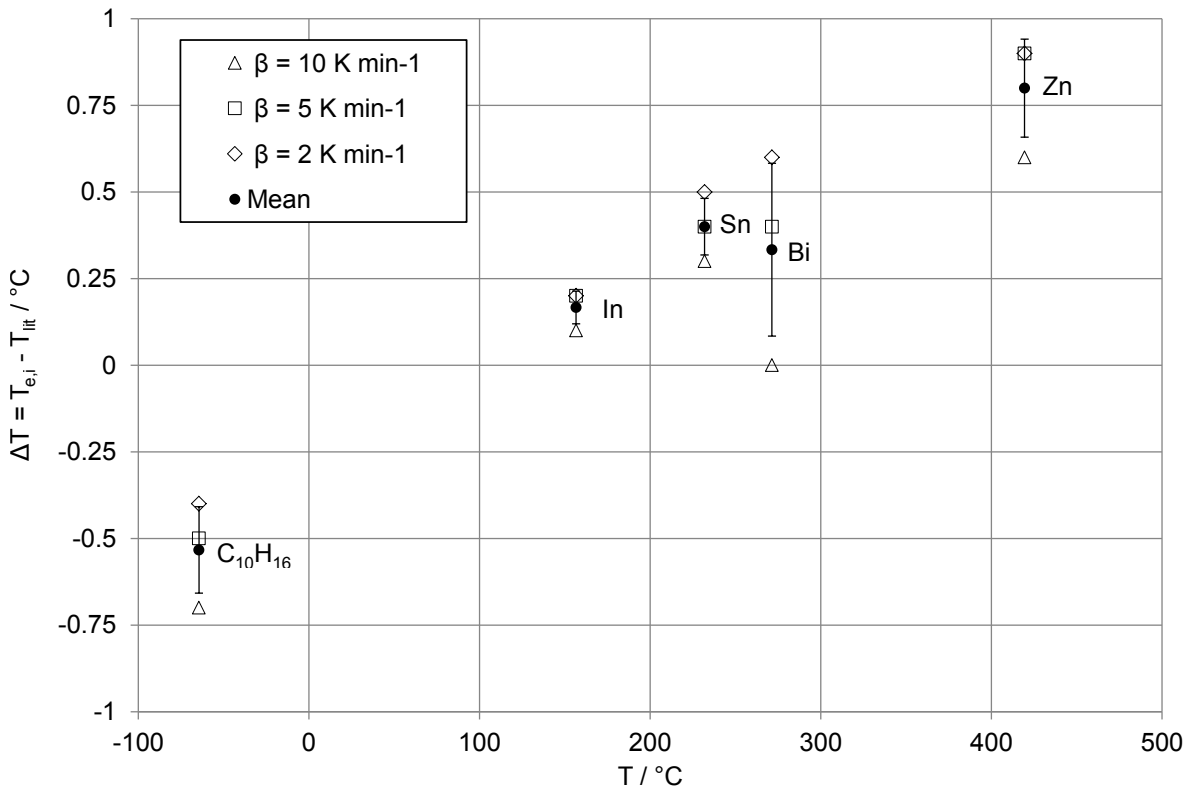


FIGURE 4.1: Extrapolated initial transition temperatures $T_{e,i}$ of adamantane ($C_{10}H_{16}$), indium, tin, bismuth and zinc at $\beta = 2\text{ K min}^{-1}$, 5 K min^{-1} and 10 K min^{-1}

Figure 4.1 indicates, that faster heating rates lead to higher evaluated $T_{e,i}$ of the phase transition process. Furthermore, some substances show higher standard deviations of the evaluated mean $T_{e,i}$. This effect may be attributed to the thermal conductivity λ of the examined reference. In table 4.1 the material properties for T_t , Δh_t and λ of the used references are summarized.

	T_t °C	Δh_t J g ⁻¹	$\lambda(0^\circ\text{C})$ W m ⁻¹ K ⁻¹	Reference
Adamantane	-64.43	24.05	-	[68]
Indium	156.6	28.62	84	[33, 69]
Tin	231.93	60.40	68	[33, 69]
Bismuth	271.4	53.84	8	[33, 70]
Zinc	419.53	108.11	121	[33, 69, 3]

TABLE 4.1: Material properties T_t , Δh_t and λ of the applied DSC calibration references

Heat calibration results

The measured DSC signals of the different phase transitions in the temperature calibration can also be used to determine the sensitivity $S_{DSC}(T_t)$ of the DSC sensor. As shown in equation 3.15 on page 28, $S_{DSC}(T_t)$ is evaluated for each phase transition at $\beta = 2 \text{ K min}^{-1}$, 5 K min^{-1} and 10 K min^{-1} . A linear baseline U_{BL} between T_i and T_f for each heating rate β was constructed.

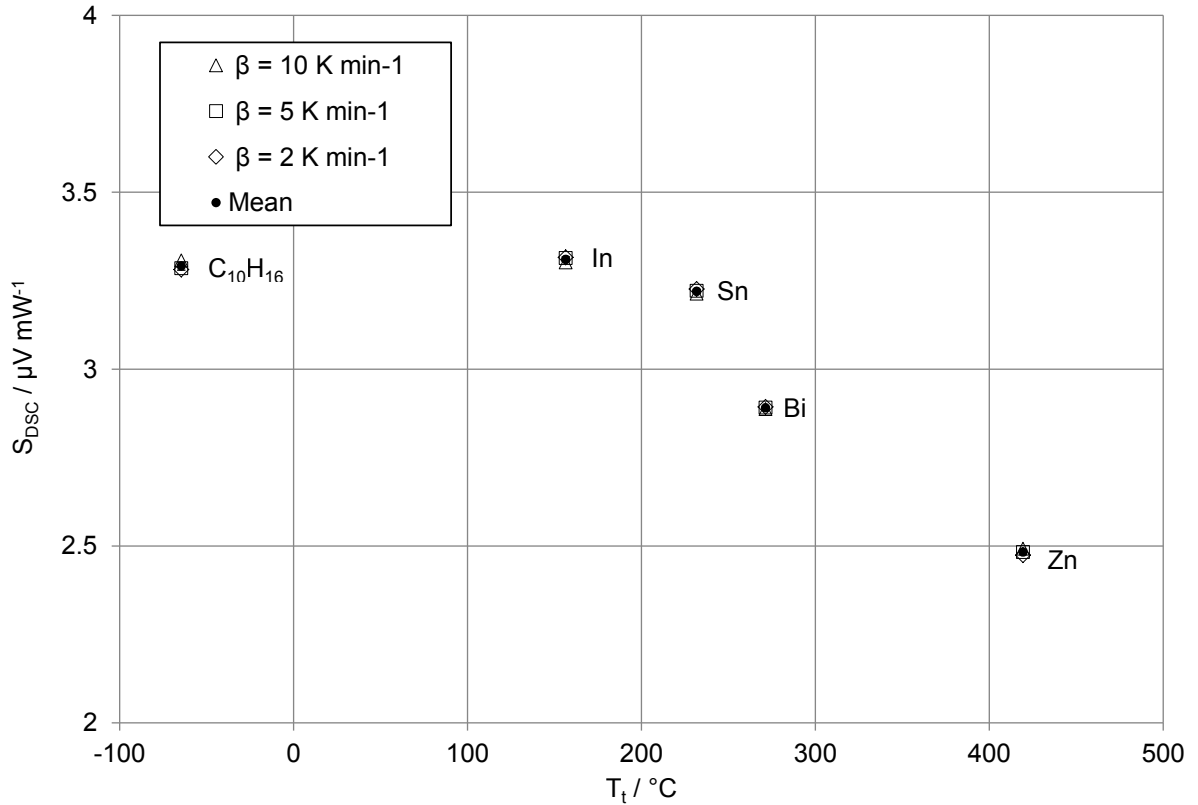


FIGURE 4.2: Evaluated sensitivity $S_{DSC}(T_t)$ of the DSC sensor based on adamantane ($\text{C}_{10}\text{H}_{16}$), indium, tin, bismuth and zinc transitions at $\beta = 2 \text{ K min}^{-1}$, 5 K min^{-1} and 10 K min^{-1}

As it can be seen in figure 4.2 $S_{DSC}(T_t)$ is decreasing with temperature and there is almost no significant change at different heating rates β .

Heat flow calibration results

Another possibility to determine the sensitivity $S_{DSC}(T)$ of a DSC is the use of a heat flow calibration (s. 3.6.2 on page 28). Three zero line measurements from $T = -100$ to 500 °C with empty aluminum crucibles at $\beta = 2 \text{ K min}^{-1}$, 5 K min^{-1} and 10 K min^{-1} were performed. Afterwards, a standard reference $\alpha\text{-Al}_2\text{O}_3$ sapphire with a mass of $m = 42.17 \text{ mg}$ was placed into the sample side crucible and measured in the same temperature range with the defined heating rates. Furthermore, one additional run with $\beta = 10 \text{ K min}^{-1}$ was conducted, to analyze the repeatability at the same heating rate.

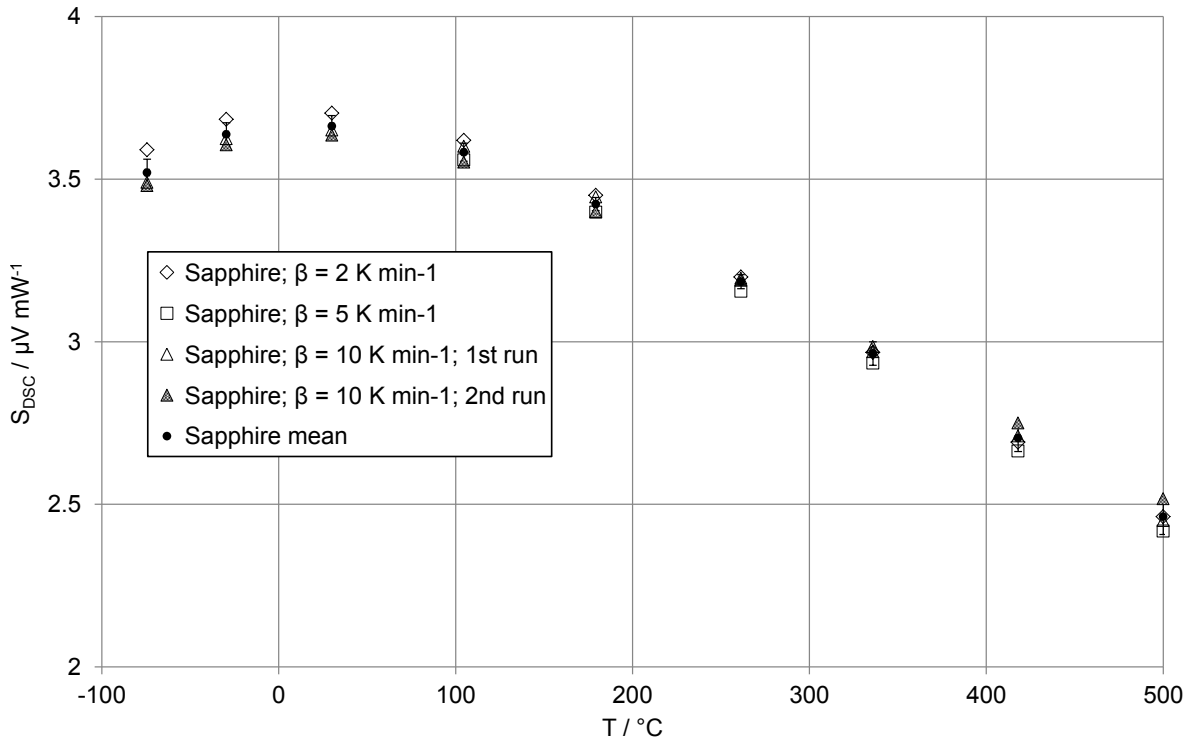


FIGURE 4.3: Evaluated sensitivity $S_{DSC}(T)$ of the DSC sensor based on standard reference $\alpha\text{-Al}_2\text{O}_3$ sapphire measurements at $\beta = 2 \text{ K min}^{-1}$, 5 K min^{-1} and 10 K min^{-1}

Figure 4.3 represents the evaluated sensitivity $S_{DSC}(T)$ according equation 3.16. The uncertainty bars indicate the standard deviation on the measured results, which show higher deviations at lower and higher temperatures. The evaluated $S_{DSC}(T)$ at $\beta = 10 \text{ K min}^{-1}$ shows also larger deviations at high temperature. Interestingly, one conclusion that can be drawn from this survey is that there is no significant connection between the evaluated $S_{DSC}(T)$ and the heating rate β .

Comparison of heat and heat flow calibration

Figure 4.4 compares the evaluated sensitivity $S_{DSC}(T)$ based on heat and heat flow calibrations under the same experimental conditions. The depicted mean values are calculated over the results of the different heating rates, the uncertainty bar is defined by the standard deviation of the single results.

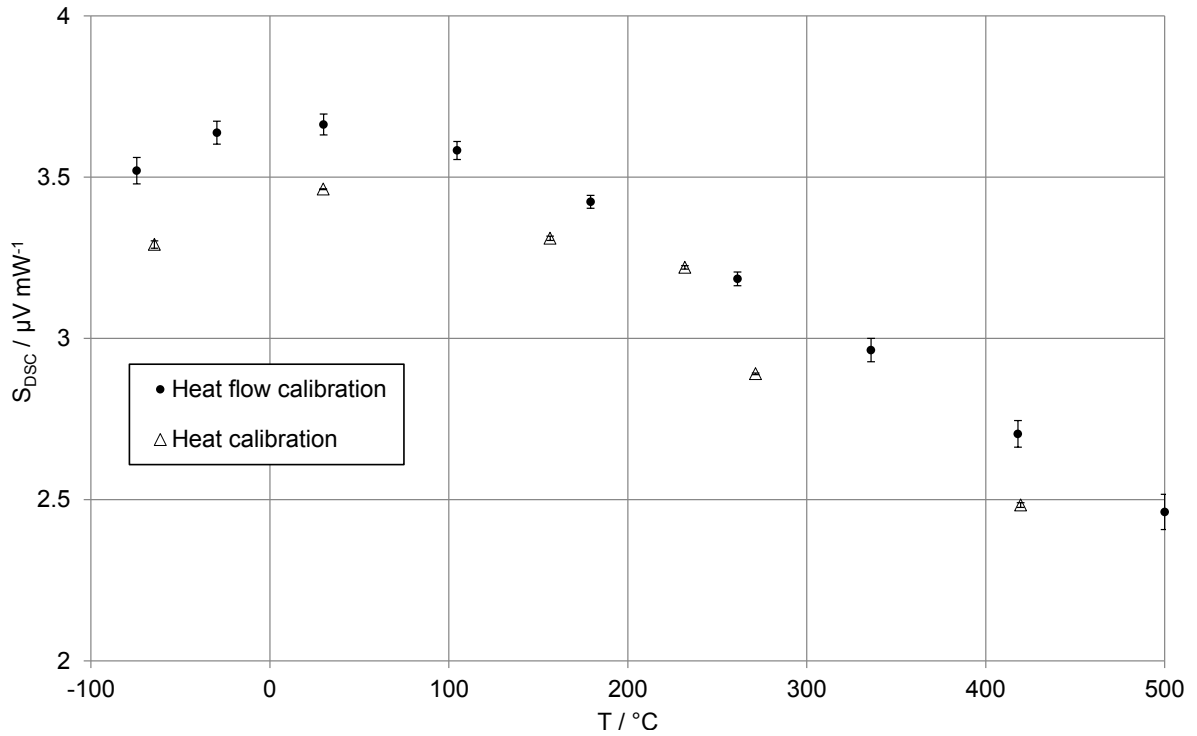


FIGURE 4.4: Comparison of the sensitivity $S_{DSC}(T)$ based on heat and heat flow calibrations under the same experimental conditions

The heat calibration shows hardly any heat rate dependency but a low temperature resolution due to the small amount of different reference standards. This small amount of data as well as runaway values allow no heat calibration function for the $S_{DSC}(T)$ without a mathematical weighting of single substances.

The heat flow calibration also shows hardly any heat rate dependency with the investigated heating rates. As shown in equation 3.16, the temperature resolution only depends on the heating rate β and the time resolution of the data acquisition system. The depicted values in figure 4.4 only show an extraction of the available data. Due to that, a smooth polynomial function for $S_{DSC}(T)$ can be modeled.

The most significant deviation is the difference in $S_{DSC}(T)$ values between heat and heat flow calibrations. Heat flow calibrations based on the $c_p(T)$ of the used reference standards lead to higher $S_{DSC}(T)$ values than the shown heat calibration based on the transition enthalpies Δh_t of the used reference substances. This result is connected to the temperature differences ΔT measured by the DSC sensor (s. figure 3.3 and 3.4). A phase transition (depending on mass m and phase transition enthalpy Δh_t) leads to bigger differences ΔT and a bigger heat flow rate ϕ compared to the ΔT caused by heat capacity differences. A similar statement was done by [30] by comparing heat flow calibrations with different reference standard masses. Due to that, it is assumed that the evaluated sensitivity $S_{DSC}(T)$ strongly depends on the occurring heat flow rate ϕ .

In order to have an accurate temperature calibration, the influence of the thermal conductivity the reference material is significant. Due to that, slow heating rates are necessary to reduce the uncertainty in temperature measurements in the DSC.

4.2.3 Enthalpy curve measurement of organic PCMs

Heating and cooling rate tests

Based on the measurement protocols defined in [63] preliminary DSC measurements are necessary, to identify a suitable heating and cooling rate for the analyzed PCM. As already shown with the temperature calibration using reference standards in 4.2.2, the heating rate β effects the evaluated $T_{e,i}$ of the phase transition peak. A higher accuracy in the temperature measurement can be achieved by lowering the heating rate β .

According [63] it was defined, that several melting and solidification cycles (heating and cooling) of the PCM should be measured. The heating and cooling rate β should be reduced by a half for each cycle. The procedure recommends, that a suitable β is reached when the peak temperature difference between two phase transition peaks in the heating or the cooling cycle of the DSC signal is $\Delta T_{pk} \leq 0.2$ K.

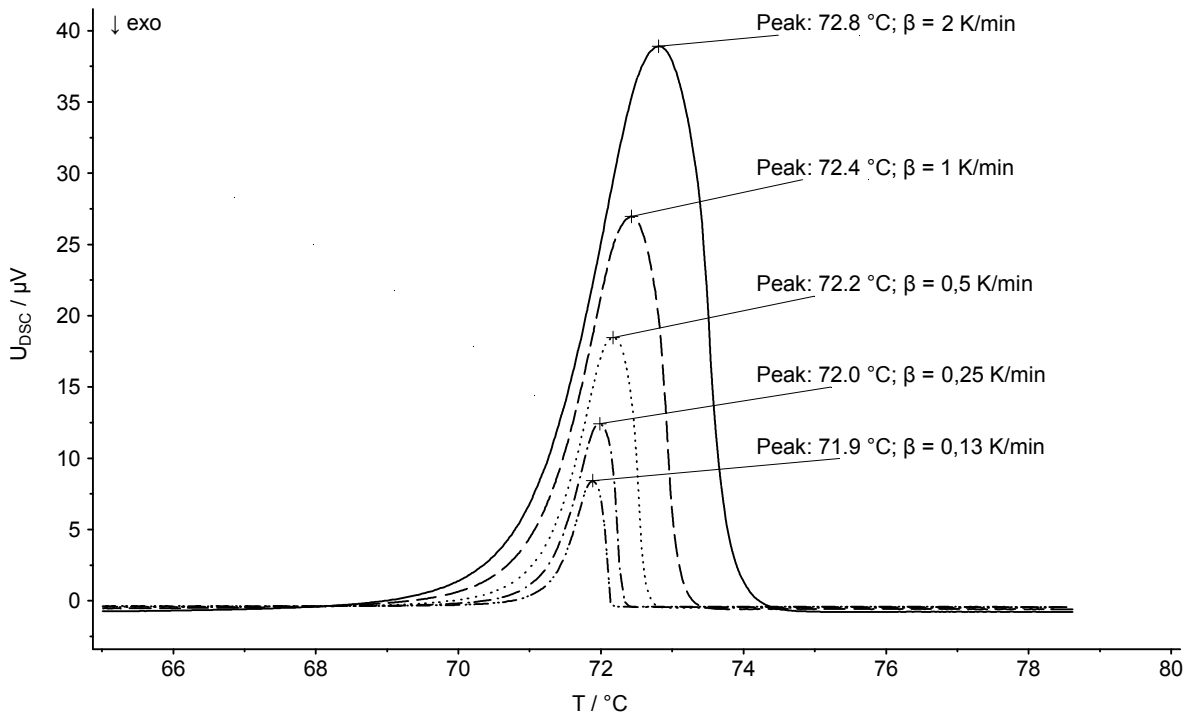


FIGURE 4.5: Heating rate test on an organic PCM Rubitherm RT70HC

Figure 4.5 depicts the heating rate test for the melting of a commercially available organic PCM Rubitherm RT70HC in the DSC. Starting from $\beta = 2 \text{ K min}^{-1}$, the heating rate was reduced by a half until the peak temperature difference was $\Delta T \leq 0.2$ K. In case of the shown paraffin wax, further investigations were done with $\beta = 0.25 \text{ K min}^{-1}$.

Without doubt, the measured peak temperature T_{pk} in a DSC experiment is connected to β , but it should be emphasized, that it depends on the sample mass m_S as well. For that

reason, it has to be found a trade-off between the m_S being representative for the bulk and β .

Calibration

Following the protocol used in [63], a temperature and enthalpy (heat or heat flow) calibration should be done with the evaluated heating rate in the measured temperature range.

When examined critically, this approach turns out to be limited. As already shown in section 4.2.2, it is recommended to use slower heating rates to evaluate the $T_{e,i}$ of the measured reference standards. The sensitivity $S_{DSC}(T)$ of the DSC sensor strongly depends on the heat flow rate ϕ as shown in figure 4.4 and, furthermore, very slow heating rates lead to a small ΔT before and after the phase transition area and to a small SNR. Therefore, it is questionable, if one calibration approach is enough to evaluate ΔH in the phase transition area as well as before and after the phase transition.

Measurement procedure and data representation

The complete measurement protocol defined in [63] was applied on a laboratory grade octadecane paraffin wax for the round robin test. In [71] a melting temperature of $T_t = 28.15^\circ\text{C}$ and a phase transition enthalpy of $\Delta h_t = 241.65\text{ J g}^{-1}$ is reported for the pure octadecane.

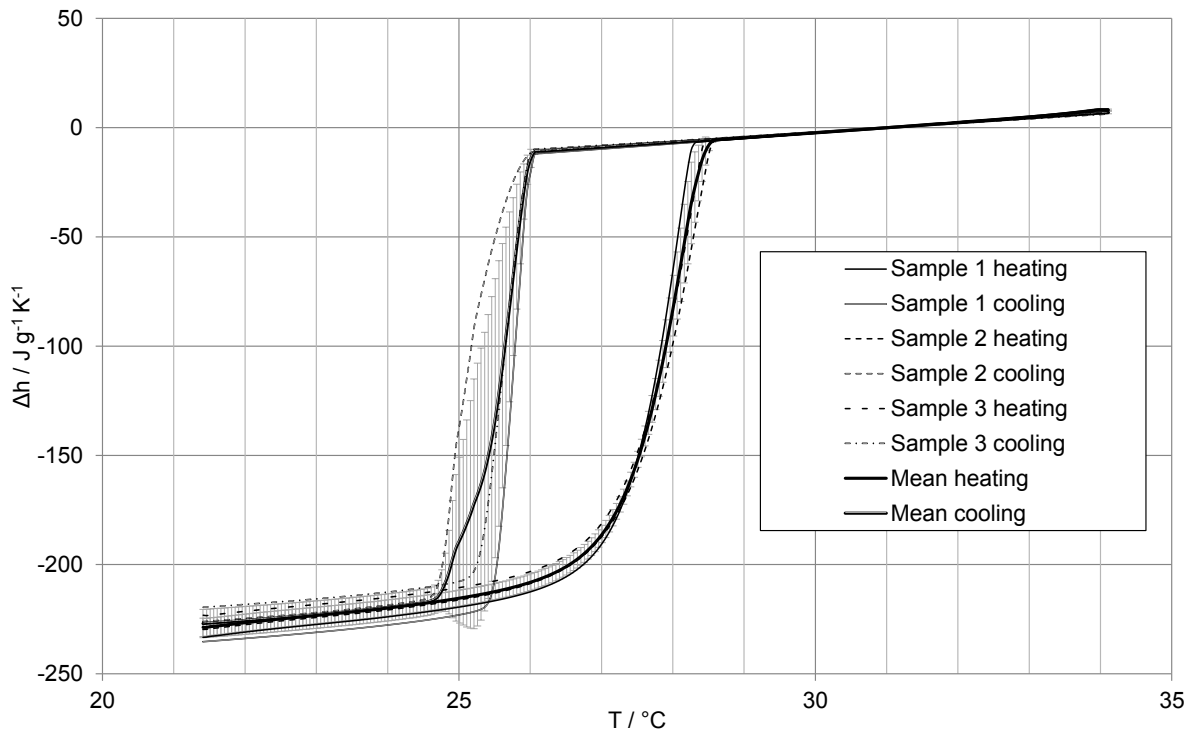


FIGURE 4.6: Data representation of the enthalpy change Δh of a paraffin wax PCM from a DSC measurement according [63]

The heating and cooling rate test revealed a $\beta = 0.25\text{ K min}^{-1}$ for a sample mass of $m_S \approx 10\text{ mg}$. After defining the heating and cooling rate β , the temperature and heat calibration of the

DSC sensor based on water, gallium and indium was performed. Subsequently, a measurement protocol with four heating and cooling segments between $T = 21$ to 36 °C on three different samples was defined.

The analysis of the heat flow is based on [36] as already shown in section 3.6.3, which requires additional zero line measurements and a baseline construction between the isothermal segments before and after the heating or cooling segment. The data is represented as an enthalpy change Δh versus temperature T with a defined reference temperature, at which $\Delta h = 0 \text{ J g}^{-1}$.

Figure 4.6 represents the results of the measured octadecane paraffin wax. A reference temperature of $T = 31$ °C for $\Delta h = 0 \text{ J g}^{-1}$ was defined. The measured heating segments show reproducibility over all measured samples. In the cooling segment, strong deviations occur which might be connected to different nucleation behavior of the different samples.

The evaluated extrapolated initial temperature for melting was $T_{e,i} = 27$ °C and for the crystallization $T_{e,i} = 26.1$ °C. Comparing Δh between $T = 24$ and 31 °C results in $\Delta h = -219.8 \text{ J g}^{-1}$ with $\sigma = 3.7 \text{ J g}^{-1}$ for the melting and 219.5 J g^{-1} with $\sigma = 6.2 \text{ J g}^{-1}$ for the crystallization. These results were also used for a round robin test and were contributed to [63].

4.2.4 Specific heat capacity measurements

The work of the IEA SHC Task 42 ECES Annex 29 test and characterization subtask on PCM was mainly focusing on a temperature accurate enthalpy change measurement protocol in the phase transition region. By lowering the heating rate β , the influence of the thermal transport properties of the measured sample could be decreased. The drawback of this protocol is the loss of sensitivity of a disc type heat flow DSC sensor due to small temperature gradients, especially before and after the phase transition. Consequently, a detailed investigation on the specific heat capacity $c_p(T)$ of a PCM was performed.

Material and measurement procedure

The chosen organic PCM is a commercially available material *Rubitherm RT70HC* with a melting temperature range between 69 and 71 °C and a specific heat capacity of $c_p = 2 \text{ J g}^{-1}$ designated by the material manufacturer.

The first part of the experiments are based on the measurement protocol according [63]. The heating rate test for the enthalpy curve evaluation resulted in $\beta = 0.25 \text{ K min}^{-1}$ as already shown in figure 4.5 for a sample mass $m_S \approx 10 \text{ mg}$. Zero line, reference and sample measurements were applied with this heating rate in the temperature range between $T = 55$ and 75 °C. The second part of the experiments are based on $\beta = 10 \text{ K min}^{-1}$, as recommended by DIN EN ISO 11357-4 [35] with a temperature range of $T = 55$ to 85 °C.

All experiments were done in aluminum crucibles with $V = 25 \mu\text{l}$ and cold welded lids in a nitrogen gas atmosphere with 40 ml min^{-1} . Three zero line, three reference ($\alpha\text{-Al}_2\text{O}_3$ sapphire with $m_R = 42.18 \text{ mg}$) and three sample measurements ($m_S \approx 10 \text{ mg}$) were performed yielding 9 individual measurements for each heating rate.

Data analysis and uncertainty calculation

Several zero line, reference and sample material DSC measurements are necessary to determine an expanded combined standard uncertainty u_c of the evaluated $c_p(T)$. As described in DIN EN ISO 11357-4 [35] $c_p(T)$ is evaluated by the following equations, where $U_{0,i}(T)$ are the individual DSC signals of the zero line measurements, $U_{Ref,i}(T)$ the individual DSC signals of the sapphire reference and $U_{S,i}(T)$ the individual DSC signals of the samples, n_0 , n_{Ref} or n_S the number of individual runs for each measurement type, $c_{p,Ref}(T)$ the specific heat capacity of the reference sapphire, m_{Ref} the mass of the reference sapphire and $m_{S,i}$ the mass of the individual sample.

$$\overline{U_0(T)} = \frac{1}{n_0} \sum_{i=1}^{n_0} U_{0,i}(T) \quad (4.1)$$

$$\overline{U_{Ref,corr}(T)} = \frac{1}{n_{Ref}} \sum_{i=1}^{n_{Ref}} U_{Ref,i}(T) - \overline{U_0(T)} \quad (4.2)$$

$$\overline{c_{p,S}(T)} = c_{p,Ref}(T) \cdot \frac{1}{n_S} \sum_{i=1}^{n_S} \frac{m_{Ref}}{m_{S,i}} \cdot \frac{U_{S,i}(T) - \overline{U_0(T)}}{\overline{U_{Ref,corr}(T)}} \quad (4.3)$$

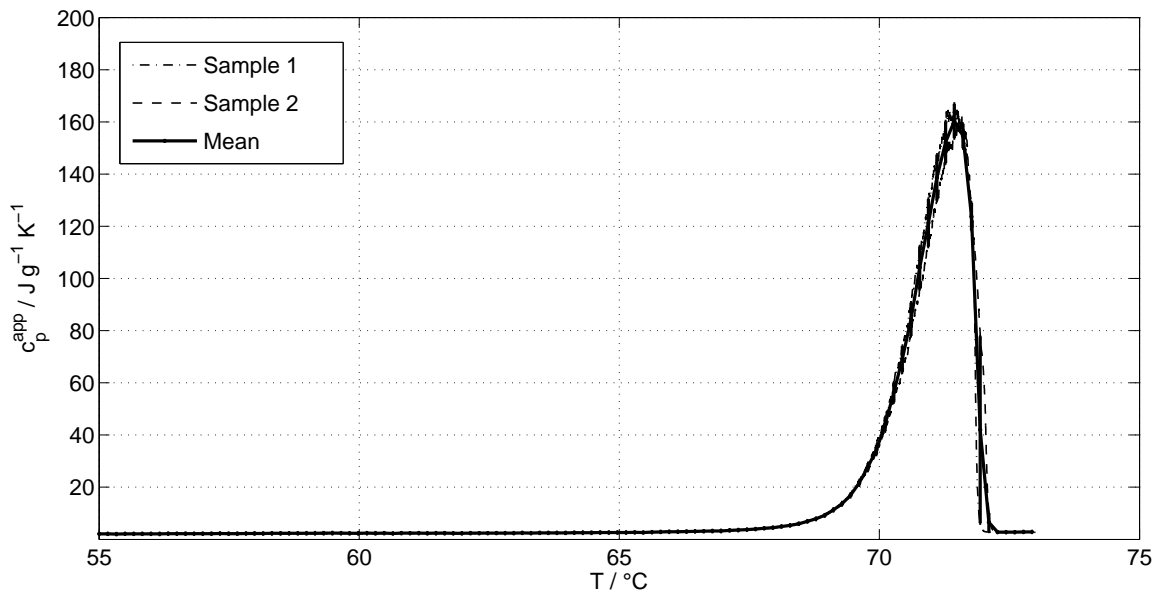
In the next step the expanded combined standard uncertainty calculation based on the propagation of uncertainty with several sensitivity coefficients and a coverage factor of 2 according [72] is calculated with

$$u_{c,95\%}^2 = 2 \left(\left(\frac{\partial c_{p,S}(T)}{\partial U_S(T)} \right)^2 u_{U_S(T)}^2 + \left(\frac{\partial c_{p,S}(T)}{\partial U_{Ref}(T)} \right)^2 u_{U_{Ref}(T)}^2 + \left(\frac{\partial c_{p,S}}{\partial c_{p,Ref}(T)} \right)^2 u_{c_{p,Ref}(T)}^2 + \left(\frac{\partial c_{p,S}(T)}{\partial U_0(T)} \right)^2 u_{U_0(T)}^2 \right) \quad (4.4)$$

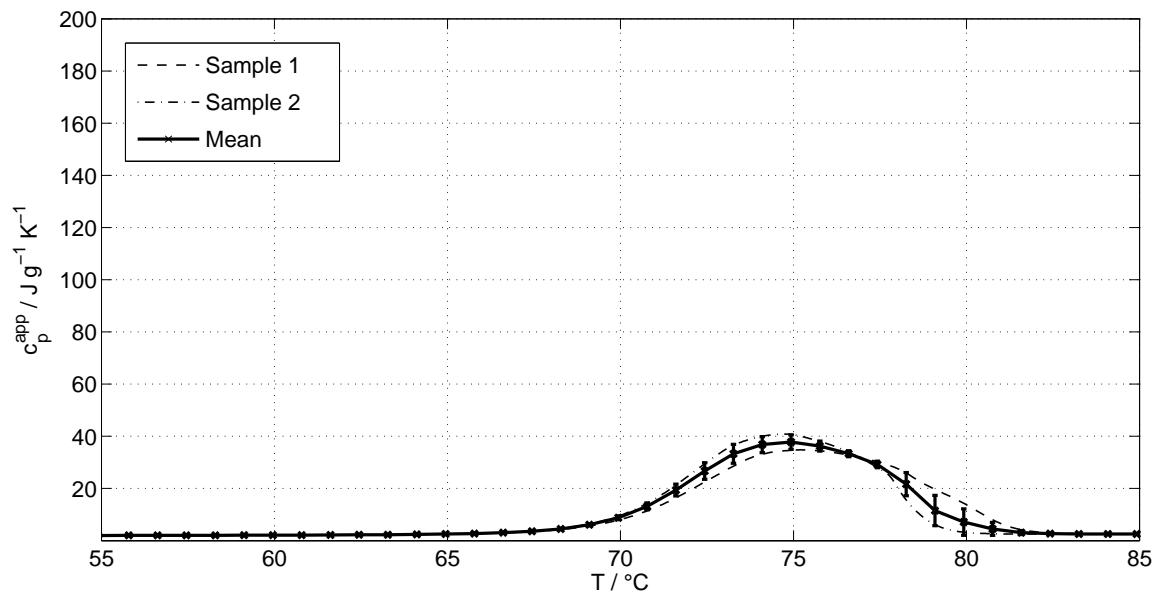
where $u_{U_S(T)}$ is the standard deviation of the sample measurements, $u_{U_{Ref}(T)}$ the standard deviation of the reference measurements, $u_{c_{p,Ref}(T)}$ the uncertainty given from the reference certificate and $u_{U_0(T)}$ the standard deviation of the zero line measurements.

Results

Figure 4.7 depicts the evaluated $c_p^{app}(T)$ for the melting peak for *RT70HC* with $\beta = 0.25 \text{ K min}^{-1}$ and 10 K min^{-1} . $c_p^{app}(T)$ is based on the data evaluation and uncertainty calculation shown in section 4.2.4. While $\beta = 0.25 \text{ K min}^{-1}$ leads to a sharp peak, the results for $\beta = 10 \text{ K min}^{-1}$ show a smeared representation of the melting area. In table 4.2 the results for the characteristic temperatures and transition enthalpies Δh_t are shown, while $\Delta h_t(1)$ is based on a heat flow calibration (s. section 3.6.2) and $\Delta h_t(2)$ is based on a heat calibration (s. section 3.6.2).



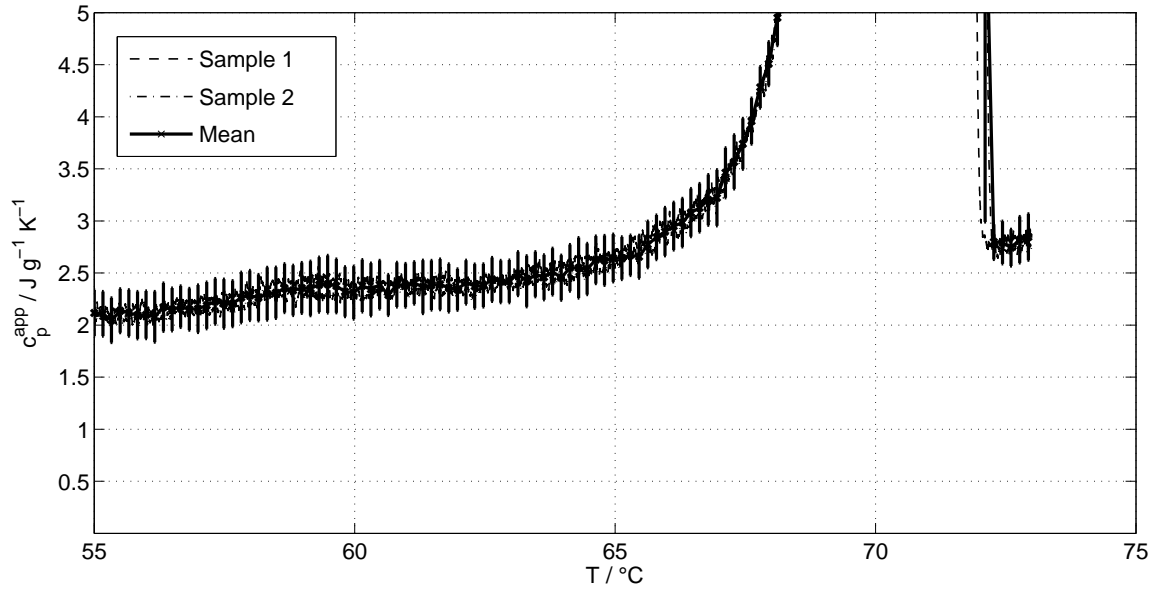
(A) Evaluated $c_p^{app}(T)$ with $\beta = 0.25 \text{ K min}^{-1}$



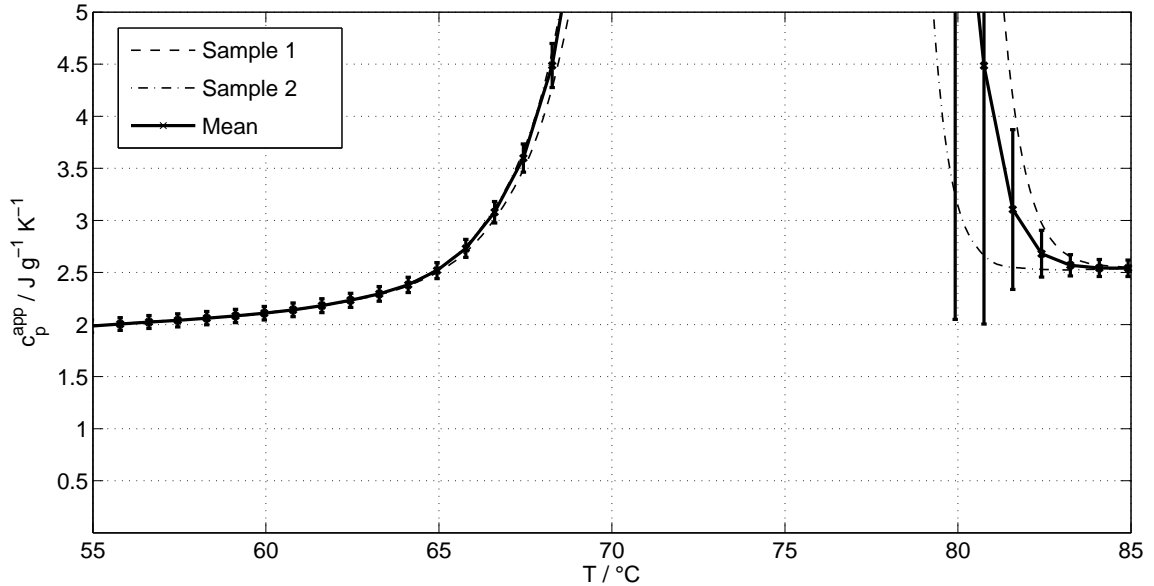
(B) Evaluated $c_p^{app}(T)$ with $\beta = 10 \text{ K min}^{-1}$

FIGURE 4.7: Evaluated $c_p^{app}(T)$ of Rubitherm *RT70HC* with $\beta = 0.25 \text{ K min}^{-1}$ and 10 K min^{-1}

Figure 4.8 is focusing on the $c_p^{app}(T)$ in the solid phase before the melting of the PCM and the liquid phase afterwards. Due to the different heating rates with $\beta = 0.25 \text{ K min}^{-1}$ and 10 K min^{-1} , the final temperature of the melting process T_f differs. Additionally, the evaluated uncertainties for $c_p^{app}(T)$ are bigger at $\beta = 0.25 \text{ K min}^{-1}$ compared to $\beta = 10 \text{ K min}^{-1}$. In table 4.3 the results for the evaluated $c_p^{app}(T)$ at a temperature of $T = 60^\circ\text{C}$ are shown.



(A) Detailed view of $c_p^{app}(T)$ with $\beta = 0.25 \text{ K min}^{-1}$



(B) Detailed view of $c_p^{app}(T)$ with $\beta = 10 \text{ K min}^{-1}$

FIGURE 4.8: Detailed view of $c_p^{app}(T)$ before and after the melting process of Rubitherm RT70HC with $\beta = 0.25 \text{ K min}^{-1}$ and 10 K min^{-1}

The evaluated characteristic temperatures, described in table 4.2, show only marginal differences for the $T_{e,i}$ but large deviations for the $T_{e,f}$. At $\beta = 0.25 \text{ K min}^{-1}$, the transition enthalpy evaluated through the heat flow calibration $\Delta h_t(1)$ shows a large deviation with respect to the transition enthalpy evaluated through the heat calibration $\Delta h_t(2)$. This may

β K min ⁻¹	$T_{e,i}$ °C	σ °C	$T_{e,f}$ °C	σ °C	$\Delta h_t(1)$ J g ⁻¹	σ J g ⁻¹	$\Delta h_t(2)$ J g ⁻¹	σ J g ⁻¹
0.25	70.0	0.1	72.0	0.1	228.1	0.1	246.2	0.1
10	69.7	0.1	79.9	1.1	243.5	2.2	243.1	0.6

TABLE 4.2: Measured characteristic temperatures and transition enthalpies for *Rubitherm RT70HC* with $\beta = 0.25$ K min⁻¹ and 10 K min⁻¹

be attributed to the difference of the sensitivity $S_{DSC}(T)$ as already shown in section 4.2.2. This effect is not seen at $\beta = 10$ K min⁻¹.

β K min ⁻¹	T °C	c_p^{app} J g ⁻¹ K ⁻¹	u_c J g ⁻¹
0.25	60	2.38	0.25
10	60	2.14	0.07

TABLE 4.3: Evaluated c_p^{app} at $T = 60$ °C for *RT70HC* with 0.25 K min⁻¹ and 10 K min⁻¹

Focusing on the results c_p^{app} in the solid phase at $T = 60$ °C it can be seen, that there is a large deviation between 0.25 K min⁻¹ and 10 K min⁻¹. While the evaluated uncertainty at $\beta = 0.25$ K min⁻¹ is 0.25 J g⁻¹ (10.5 %), it is only 0.07 J g⁻¹ (3.3 %) for $\beta = 10$ K min⁻¹.

4.2.5 Cycling tests

As already described in [65], HDPE was characterized as a promising PCM candidate for LTES. Due to the fact that most applications have several charging and discharging cycles, the influence on the phase transition enthalpy Δh_t is relevant.

Former experiments based on dilatometry experiments resulted in a strong volume expansion in the melting process of the HDPE with $V(160\text{ °C}) / V(25\text{ °C}) \approx 1.2$. Due to that, the HDPE PCM sample was placed into cold welded steel crucibles to overcome deformation of the crucible during the DSC experiments. The HDPE was measured with a sample mass of $m_S = 8.85$ mg under a nitrogen atmosphere with a gas flow of 40 ml min⁻¹.

The sample was cycled 1020 times in the DSC with a heating and cooling rate of $\beta = 10$ K min⁻¹ and a temperature range between $T = 80$ to 160 °C. The results have shown that it actually stabilizes around 90 % of the initial phase transition enthalpy. However, for further details on the screening process and the characterization, the reader is referred to [65].

4.3 Thermal Conductivity and thermal diffusivity measurements

This section describes the experiments for evaluating the thermal diffusivity $a(T)$ and thermal conductivity $\lambda(T)$ based on measurements of an organic PCM *Rubitherm RT70HC*. Two different measurement techniques, the LFA and THB method, were applied to measure the thermal transport properties of the solid and the liquid PCM. For a better understanding of the influence of the used sample holder system in the LFA, further numerical simulations were performed.

4.3.1 LFA experiments

Equipment

A *NETZSCH LFA 467* light flash device is used to measure the thermal diffusivity of the various PCM samples. A measurement range from $a = 0.01$ to $1000 \text{ mm}^2 \text{ s}^{-1}$, a temperature range between $T = -100$ and $500 \text{ }^\circ\text{C}$ and a sample dimension ranging from $d = 6$ to 25.4 mm diameter and $\delta = 0.01$ to 6 mm thickness can be used to determine the thermal diffusivity $a(T)$. The key technical specification for this device can be found in table 5.3.

Sample preparation

Three different kinds of sample preparation have been performed to measure in the solid and liquid phase of the PCM in the LFA. The sample was measured as cylindrical shaped solid with and without containment. The containment is needed to measure the PCM sample also in the liquid phase.



FIGURE 4.9: left: Solid sample in cylindrical shape and graphite coated; middle: Aluminum container for liquids with sample and lid, assembled with graphite coated bottom; right: Polyether Ether Ketone (PEEK) ring with sample inside and steel support outside, assembled with two steel plates on the upper and lower side of the PEEK ring with graphite coating

As shown in figure 4.9 a graphite coating is needed for all three kinds of sample preparation. As described by [73] a black coating is used to increase the energy absorption and has only a marginal influence on the measured $a(T)$ as long as the coating is very thin and has a high thermal conductivity in relation to the sample itself. More details about the graphite coating can be found in section 5.3.3.

The main difference between a solid measurement with or without containment is the additional influence of the containment itself. In the LFA method it is necessary to use a containment for the liquid phase, otherwise the liquid sample would flow down and cover the LFA optics. Due to that it is important to fill the containment completely and to ensure that there

are no air bubbles or gaps between the containment layers and the sample. A bad sample preparation would lead to different thermal resistances R_{th} between the layers.

PCM sample	δ mm	diameter mm
Solid 1	1.091	12
Solid 2	1.093	12
Aluminum containment	0.48	12
Steel/PEEK containment	1.707	14.8

TABLE 4.4: PCM sample dimensions for the LFA experiments

Measurement protocol

The prepared solid without containment were measured at 25 °C, 40 °C and 50 °C while the results for the two samples in the different containment systems were measured in the liquid phase of the PCM between 80 and 90 °C. This temperature regions were chosen to ensure to measure beyond the melting area (s. figure 4.5). Additionally, the samples in the containment were also measured in the solid phase and compared to the sample data without containment. All measurements where done under ambient gas conditions. The light pulse energy was adjusted by the supplied light voltage U while the pulse length was fixed with $t = 300 \mu\text{s}$. For each temperature point of each sample, three measurements were performed.

Data analysis

For the data analysis two different models are applied to evaluate $a(T)$. In case of the solid samples without containment, the model described by *Cowan* [44], including heat loss effects, was applied.

For the measurements in the aluminum and the steel/PEEK containment respectively, a special three layer model according to *Lee* [74] is applied. For this model, $\rho(T)$, $c_p(T)$ and $\alpha(T)$ for all layers as well as $a(T)$ of the sample holder layers have to be known. The needed material properties for the containment are provided by the manufacturer. Specific heat capacity $c_p(T)$ data for *Rubitherm RT70HC* is used from the DSC measurements shown in figure 4.8b and density data $\rho(T)$ is adopted from the designated manufacturer data with $\rho = 770 \text{ kg m}^{-3}$ in the liquid and $\rho = 880 \text{ kg m}^{-3}$ in the solid phase.

The heat transfer between the sample holder layers and the sample itself is also influenced by the thermal resistance R_{th} between these layers. By comparing the data of the solid with and without containment, the significance of this influence can be verified.

The uncertainty of the evaluated $a(T)$ results are calculated based on the sample standard deviation according equation 4.5 where a_i is the measured individual result and \bar{a} the mean value of the individual results at each temperature point.

$$\sigma = \sqrt{\frac{1}{n-1} \sum_{i=1}^n (a_i - \bar{a})^2} \quad (4.5)$$

Results

The thermal diffusivity results $a(T)$ of the organic *Rubitherm RT70HC* PCM sample in the different containments are shown in figure 4.10.

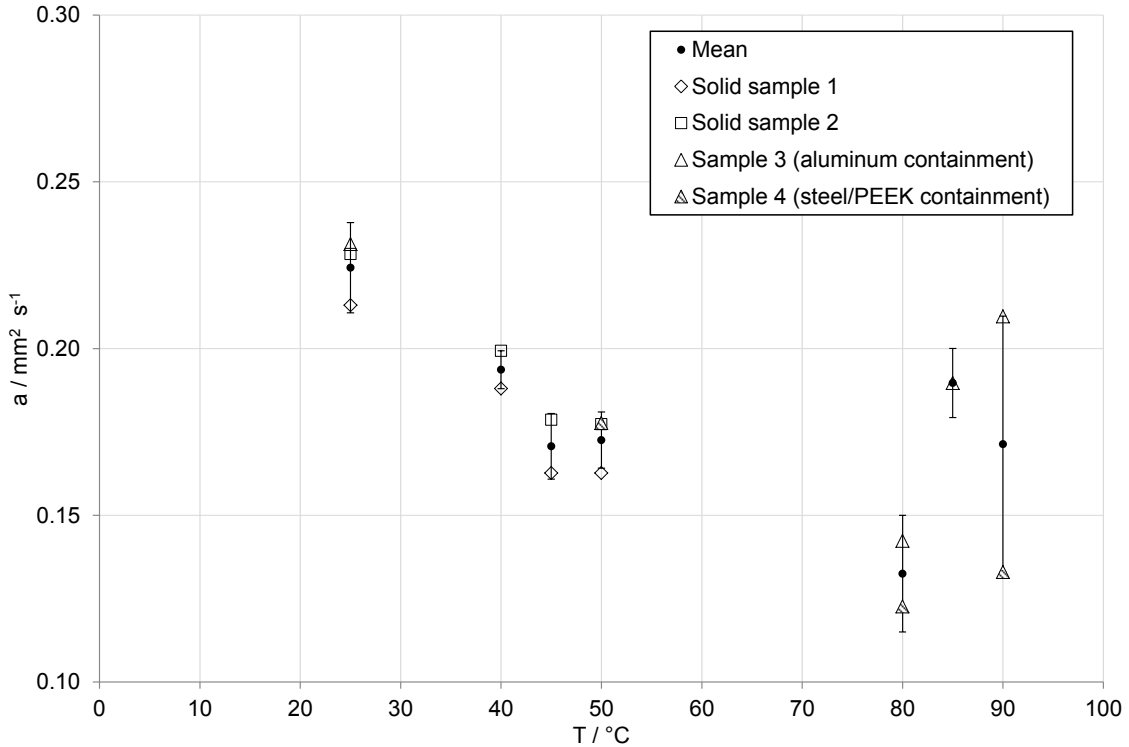


FIGURE 4.10: Thermal diffusivity $a(T)$ of an organic PCM *Rubitherm RT70HC* in solid and liquid phase

The LFA shows repeatable and reproducible results for the solid PCM measurement over the various samples with and without containment. The results at $T = 25^\circ\text{C}$ for the aluminum containment and at $T = 50^\circ\text{C}$ for the steel/PEEK containment show similar $a(T)$ data compared to the solid measurements without containment. These results indicate, that the applied three layer model and thermal resistance between the layers in the containment measurements yield comparable $a(T)$ data. Due to that result in the solid phase of the PCM, the two samples in the different containment systems were heated over the phase change temperature and measured in the liquid phase.

In liquid phase, the two samples in the containment systems show diverse results.

In case of the aluminum containment, it was not possible to open the lid after the measurement without destroying the sample. It is assumed, that due to the liquid capillary ascension the liquid is lifted at the wall and so sample thickness δ is changing during the measurement. The steel/PEEK containment could be opened after the measurement without destroying the sample. The steel support and the PEEK ring of the container are slightly covered by the wax which is assumed to be caused by the low viscosity of the liquid sample and the tightness of the sample holder system. This would also lead to the assumption that the thickness of the sample is changing during the measurement and so a misinterpretation of the thermal diffusivity occurs.

A detailed numerical investigation on the influence of a liquid sample holder system on the evaluated thermal diffusivity results based on Finite Element Method (FEM) can be found in section 4.4.

4.3.2 THB experiments on PCM

Equipment

For the THB measurements a *LINSEIS THB 100* dynamic measurement system was used in combination with a kapton foil sensor with a sensor size of 42 mm x 22 mm. This sensor can be applied for a thermal conductivity range between $\lambda = 0.01$ and $1 \text{ W m}^{-1} \text{ K}^{-1}$ and a temperature range between $T = -100$ and $200 \text{ }^\circ\text{C}$. For liquid measurements, a kapton foil sensor with an additional metal frame is used for a better mechanical stiffness during the measurement. A lab furnace *MEMMERT UFP 500* was employed to place the PCM sample and the sensor inside and measure from room temperature to $T_{max} = 90 \text{ }^\circ\text{C}$ at ambient atmospheric conditions. A detailed description to the THB method can be found in section 3.9.

Calibration and sample preparation

For calibration of the temperature and thermal conductivity different reference standard materials are applied. Due to the low conductivity of the organic PCM, a certified PMMA standard with $\lambda(20 \text{ }^\circ\text{C}) = 0.1934 \text{ W m}^{-1} \text{ K}^{-1}$ was used to calibrate the kapton foil sensor for solid state measurements whereas water with $\lambda(20 \text{ }^\circ\text{C}) = 0.5984 \text{ W m}^{-1} \text{ K}^{-1}$ was used to calibrate the kapton foil sensor with the metal frame for liquid state measurements.



FIGURE 4.11: left: Preparation of two sample blocks and placed foil sensor between the blocks with a defined contact pressure; right: Melting of the PCM in the lab furnace and placed metal frame foil sensor in the PCM liquid

For solid and liquid phase measurements two different protocols for sample preparation have been applied as shown in figure 4.11. To prepare two solid blocks of the *Rubitherm RT70HC* PCM, the granular precursor material was put into plastic cups with inner dimensions of 50 mm x 50 mm x 10 mm and melted at $T = 80 \text{ }^\circ\text{C}$ in the lab furnace. After the whole PCM was liquid, the furnace was cooled down to room temperature. The resulting solidified PCM had a flat surface on the bottom side of the cup. Two solid blocks with a thickness of $\delta \approx 5 \text{ mm}$ are prepared and the foil sensor was placed between the two flat sides of the solid block for proper contact conditions. The sample blocks with the THB foil sensor between them was placed inside a press to apply a slight constant pressure for controlled contact conditions inside the lab furnace.

The liquid sample was prepared in a glass beaker by melting the granular PCM at $T = 80^\circ\text{C}$ in the lab furnace. A volume of $V \approx 250$ ml was occupied by the liquid PCM and the metal frame THB sensor was placed in the middle of the glass until the whole sensor area was covered by the liquid PCM.

Measurement protocol

All THB experiments in the solid and liquid state of the *Rubitherm RT70HC* are performed with an adjusted heating current of $I = 40$ mA for the current source and a data acquisition time of $t = 30$ s. To measure at different adjusted furnace temperatures, several temperature measurements with the THB system were performed until a stable temperature was indicated by the foil sensor. This protocol should reduce the risk of a thermal gradient ΔT inside the sample before starting a measurement.

The solid PCM was measured at the temperatures $T = 40^\circ\text{C}$ and 50°C . The experiment was repeated three times with the same sample blocks but with a re-positioned foil sensor between them. This procedure should demonstrate the influence of different contact conditions between the blocks and the foil sensor on the indicated thermal conductivity.

The liquid PCM was measured at $T = 80^\circ\text{C}$ and 90°C with the metal frame THB sensor. In that measurements, the sensor position was again changed three times to evaluate the repeatability of the applied procedure.

Results

The measured thermal conductivity $\lambda(T)$ results for the solid and liquid *Rubitherm RT70HC* are summarized in figure 4.12.

In the solid phase at $T = 40^\circ\text{C}$ and 50°C , the standard deviation of the individual results s. equation 4.5) is significant higher than for the liquid phase. This effect may be connected to the different contact conditions and varying thermal resistance R_{th} between the THB foil sensor and the solid PCM blocks.

In the liquid phase, the spreading of the individual results is much lower which appears to be connected to better contact conditions between the THB sensor and the liquid in comparison to the solid phase results.

4.3.3 Comparison of the THB and LFA thermal conductivity results

To compare the two different measurement methods, the thermal diffusivity $a(T)$ result from the LFA experiment is just one factor to calculate the thermal conductivity $\lambda(T)$ according to equation 4.6.

$$\lambda(T) = a(T) \cdot c_p(T) \cdot \rho(T) \quad (4.6)$$

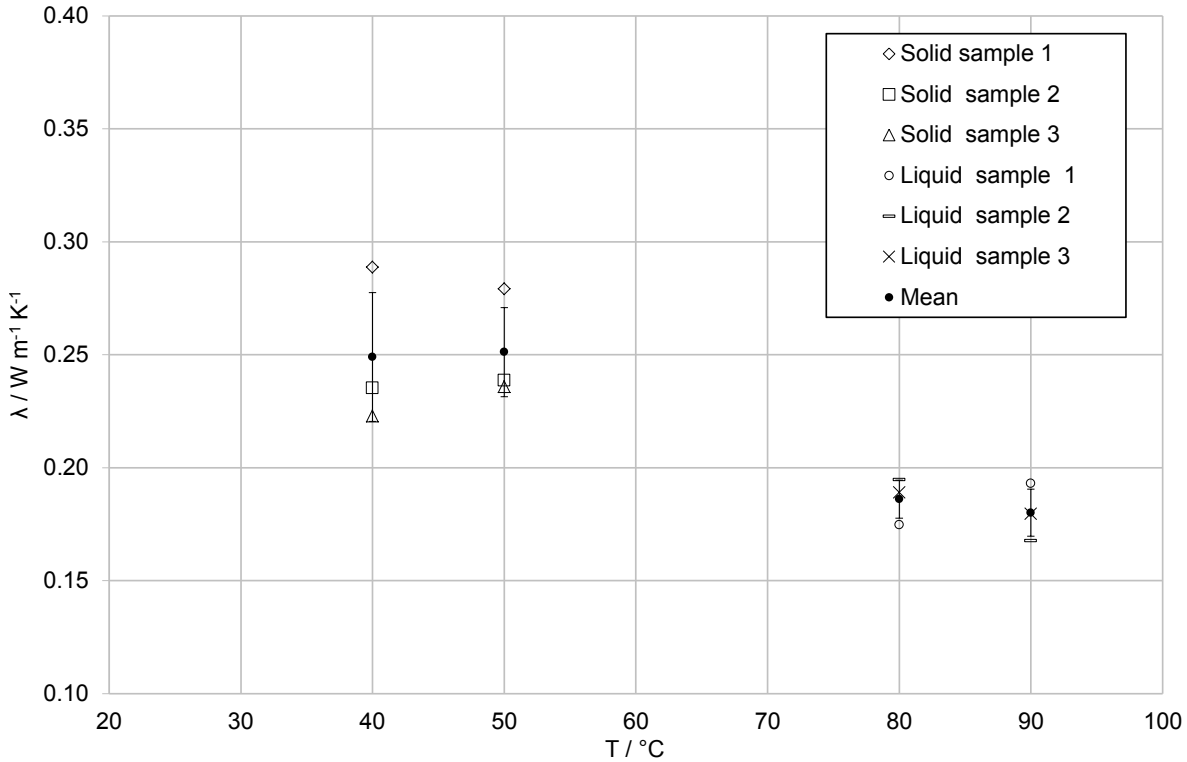


FIGURE 4.12: Thermal conductivity $\lambda(T)$ of an organic PCM *Rubitherm RT70HC* in solid and liquid phase based on THB measurements

While $a(T)$ results from the LFA measurements and $c_p(T)$ from the DSC experiments, as shown in section 4.2.4, density data is taken from the manufacturer data sheet for *Rubitherm RT70HC* with $\rho = 770 \text{ kg m}^{-3}$ in the liquid and $\rho = 880 \text{ kg m}^{-3}$ in the solid phase.

The expanded combined standard uncertainty calculation according [72] is calculated as shown in equation 4.7.

$$u_{c,95\%}^2 = 2 \left[\left(\frac{\partial \lambda(T)}{\partial a(T)} \right)^2 u_{a(T)}^2 + \left(\frac{\partial \lambda(T)}{\partial c_p(T)} \right)^2 u_{c_p(T)}^2 + \left(\frac{\partial \lambda(T)}{\partial \rho(T)} \right)^2 u_{\rho(T)}^2 \right] \quad (4.7)$$

$u_{a(T)}$ is based on the standard deviation as shown in equation 4.5 and $u_{c_p(T)}$ is calculated from the expanded combined standard uncertainty calculation as shown in equation 4.4. Due to the unknown $u_{\rho(T)}$ of the given solid and liquid density from the manufacturer data sheet, an assumption with 3 percent was estimated from own experience.

Comparing the thermal conductivity results shown in figure 4.13, a small deviation between the evaluated solid and a big deviation in the liquid phase can be seen. The uncertainties in the solid THB measurements seem to be higher, which is linked to the varying results under different contact conditions. Focusing on the uncertainties of the solid LFA measurements, they are slightly smaller compared to the THB results. The uncertainty in the solid LFA measurements could even be smaller, due to the fact that also three layer measurements are considered.

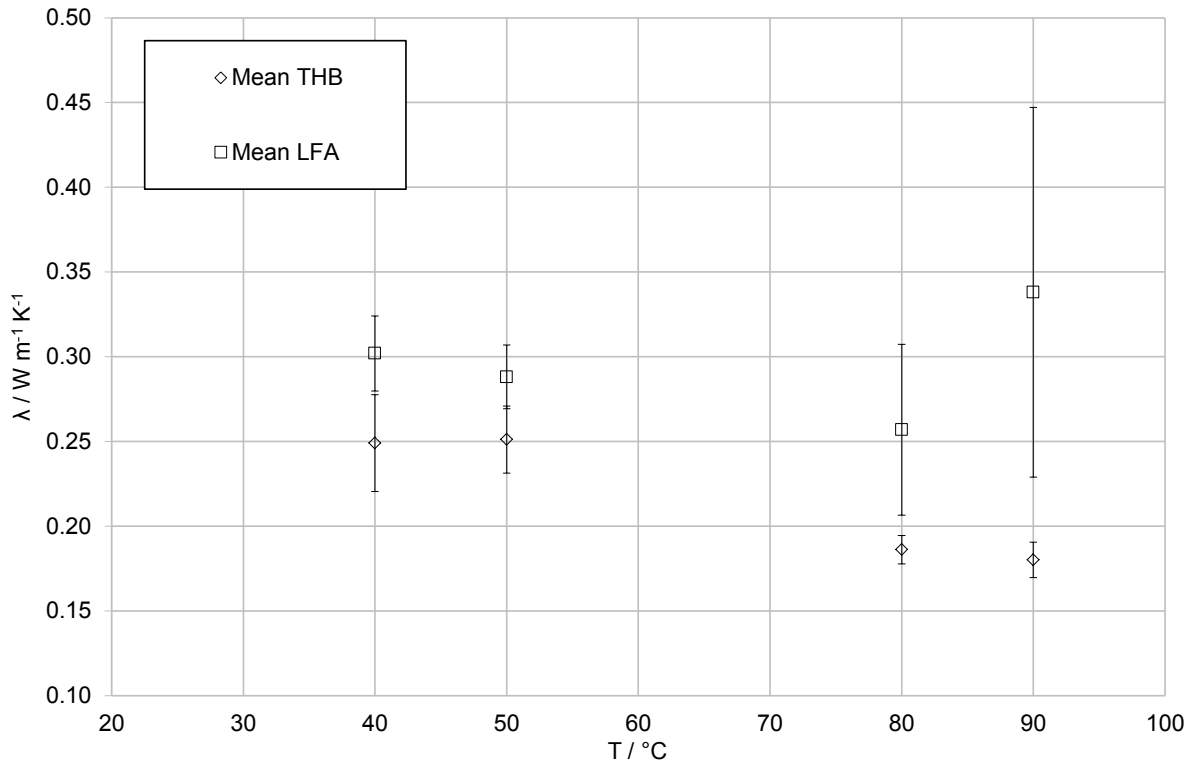


FIGURE 4.13: Thermal conductivity $\lambda(T)$ of *Rubitherm RT70HC* based on LFA, DSC and THB measurements

In the liquid phase, the already mentioned problems with the containment of the sample in LFA measurements lead to high uncertainties. Due to that, a detailed investigation on the influences of a liquid sample holder system on the measured thermal diffusivity in the LFA experiment is shown in section 4.4. THB measurements show small uncertainties in the liquid phase which may be connected to much better contact conditions compared to the solid experiments.

4.4 Applicability of LFA liquid sample holder systems

A detailed investigation on the liquid sample holder system influence in a LFA experiment is done by a numerical simulation with FEM. A 2D axisymmetric model of the steel/PEEK containment is developed based on thermal conduction FE-elements, which are able to calculate transient temperature fields. A defined heat flux density \dot{q} is applied on the bottom side of the model, simulating the LFA laser beam. Furthermore, by applying surface radiation elements, radiation transport to the surroundings as well as to a defined node is modeled, to simulate the LFA IR detector.

This FEM model is used to calculate the temperature field inside the steel/PEEK containment with pure water as sample. In the end, this simulation results are compared to real LFA experiments with pure water.

4.4.1 FE Modell

Geometry

A 2-D axisymmetric geometry was designed in ANSYS based on the dimensions of the steel/PEEK LFA liquid containment. As shown in figure 4.14, the sample (blue) and the PMMA ring (red) have a thickness of $\delta = 1.5$ mm while the sample diameter is $d = 15$ mm being equivalent to the inner diameter of the PMMA ring. The outer diameter of the PMMA ring is $d = 18$ mm, the same diameter as the steel cover plates (violet) with a thickness of $\delta = 0.1$ mm.

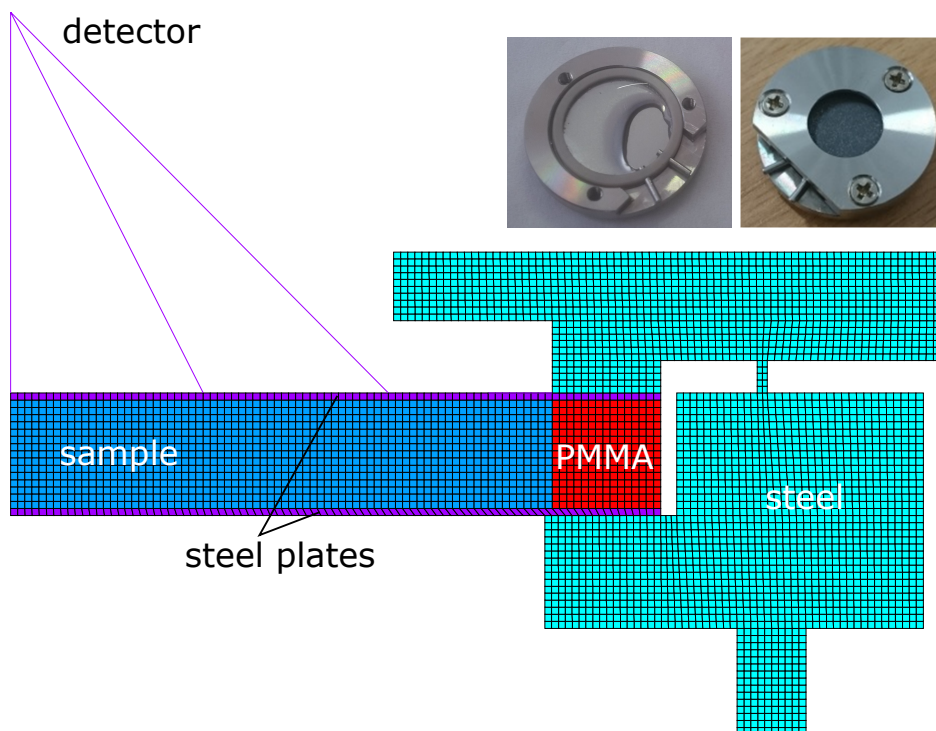


FIGURE 4.14: FEM 2-D model of the LFA experiment with the steel/PEEK containment

Mesh and element types

The mesh was programmed with 2-D thermal solid elements. This element is rectangular and has four nodes, one node on each corner. The node has only one single degree of freedom, which is the temperature. This element type can be used for steady states and transient temperature field calculations.

Density $\rho(T)$, specific heat capacity $c_p(T)$ and thermal conductivity $\lambda(T)$ are the needed input parameters to calculate a transient temperature field solution. The used thermal solid elements use the first law of thermodynamics and *Fourier's law* to compute a differential control volume according to the ANSYS documentation [75].

$$\rho(T) \cdot c_p(T) \cdot \left(\frac{\partial T}{\partial t} + v_x \frac{\partial T}{\partial x} + v_y \frac{\partial T}{\partial y} + v_z \frac{\partial T}{\partial z} \right) = \frac{\phi(t)}{V} + \frac{\partial}{\partial x} \left(\lambda_x \frac{\partial T}{\partial x} \right) + \frac{\partial}{\partial y} \left(\lambda_y \frac{\partial T}{\partial y} \right) + \frac{\partial}{\partial z} \left(\lambda_z \frac{\partial T}{\partial z} \right) \quad (4.8)$$

As shown in equation 4.8, additional velocity vectors v in the Cartesian coordinate system are used to describe the heat transport in the 3-D room. The heat flow per volume ϕ/V is described as heat generation rate which has the unit W m^{-3} .

The heat generation rate represents the heat sources and heat sinks distributed in the volume related to the respective volume. The boundary and transition conditions to solve the differential equation are defined by the spatial finite elements.

The generated FE mesh uses quadrilateral-shaped elements where the nodes between two different materials were merged to reduce the number of nodes. So the contact area between the components (sample, steel plates, PMMA, etc.) are thermal ideal or the thermal resistance $R_{th} = 0 \text{ m}^2 \text{ K}^{-1} \text{ W}^{-1}$. The side length of the used quadrilateral-shaped elements is $l \approx 0.1 \text{ mm}$.

For the simulation of thermal radiation, thermal surface elements were used to cover the outer nodes of the FE model. These thermal surface elements allow a radiation simulation between a surface area and an extra node. This extra node simulates the ambient temperature with $T = 23 \text{ }^\circ\text{C}$.

Additionally, a radiation exchange between three points off the upper cover steel plate (center, middle and edge) and a detector node (s. violet lines in figure 4.14) were modeled, to analyze the response of the IR detector from these defined positions. The FE software uses the *Stefan-Boltzmann-Law* to calculate the heat flow due to radiation effects.

$$\phi = A_i \cdot \epsilon_i \cdot F_{i,j} \cdot \sigma_B \cdot (T_i^4 - T_j^4) \quad (4.9)$$

According equation 4.9, A_i is the area of the emitter i , $F_{i,j}$ is the form factor between the areas A_i and A_j , ϵ_i is the emissivity of the surface i , σ_B is the *Stefan-Boltzmann* constant. The emissivity is defined as the ratio of the radiation emitted by the surface to the radiation

emitted by a black body at the same temperature. In the used FE software, radiation exchange between surfaces is restricted to gray-diffuse surfaces implying that emissivity does not depend on wavelength. In case of the LFA experiment, only the transient behaviour of the IR detector signal is interpreted and not the actual heat flow or temperature. Due to that, the actual emissivity ϵ and the form factor F are insignificant in this observation.

Material data

The following tables represent the used thermophysical data for $c_p(T)$, $\lambda(T)$ and $\rho(T)$ of the sample and the sample containment used in the FEM simulation. The emissivity ϵ was estimated with $\epsilon = 0.8$ for the graphite coated sample cover sheets and $\epsilon = 0.5$ for the steel surfaces.

T °C	ρ kg m ⁻³	c_p J kg ⁻¹ K ⁻¹	λ W m ⁻¹ K ⁻¹
20	7759	475	10.7
50	7749	490	11.2
100	7731	501	12.2
200	7694	518	14.1

TABLE 4.5: Thermophysical data of X15CrNiSi25-20 according [76]

T °C	ρ kg m ⁻³	c_p J kg ⁻¹ K ⁻¹	λ W m ⁻¹ K ⁻¹
20	1294	1200	0.29
50	1294	1300	0.31
100	1294	1550	0.35
200	1294	2400	0.42

TABLE 4.6: Thermophysical data of PEEK supplied by the containment manufacturer

T °C	ρ kg m ⁻³	c_p J kg ⁻¹ K ⁻¹	λ W m ⁻¹ K ⁻¹
20	998	4182	0.61
50	988	4182	0.64
100	975	4194	0.67
200	958	4219	0.68

TABLE 4.7: Thermophysical data of water according [3]

Load and solution settings

The laser beam is simulated by a transient heat flux density of $\dot{q} = 1 \text{ MW m}^{-2}$ with a duration of $t = 0.3 \text{ ms}$. This heat flux density is applied on all nodes of the bottom surface of the model, the bottom cover steel plate and steel support. A transient analysis of the temperatures of all nodes was done over $t = 60 \text{ s}$.

4.4.2 LFA measurements with water

In order to have comparable measurement results to the FEM simulation, pure water is measured at room temperature inside the steel/PMMA containment. The used LFA equipment, the steel/PMMA containment as well as the data analysis are similar to the liquid PCM measurements shown in 4.3.1. The containment was filled with liquid water using an inject at the filling holes of the PMMA ring. The three layer model according [74] was applied with the needed material properties for the steel cover plates (s. table 4.5) and the water (s. table 4.7).

In total, 7 samples were prepared and measured at room temperature with varying pulse duration $t = 150 \mu\text{s}$, $300 \mu\text{s}$ and $600 \mu\text{s}$ of the light pulse and varying diameters of the field of view of the detector optics with $d = 3.4 \text{ mm}$, 8.6 mm , 10.5 mm and 12 mm .

Results

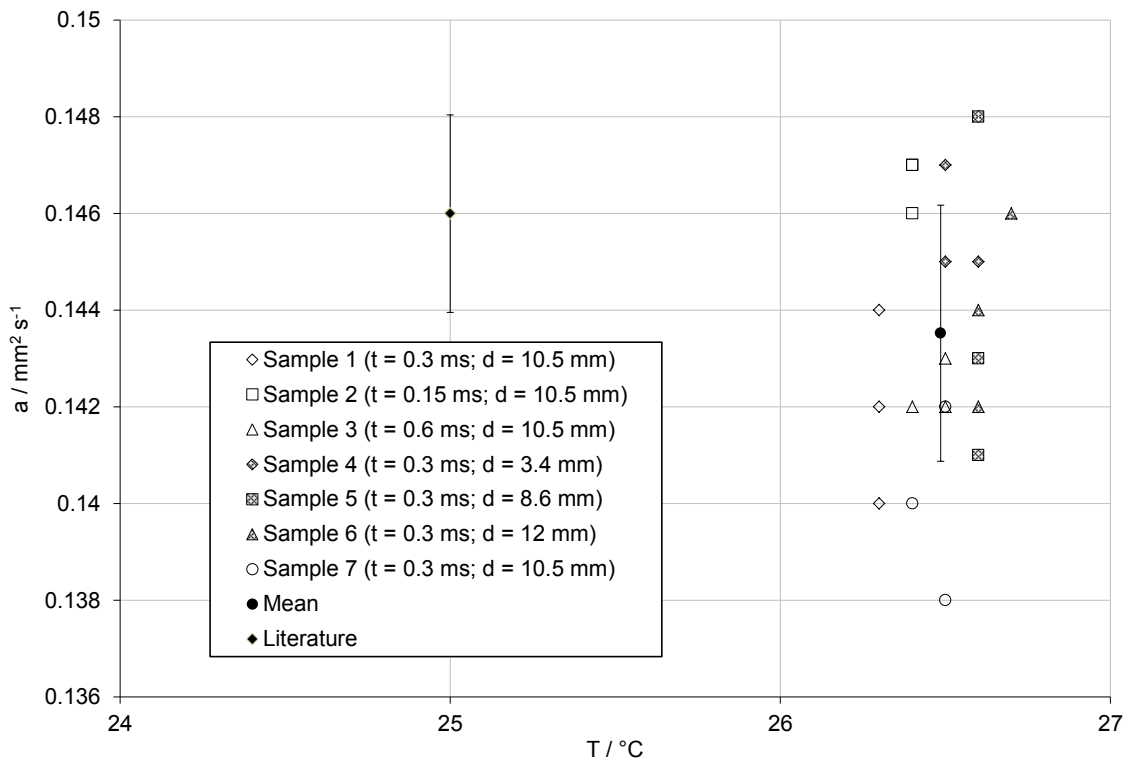


FIGURE 4.15: Thermal diffusivity of water measured with the steel/PEEK containment in the LFA experiment

In figure 4.15 the evaluated thermal diffusivity of water as well as the literature value from [77] are displayed. The literature value is given at $T = 25^\circ\text{C}$ while the evaluated thermal diffusivity data is between $T = 26$ to 27°C . The evaluated mean value is in the uncertainty range of the literature value given by [77]. Therefore, no significant relation between varying pulse duration t and field of view of the detector optics d could be derived.

4.4.3 FE results and comparison to laser flash measurements

In figure 4.16 the qualitative FEM analysis result of the time and spatial dependent temperature field inside the sample and the steel/PEEK containment is shown.

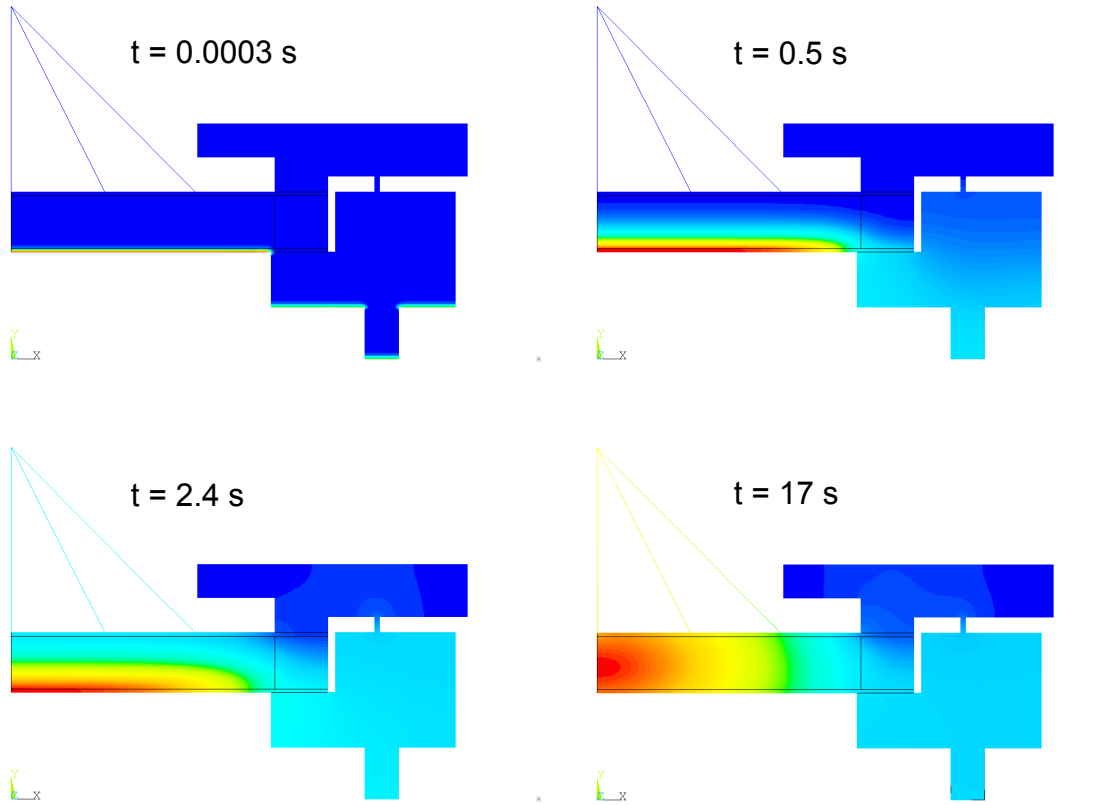


FIGURE 4.16: Qualitative FEM analysis result of the time and spatial dependent temperature field inside the water sample and the steel/PEEK containment

The first shown result at $t = 300 \mu\text{s}$ depicts the temperature distribution at the end of the applied heat pulse. At this time, a small temperature gradient at the lower cover steel plate and the steel support ring is visible. After $t = 0.5 \text{ s}$ an inhomogeneous temperature gradient over the thickness of the sample can already be observed. The temperature gradient at the edge of the water sample differs from the gradient in the center of the sample. Temperature results at $t = 2.4 \text{ s}$ and $t = 17 \text{ s}$ show the further propagation of the inhomogeneous temperature field to the top face of the cover steel plate. Due to the thermal mass of the PMMA ring as well as the steel support, heat of the light pulse is consumed by this components leading to lower temperatures at the edge of the sample and the upper cover steel plate.

For a more detailed analysis, the radiation exchange between three points of the upper cover steel plate (center, middle and edge) and the detector node as well as detector response of the LFA experiment are compared and shown in figure 4.17.

The inhomogeneous propagation of the temperature field inside the water sample and the

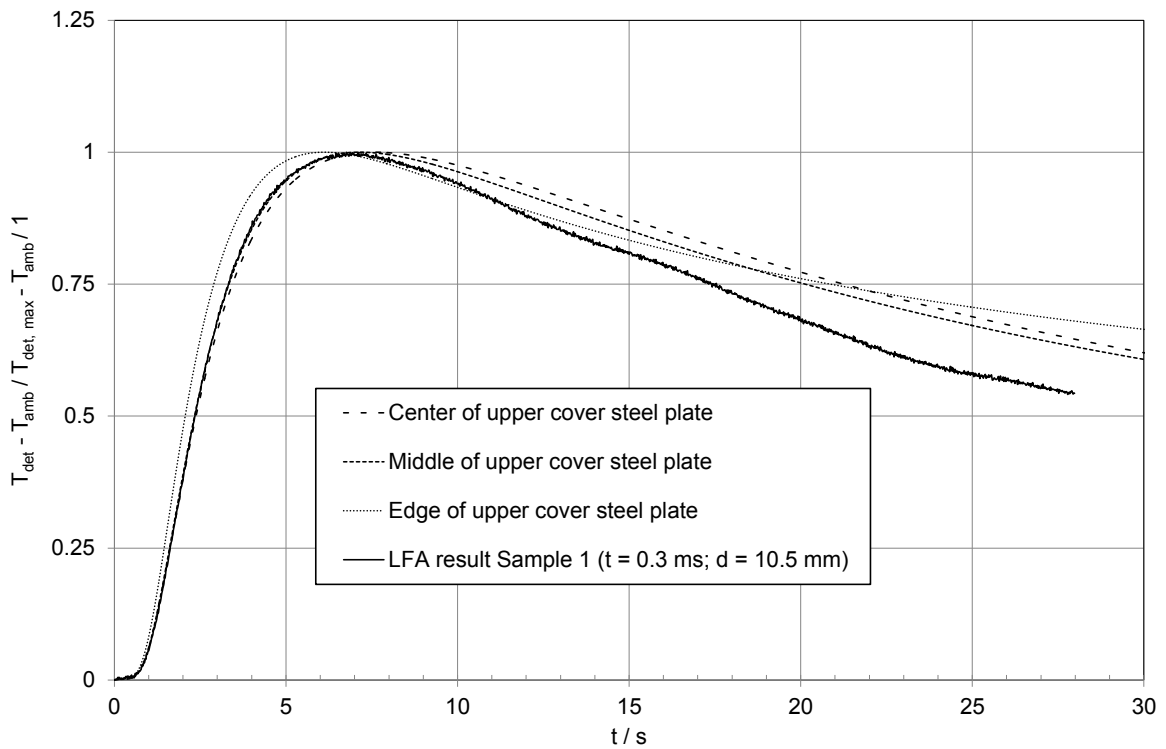


FIGURE 4.17: FEM analysis result of the modeled detector node temperature due to the radiation exchange between center, middle and edge of the upper cover steel plate

steel/PEEK containment can also be seen on the radiation exchange between the upper cover steel plate and the detector node in the simulation. Due to the heat transport from the sample to the PMMA ring and the steel support of the containment, the maximum temperature T_{max} is reached earlier than in the center or in the middle of the upper steel cover plate. Furthermore, the LFA measurement indicates a faster cooling after reaching the maximum in the signal which may be connected with additional heat loss. The developed FEM model only considers radiation transport to the ambient but no convection losses which occur additionally in the LFA experiment. The calculated FEM and measured LFA half times $t_{1/2}$ and thermal diffusivities $a(T)$ according to the *Parker* model [41], including all three layers of the containment, are shown in table 4.8.

Type	$t_{1/2}$ s	$a(T)$ $\text{mm}^2 \text{s}^{-1}$
FE center	2.38	0.131
FE middle	2.34	0.134
FE edge	2.06	0.151
LFA sample 1	2.36	0.135

TABLE 4.8: Thermal diffusivity $a(T)$ according to [41] of the three layer containment (steel plate / water sample / steel plate) from FEM simulations and measured via LFA experiment

4.5 Conclusion

The results on PCM measurements by the disc type heat flow DSC method have shown, that the chosen calibration procedure has a strong influence on the calibration result. For a higher accuracy in temperature calibration and subsequent characteristic temperature measurements of organic PCMs, low heating rates β are necessary due to the thermal transport properties of the investigated material. Results for the heat and heat flow calibration indicate, that the sensitivity of the used DSC sensor strongly depends on the heat flow rate $\phi(T)$. On this basis, it can be concluded that the accuracy of a measured phase transition enthalpy Δh_t is associated with the used caloric calibration of the DSC sensor.

Enthalpy curve measurements of organic PCM according to the developed standard defined in [63] have shown their assets in the phase change region. Low heating rates β avoid thermal gradients in the sample and increase the accuracy of the evaluation of characteristic temperatures. A defined heat calibration based on phase transition standard reference materials lead to comparable phase transition enthalpy values. These results could be confirmed by a round robin test organized by the *IEA SHC Task 42 ECES Annex 29* using an octadecane paraffin wax.

Specific heat capacity DSC measurements of an organic PCM *Rubitherm RT70HC* in the temperature regions before and after the phase change have shown, that the recommended heating rates β in [63] lead to high uncertainties in the $c_p(T)$ evaluation. Due to the low heating rates, the heat flow rates ϕ get smaller and the temperature difference ΔT between reference and sample side of the DSC sensor gets lower. This effect tends to noisy signals and higher uncertainties in the specific heat capacity c_p^{app} evaluation. This can be avoided by additional measurements with faster heating rates according to [35].

Additional tests on HDPE have demonstrated the applicability of a DSC device for simulating several charging and discharging cycles as already published in [65].

Thermal diffusivity measurements based on the LFA method have shown their benefit applied on solids. Liquid capillary ascension, low viscosity as well as the sample preparation itself are the experienced challenges when measuring an organic PCM *Rubitherm RT70HC* in the investigated LFA containment systems. Thermal conductivity measurements based on the THB method have shown the contrary behavior. A precise sample preparation of the solid is needed to fulfill adequate contact conditions between the sensor and the sample. In liquid phase, low uncertainties are observed which may be connected to ideal contact conditions between the foil sensor and the liquid.

A detailed investigation on the temperature field of a steel/PEEK containment filled with pure water based on FEM calculation and comparative LFA measurements experiments have shown, that the heat transport from the sample to the PMMA ring and the steel support lead to different maximum temperatures on the upper steel cover and the measured detector signal.

Chapter 5

TCM measurement methods and evaluated thermophysical properties

5.1 Introduction

This chapter summarizes the experiences with TCM measurements based on the STA, DSC, LFA, THB and HFM method. While the first part of this chapter describes measurement protocols to evaluate sorption isotherms and sorption enthalpy of zeolites based on STA, the second part is focusing on specific heat capacity $c_p(T)$ and effective thermal conductivity $\lambda_{eff}(T)$ of different powdery TCM candidates. The results which have been observed during this work were published in several conference proceedings and scientific papers as described in the following paragraphs.

The first investigations were conducted on sorption materials for TCES, starting with STA measurements on water uptake and enthalpy change of a natural zeolite (clinoptilolite) impregnated with inorganic salts ($MgSO_4$, $MgCl_2$, $LiCl$). These results were presented at the *EuroSun 2014: International Conference on Solar Energy and Buildings* in September 2014 in Aix-les-Bains, France and published in the conference proceedings [78].

A detailed investigation on the thermophysical properties of the zeolite *Köstrolith 4AK* was presented at the *Arbeitskreis Thermophysik* conference in March 2015 in Aachen, Germany [79] and at the *Sorption Friends* conference in September 2015 in Sicily, Italy [80]. This data was also used for a further journal paper in the field of Computational Fluid Dynamics (CFD) simulations of a rotating adsorption reactor and published in the *Applied Thermal Engineering* journal [81].

After these studies, the focus was shifted to TCMs based on chemical reactions. Several STA measurements on the CuO/Cu_2O redox reaction were conducted which were contributed to the journal paper "High-Temperature Energy Storage: Kinetic Investigations of the CuO/Cu_2O Reaction Cycle" published in the journal *Energy and Fuels* in 2017 [82].

An overview about challenges in measuring powdery TCM by STA, DSC, THB and LFA was presented at the *Arbeitskreis Thermophysik* conference in March 2017 in Selb, Germany [83].

A detailed investigation on "Thermal conductivity measurements of calcium oxalate monohydrate $\text{CaC}_2\text{O}_4 \cdot \text{H}_2\text{O}$ as thermochemical heat storage material" was presented at *33rd International Thermal Conductivity Conference (ITCC)* in May 2017 in Logan, Utah [84]. The corresponding conference paper is submitted but not published at this time.

Research on the "Specific heat capacity of metal hydroxides for thermochemical energy storage" was presented at the *Journal of Thermal Analysis and Calorimetry Conference*, in June 2017 in Budapest, Hungary [85].

The last lecture relating to this work was given at the *21st European Conference on Thermophysical Properties (ECTP)* in September 2017 in Graz, Austria with the topic "Effective thermal conductivity measurements of packed beds for thermochemical energy storage" [86].

All contributions regarding uncertainty assessment of LFA measurements were presented at the *30th ITCC* in September 2009 in Pittsburgh, Pennsylvania and are published in the corresponding conference proceedings [87].

5.2 Sorption and composite measurements via STA

As already described in section 2.4, following criteria define a specified sorption material in a selected TCES application:

- Sorption isotherms or uptake of the fluid phase
- Enthalpy change due to sorption effects
- Reaction rate or kinetics
- Decomposition temperatures
- Cycling stability

These application dependent and material specific properties are needed in the beginning of a TCES design process to identify, if the required thermal power and storage capacity can be reached with the investigated sorption material.

Simultaneous Thermal Analysis (STA) (s. section 3.7) is a possible measurement method, to analyze these needed data based on application conditions. The combination of a TGA with a DSC sensor as well as defined gas conditions in the sample chamber allows to measure sorption effects which are influencing the sample mass as well as the generated heat flows.

5.2.1 Equipment and setup

For thermogravimetric and calorimetric investigations two different STA measurement systems from *NETZSCH*, the model *STA 449 F1* (s. figure 5.1) and *STA 449 F5* were used.

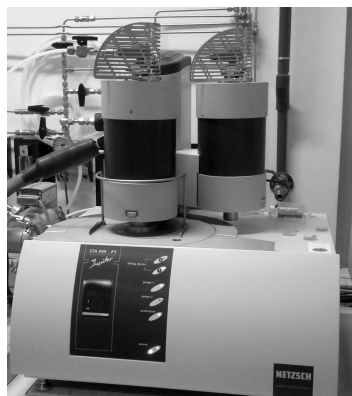


FIGURE 5.1: STA system *NETZSCH STA 449 F1* with exchangeable steel and rhodium furnace

There are some different technical specifications which are shown in table 5.1. The important specifications are the applicable temperature range, balance sensitivity, sample carrier types and possible extensions like coupling to Evolved Gas Analysis (EGA) systems.

STA System	STA 449 F1	STA 449 F5
Furnace	Rhodium	Silicon Carbide
Temperature range /°C	25-1650	25-1600
2nd furnace	Steel	NA
Temperature range /°C	-120 - 1000	NA
Heating rate /K min ⁻¹	0.1 - 50	0.001-50
External cooling	nitrogen (liquid/gaseous)	free cooling
Balance weighing range /g	5	35
Balance digital resolution /µg	0.025	0.1
Gases	N ₂ , O ₂ , He, Ar, H ₂ O	N ₂ , O ₂ , He, Ar
Mass flow Controller	yes (external)	yes
Rotary vane pump	yes	yes
Sample carrier type	TGA, TGA-DTA, STA	TGA, TGA-DTA, STA
Thermocouple	S, E, K, B, P	S, P
Automatic sample changer	no	yes
FTIR gas analysis	yes	no
MS gas analysis	yes	no
Humidity generator	yes	no
Turbo pump	yes	no

TABLE 5.1: Comparison between the STA 449 F1 and STA 449 F5 STA systems used

5.2.2 Gas conditions

As shown in table 5.1 the STA 449 F1 system is additionally connected to a humidity generator *ProUmid MHG32* which is used for defined humidity in the sample chamber. All shown gas configurations are controlled via separate MFCs at the gas inlet of the STA system. The performed sorption measurements were done at ambient pressure conditions p_{amb} but varying partial pressures of nitrogen N₂ and water vapor H₂O.

$$p_{amb} = p_{N_2} + p_{H_2O} \quad (5.1)$$

5.2.3 Characterization of clinoptilolite and salt-based composites

A TCES-application for space heating and hot water was developed as open sorption storage as shown in [88]. Different zeolites and salt-based composites were developed and measured inside the reactor to test the achievable thermal power and storage capacity [78, 89].

Name	Clinoptilolite %	MgSO ₄ %	MgCl ₂ %	LiCl %
Composite 1	78	11	11	0
Composite 2	85	7.5	7.5	0
Composite 3	85	10.5	0	4.5

TABLE 5.2: Mass fraction of the three different composite materials based on a clinoptilolite zeolite

These novel materials were also analyzed by STA measurements. The composites are based on a clinoptilolite, which is a natural zeolite and an economic alternative to synthetic zeolites, as substrate material and different salt mixtures MgSO_4 , MgCl_2 and LiCl . These TCMs were measured at defined temperature and humidity specified by the application. For a more detailed description on the material development, reactor design and reactor measurement the reader is referred to [88, 78, 89].

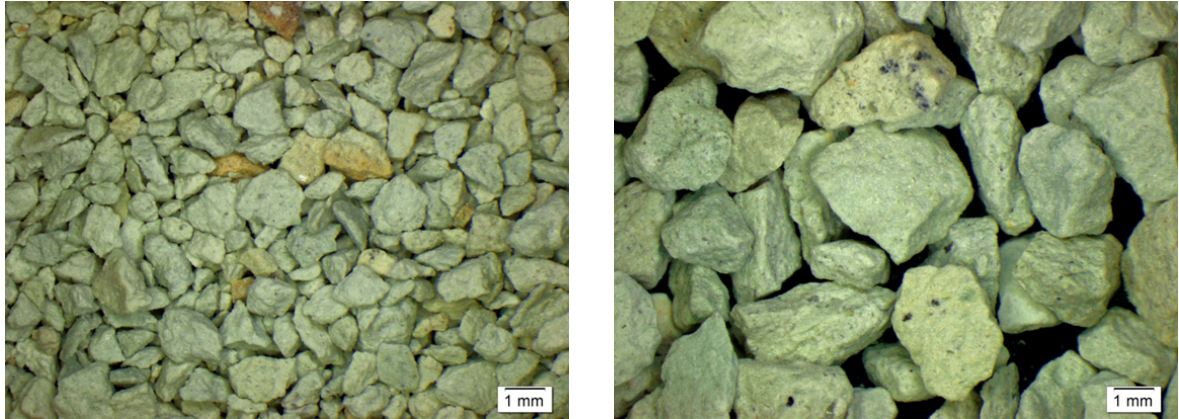


FIGURE 5.2: Natural clinoptilolite with a particle size between 0.2 and 5 mm

DSC calibration protocol

To evaluate the enthalpy of sorption and hydration effects it is necessary to calibrate the used DSC sensor. The used temperature calibration is based on the phase transition temperatures T_t of indium, tin and bismuth, whereas sensitivity calibration $S_{DSC}(T)$ was performed by the use of a heat flow calibration standard (s. section 3.6.2).

The sensitivity $S_{DSC}(T)$ of a DSC sensor depends on the sample carrier, the DSC thermocouple type, the prevailing gas conditions and the crucible material. For the characterization of the used clinoptilolite and salt-based composites, a type K DSC sensor and N_2 gas with a purity of 99.999 % ($\text{O}_2 \leq 3$ ppm; $\text{H}_2\text{O} \leq 5$ ppm) was used. A nitrogen gas atmosphere yields a higher sensitivity of the DSC sensor than for e.g. helium (at temperatures above room temperature, s. section 5.3.2) and is also the calibrated gas for the used MFC in the used humidity generator.

For the calibration experiments, several phase transition standard, zero line and sapphire measurements were performed using Pt/Rh crucibles between $T = 30$ and 250 °C with $\beta = 5$ K min⁻¹. The used sapphire reference standard has a mass of $m_{Ref} = 111.44$ mg thus being rather heavy in comparison to other sapphire reference standards. The motivation for using a higher mass of the reference standard is a higher heat capacity C_p and, subsequently, higher heat flow rates $\phi(T)$ even for a small β .

Measurement protocol

To have comparable results of the current load and the resulting exo- and endothermic effects of the measured clinoptilolite and salt-based composites the following protocol was chosen:

- As first step the material was filled as delivered into the Pt/Rh crucible and the current mass of the sample was weight inside the STA. The used sample masses are between $m_S = 50$ to 75 mg.
- Then, the sample was heated to $T_{max} = 250^\circ\text{C}$, which was assumed as the maximum temperature being delivered by the used solar panels. The sample was kept at $T_{max} = 250^\circ\text{C}$ until the mass stayed constant with $t \approx 1$ to 3 h. This measurement was done using a N_2 gas flow of 100 ml min^{-1} to transport the evolving water vapor to the gas outlet of the furnace. During the drying process, the coupled Mass Spectrometry (MS) and Fourier-Transform Infrared Spectroscopy (FTIR) devices were activated for the characterization of the evolved gases from the material (e.g. water vapor).
- After this preconditioning of the sample, the STA was cooled down to room temperature and the initial mass m_i of the sample was defined.
- Subsequently, the sorption experiment started according a defined temperature and water vapor program as shown in figure 5.3. Three temperatures with $T = 35^\circ\text{C}$, 50°C and 65°C and two partial pressures water vapor $p_{\text{H}_2\text{O}} = 12.5 \text{ mbar}$ and 20 mbar were defined for the adsorption while desorption took place at $T = 200^\circ\text{C}$ and $p_{\text{H}_2\text{O}} = 0 \text{ mbar}$.

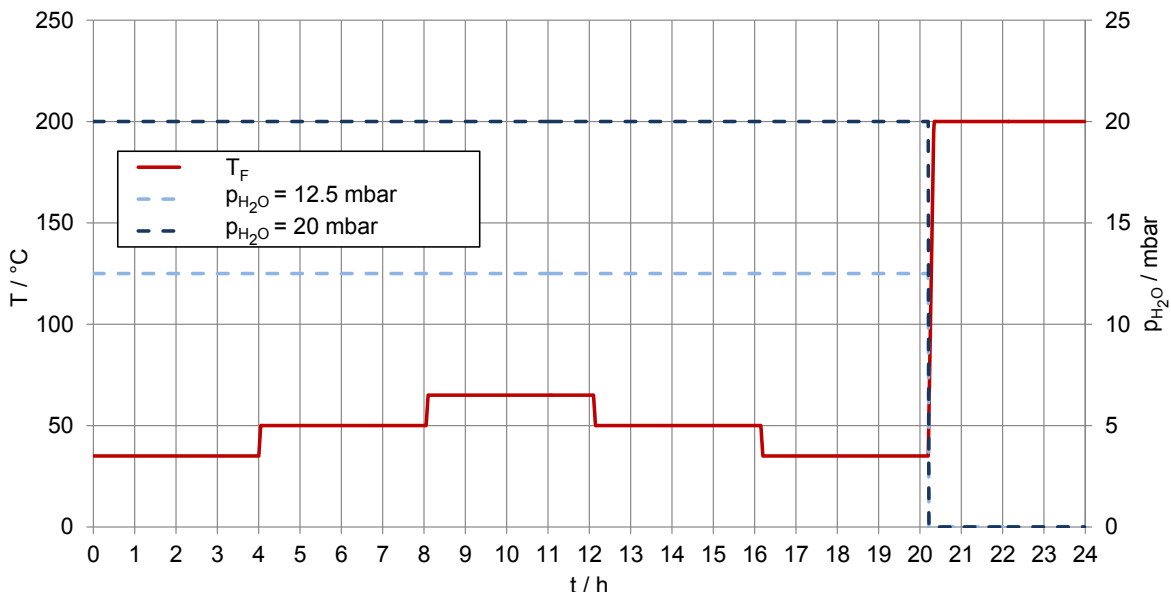


FIGURE 5.3: Furnace temperature program $T_F(t)$ and water vapor pressure $p_{\text{H}_2\text{O}}$ during the clinoptilolite and salt-based composites STA measurements

Results

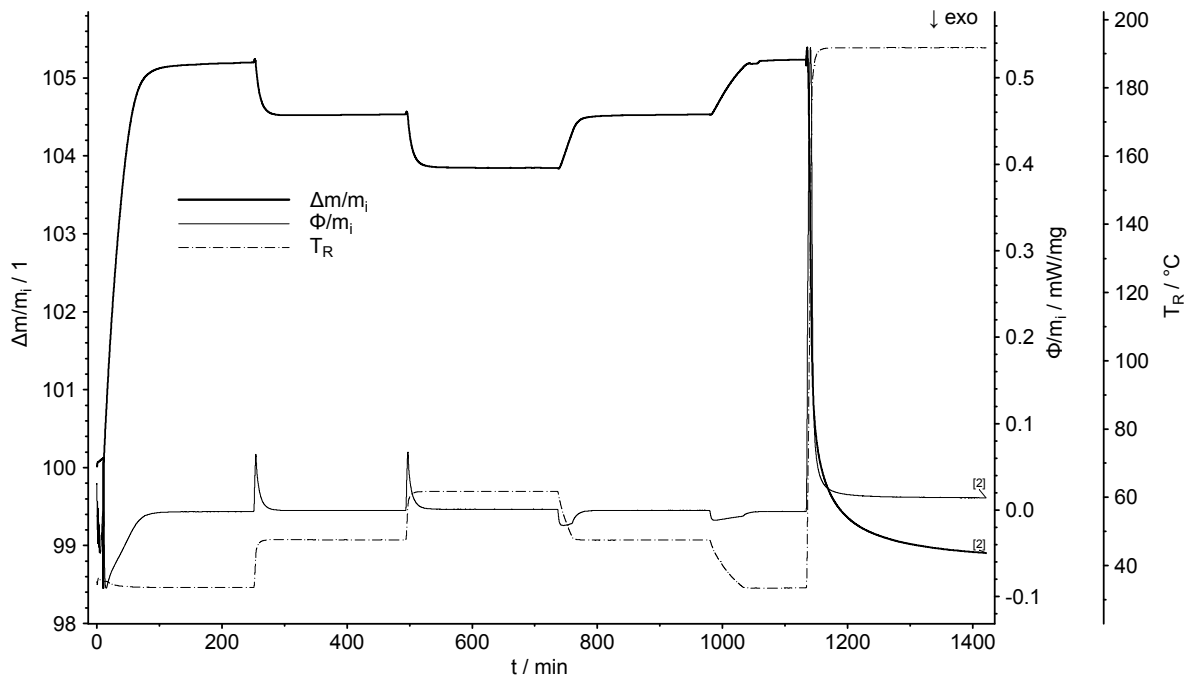


FIGURE 5.4: Clinoptilolite mass change $\Delta m/m_i$ and specific heat flow rate ϕ/m_i at a water vapor pressure $p_{H_2O} = 12.5$ mbar from STA measurements

In figure 5.4 as an example an experimental result from the STA of the pure clinoptilolite at $p_{H_2O} = 12.5$ mbar can be seen. While the TGA shows the water uptake or release at the different temperature steps, the DSC depicts the corresponding heat flow rate due to phase transitions (condensation and evaporation), binding energies (*Van der Waals* forces) and heat capacity changes.

The enthalpy change Δh between the different temperature steps is calculated based on equation 3.22. As shown in [30], several different possibilities of baseline constructions are available and used for different effects. In case of the measured DSC peaks it was decided to use horizontal baselines between T_i and T_f starting from the measured heat flow after the peak $\phi(T_f)$. This procedure was applied with all following sorption measurements to have comparable enthalpy data over all material candidates.

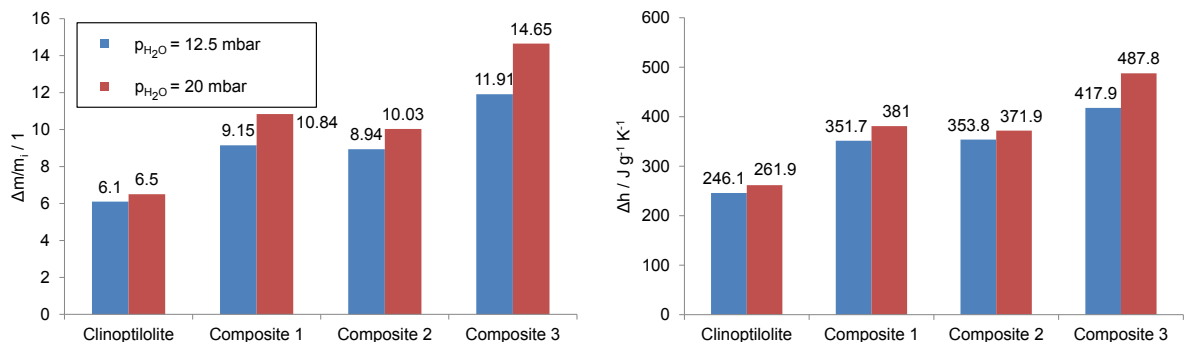


FIGURE 5.5: $\Delta m/m_i$ and Δh between $T = 35$ and 200 °C of clinoptilolite and salt-based composites

To compare the performance of the different developed composites and the pure clinoptilolite, the mass change $\Delta m/m_i$ and the enthalpy change Δh of the desorption process between $T = 35$ and 200 °C at two different p_{H_2O} levels are evaluated. As already described in [78], composite 3 shows the highest mass change $\Delta m/m_i$ and enthalpy change Δh under the defined experimental conditions.

Additional FTIR results during the preconditioning process were used to analyze the evolved gases. As it could be seen for composite 3, hydrogen chloride HCl was found in the gas phase IR spectrum at temperatures above $T \geq 110$ °C. Therefore, this material could not be used for open sorption applications above this temperature.

5.2.4 Characterization of a synthetic zeolite

A further STA experiment was designed to compare and validate the developed sorption measurement protocol to available literature data [90] for a synthetic zeolite 4A. The material is a commercially available zeolite with the product name *Köstrolith 4A* from the company *Chemiewerk Bad Köstritz* in Germany with a pore size of 0.4 nm and a particle size of 1.6 to 2.5 mm.



FIGURE 5.6: Molecular sieve *Köstrolith 4A* from the company *Chemiewerk Bad Köstritz* in Germany

The calibration of the used DSC sensor as well as sensor type, crucibles and applied gases are similar to the already described protocol in section 5.2.3.

Measurement protocol

The experimental design is comparable to the STA experiments shown for clinoptilolite and the salt-based composites. In case of the zeolite 4A measurement, a maximum temperature of $T_{max} = 230$ °C and three adsorption steps with $T_F = 35$ °C, 55 °C and 80 °C at three different water vapor partial pressures $p_{H_2O} = 6$ mbar, 12 mbar and 24 mbar are applied. The sample was placed into a Pt/Rh crucible without lid and being weighted inside the STA. In contrast to the composite measurements before, no separate preconditioning is conducted because desorption of the zeolite takes place before and after an adsorption step during one measurement run. Additional, EGA is uncoupled from the gas outlet during the zeolite 4A STA experiments due to pure physisorption experiments. The sample mass is evaluated

directly before a new measurement run and resulted in $m_S = 39.5$ to 46.7 mg at ambient conditions.

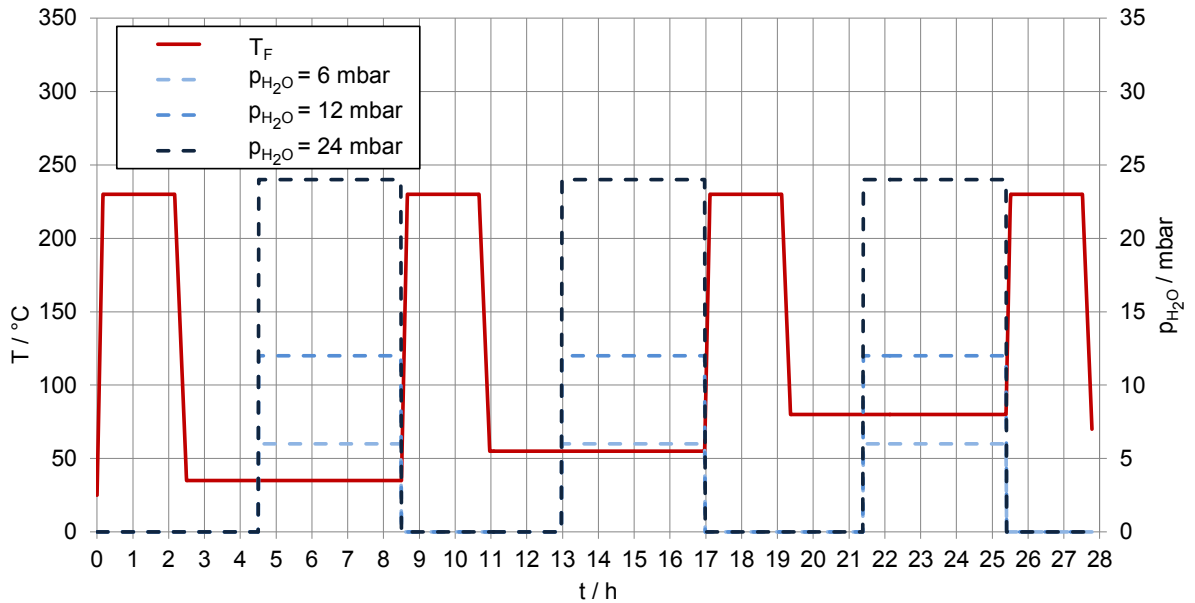


FIGURE 5.7: Furnace temperature program $T_F(t)$ and water vapor pressure p_{H_2O} during the zeolite 4A STA measurements

Figure 5.7 represents the applied temperature and humidity parameters during the STA experiment. Between the different adsorption temperatures, the humidity generator was switched off to ensure a dry N_2 atmosphere and the furnace dried the material at $T_{max} = 230$ °C for $t = 2$ hours. During the adsorption steps at $T_F = 35$ °C, 55 °C and 80 °C, the humidity generator was switched on after a two hour delay to ensure isotherm sample conditions. Each following adsorption step has a duration of $t = 4$ hours.

Sorption isotherm and enthalpy results

The measured water uptake $\Delta m/m_i$ and enthalpy change Δh according to the defined measurement protocol are shown in figure 5.8. The evaluated data is compared with the integral adsorption enthalpy data from [90].

The programmed temperature $T_F(t)$ is controlled by the furnace thermocouple and not at the reference side T_R of the DSC sensor. Due to that, the measured adsorption temperatures T are slightly lower as the defined furnace temperatures T_F which is connected to the heat losses between the actual furnace temperature and the measured temperature at the reference side T_R of the DSC sensor.

As expected, the water uptake $\Delta m/m_i$ and enthalpy change Δh is higher at lower temperatures and higher partial pressure of water vapor p_{H_2O} . The reported data from [90] show slight differences in the used temperature and humidity for the adsorption process compared to the used parameters. Nevertheless, a good reproducibility is shown in the evaluated STA data. Literature data as well as the measured and evaluated sorption data in figure 5.8 describe no uncertainty estimation. This is due to missing sample measurements to check the reproducibility for several sample measurements.

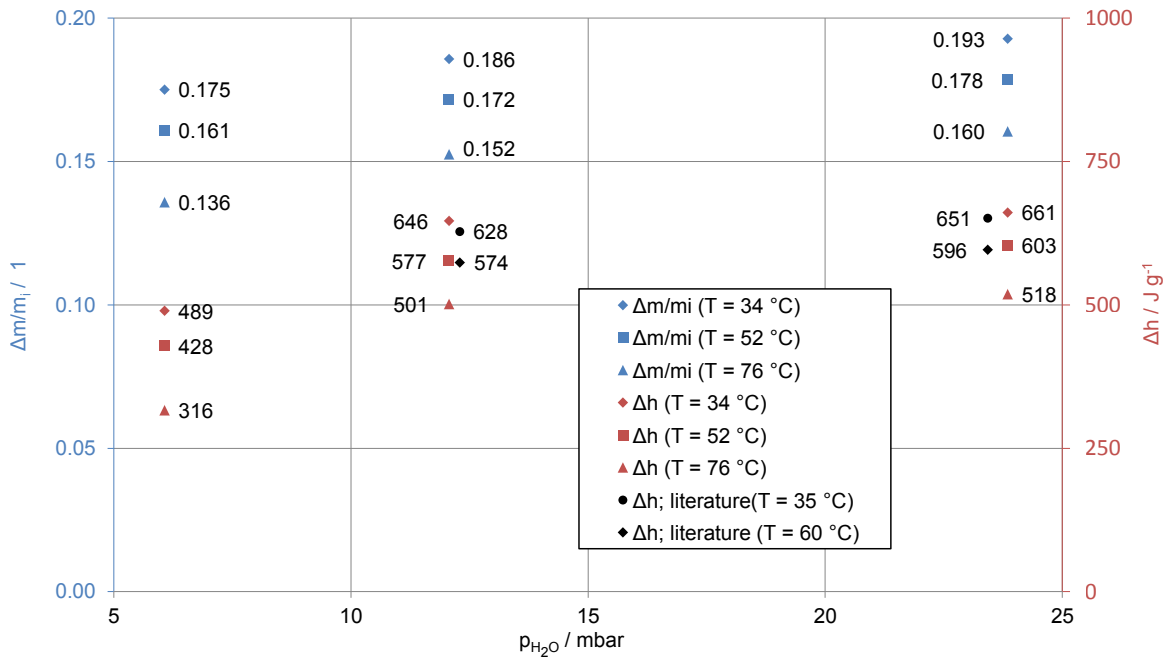


FIGURE 5.8: Zeolite 4A water uptake and enthalpy change results from STA measurements

Sorption rate results

The results on water uptake and enthalpy change shown in figure 5.8 are integral results from the measured mass change Δm and the heat flow rate ϕ . Due to a transient STA measurement, it is possible to compare the time dependent behavior of $\Delta m(t)$ and $\phi(t)$.

It is very doubtful whether a meaningful comparison can be made between a kinetic analysis and the experimental results. The measured quantities $\Delta m(t)$ and $\phi(t)$ depend on mass and heat transport inside the sample. A change of the sample size, the available surface for the solid-gas interaction or varying amounts of particles would lead to different results of $\Delta m(t)$ and $\phi(t)$. In this work, all measurements were done using the same sample to compare $\Delta m(t)$ and $\phi(t)$ at different temperature levels and water vapor pressures.

The results in figure 5.9 represent the time dependent adsorption behavior at $T = 34^\circ\text{C}$ of the measured zeolite 4A. The sorption or water uptake rate $\Delta m(t)/m_i$ strongly depends on the available water vapor pressure p_{H_2O} . While the water uptake at $p_{H_2O} = 24$ mbar ends after $t \approx 1.5$ h it is still not finished after $t \approx 3.5$ h for $p_{H_2O} = 6$ mbar.

The heat flow rate curves $\phi(t)$ indicate the behavior of the thermal power in a possible TCES application. As it can be seen in figure 5.9, the peak of the heat flow rate ϕ_{max} for all measured water vapor pressures $p_{H_2O} = 6$ mbar, 12 mbar and 24 mbar is reached right after the start of the experiment at $t \approx 5$ min.

These results were used for a transient numerical description of the adsorption behavior of

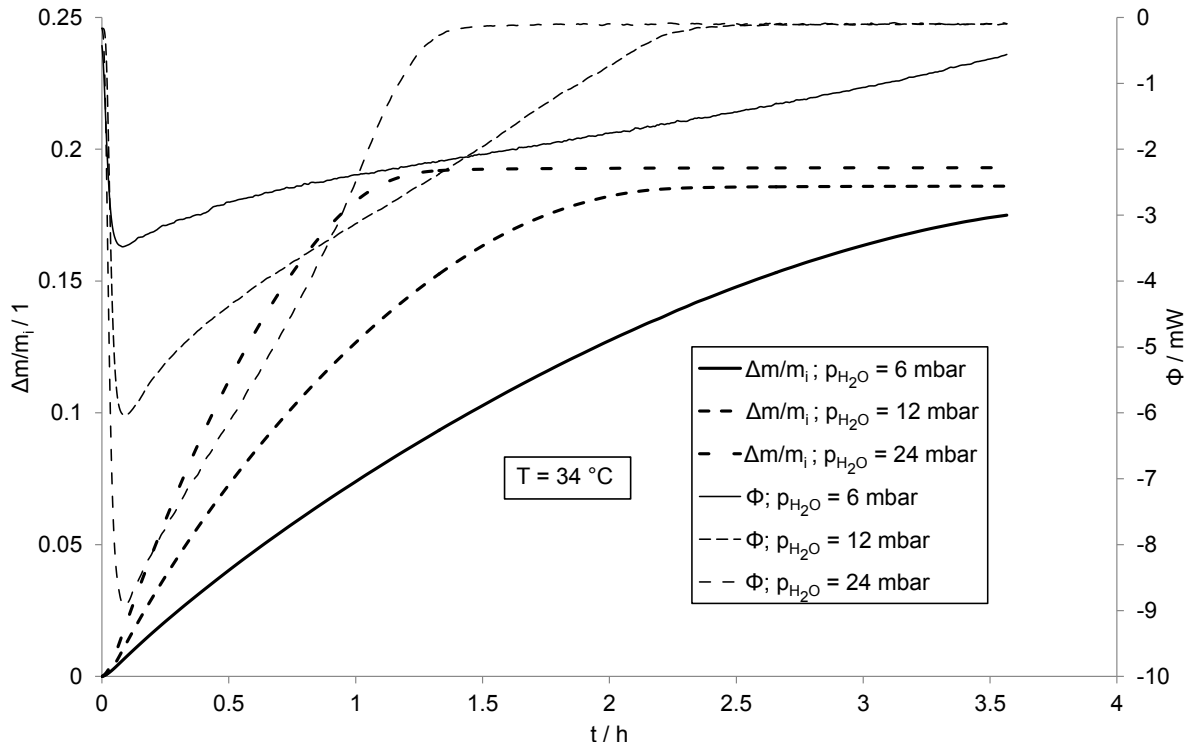


FIGURE 5.9: Zeolite 4A $\Delta m(t)/m_i$ and $\phi(t)$ at $T = 34\text{ }^\circ\text{C}$ and different water vapor pressures $p_{H_2O} = 6\text{ mbar}$, 12 mbar and 24 mbar

the used zeolite 4A in a moving bed reactor by CFD simulations. The experimental curves as shown in figure 5.9 for all measured temperatures $T_F = 35\text{ }^\circ\text{C}$, $55\text{ }^\circ\text{C}$ and $80\text{ }^\circ\text{C}$ and pressures $p_{H_2O} = 6\text{ mbar}$, 12 mbar and 24 mbar have been fitted to polynomial functions representing the energy and mass change rate at the experimental conditions. For further informations, the reader is referred to [81].

5.3 Characterization of TCMs based on chemical reactions

This section concentrates on methods for the evaluation of the specific heat capacity $c_p(T)$ and the effective thermal conductivity $\lambda_{eff}(T)$ of different powdery TCM candidates. The challenges and possible applications of the STA, DSC, LFA and THB method are shown. While the STA method is mainly used to identify reaction free temperature intervals or cycling stability, DSC is applied for the evaluation of the specific heat capacity $c_p(T)$. Further LFA and THB measurements on compacted and packed bed configurations of the powdery materials are performed to evaluate the thermal transport properties $a_{eff}(T)$ and $\lambda_{eff}(T)$.

The first part of this section addresses the measurement protocols development, including the equipment and setup specifications, the used gas conditions, sample preparations, temperature programs and data analysis of the different methods. The second part is focusing on the evaluated results on four different possible TCMs: $\text{CaC}_2\text{O}_4 \cdot \text{H}_2\text{O}$, H_3BO_3 , $\text{Ca}(\text{OH})_2$ and $\text{Mg}(\text{OH})_2$. Finally, the measured results are discussed and compared to available literature data.

5.3.1 STA measurements

As already shown in section 5.2, the STA method is a powerful method to identify different characteristics of the investigated materials and reactions. For the evaluation of thermophysical properties like specific heat capacity $c_p(T)$ it is a prerequisite, that the material is stable and for instance no mass change due to reaction or degradation occurs in the investigated temperature range. In that case, the STA method is used to identify reaction free temperature intervals of the different investigated TCM candidates. As a result it can be determined whether the reactant or product of the measured reaction exist at a certain temperature.

In addition, several tests to observe the time behavior of the reaction conversion related to sample mass m_S and applied heating rate β were performed. Finally, cycling experiments were realized to investigate the repeatability of selected reactions.

Equipment, setup and gas conditions

The used STA equipment and possible setups were already shown in section 5.2.1. Depending on the measurement problem, different gases are used during the measurements. Most of the experiments started from the thermal discharged form or product (s. section 2.4) to the thermal charged form or reactants. In this case, mainly N_2 was used as gas atmosphere under ambient pressure conditions. One exception are cycling tests on CuO , where the forth and back redox reaction was triggered by additional O_2 .

Sample preparation and crucibles

For pure TGA experiments, Al_2O_3 with a volume between $V = 0.2$ and 5 mL is used with different sample masses. The crucible was filled up with the powdery sample material to

the desired mass. For STA experiments, aluminum or platinum crucibles are used due to their high thermal conductivity. According the VDI heat atlas [69], aluminium has a thermal conductivity of $\lambda_{Al} = 236 \text{ W m}^{-1} \text{ K}^{-1}$ and platinum $\lambda_{Pt} = 73 \text{ W m}^{-1} \text{ K}^{-1}$ at $T = 0^\circ\text{C}$ in comparison to Al_2O_3 with $\lambda_{\text{Al}_2\text{O}_3} = 24.2$ to $37.2 \text{ W m}^{-1} \text{ K}^{-1}$ (depending on purity and porosity) at $T = 18$ to 31°C as reported by [91].

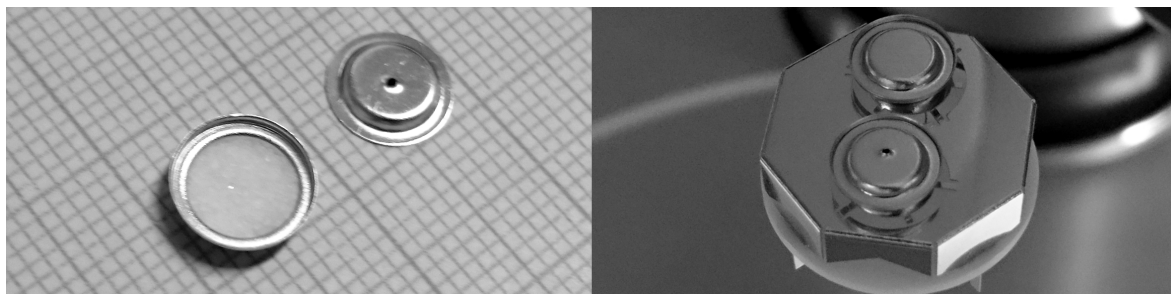


FIGURE 5.10: B_2O_3 sample in aluminum crucible and cold welded pierced crucible on a STA type S sensor

All samples measured as TGA only in the Al_2O_3 crucibles had no lid on the top. For STA measurements it was decided to cover aluminum or platinum crucibles with a pierced lid to reduce convection losses as compared to open crucibles. In case of the aluminum crucibles, additionally cold welded lids are used to avoid the possibility to leap up during the measurement. The pierced hole in the lid is necessary that evolved gases are able to escape from the sample crucible. Sample and crucible mass at room temperature are directly measured in the STA system prior to the measurement.

Temperature program

Investigated TCM candidates show their reactions from the thermal discharged to the thermal charged form above room temperature at ambient pressure conditions. Due to that, all TGA and STA experiments were started at ambient conditions. To avoid e.g. dehydration of the thermal discharged material there was no vacuum conditioning before starting the measurement runs.

For identification of reaction free temperature intervals, TGA and STA measurements with a heating rate between $\beta = 2$ to 5 K min^{-1} were performed. The maximum temperature T_{max} was adapted to the particular material. Additional performed experiments can not be generalized here and are described in detail for each measured TCM candidate in section 5.4 starting at page 96.

Data Analysis

For data analysis of STA results the *NETZSCH Proteus 6.1.0* measurement and evaluation software was used. Measurement data of the balance and the DSC sensor can be directly loaded into the software and mass change $\Delta m/m_i$ and DSC sensor voltage U_{DSC} curves can be directly plotted versus temperature or time. The implemented software features allow to calculate mass change steps Δm , onset temperatures $T_{e,i}$, peak temperatures T_{pk}

and inflection points of the TGA curves as well as the resulting heat flow rate $\phi(T)$ for an enthalpy calibrated DSC sensor (s. section 3.6) or the measured peak area (s. equation 3.22).

5.3.2 DSC protocol and data analysis for specific heat capacity evaluation

Equipment and setup

For specific heat capacity $c_p(T)$ evaluation of the investigated TCM candidates, a commercial heat flow DSC from NETZSCH, namely *DSC 204 F1 Phoenix* was used. The operating principle is already described in section 3.6 and the used equipment and setup can be found in section 4.2.1.

Gas conditions

All $c_p(T)$ DSC experiments are analyzed using helium as purge gas for inert gas conditions. Helium has a higher thermal conductivity with $\lambda_{He} = 0.1536 \text{ W m}^{-1} \text{ K}^{-1}$ compared to argon $\lambda_{Ar} = 0.0177 \text{ W m}^{-1} \text{ K}^{-1}$ or nitrogen $\lambda_{N_2} = 0.0256 \text{ W m}^{-1} \text{ K}^{-1}$ at $T = 25 \text{ }^\circ\text{C}$ according to the VDI heat atlas [69]. Therefore, helium leads to a lower sensitivity S_{DSC} of the DSC sensor due to a better heat transport in comparison to other common used DSC gases. Ehrenstein et al. [11] has noted, that helium is applied for measurements below room temperature due to faster stable temperature conditions in the measurement cells.

Sample preparation and crucibles

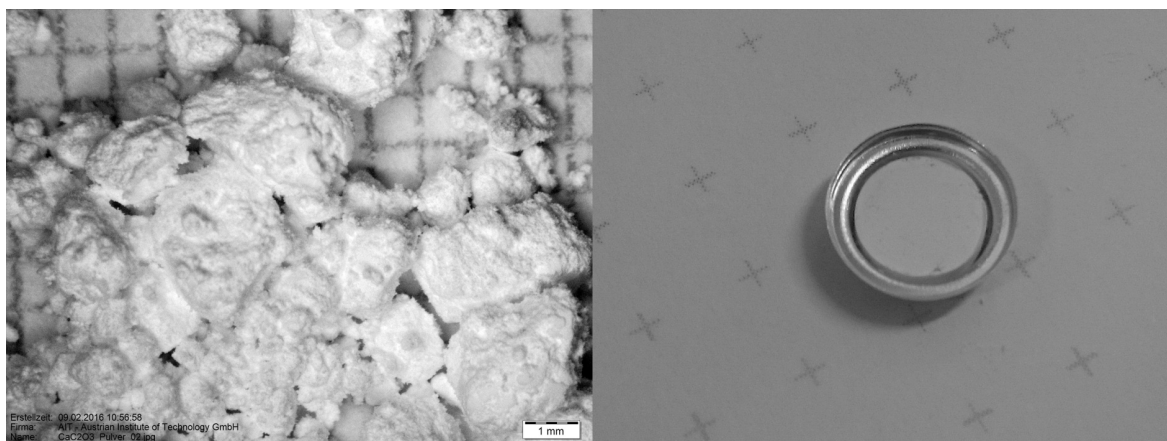


FIGURE 5.11: $\text{CaC}_2\text{O}_4 \cdot \text{H}_2\text{O}$ powder material and pressed cylindrical shaped $\text{CaC}_2\text{O}_4 \cdot \text{H}_2\text{O}$ DSC sample in aluminum crucible

In order to get good contact conditions between a powdery TCM and the crucible bottom, the material is compacted and pressed into cylindrical shaped samples as shown in figure 5.11. Due to compaction it is also possible to get a higher density which helps to increase the overall sample mass.

Aluminum crucibles with $25 \mu\text{L}$ volume are filled with the different TCMs. In total, three samples per material were prepared. The corresponding crucible lids were pierced and cold welded on the crucible top. Prior to this weighing of the empty crucible with lid and the

sample was performed to know the initial masses of the crucible and the sample before the DSC measurement run.

Temperature program

The measurement started with a cooling segment to $T_{min} = -50^\circ\text{C}$ using gaseous nitrogen for cooling of the furnace. After that, an isothermal segment prior to the heating with $t = 5$ min was applied to achieve a stable DSC zero line. This stable zero line is reached due to minimization of the temperature gradient between sample and reference side of the DSC sensor ($\Delta T = T_S - T_R$, s. section 3.6). The subsequent heating segment used a heating rate of $\beta = 10 \text{ K min}^{-1}$ to the defined T_{max} as recommended by [36]. Finally, the system is cooled down to room temperature with $\beta = 10 \text{ K min}^{-1}$.

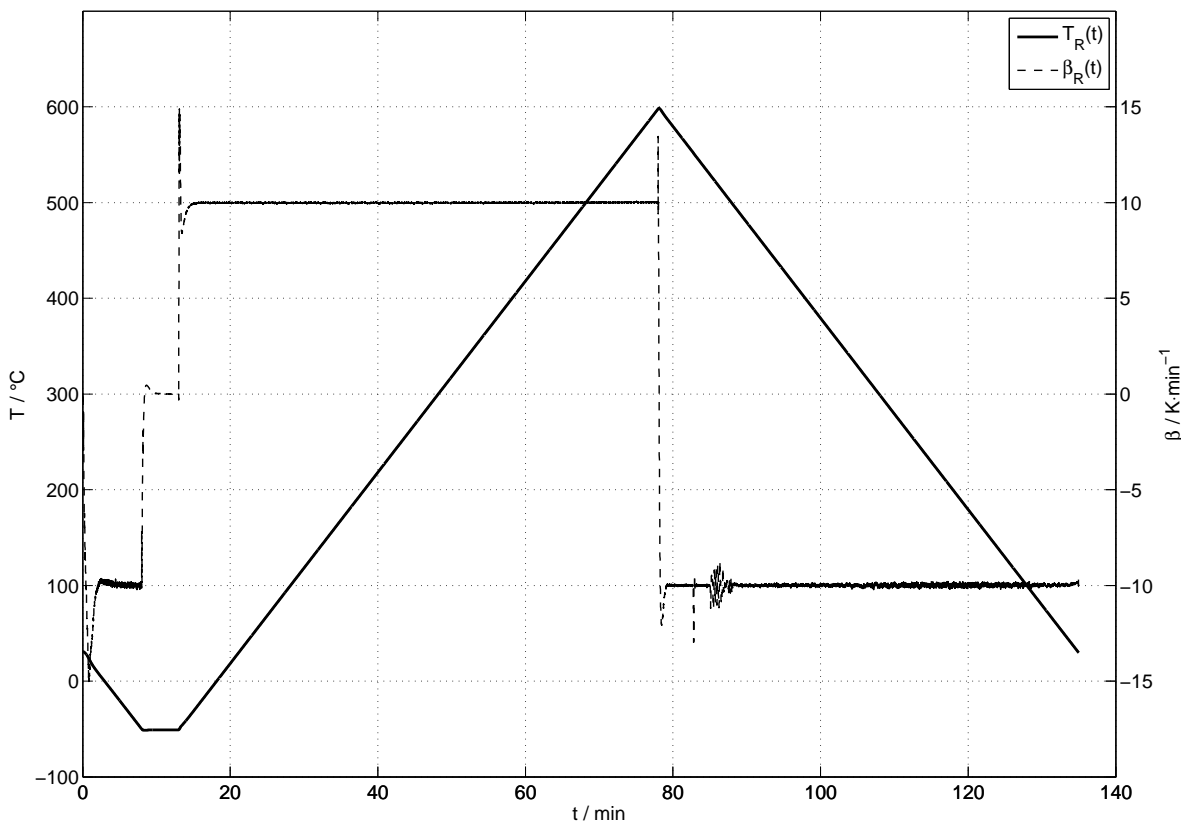


FIGURE 5.12: Time-dependent temperature and heating rate progress for $c_p(T)$ measurements in the heat flow DSC

Figure 5.12 displays the measured temperature on the reference side of the DSC sensor T_R with the associated heating rate β of two empty aluminum crucibles. For the evaluation of $c_p(T)$ only the heating segment of the whole temperature program is used. Focusing on the heating rate β in the heating segment between $t = 13$ and 15 min it can be seen, that this time is necessary until a stable heating rate β is reached in the system. Due to that, T_{min} for the evaluation of $c_p(T)$ is higher than the programmed starting temperature of the heating segment predetermined through constant heating rate conditions.

Data Analysis

As described in section 4.2.4 several zero line, reference and sample measurements are necessary to determine $c_p(T)$ with an uncertainty budget based on these data. To automatize this process, a *MATLAB* script which is able to process several DSC raw data files was developed.

In a first step, the script is plotting the loaded raw data U_{DSC} into one diagram. Figure 5.13 depicts an example for the DSC experiments of $\text{CaC}_2\text{O}_4 \cdot \text{H}_2\text{O}$ with three zero line, three $\alpha\text{-Al}_2\text{O}_3$ sapphire reference and three sample measurements.

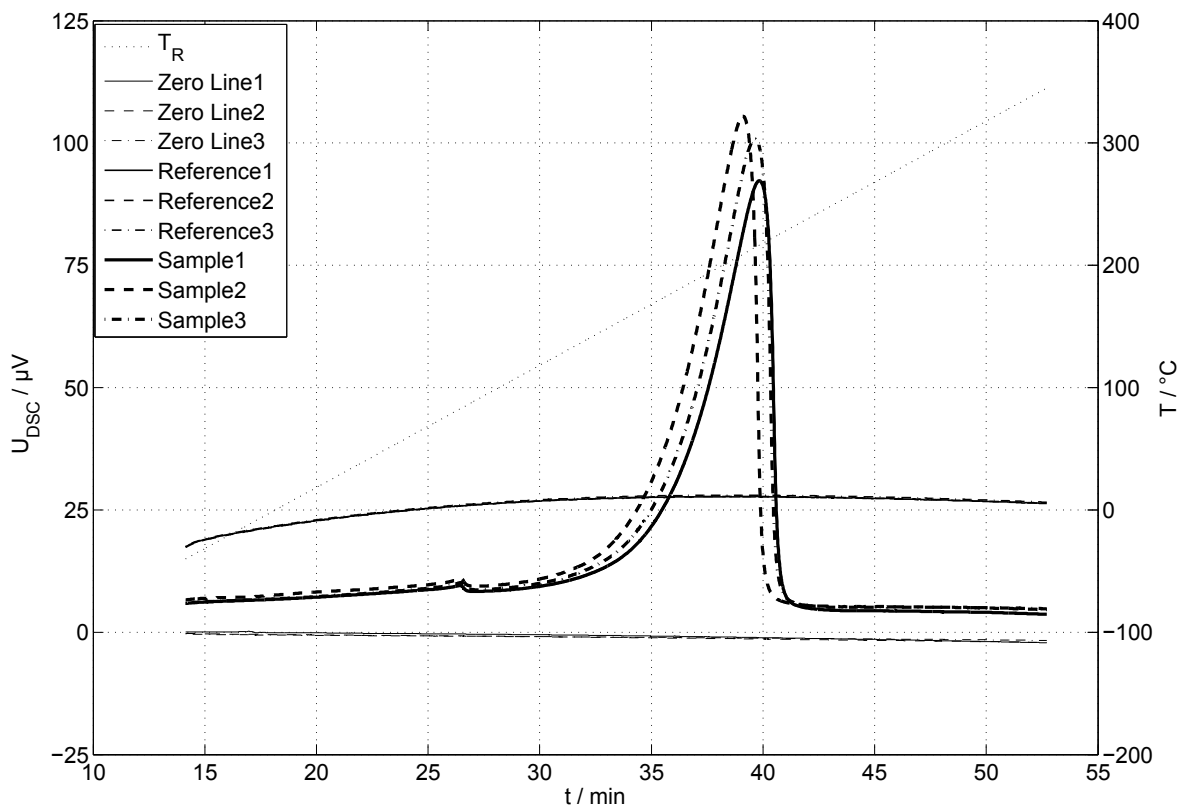


FIGURE 5.13: Plot of DSC raw data files as input for the $c_p(T)$ and uncertainty calculation for $\text{CaC}_2\text{O}_4 \cdot \text{H}_2\text{O}$

A synthetic $\alpha\text{-Al}_2\text{O}_3$ sapphire (SRM 720) from the National Bureau of Standards (NBS) with the corresponding certificate is used as standard reference material. The corresponding certificate contains the enthalpy and heat-capacity data in a temperature range from 10 to 2250 K. The given heat capacity values have an accuracy in a range within ± 0.1 to 0.3% in the temperature range of 70 to 1173 K.

Figure 5.13 is already an extraction from the whole measurement program as shown in figure 5.12. For further evaluation of $c_p(T)$ only the measurement data in the heating segment of the DSC signals is needed. Due to the fact that $c_p(T)$ of the reference sapphire is only available in a 10 K interval and the measured DSC data has a higher resolution (approx. 30 samples K^{-1} for a heating rate $\beta = 10 \text{ K min}^{-1}$), it is necessary to calculate a polynomial function representing $c_p(T)$ of the reference sapphire in the temperature range of interest.

The used curve fit is based on a 3rd degree polynomial which coefficients are calculated by a standard *MATLAB* function called *polyfit*, available in software version *R2010b*. The coefficients of the polynomial are re-assessed for every chosen temperature range in the developed script. It was decided not to use polynomial functions with higher degrees because $c_p(T)$ of the reference sapphire is only a weak function of temperature and there are no inflection points in the investigated temperature range starting from $-50\text{ }^\circ\text{C}$.

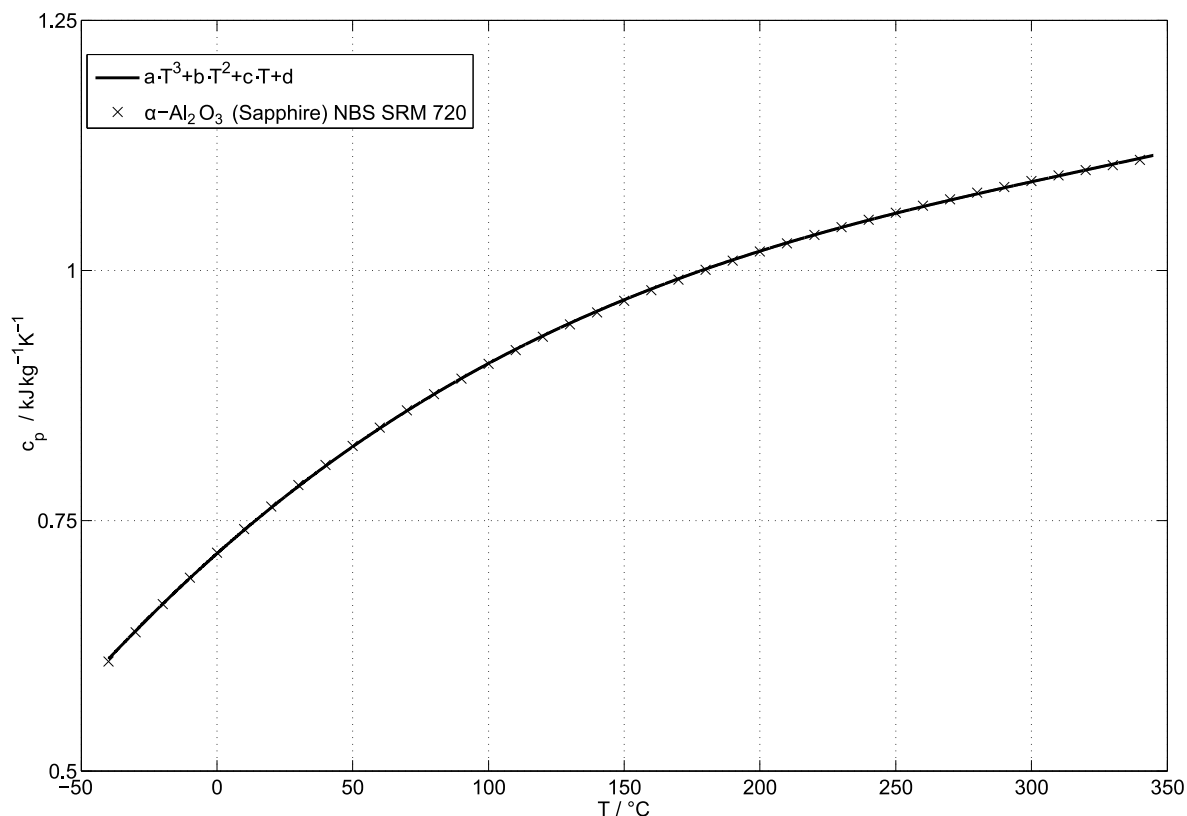


FIGURE 5.14: $c_p(T)$ of the reference sapphire NBS SRM 720 and the applied polynomial model

As already shown in figure 5.12 it is necessary to set a temperature window starting at a higher temperature than the programmed heating segment to fulfill a constant heating rate β in the DSC system. This is also realized in the developed script by defining a temperature window. In case of the temperature program in figure 5.12 this would start at $T = -30\text{ }^\circ\text{C}$ or at $t = 13$ to 15 min.

With the loaded DSC raw measurement data, $c_p(T)$ based on [92] can be calculated according to equation 4.3 and the combined measurement uncertainty based on [72] can be assessed according to equation 4.4. Finally, a plot as well as a file list with the calculated $c_p^{app}(T)$ and the corresponding uncertainty $u_c(T)$ is generated as output of the programmed script (s. figure 5.15).

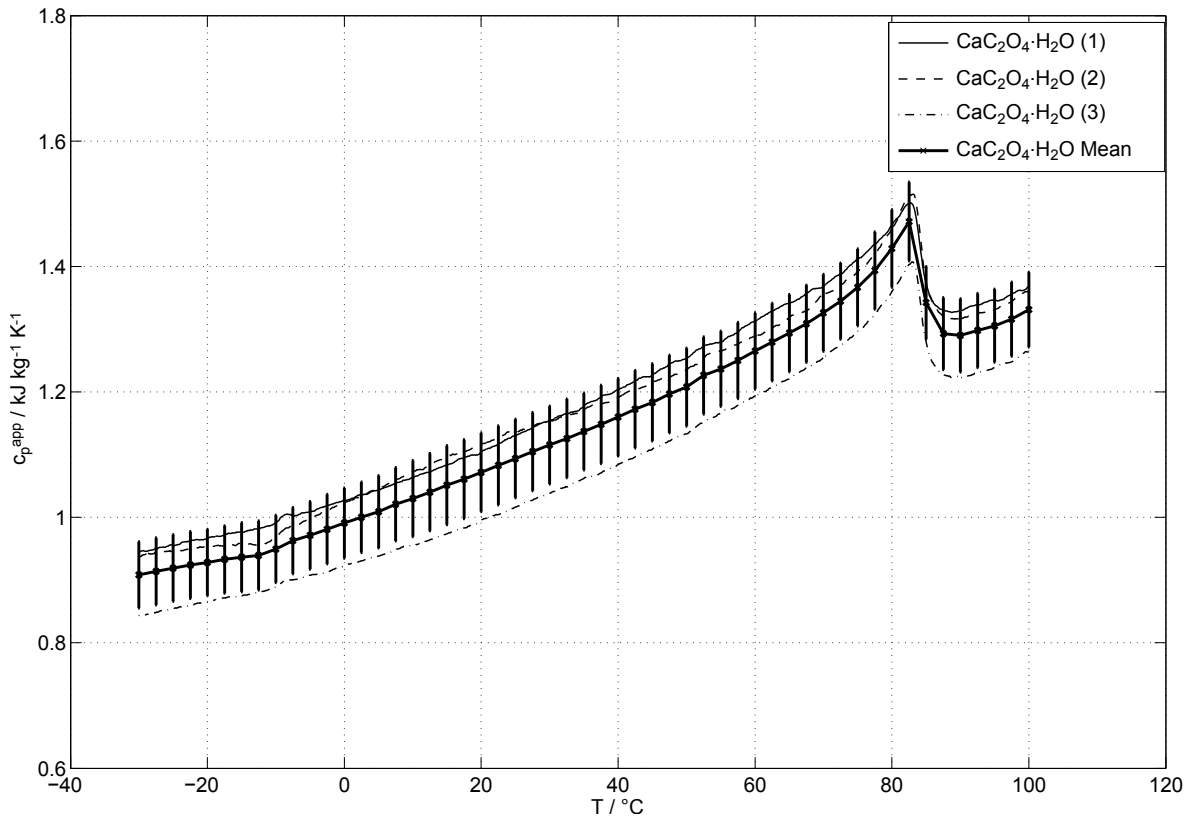


FIGURE 5.15: Plot of the apparent specific heat $c_p^{app}(T)$ and the corresponding uncertainty u_c for $\text{CaC}_2\text{O}_4 \cdot \text{H}_2\text{O}$

5.3.3 LFA experiments on compacted TCM

Equipment and Setup

For thermal diffusivity measurements, a *NETZSCH LFA 467* device was applied. This LFA can be used to measure thermal diffusivity $a(T)$ between $T = -100$ and 500 °C. A xenon flash lamp can deliver different pulse energies up to $Q = 10$ J per pulse and the pulse length can be varied between $t = 20$ and 1200 μs . The built-in Mercury Cadmium Telluride (MCT) detector is a liquid nitrogen cooled IR detector for the above mentioned temperature range. A summary of the key technical specifications can be found in table 5.3.



FIGURE 5.16: Light flash analysis system *NETZSCH LFA 467 HyperFlash*

LFA System	LFA 467 HyperFlash
Furnace	Steel Furnace
Temperature range / °C	-100 - 500
Max. heating rate / K min ⁻¹	50
External cooling	nitrogen (liquid/gaseous)
Detector	MCT
Thermal diffusivity range / mm ² s ⁻¹	0.01 - 1000
Flash lamp pulse width / μs	20 - 1200 (1 μs steps)
Max. pulse energy / J	10
Atmosphere	He
Vacuum	$p < 150$ mbar
Gas Control	Mass flow controller
Automatic Sample Changer	4 cylindrical samples ($d = 24.7$ mm) 4 cylindrical samples ($d = 12.7$ mm)
Special sample holder	Pressure and liquids sample holder

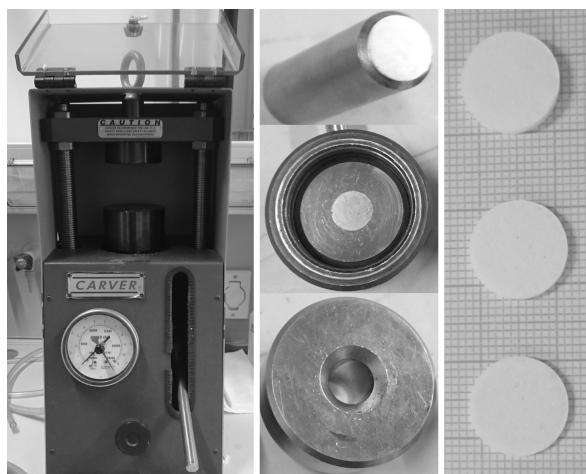
TABLE 5.3: Key technical specification for NETZSCH LFA 467

Gas conditions

All LFA experiments were conducted in a helium atmosphere. The reason for helium as inert gas condition are based on the same considerations as already described for DSC experiments in section 5.3.2. Due to a higher thermal conductivity of helium below room temperature as other usable inert gases (e.g. nitrogen or argon) stable temperature conditions in the measurement cell are reached faster, especially, for low temperatures.

Sample preparation

To analyze the thermal diffusivity of a compressed TCM bulk, the samples were prepared by pressing cylindrical pills with a diameter of $d = 12.7$ mm with a laboratory press (s. figure 5.17).

FIGURE 5.17: Carver lab press with a cylinder tool kit for 12.7 mm samples and compacted H₃BO₃ samples

The powdery TCM is filled into the cylinder tool kit and pressed with different forces. The used lab press could apply a maximum force of $F_{max} = 108$ kN. Preparation of different TCM has shown, that different forces are necessary to regain unbroken samples upon removal from the cylinder tool kit. Once this force is known, several cylindrical samples with similar thickness can be prepared through measuring the initial weight of the TCM before filling it into the cylinder tool kit. Finally, the different densities of the compressed bulk samples is evaluated by sample mass, diameter and thickness.

Most of the compacted samples are shiny on the upper and lower flat surface which is disadvantageous for LFA experiments due to higher reflection and less absorption of the energy pulse from the light source. As described by [73], a metal deposit is used to make translucent samples opaque and a black coating is used to increase the energy absorption. The study concluded, that the coating and the material with their properties thermal resistance $R_{th} = \delta / \lambda$, thermal capacitance $\rho \cdot c_p \cdot \delta$, characteristic time $\tau = \delta^2 / a$ and contact resistance $R_{th,cont}$ between them have to met the following criteria to be neglected in the LFA experiment. In the study of [73] the following equations are defined:

$$R_{th,coat} \cdot (\rho_{coat} \cdot c_{p,coat} \cdot \delta_{coat}) = \tau_{coat} \ll R_{th,S} \cdot (\rho_S \cdot c_{p,S} \cdot \delta_S) = \tau_S \quad (5.2)$$

$$\rho_{coat} \cdot c_{p,coat} \cdot \delta_{coat} \ll \rho_S \cdot c_{p,S} \cdot \delta_S \quad (5.3)$$

$$R_{th,cont} \cdot (\rho_{coat} \cdot c_{p,coat} \cdot \delta_{coat}) = \tau_{cont} \ll R_{th,S} \cdot (\rho_S \cdot c_{p,S} \cdot \delta_S) = \tau_S \quad (5.4)$$

The first equation describes that the thickness of the coating should be very thin and the coating material should have a high thermal conductivity in comparison to the sample material. The second equation indicates, that the heat capacity of the coating should be much smaller compared to the heat capacity of the sample material and the third equation shows, that the contact resistance between coating and sample material should be as low as possible.

In case of the investigated TCM, a graphite aerosol for conductive coatings was used. It contains a high level of pure and fine graphite powder and a thermoplastic binding agent. The black color makes it usable as absorbent coating for the LFA application. The aerosol is sprayed from a short distance (approx. 20 to 30 cm) on top and bottom side of the LFA sample until the shiny flat surfaces are covered by the graphite.

Temperature program, pulse and detector settings

A maximum of three prepared compressed and coated TCM samples are put into the sample holder system of the used LFA. The defined temperature program uses steps with $\Delta T = 25$ °C and the temperature limits T_{min} and T_{max} are defined according to the preliminary STA results of the observed TCM. The pulse duration of the xenon light source was defined with $t = 300$ μ s with a lamp voltage of $U = 230$ V.

The MCT detector acquisition time and amplification of the detector output voltage is regulated through the measurement software. The detector signal was recorded with 2000 data points per shot. The used helium gas atmosphere had a flow rate of 20 ml min^{-1} .

The implemented optics were used to zoom on a spot with a diameter $d = 8.9 \text{ mm}$, which corresponds to 70 percent of the sample diameter with $d = 12.7 \text{ mm}$. A summary of the defined parameters can be found in table 5.4.

LFA parameter	Value
Sample diameter d / mm	12.7
Nr. of samples	max. 3
Flash lamp pulse width / μs	300
Flash lamp pulse voltage / V	230
Detector acquisition time	automatic
Detector signal amplification	automatic
Optical zoom diameter / mm	8.9 (70 %)
Atmosphere	He
Flow rate / ml min^{-1}	20

TABLE 5.4: Measurement parameters NETZSCH LFA 467

Data Analysis

The LFA detector signal was analyzed by applying the *Cowan* model, as described in [44]. At least 5 measurements at one temperature point were performed. For each shot, the results are exported to an own developed *MATLAB* script which is processing the following data:

- Temperature (T)
- Diffusivity (a)
- Half time ($t_{1/2}$)
- Number of data points (i)
- Data acquisition duration (t_{acq})
- Pulse voltage (U)
- Puls length (t)
- Standard deviation (σ)

Additional meta information is stored for each sample, containing the sample name, sample thickness δ and diameter d , gas conditions and applied model. These results of several samples for one material is processed for a mean calculation and uncertainty assessment.

A detailed description on the used uncertainty assessment of LFA thermal diffusivity results is already published in [87]. The combined measurement uncertainty for the thermal diffusivity u_a is calculated based on three contributions as shown in equation 5.7.

$$u_{a, ESU}^2 = a^2 \cdot \left[\frac{4 \cdot u_{\delta}^2}{\delta^2} + \left(\frac{a \cdot \pi^2}{\ln(0.25) \cdot \delta^2} \right)^2 \cdot u_{t_{1/2}}^2 \right] \quad (5.5)$$

$$u_{a, SSU}^2 = \sigma(a)^2 = \frac{1}{n-1} \sum_{i=1}^n (a_i - \bar{a})^2 \quad (5.6)$$

$$u_a^2 = u_{a, ESU}^2 + u_{a, SSU}^2 + u_{a, MSU}^2 \quad (5.7)$$

According to [87], the first equation describes the Equipment Specific Uncertainty (ESU) of the laser flash method based on the *Parker* model [41]. It includes the uncertainty of the thickness u_{δ} and the time $u_{t_{1/2}}$. While u_{δ} comes from the certificate of the used micrometer gauge, $u_{t_{1/2}}$ is estimated by the ratio t_{acq}/i , where i represents the number of recorded data points.

The Sample Specific Uncertainty (SSU) is based on the standard deviation of the single results. The third part, called Model Specific Uncertainty (MSU), represents the standard deviation of the applied model to the measured curve which is calculated by the measurement software.

Thereafter, when the thermal diffusivity data $a_{eff}(T)$ is known, the effective thermal conductivity $\lambda_{eff}(T)$ is calculated according equation 4.6. The needed specific heat capacity $c_p(T)$ and corresponding uncertainty is already known from the DSC experiments. The additional needed bulk density ρ_B is evaluated by mass m and volume V of the compacted samples at room temperature. The corresponding uncertainty u_{ρ_B} is evaluated through the standard deviation σ of the measured density results of the individual samples.

The expanded combined standard uncertainty calculation for $\lambda_{eff}(T)$ according to [72] is shown in equation 4.7.

5.3.4 THB experiments on powdery TCM

Equipment

As already shown in section 4.3.2, a *LINSEIS THB 100* dynamic measurement system in combination with a metal frame kapton foil sensor (42 mm x 22 mm) is applied to evaluate the effective thermal conductivity $\lambda_{eff}(T)$ of the analyzed TCMs. The samples with the attached foil sensor are placed inside a lab furnace *MEMMERT UFP 500* which can reach a maximum temperature of $T_{max} = 250$ °C at ambient atmospheric conditions. A detailed description to the THB method can be found in section 3.9.

Calibration and sample preparation

For calibration of the measured temperature T and the thermal conductivity λ , water is used as reference standard with $\lambda(20$ °C) = 0.5984 W m⁻¹ K⁻¹. To fulfill good contact conditions between the surface of the foil sensor and the sample itself, it is necessary to use a liquid reference due to the thickness of the metal frame around the kapton foil sensor.



FIGURE 5.18: THB sensor calibration with water and immersed into the powdery sample inside the lab furnace

The sample is filled into a measuring glass beaker with a volume of $V \approx 100 \text{ cm}^3$ and shaken under defined conditions until no optical volume change was noticed anymore. After that, the volume was measured by the measuring cup scale and weight with a lab balance. Finally, the sensor was immersed into the sample and placed inside the lab furnace.

Temperature program and data analysis

Starting from room temperature, several temperature points with temperature steps of $\Delta T_F = 25^\circ\text{C}$ are predefined on the used lab furnace. If a programmed furnace temperature point is reached, several temperature measurements with the foil sensor inside the sample are performed until a stable temperature is indicated by THB system. This protocol should reduce the risk of a thermal gradient ΔT inside the sample before starting a thermal conductivity measurement. For each programmed temperature point, five subsequent thermal conductivity measurements are performed.

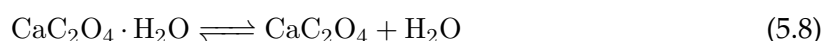
All THB experiments of the investigated TCMs are performed with different heating currents and data acquisition times. These parameters were adapted to the individual sample and can not be generalized.

A developed *MATLAB* script imports the evaluated temperatures and thermal conductivity data from the *LINSEIS THB 100* system and calculates the mean value as well as the standard deviation σ for $\lambda_{eff}(T)$.

5.4 Thermophysical properties of promising TCM candidates

5.4.1 Calcium oxalate monohydrate $\text{CaC}_2\text{O}_4 \cdot \text{H}_2\text{O}$

Calcium oxalate monohydrate $\text{CaC}_2\text{O}_4 \cdot \text{H}_2\text{O}$ is a stable monohydrate and is also known as the mineral Whewellite. It is used as a mass calibration standard for TGA devices due to the reproducible dehydration, decomposition to CaCO_3 and further decomposition to CaO in the temperature range between $T = 25$ and 800°C and is documented in several publications [93, 94, 95]. With focus on TCES, the dehydration reaction of $\text{CaC}_2\text{O}_4 \cdot \text{H}_2\text{O}$ to CaC_2O_4 was analyzed. The equilibrium for the hydration/dehydration reaction can be written as:



As precursor material for all experiments a commercial available product with the name *Calcium oxalate monohydrate, European Pharmacopoeia (EP) Reference Standard* from Sigma-Aldrich was analyzed.

Thermal decomposition

As preliminary experiment, several $\text{CaC}_2\text{O}_4 \cdot \text{H}_2\text{O}$ samples were analyzed with the STA method to define initial T_i and final temperatures T_f of the dehydration reaction. The samples were heated up from room temperature to 950°C in a platinum-rhodium crucible with a volume of $V = 85 \text{ mm}^3$ with a pierced lid. A constant gas flow of 40 ml min^{-1} of nitrogen was applied during the measurement runs which was controlled by the internal MFC.

Two different experiments were performed to understand the influence of the initial mass m_i and heating rate β on the resulting temperatures T_i and T_f of the dehydration reaction. Although focusing on dehydration, also the second reaction from calcium oxalate to calcium carbonate $\text{CaC}_2\text{O}_4 \longrightarrow \text{CaCO}_3 + \text{CO}$ and to calcium oxide $\text{CaCO}_3 \longrightarrow \text{CaO} + \text{CO}_2$ are considered in the STA measurement runs.

In the first experiment (s. figure 5.19), two different initial sample masses m_i using the same heating rate $\beta = 20 \text{ K min}^{-1}$ are measured while in the second experiment (s. figure 5.20) three different heating rates with $\beta = 20 \text{ K min}^{-1}$, 10 K min^{-1} and 5 K min^{-1} are applied. For the second experiment, no zero line measurement and correction has been performed, leading to a slight mass gain up to 100°C .

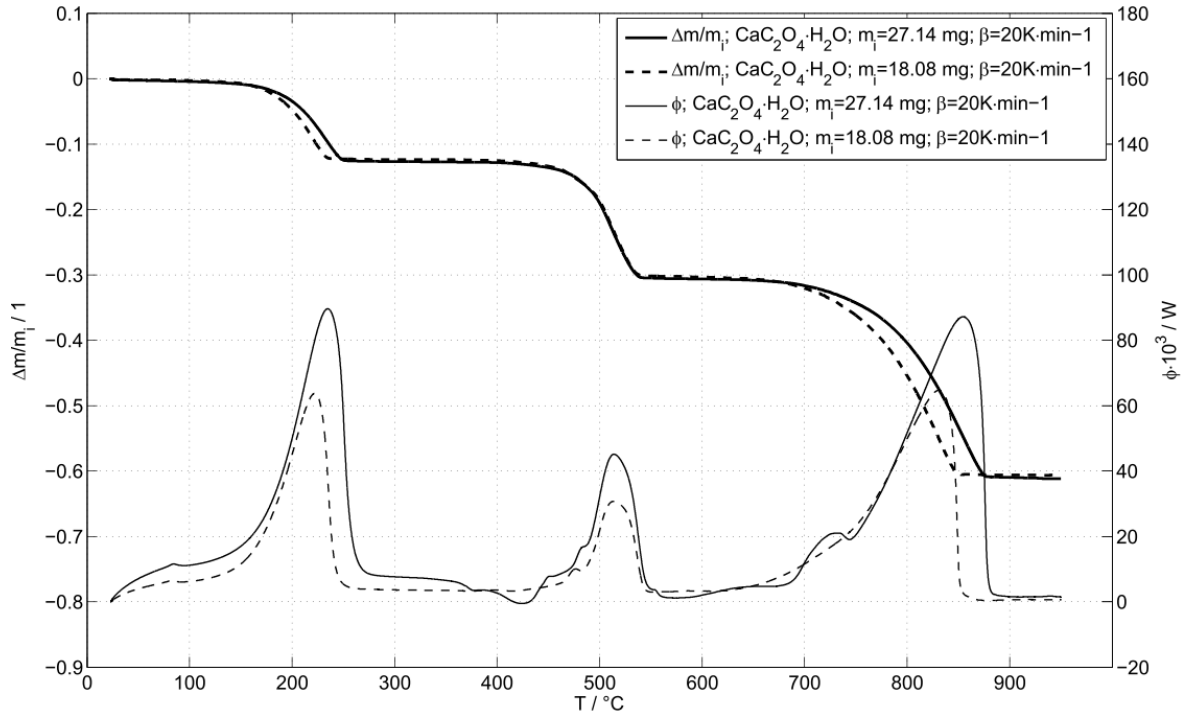


FIGURE 5.19: STA result at $\beta = 20 \text{ K min}^{-1}$ for $\text{CaC}_2\text{O}_4 \cdot \text{H}_2\text{O}$ using two different sample masses

As it can be seen from figure 5.19, the mass loss $\Delta m/m_i$ for the two different samples in the dehydration reaction is comparable with 12.19 % and 12.06 % of the initial mass m_i . The dehydration reaction starts at the same temperature $T_i = 100 \text{ }^\circ\text{C}$, but the final temperature T_f is depending on the initial sample mass m_i at the same heating rate $\beta = 20 \text{ K min}^{-1}$. The first sample had a higher initial mass and figure 5.19 is indicating a higher final temperature T_f of the dehydration reaction compared to the second sample.

The heat flow $\phi(t)$ from the DSC measurements show almost similar temperature behaviors as the mass signal from the thermobalance. The dehydration effect starts with $T_i = 100 \text{ }^\circ\text{C}$ and is practically identical with the measured T_i from the TGA signal. The final temperature T_f is again higher for the first sample with the higher initial mass compared to the second sample.

On closer examination of both measurements, there is a considerable delay of the final dehydration temperature T_f between ϕ and $\Delta m/m_i$. Although the dehydration reaction shows no mass loss anymore, the DSC peak has not ended at this temperature point. As described by Höhne et al [30], these phenomenons are based on thermal lags caused by the DSC apparatus and the sample itself. The differences of the heat flow peak maxima of the dehydration reaction are also connected to the mass difference of the initial mass between the two measured samples m_i .

Furthermore, both heat flow curves indicate a small endothermic effect at $T_{pk} = 80 \text{ }^\circ\text{C}$. In line with an earlier work by [93], a phase transition between two different phases of the precursor $\text{CaC}_2\text{O}_4 \cdot \text{H}_2\text{O}$ was found in the Raman spectrum which were not detected in the applied TGA-Differential Thermal Analysis (DTA) system. The higher sensitivity of the used

TGA-DSC sensor leads to better heat flow detection capabilities compared to the applied TGA-DTA system by [93]. This setup difference might be the reason for the identification of the phase transition using the DSC sensor.

In the study [95], a reaction enthalpy of $\Delta h_r = 455.1 \text{ J g}^{-1}$ is reported for the dehydration reaction between 132 and 220 °C. Integration of the measured heat flow $\phi(t)$, subtracting a linear baseline between 100 and 300 °C, results in $\Delta h_r = 439 \text{ J g}^{-1}$ and $\Delta h_r = 433 \text{ J g}^{-1}$, respectively, for the two observed dehydration reactions.

Figure 5.20 shows the decomposition of $\text{CaC}_2\text{O}_4 \cdot \text{H}_2\text{O}$ with different applied heating rates. The TGA signal for $\beta = 5 \text{ K min}^{-1}$ shows a lower final temperature of the dehydration step with $T_f = 201 \text{ °C}$ in comparison to $\beta = 10 \text{ K min}^{-1}$ with $T_f = 218 \text{ °C}$ and $\beta = 20 \text{ K min}^{-1}$ with $T_f = 233 \text{ °C}$. The DSC signal shows a similar behavior relating T_i and T_f of the reactions. Focusing on the dehydration reaction, T_i is not changing and T_f is getting higher with faster heating rates.

The influence of the heating rate β and the thermal transport properties of the sample setup on the evaluated characteristic temperatures of the DSC signal are similar to the already described observations on PCM measurements in section 4.2. The different DSC peak signal heights can also be traced back to the smaller temperature difference at low heating rates between sample and reference side of the DSC sensor, as described in section 3.6.

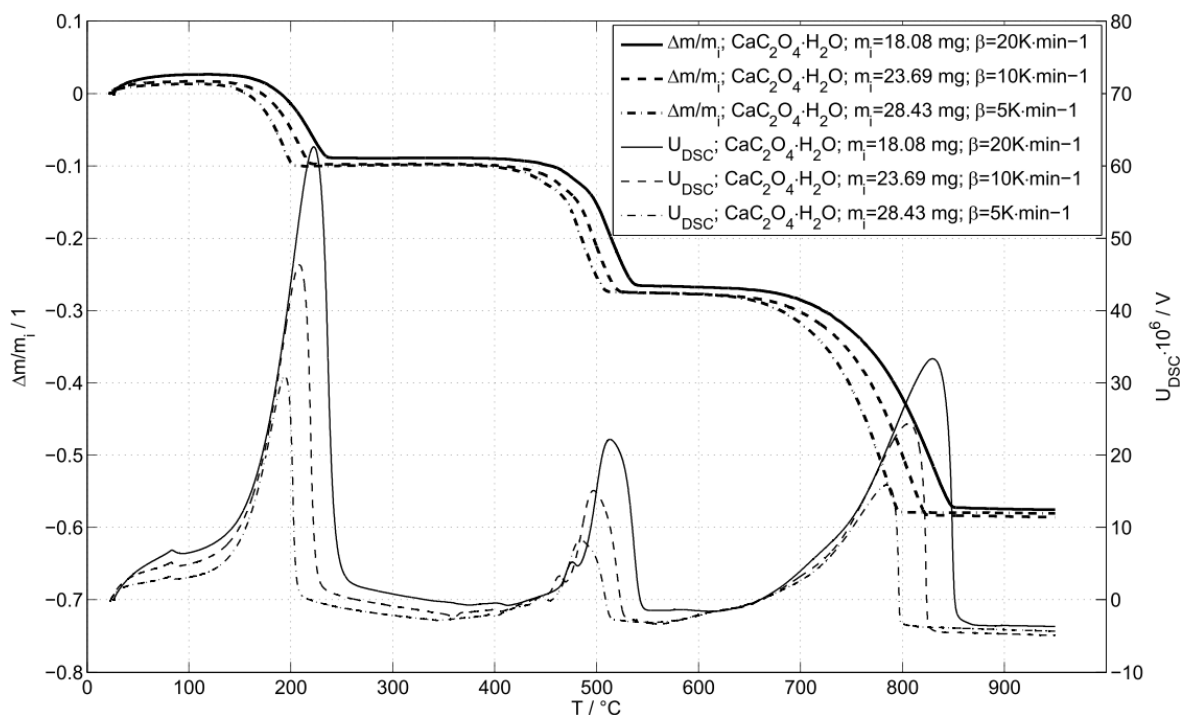


FIGURE 5.20: STA result of $\text{CaC}_2\text{O}_4 \cdot \text{H}_2\text{O}$ using three different heating rates $\beta = 20 \text{ K min}^{-1}$, 10 K min^{-1} and 5 K min^{-1}

Apparent specific heat capacity

The apparent specific heat capacity $c_p^{app}(T)$ for $\text{CaC}_2\text{O}_4 \cdot \text{H}_2\text{O}$ and CaC_2O_4 was measured according to the protocol described in section 5.3.2 except the chronology. For the evaluation of $c_p^{app}(T)$ of the hydrated $\text{CaC}_2\text{O}_4 \cdot \text{H}_2\text{O}$ and the anhydrous CaC_2O_4 material, the identical sample was measured twice by using two consecutive heating and cooling cycles. In the first cycle the hydrated form and in the second cycle the anhydrous form was analyzed to avoid re-hydration of the sample under ambient conditions. For the calculation of $c_p^{app}(T)$ of CaC_2O_4 the mass was corrected according to the results from section 5.4.1.

The STA results in figure 5.19 and 5.20 indicating the initial temperature $T_i = 100^\circ\text{C}$ for dehydration and $T_i = 350^\circ\text{C}$ for the reaction from calcium oxalate to calcium carbonate which defines the maximum temperatures for the evaluation of $c_p^{app}(T)$.

The result for $c_p^{app}(T)$ for $\text{CaC}_2\text{O}_4 \cdot \text{H}_2\text{O}$ shows again the endothermic phase-transition at $T_{pk} = 80^\circ\text{C}$ as already discussed in section 5.4.1. Due to the fact, that a phase transition is not part of the specific heat capacity of a material, a second degree polynomial between $T = 10$ and 90°C was used to interpolate a possible peak baseline. Additional found literature data from Latimer et al. [96] for $\text{CaC}_2\text{O}_4 \cdot \text{H}_2\text{O}$ is also displayed in figure 5.21. This data was measured between $T = -254.15$ and 26.85°C and is assumed with a combined uncertainty $u_c = 5\%$. The evaluated and literature $c_p(T)$ data from [96] show a good agreement in the overlapping temperature range between $T = -30$ and 0°C .

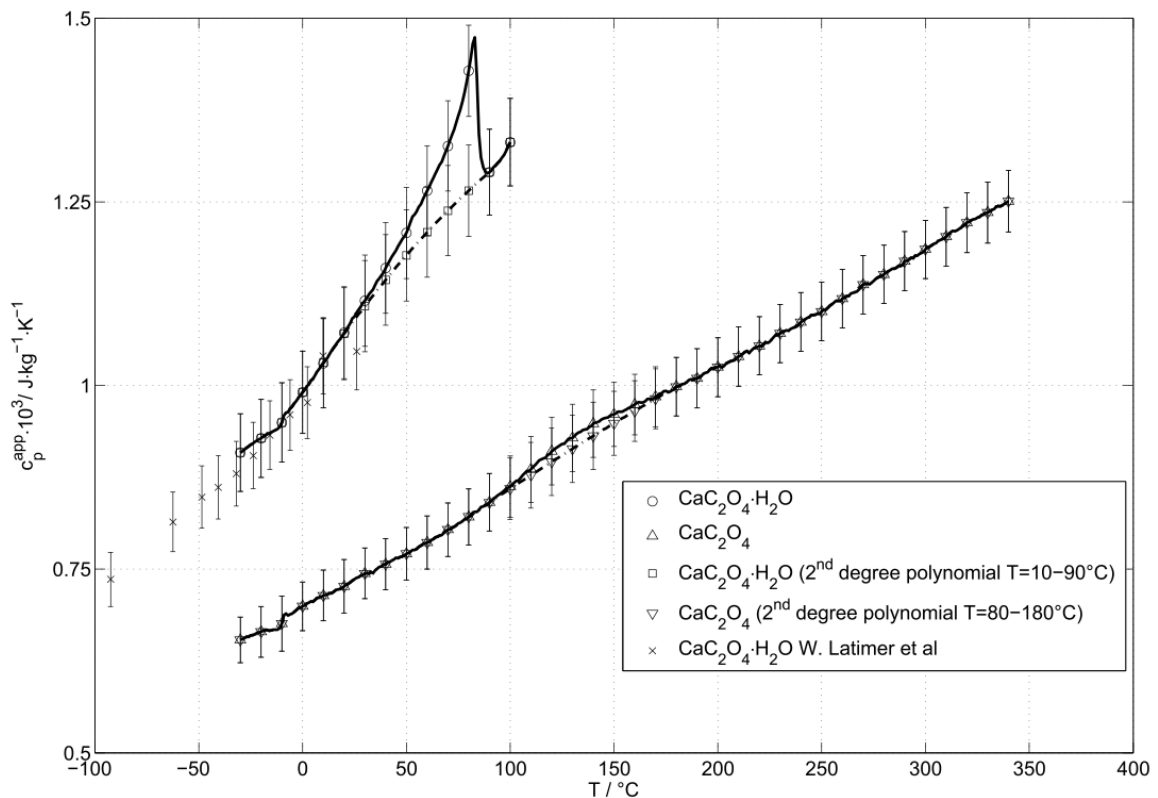


FIGURE 5.21: $c_p^{app}(T)$ of $\text{CaC}_2\text{O}_4 \cdot \text{H}_2\text{O}$ and CaC_2O_4

The results of $c_p^{app}(T)$ of CaC_2O_4 also show some endothermic effect in the temperature range $T = 80$ to 180 °C. This small effect may be associated with a dehydration starting again at $T_i = 100$ °C and was also smoothed with second degree polynomial as shown in figure 5.21.

Effective thermal diffusivity and conductivity

To evaluate the thermal diffusivity $a(T)$, the LFA method according to subsection 5.3.3 was applied. Three pressed and graphite coated cylindrical shaped samples were prepared and measured in the temperature range from $T = -50$ to 350 °C. The prepared samples had a mean bulk density of $\rho_B = 1638$ kg m^{-3} at ambient conditions.

THB measurements according to section 5.3.4 were performed, starting from $\text{CaC}_2\text{O}_4 \cdot \text{H}_2\text{O}$ as precursor with an initial bulk density of $\rho_B = 386$ kg m^{-3} at ambient conditions. The material was measured from $T = 25$ to 100 °C and dehydrated at $T = 200$ °C. The resulting product CaC_2O_4 was measured during the cooling process between $T = 200$ and 25 °C and a bulk density of $\rho_B = 337$ kg m^{-3} was determined.

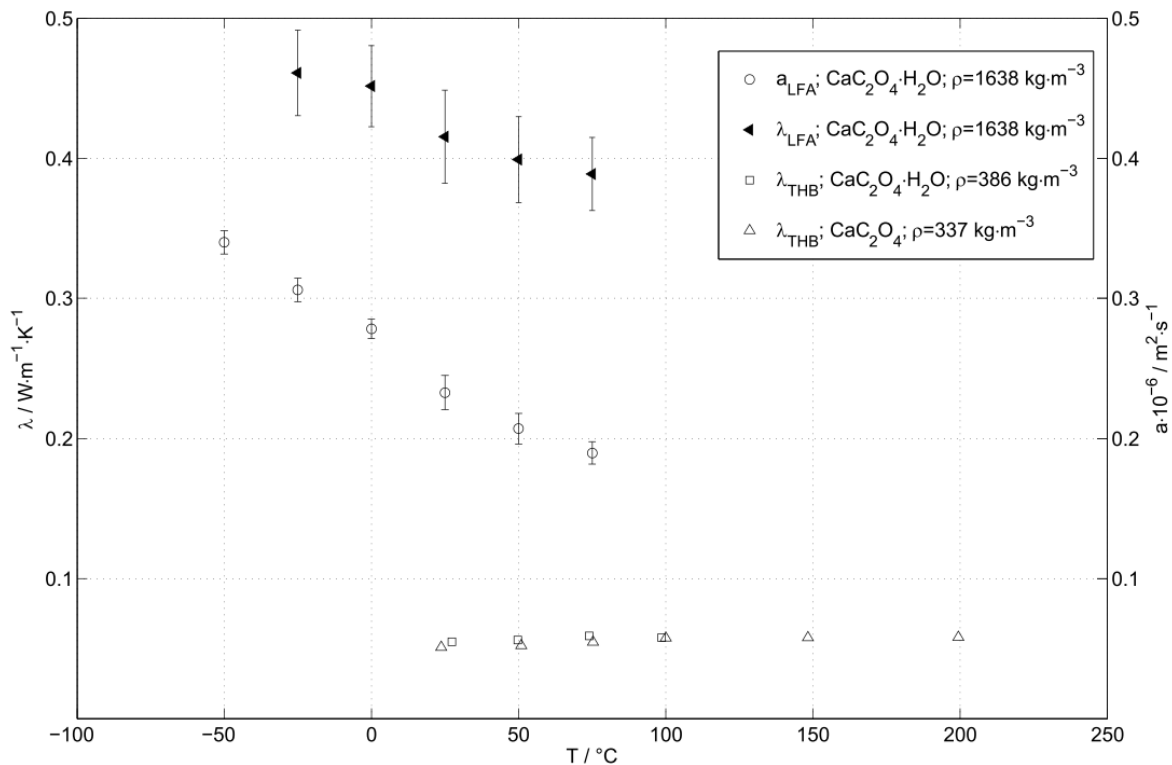


FIGURE 5.22: λ_{eff} and a_{eff} of $\text{CaC}_2\text{O}_4 \cdot \text{H}_2\text{O}$ and CaC_2O_4

As represented in figure 5.22, $a_{eff}(T)$ for $\text{CaC}_2\text{O}_4 \cdot \text{H}_2\text{O}$ decreases from 0.340 to 0.190 $\text{mm}^2 \text{s}^{-1}$ in the temperature range from $T_i = -50$ to 75 °C. Although the LFA experiments were performed up to $T = 350$ °C, no repeatable results could be achieved at $T \geq 100$ °C. According the results from 5.4.1 it can be concluded, that $\text{CaC}_2\text{O}_4 \cdot \text{H}_2\text{O}$ starts to dehydrate at $T \approx 100$ °C and ends at a final temperature $T_f \approx 201$ °C for $\beta = 5$ K min^{-1} . At $T \geq 100$ °C, the LFA samples showed a cracked surface and the samples were destroyed upon removing from

the sample holder system. Due to that, evaluation of $a_{eff}(T)$ and $\lambda_{eff}(T)$ for the compacted CaC_2O_4 was not possible.

Due to the measured $a_{eff}(T)$ result it was assumed to calculate $\lambda_{eff}(T)$ for $\text{CaC}_2\text{O}_4 \cdot \text{H}_2\text{O}$ between $T = -25$ and 75°C according to equation 4.6. The $c_p(T)$ data is based on the measured and calculated polynomial data from 5.21 and ρ_B is the bulk density at ambient conditions. At $T = 25^\circ\text{C}$ the calculation of $\lambda_{eff}(T)$ of the compacted sample yields $0.415 \text{ W m}^{-1} \text{ K}^{-1}$ with a combined uncertainty of $u_c = 0.033 \text{ W m}^{-1} \text{ K}^{-1}$.

Direct THB measurements in the packed bed for $\text{CaC}_2\text{O}_4 \cdot \text{H}_2\text{O}$ with a bulk density of $\rho_B = 386 \text{ kg m}^{-3}$ yielded $\lambda_{eff} = 0.055$ to $0.058 \text{ W m}^{-1} \text{ K}^{-1}$ in a temperature range $T = 25$ to 100°C . CaC_2O_4 with a bulk density of $\rho_B = 337$ yield a $\lambda_{eff} = 0.051$ to $0.058 \text{ W m}^{-1} \text{ K}^{-1}$ in a temperature range from $T = 25$ to 200°C .

5.4.2 Boric acid H_3BO_3

According to [97] boric acid is used in many industries with the largest use in the glass and ceramic industry. It converts to a metaboric acid HBO_2 below 150°C and builds boron oxide above 150°C by losing all of its water.



In the following measurements boron trioxide from *Sigma-Aldrich* with the name *Boric anhydride puriss. p.a., 98% (T)* and boric acid from *Carl Roth* with the name *Boric acid 99.8 %, p.a., ACS, ISO* was used.

Thermal decomposition

Several dehydration experiments by using different heating rates and sample masses for H_3BO_3 and B_2O_3 have been performed. In the STA measurements, aluminum crucibles with a pierced lid, as already shown in figure 5.10, are used. Furthermore, a pure TGA experiment using an Al_2O_3 cup for a bigger volume or mass was used to analyze the mass change behavior on the dehydration step. The samples were heated up from room temperature to 590°C with a nitrogen gas flow of $\dot{V} = 40 \text{ ml min}^{-1}$.

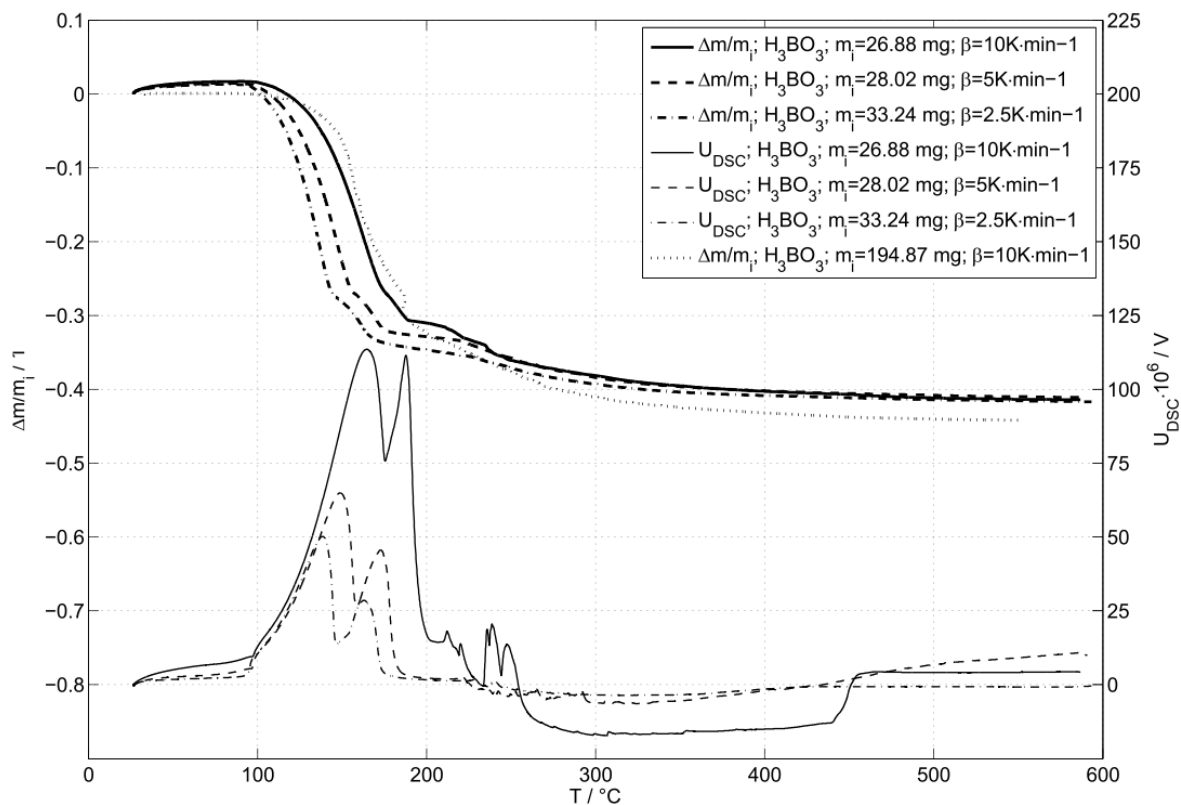


FIGURE 5.23: STA result for H_3BO_3 using three different heating rates $\beta = 10 \text{ K min}^{-1}$, 5 K min^{-1} and 2.5 K min^{-1}

The conducted experiments show the dependency of T_{pk} on β , but also the dependency of $\Delta m/m_i$ of the sample on the overall curve shape at the same heating rate.

In [97], a two step dehydration reaction in their TGA-DTA experiment with DTA peaks at $T_{pk} = 159^\circ\text{C}$ and 181°C , respectively, at a heating rate $\beta = 3\text{ K min}^{-1}$ is reported. Comparing this DTA peak temperatures from [97] with the own measured DSC data, measured with $\beta = 2.5\text{ K min}^{-1}$, this two peaks can be found at $T_{pk} = 140^\circ\text{C}$ and $T_{pk} = 163^\circ\text{C}$.

A detailed look on the two TGA curves with the same heating rate $\beta = 10\text{ K min}^{-1}$ but different initial weights $m_i = 194.87\text{ mg}$ and 26.88 mg show different dehydration behaviors. These effects are linked to unequal sample geometries and due to differing heat and mass transport time scales. Additional, there seems to be a cooling effect at $T = 187^\circ\text{C}$ for $m_i = 194.87\text{ mg}$ which may be associated with the higher amount of consumed heat for the dehydration compared to the sample with $m_i = 26.88\text{ mg}$.

The initial temperature of the first dehydration starts at $T_i = 90^\circ\text{C}$, which is comparable for all TGA and DSC curves for that substance. The starting temperature of the subsequent step is overlapped by the first one. Indeed, there is a continuous mass loss until the end of the measurement which [97] describes as subsequent boiling of B_2O_3 .

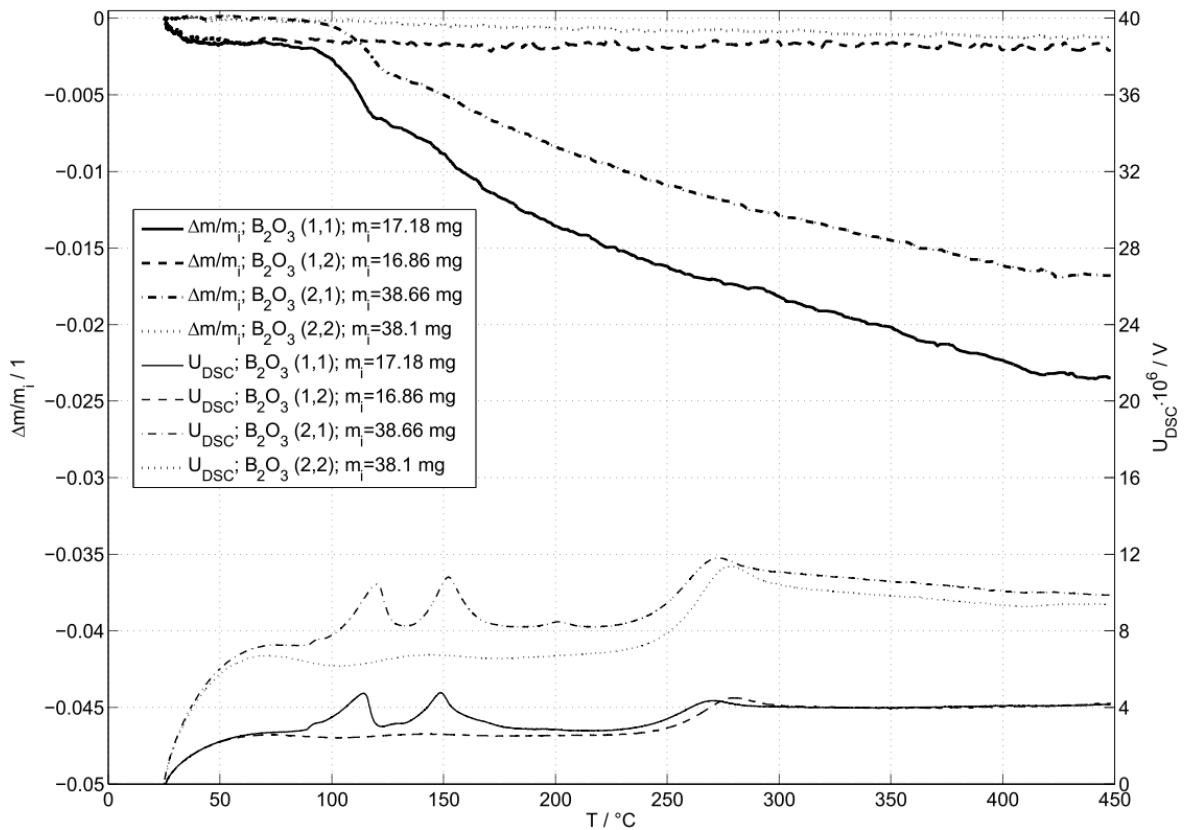


FIGURE 5.24: STA result for B_2O_3 using two subsequent heating cycles

Additional measurements on B_2O_3 in the STA are shown in figure 5.24. Two subsequent heating cycles on the same sample with $\beta = 10 \text{ K min}^{-1}$ from room temperature up to $450 \text{ }^\circ\text{C}$ indicate similar STA signals as already seen for H_3BO_3 in figure 5.23. This may be attributed to the hygroscopic nature of B_2O_3 by forming H_3BO_3 with the available ambient humidity. In the second heating cycle there is no mass change visible at all but again a DSC signal step starting at $T_i = 220 \text{ }^\circ\text{C}$. This effect may be connected to a phase transition of B_2O_3 .

Apparent specific heat capacity

The apparent specific heat capacity $c_p^{app}(T)$ of H_3BO_3 was evaluated up to $T = 80 \text{ }^\circ\text{C}$ due to the preliminary test results from the STA measurements which show the dehydration starting slightly above this temperature (s. figure 5.23).

For B_2O_3 the defined maximum temperature was $T_{max} = 200 \text{ }^\circ\text{C}$, defined through the measured heat consuming effects starting at $220 \text{ }^\circ\text{C}$ shown in figure 5.24. The STA results of B_2O_3 indicated, that there is some H_3BO_3 content in the first heating cycle of the experiment. This result lead to two consecutive DSC measurement runs to eliminate the H_3BO_3 content. To evaluate $c_p^{app}(T)$ of B_2O_3 only the second heating cycle was considered.

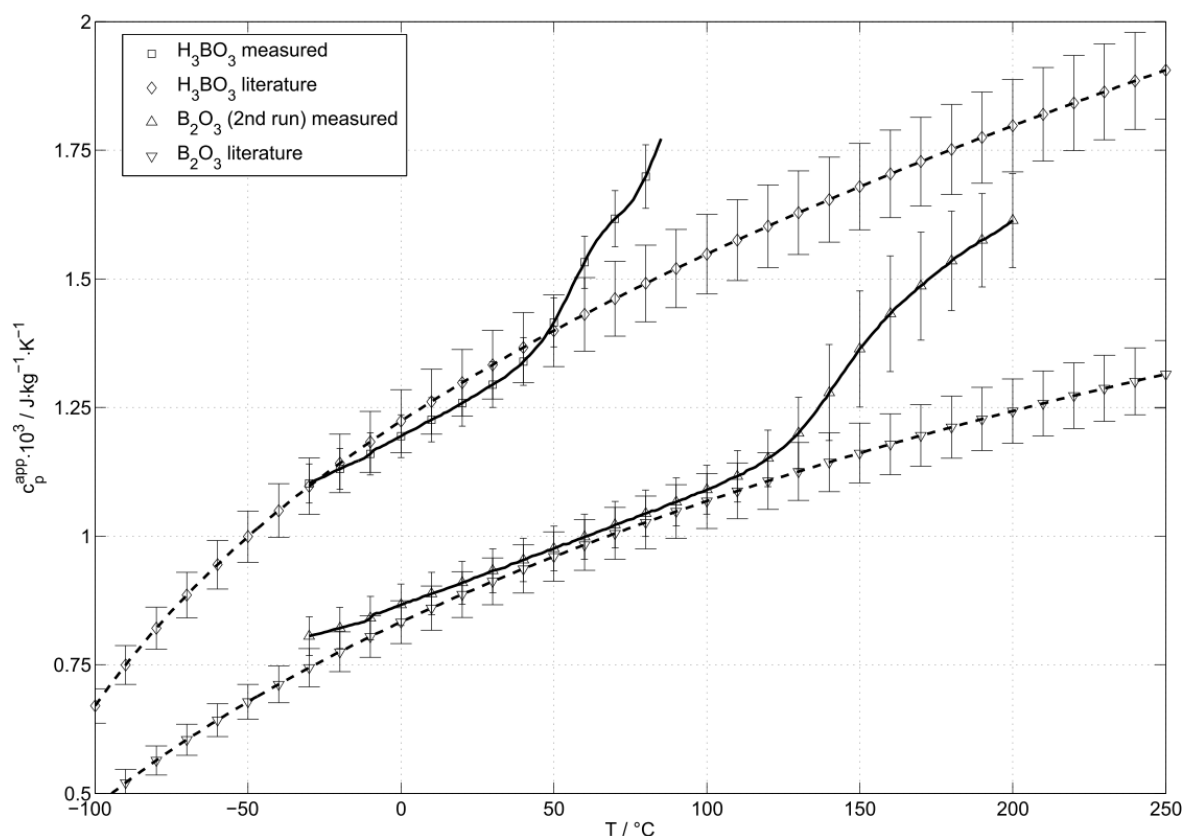


FIGURE 5.25: $c_p^{app}(T)$ of H_3BO_3 and B_2O_3

The graphs in figure 5.25 show the measured $c_p^{app}(T)$ and literature data from [98] of H_3BO_3 and B_2O_3 . For H_3BO_3 , Chase et al. is taking the data of [99] below $T = 25 \text{ }^\circ\text{C}$ and is estimating

$c_p(T)$ for temperatures above $T = 25\text{ }^\circ\text{C}$ with the values of the constituent oxides. In this case, no uncertainty values are available and are assumed with $u_c = 5\%$ of the $c_p(T)$ value.

The $c_p(T)$ literature data for B_2O_3 is also based on [98], who combined two different sets of $c_p(T)$ data below and above $T = 25\text{ }^\circ\text{C}$ and combined them by a polynomial approach. Furthermore, [98] describes the highest deviation of the observed enthalpy data with $u_c = 5\%$ at $T = 86.85\text{ }^\circ\text{C}$. This value was used for the uncertainty over the whole displayed temperature range as shown in figure 5.25.

The measured $c_p^{app}(T)$ and the corresponding literature data are consistent for H_3BO_3 up to $T = 50\text{ }^\circ\text{C}$ and for B_2O_3 up to $T = 100\text{ }^\circ\text{C}$. The sudden increase of the measured $c_p^{app}(T)$ may be attributed to dehydration and phase transition effects which are not part of the specific heat capacity as described in section 3.6.3.

Effective thermal diffusivity and conductivity

Thermal diffusivity measurements based on the LFA method as described in section 5.3.3 were applied. Three pressed and graphite coated cylindrical shaped samples were prepared and measured in the temperature range from $T = -50$ to $75\text{ }^\circ\text{C}$. The prepared samples had a mean bulk density of $\rho_B = 1436\text{ kg m}^{-3}$ at ambient conditions.

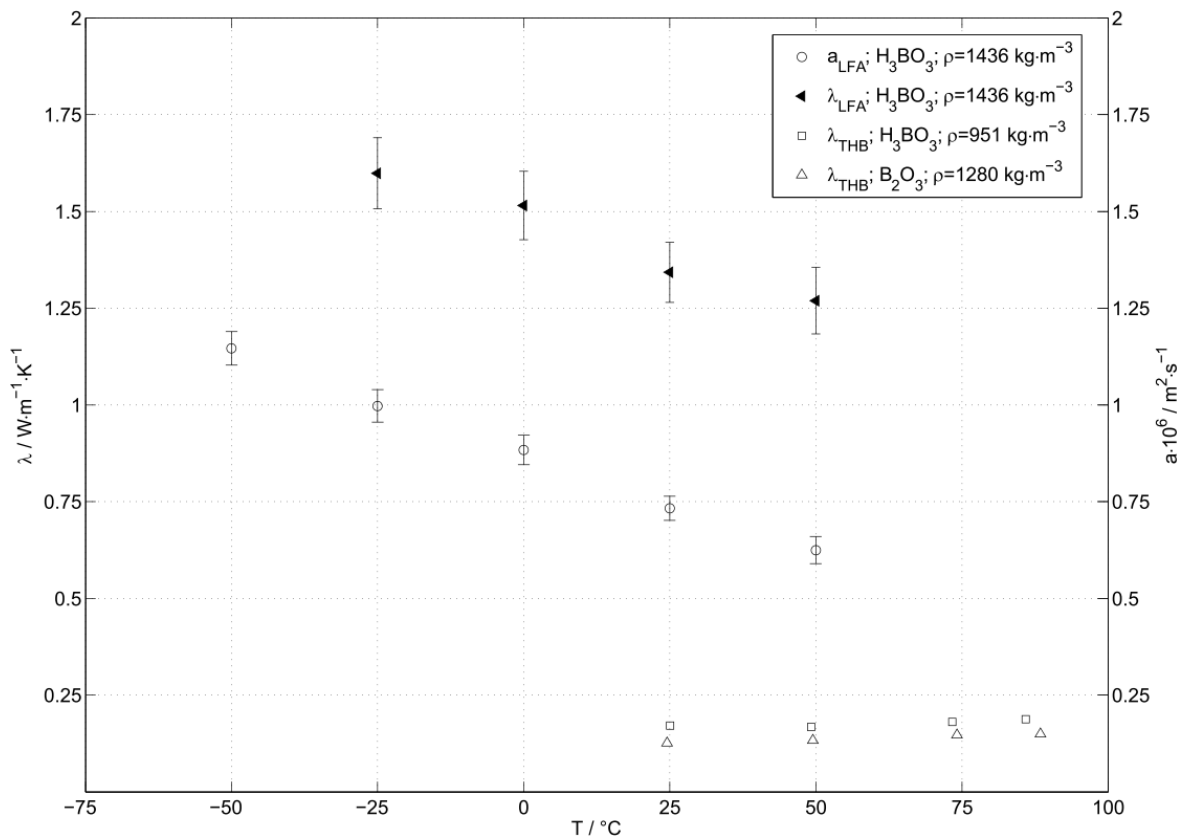


FIGURE 5.26: λ_{eff} and a_{eff} of H_3BO_3 and B_2O_3

The THB measurements according to section 5.3.4 were performed using two samples for H_3BO_3 and B_2O_3 . The measured initial bulk densities were $\rho_B = 951 \text{ kg m}^{-3}$ for H_3BO_3 and $\rho_B = 1280 \text{ kg m}^{-3}$ for B_2O_3 at ambient conditions. Both substances were measured from $T = 25$ to $90 \text{ }^\circ\text{C}$.

Figure 5.26 shows the measured thermal diffusivity results for H_3BO_3 , which decreases from $a_{eff}(T) = 1.146$ to $0.624 \text{ mm}^2 \text{ s}^{-1}$ in the temperature range from $T = -50$ to $50 \text{ }^\circ\text{C}$. According the STA results from figure 5.23 it can be concluded, that H_3BO_3 should show no dehydration in this temperature interval. λ_{eff} for H_3BO_3 was calculated between $T = -25$ and $50 \text{ }^\circ\text{C}$ based on the measured $a_{eff}(T)$, $c_p^{app}(T)$ and the bulk density ρ_B at ambient conditions.

Direct THB measurements in the packed bed for H_3BO_3 with a bulk density of $\rho_B = 951 \text{ kg m}^{-3}$ yielded $\lambda_{eff} = 0.168$ to $0.187 \text{ W m}^{-1} \text{ K}^{-1}$ in a temperature range from $T = 25$ to $90 \text{ }^\circ\text{C}$. The B_2O_3 with a bulk density of $\rho_B = 1280 \text{ kg m}^{-3}$ yielded $\lambda_{eff} = 0.126$ to $0.149 \text{ W m}^{-1} \text{ K}^{-1}$ in the same temperature range from $T = 25$ to $90 \text{ }^\circ\text{C}$.

5.4.3 Calcium hydroxide $\text{Ca}(\text{OH})_2$

Based on [100, 101, 17, 102] there is already a lot of research activities done, investigating calcium hydroxide as potential TCM. The following reversible reaction is studied in detail in the above mentioned articles.



Schaube et al [17] did extensive thermal analysis on the hydration and dehydration reaction. Measured quantities are reaction enthalpies, heat capacities, influence of the heating rate on dehydration temperatures, equilibrium temperatures and cycling stability.

In the following measurements, calcium oxide from *Sigma-Aldrich* with the name *Calcium Oxide 96-100, 5%puriss* and calcium hydroxide from *Merck* with the name *Calciumhydroxid for analysis EMSURE ACS, Reag. Ph Eur* was analyzed.

Thermal decomposition

Figure 5.27 represents the measured STA signals for $\text{Ca}(\text{OH})_2$ with the heating rates $\beta = 10 \text{ K min}^{-1}$, 5 K min^{-1} and 2 K min^{-1} and CaO with $\beta = 5 \text{ K min}^{-1}$ in a temperature range $T = 50$ to $550 \text{ }^\circ\text{C}$.

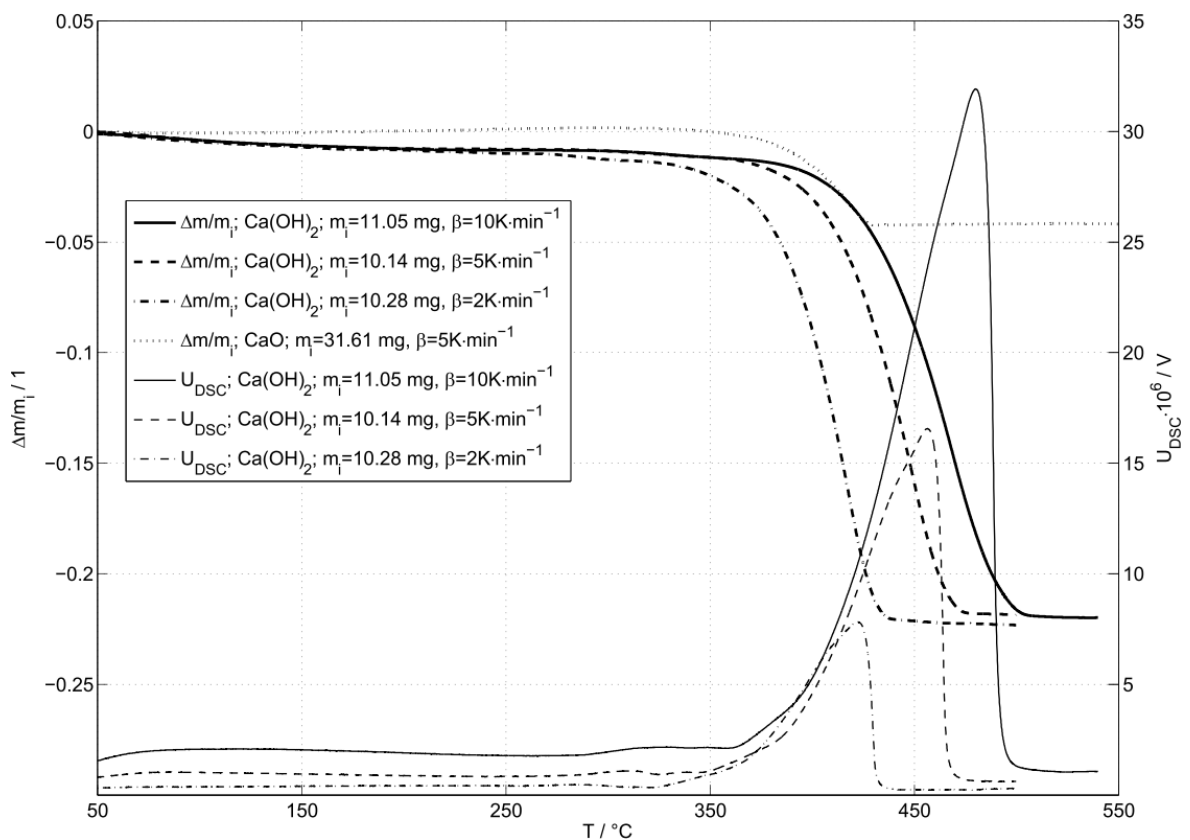


FIGURE 5.27: STA results for $\text{Ca}(\text{OH})_2$ and CaO using three different heating rates $\beta = 10 \text{ K min}^{-1}$, 5 K min^{-1} and 2.5 K min^{-1}

The $\text{Ca}(\text{OH})_2$ TGA result shows a mass loss of $\Delta m/m_i = -0.22$ in the measured temperature range. The repeatable mass loss of $\Delta m/m_i = -0.01$ between $T = 50$ and 250°C may be interpreted as desorption of water. The applied heating rate β has a strong effect on the evaluation of the measured dehydration temperatures. Schaube et al [17] described the dehydration temperature as the temperature, where a mass loss or gain of $\Delta m/m_i = 0.01$ could be detected and describes temperatures between $T = 293.7$ and 350.6°C for $\beta = 0.03$ to 10 K min^{-1} according to this procedure. Due to that, the same procedure was applied on the measured $\text{Ca}(\text{OH})_2$ STA data. The mass loss of -1% between $T = 50$ and 250°C before the dehydration reaction is added to the $\Delta m/m_i = 0.01$ definition by [17], leading to the evaluation of the dehydration temperature at $\Delta m/m_i = -0.02$. The evaluated dehydration temperatures are shown in table 5.5.

	$\beta = 2\text{ K min}^{-1}$	$\beta = 5\text{ K min}^{-1}$	$\beta = 10\text{ K min}^{-1}$
$T_{(\Delta m/m_i = -0.02)} / ^\circ\text{C}$	350	385	400
$\Delta h_r / \text{J g}^{-1}$	1240	1258	1261

TABLE 5.5: Measured $\text{Ca}(\text{OH})_2$ dehydration temperatures T and dehydration reaction enthalpies Δh_r for $\beta = 10\text{ K min}^{-1}$, 5 K min^{-1} and 2 K min^{-1}

The measured dehydration temperatures are significantly higher than the reported values from [17]. Sample specific attributes like the purity of the measured substances, particle size and bulk density but also setup specific properties like crucible and sample geometry (s. section 5.3.1) may influence the measured data.

Dehydration reaction enthalpies were evaluated from a starting temperature of $T = 250^\circ\text{C}$ for all heating rates. The upper temperature integration limit depends on the actual final temperature T_f of the dehydration reaction. In case of $\beta = 2\text{ K min}^{-1}$, the final temperature is defined with $T_f = 450^\circ\text{C}$, for $\beta = 5\text{ K min}^{-1}$ with $T_f = 480^\circ\text{C}$ and for $\beta = 10\text{ K min}^{-1}$ with $T_f = 510^\circ\text{C}$. A comparison of the specific reaction enthalpies Δh_r are shown in table 5.5. The measured specific reaction enthalpies Δh_r are slightly lower as reported in [103] which may be attributed to the added sensible heat or starting from $T = 25^\circ\text{C}$.

A separate run on a CaO sample as delivered has shown, that there is also a mass loss of $\Delta m/m_i \approx -0.04$ between $T = 50$ and 550°C . The qualitative signal shape of the TGA signal is comparable to the $\text{Ca}(\text{OH})_2$ measurement. Both materials share the same $\Delta m(T)/m_i$ characteristics which may be connected to a $\text{Ca}(\text{OH})_2$ content in the apparent CaO sample.

Apparent specific heat capacity

To analyze $c_p^{app}(T)$ of $\text{Ca}(\text{OH})_2$ and CaO , two consecutive heating cycles starting with $\text{Ca}(\text{OH})_2$ up to $T_{max} = 550^\circ\text{C}$ were performed. Preliminary CaO STA results have shown, that the delivered assumed CaO material also contained $\text{Ca}(\text{OH})_2$ as shown in figure 5.27. On this basis, it was decided to dehydrate the pure $\text{Ca}(\text{OH})_2$ to CaO in the first heating cycle and in the second heating cycle, the $c_p^{app}(T)$ from the DSC signal of the pure CaO was evaluated. After dehydration in the first heating cycle, the produced CaO sample has

a different initial mass m_i compared to the $\text{Ca}(\text{OH})_2$ precursor sample. For the $c_p^{app}(T)$ evaluation, m_i of CaO is determined through the preliminary TGA measurement. According to the measurement shown in figure 5.27, the new m_i of CaO is calculated by reducing the m_i of $\text{Ca}(\text{OH})_2$ by 22 %.

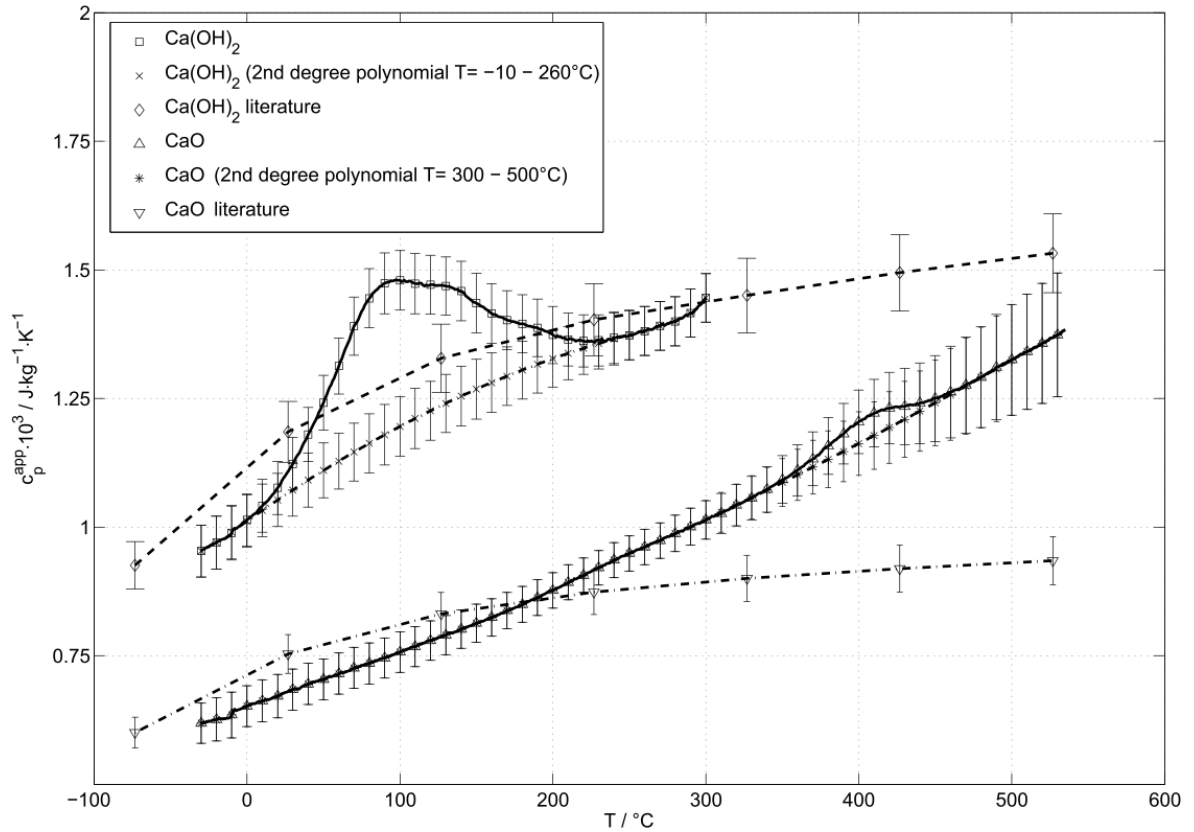


FIGURE 5.28: $c_p^{app}(T)$ of $\text{Ca}(\text{OH})_2$ and CaO

In figure 5.28 the measured and evaluated $c_p^{app}(T)$ data and literature data from the National Institute of Standards and Technology - Joint Army-Navy-NASA-Air Force (NIST-JANAF) thermochemical tables [98] are depicted. Due to the fact, that the data tables in [98] for $\text{Ca}(\text{OH})_2$ and CaO have no explicit uncertainty for the heat capacity description, an assumption has been made with $u_c = 5\%$.

Focusing on $\text{Ca}(\text{OH})_2$, the measured apparent $c_p^{app}(T)$ shows a heat consuming behavior between -10 to 260°C which is connected to a mass loss of $\Delta m/m_i = -0.01$ up to $T = 250^\circ\text{C}$ as shown in the TGA results in figure 5.27. This may be attributed to adsorbed water on the surface of the powder sample evaporating during the experiment. To eliminate this endothermic effect, a 2nd degree polynomial was used between -10 and 260°C . The evaluated $\text{Ca}(\text{OH})_2$ with the polynomial model and the NIST-JANAF data [98] share a similar slope characteristics although data from NIST-JANAF has slightly higher values over the whole temperature range. Considering the overlapping measurement uncertainties, a good comparability is given.

The specific heat capacity CaO differs considerably from the NIST-JANAF data. Considering the uncertainties, there is an overlap between -30 and 250 °C but a completely different slope of the measured curve versus the NIST-JANAF data. Although the sample was not removed from the DSC cell between the Ca(OH)_2 and CaO measurement, it appears to be again a dehydration starting at 350 °C. This may be attributed to a rehydration of the sample in the cooling segment before the second consecutive heating started. The attached polynomial model between 300 and 500 °C is smoothing the dehydration effect but is not changing the curve characteristics.

Effective thermal diffusivity and conductivity

Three pressed and graphite coated cylindrical shaped Ca(OH)_2 samples were prepared and measured based on the LFA method (s. subsection 5.3.3) in the temperature range from 25 °C to 300 °C. The prepared samples had a mean bulk density of $\rho_B = 1972 \text{ kg m}^{-3}$ at ambient conditions. Due to the dehydration behavior of the assumed CaO precursor material (s. figure 5.27) it was not considered for additional LFA measurements.

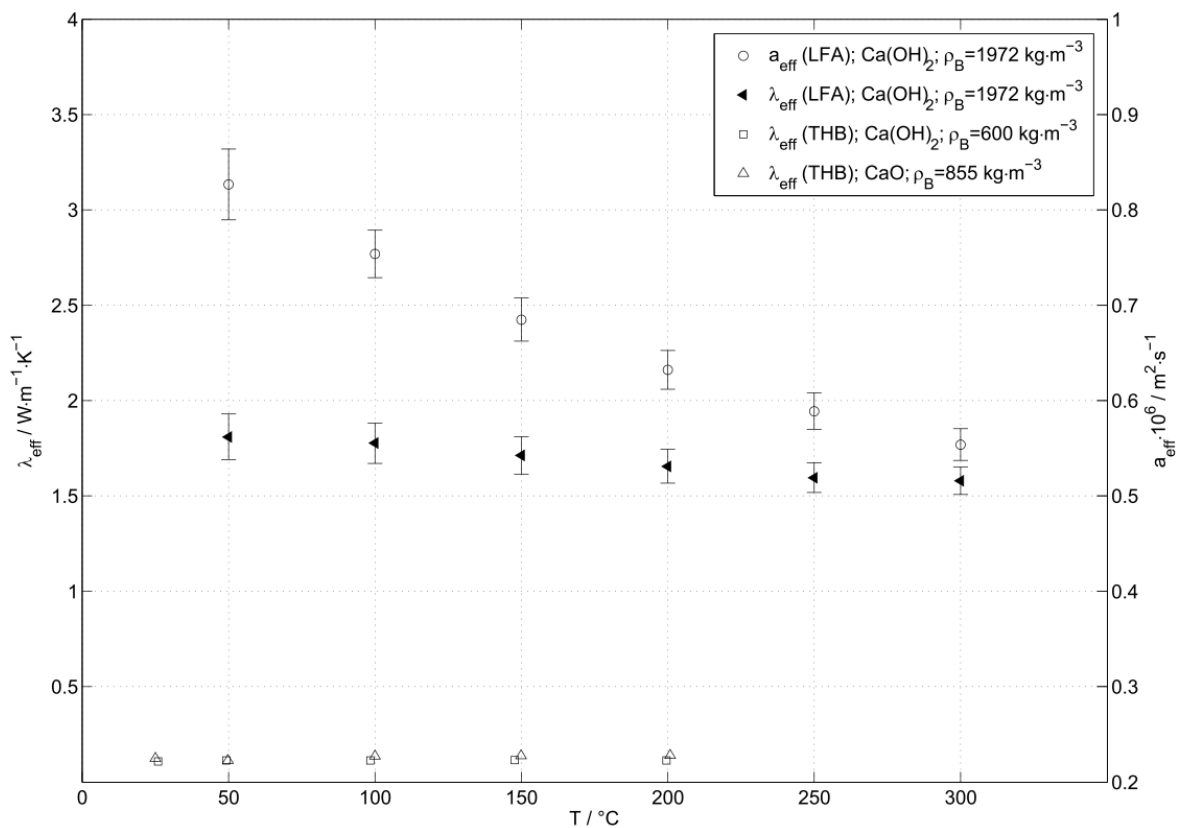


FIGURE 5.29: λ_{eff} and a_{eff} of Ca(OH)_2 and CaO

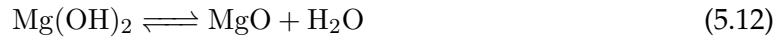
Figure 5.29 depicts the measured $a_{eff}(T)$ results for Ca(OH)_2 which decrease from $a_{eff}(T) = 0.895$ to $0.554 \text{ mm}^2 \text{ s}^{-1}$ in the temperature range $T = 50$ to 300 °C. According to the STA results from figure 5.27 it can be concluded, that the used Ca(OH)_2 precursor should show no dehydration up to this temperature. In this observation, the mass loss of $\Delta m/m_i = -0.01$ between $T = 50$ and 250 °C is neglected.

$\lambda_{eff}(T)$ for the compacted $\text{Ca}(\text{OH})_2$ samples was calculated between 25 and 300 °C based on the measured $a_{eff}(T)$ and the bulk density ρ_B at ambient conditions. The underlying $c_p^{app}(T)$ data was taken from the measurement with the eliminated endothermic effect between -10 and 260 °C as shown in figure 5.28. The evaluated $\lambda_{eff}(T)$ decreases between $T = 50$ and 300 °C with $\lambda_{eff}(T) = 1.810$ to $1.579 \text{ W m}^{-1} \text{ K}^{-1}$.

Direct THB measurements in the packed bed for $\text{Ca}(\text{OH})_2$ with $\rho_B = 600 \text{ kg m}^{-3}$ show $\lambda_{eff}(T) = 0.108$ to $0.112 \text{ W m}^{-1} \text{ K}^{-1}$ in a temperature range from 25 to 200 °C. For CaO with $\rho_B = 855 \text{ kg m}^{-3}$, $\lambda_{eff}(T)$ yielding 0.123 to $0.140 \text{ W m}^{-1} \text{ K}^{-1}$ in the same temperature range.

5.4.4 Magnesium hydroxide $\text{Mg}(\text{OH})_2$

The hydration of magnesium oxide as well as the dehydration of magnesium hydroxide for TCES is already shown by [104], where the authors focus on cycling stability and dehydration temperatures of $\text{Mg}(\text{OH})_2$ and MgO , or also in a bigger literature review by [19].



In the following measurements magnesium hydroxide from *Sigma-Aldrich* with the product name *Magnesium hydroxide BioUltra*, $\geq 99\%$ (KT) was analyzed.

Thermal decomposition

In the study of [104], isothermal and non-isothermal decomposition measurements using a STA system were performed. Main focus of this study was the cycling of the hydration and dehydration reaction. The results show, that dehydration already starts at $T = 300^\circ\text{C}$ and also sintering of the used MgO particles occur above $T = 500^\circ\text{C}$. Additionally, it was demonstrated that there is also water bound on the surface of the particles through physical adsorption evaporating below 300°C .

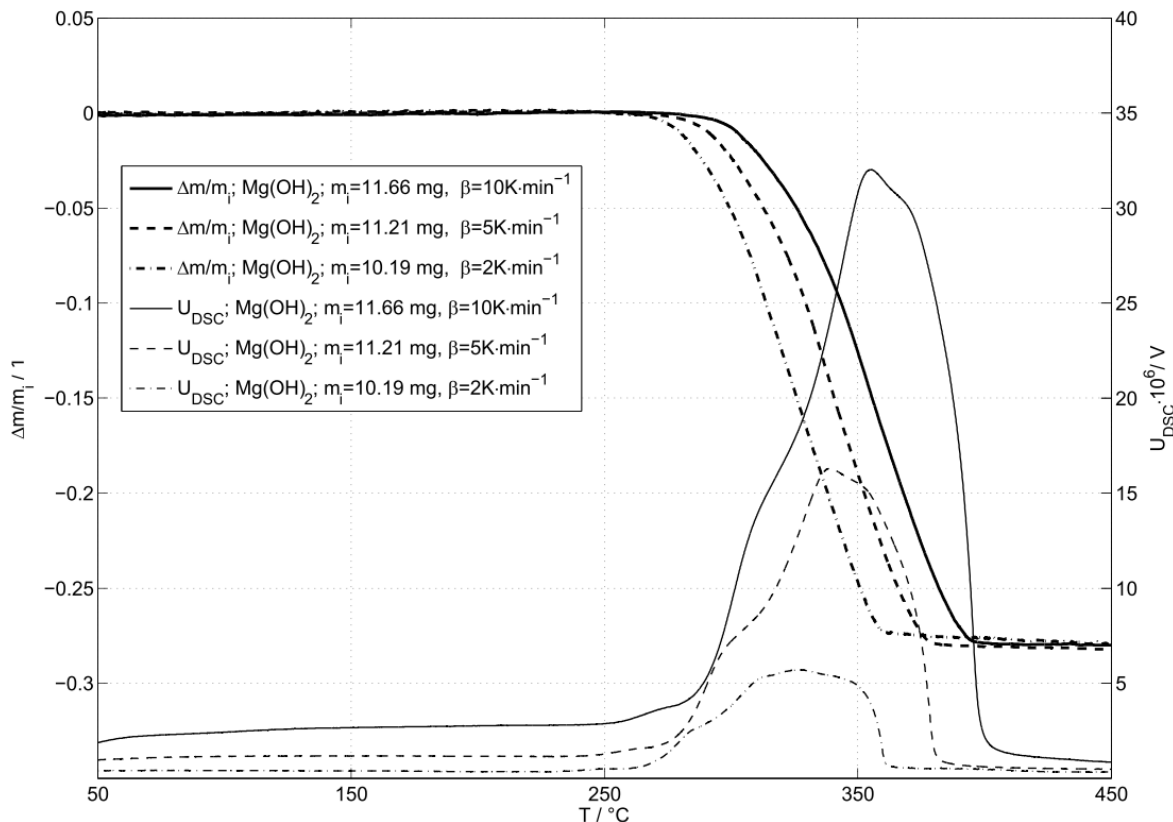


FIGURE 5.30: STA results for $\text{Mg}(\text{OH})_2$ using three different heating rates $\beta = 10, 5$ and $2.5 \text{ K} \cdot \text{min}^{-1}$

Figure 5.30 represents the measured STA data for $\text{Mg}(\text{OH})_2$ with the heating rates $\beta = 10 \text{ K} \cdot \text{min}^{-1}$, $5 \text{ K} \cdot \text{min}^{-1}$ and $2 \text{ K} \cdot \text{min}^{-1}$ in a temperature range between $T = 50$ and 450°C .

The $\text{Mg}(\text{OH})_2$ TGA result shows a mass loss of $\Delta m/m_i = -0.28$ between $T = 50$ and 450 °C. A desorption phenomenon as described in [104] up to $T = 150$ °C could not be observed with the analyzed samples. The applied heating rate β has a strong effect on the evaluation of the measured dehydration temperatures.

The lower temperature limit to evaluate the dehydration reaction enthalpy was defined with $T = 230$ °C for all heating rates. The upper limit depends on the final temperature T_f of the dehydration reaction. In case of $\beta = 2 \text{ K min}^{-1}$ the final temperature is defined with $T_f = 375$ °C, for $\beta = 5 \text{ K min}^{-1}$ with $T_f = 400$ °C and for $\beta = 10 \text{ K min}^{-1}$ with $T_f = 435$ °C. A comparison of the dehydration temperatures at a defined mass loss of $\Delta m/m_i = -0.01$ and specific reaction enthalpies Δh_r are shown in table 5.6.

	$\beta = 2 \text{ K min}^{-1}$	$\beta = 5 \text{ K min}^{-1}$	$\beta = 10 \text{ K min}^{-1}$
$T_{(\Delta m/m_i = -0.01)} / \text{°C}$	280	291	301
$\Delta h_r / \text{J g}^{-1}$	1220	1266	1278

TABLE 5.6: Measured $\text{Mg}(\text{OH})_2$ dehydration temperatures T and dehydration reaction enthalpies Δh_r for $\beta = 10 \text{ K min}^{-1}$, 5 K min^{-1} and 2 K min^{-1}

In the work from [104] several isothermal experiments on the used $\text{Mg}(\text{OH})_2$ have shown, that a full conversion to MgO can be reached at temperatures above $T_{min} > 300$ °C. In this work, based on dynamic heating segments in the STA experiments, dehydration starting at $T = 280$ °C could be observed for $\Delta m/m_i = -0.01$ and $\beta = 2 \text{ K min}^{-1}$. The measured specific reaction enthalpies Δh_r are lower as reported in [103] which may be again attributed to the added sensible heat or enthalpy change starting from $T = 25$ °C.

Apparent specific heat capacity

Two consecutive heating cycles starting with $\text{Mg}(\text{OH})_2$ up to $T_{max} = 500$ °C were performed to analyze $c_p^{app}(T)$ of $\text{Mg}(\text{OH})_2$ and MgO . Dehydration STA experiments at $\beta = 10 \text{ K min}^{-1}$ have shown, that full dehydration for $m_i \approx 11 \text{ mg}$ is reached at $T \approx 400$ °C. After dehydration in the first heating cycle, the produced MgO sample has a different initial mass m_i compared to the $\text{Mg}(\text{OH})_2$ precursor. This is determined through the preliminary TGA results from figure 5.30 and is calculated by reducing the m_i of $\text{Mg}(\text{OH})_2$ by 28 %.

Figure 5.31 shows the evaluated $c_p^{app}(T)$ DSC data and available literature data from the NIST-JANAF thermochemical tables [98]. The uncertainty for $c_p^{app}(T)$ from literature data was assumed with $u_c = 5\%$. The measured $c_p^{app}(T)$ for $\text{Mg}(\text{OH})_2$ shows, similar to the $\text{Ca}(\text{OH})_2$ measurements, a heat consuming behavior in a different temperature range between $T = 10$ to 200 °C. The preliminary STA experiment showed no mass loss in the TGA signal which may be attributed to the small initial weight m_i of the applied STA $\text{Mg}(\text{OH})_2$ samples. Again, adsorbed water being released might be a reason leading to the observed endothermic effect between 20 and 200 °C. Comparing the measured and the literature data from NIST-JANAF [98] one can see, that they are nearly identical at temperatures below 20 °C and measurement uncertainties are overlapping above the observed endothermic effect.

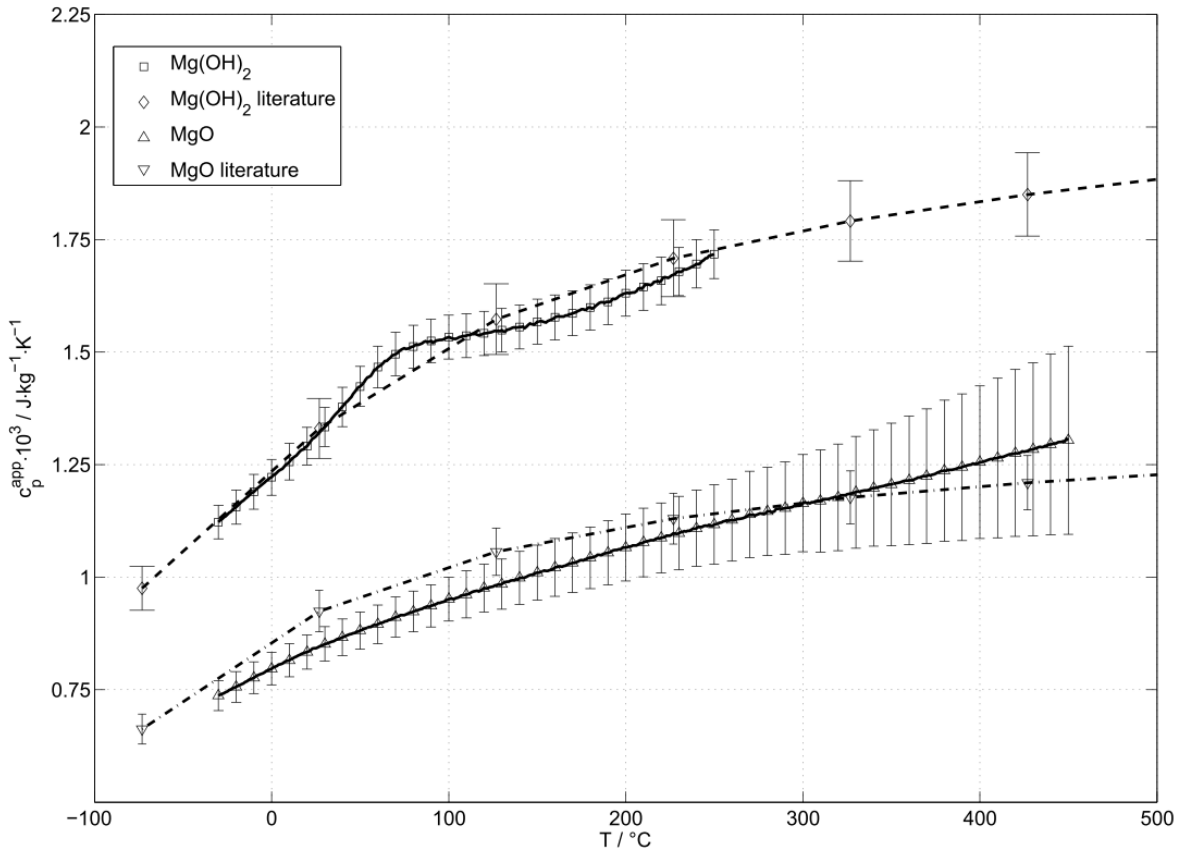
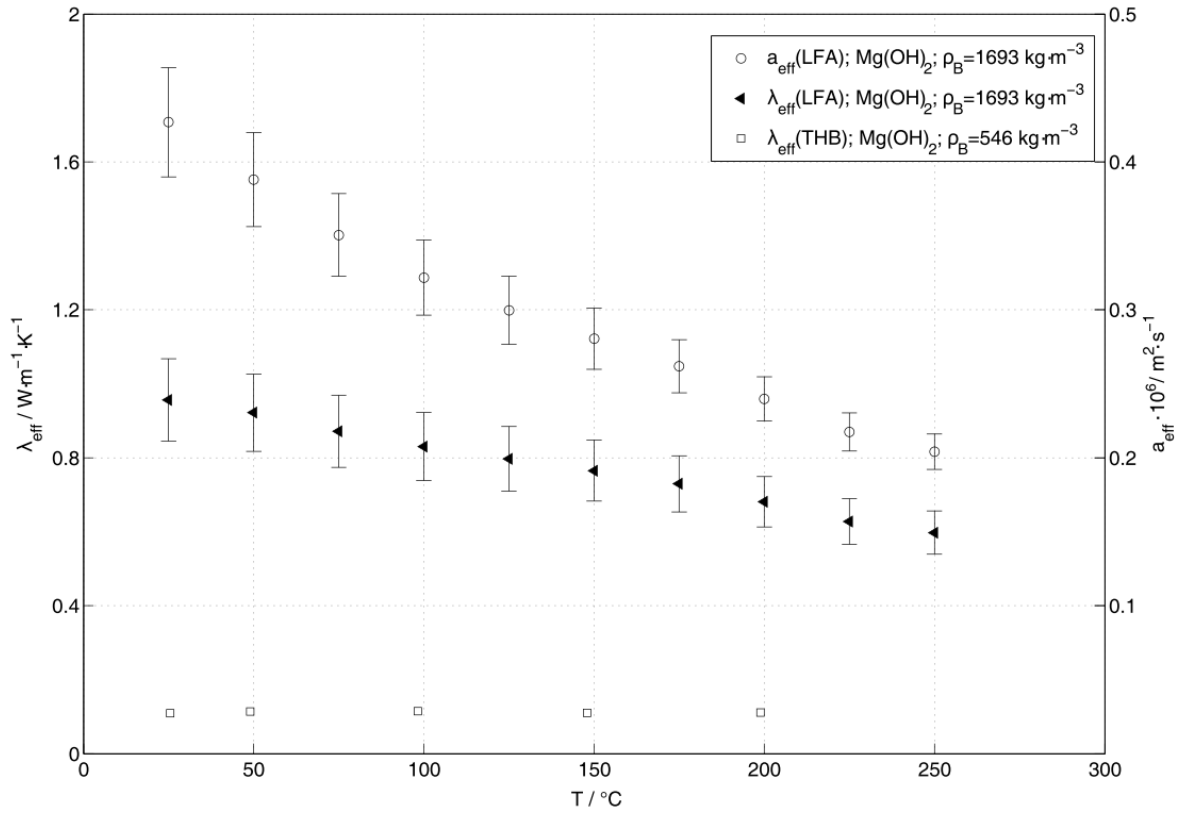


FIGURE 5.31: $c_p^{app}(T)$ of $\text{Mg}(\text{OH})_2$ and MgO

The measured $c_p^{app}(T)$ for MgO show slightly lower values as the NIST-JANAF data below 300°C . Comparing both curve characteristics, it can be seen that the slope of both curves are similar up to $T = 200^\circ\text{C}$. As it can be seen for $\text{Mg}(\text{OH})_2$, T_{max} was defined with 250°C because at this temperature the dehydration heat is already part of the measured DSC signal. Due to that, it appears that the apparent MgO sample also has some $\text{Mg}(\text{OH})_2$ content which starts to dehydrate at 250°C .

Thermal diffusivity and thermal conductivity

For LFA measurements, three pressed and graphite coated $\text{Mg}(\text{OH})_2$ samples with a bulk density of $\rho_B = 1693 \text{ kg m}^{-3}$ at ambient conditions were prepared. The prepared packed bed for THB measurements had a bulk density of $\rho_B = 546 \text{ kg m}^{-3}$ at ambient conditions. Due to the unknown chemical structure of the apparent MgO samples and the dehydration observations in former experiments, no further LFA or THB measurements were performed. Figure 5.32 summarizes the effective thermal diffusivity and conductivity results for $\text{Mg}(\text{OH})_2$. Thermal diffusivity $a_{eff}(T)$ decreases from 0.427 to $0.204 \text{ mm}^2 \text{ s}^{-1}$ in the temperature range $T = 25$ to 250°C . According the STA results from figure 5.30 it can be concluded, that the used $\text{Mg}(\text{OH})_2$ precursor should show no dehydration in this temperature range.

FIGURE 5.32: λ_{eff} and a_{eff} of $\text{Mg}(\text{OH})_2$

$\lambda_{eff}(T)$ for $\text{Mg}(\text{OH})_2$ was calculated between $T = 25$ and 250 °C based on the measured thermal diffusivity $a_{eff}(T)$ and bulk density ρ_B at ambient conditions. The additional needed $c_p(T)$ data was taken from the NIST-JANAF data [98]. Thermal conductivity $\lambda_{eff}(T)$ decreases from 0.957 to 0.597 $\text{W m}^{-1} \text{K}^{-1}$ in the temperature range $T = 25$ to 250 °C.

Direct THB measurements in the packed bed $\rho_B = 546$ kg m^{-3} at ambient conditions yield an effective thermal conductivity of $\lambda_{eff}(T) = 0.108$ to 0.112 $\text{W m}^{-1} \text{K}^{-1}$ in a temperature range from $T = 25$ to 200 °C.

5.5 Effective thermal conductivity measurements of packed beds

The motivation of this section is to compare two dynamic (THB, LFA) and one static (HFM) thermal conductivity measurement methods with a packed bed of a reference material. Several experiments using different conditions (sample preparation, gas conditions, evaluation models, etc.) should show the applicability and uncertainty contribution on the evaluated λ_{eff} result. For a detailed description of heat transport mechanism in porous media, the reader is referred to [105].

5.5.1 Reference material

YSZ, consisting of 95% ZrO_2 and 5% Y_2O_3 , as spherical shaped powder with a particle diameter of $d = 50 \mu m$, $100 \mu m$ and $200 \mu m$ as well as solid cylinders with $d = 12.7 \text{ mm}$ was chosen as reference material for the following experiments.

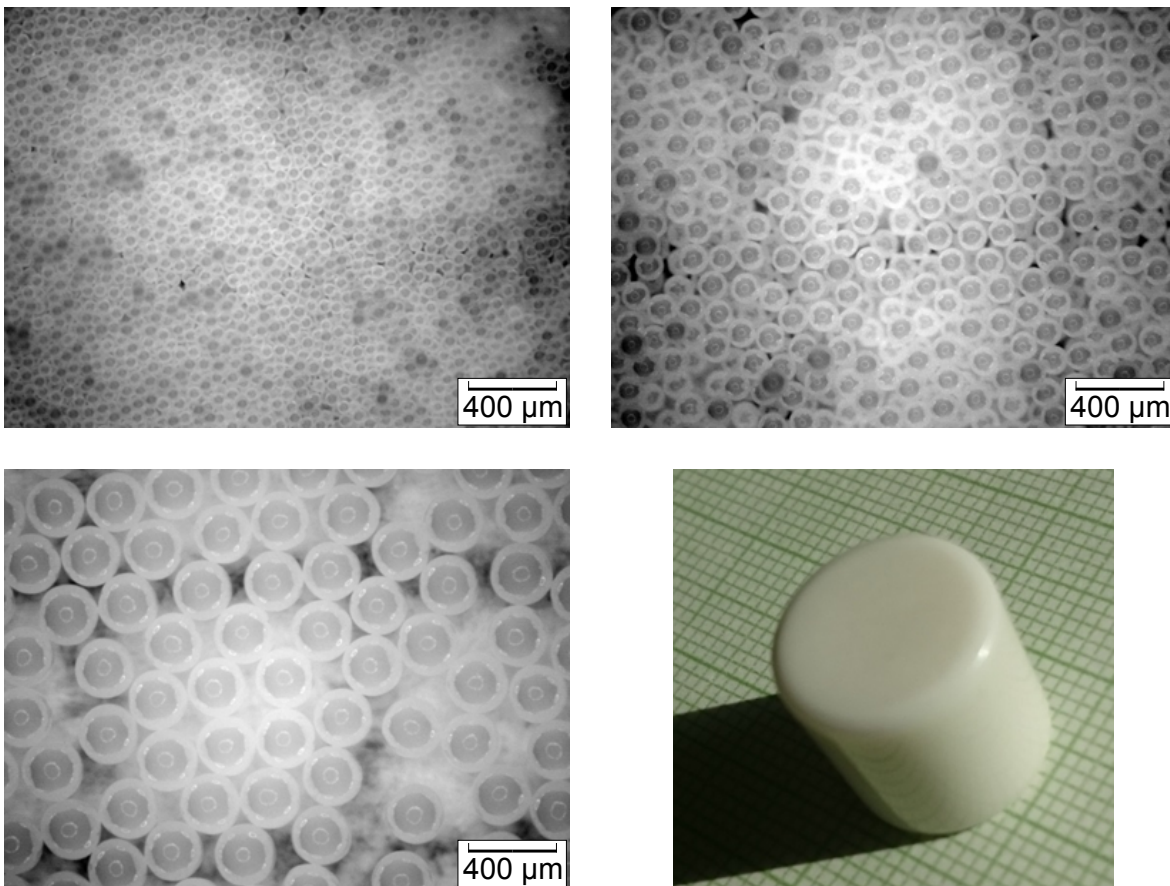


FIGURE 5.33: YSZ powder with $d = 50 \mu m$, $100 \mu m$ and $200 \mu m$ and as solid cylinder with $d = 12.7 \text{ mm}$ and $l = 10 \text{ mm}$

This high density ceramic material is used in pharmaceutical or dental applications. According to the product sheet of the material manufacturer, the solid density is defined with $\rho = 6.0 \text{ g cm}^{-3}$ and the bulk density of the powder with $\rho_B = 3.9 \text{ kg m}^{-3}$. Sieving of the powders have shown that they are monodisperse for all three different particle diameters.

5.5.2 Thermal conductivity of the solid YSZ

At first, specific heat capacity $c_p(T)$, density $\rho(T)$ as well as thermal diffusivity $a(T)$ are measured by DSC, Dilatometry and LFA to evaluate the thermal conductivity $\lambda(T)$ according to equation 4.6 of the solid YSZ.

Specific heat capacity

For the DSC experiments, a commercial heat flow DSC from *NETZSCH*, namely *DSC 204 F1 Phoenix*, was applied. The operating principle is already described in section 3.6 and the used equipment and setup can be found in section 4.2.1.

Three cylinders with $d = 5$ mm and a thickness of $\delta = 1$ mm are prepared from the solid cylinder shown in figure 5.33. The samples are measured in closed aluminum crucibles using a helium atmosphere from $T = 0$ to 300 °C with $\beta = 10$ K min⁻¹. In total, three zero line, three reference sapphire and three YSZ samples are measured and evaluated according to section 4.2.4.

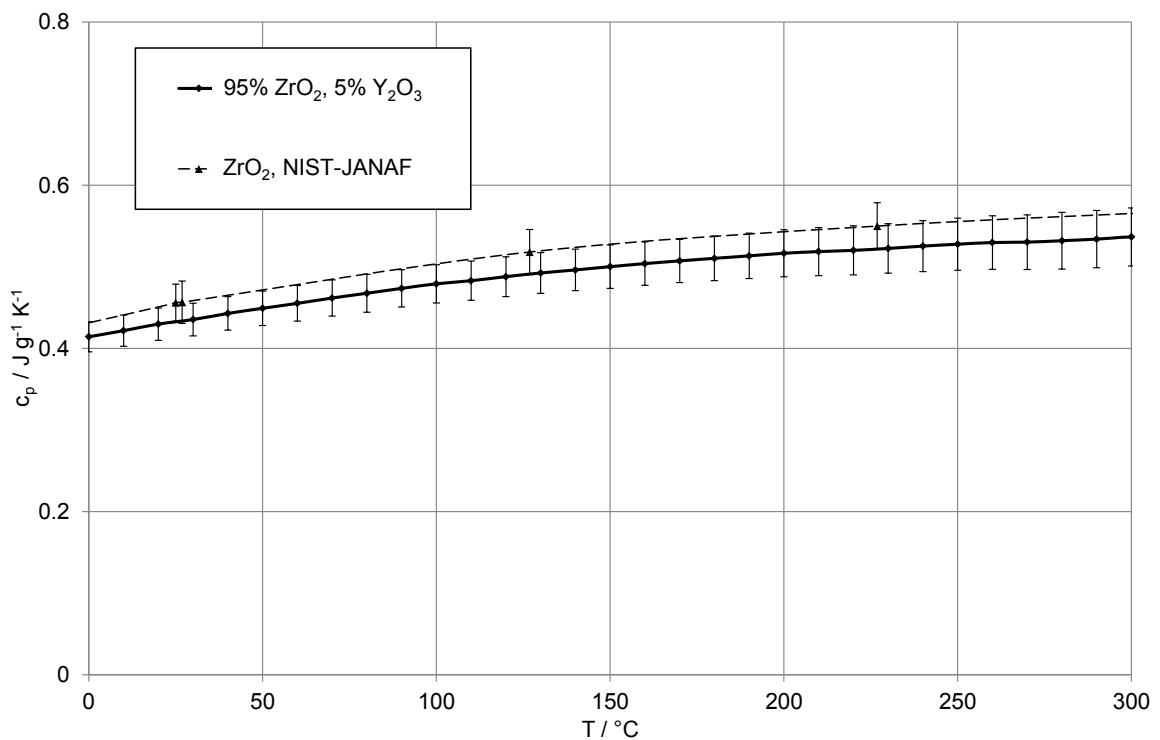


FIGURE 5.34: $c_p(T)$ of YSZ and literature values for ZrO_2 from [98]

The results on the YSZ show slightly lower values than the documented results for ZrO_2 from [98]. The uncertainty shown for the values of ZrO_2 from [98] are assumed with an uncertainty of $u_c = 5\%$.

Density of the solid

Thermal expansion measurements by a push-rod dilatometer (s. section 3.11) *NETZSCH DIL 402C* are applied on the solid cylinders of the YSZ material. No additional sample

preparation was necessary to measure the thermal expansion in the direction of the cylinder axis ($d = 12.7$ mm; $l = 10$ mm).

Three samples are measured in a static helium atmosphere from $T = 0$ to 300 °C with a heating rate of $\beta = 2$ K min⁻¹. The correction function, as described in section 3.11, is based on a cylindrical fused silica standard with $l = 12.012$ mm at ambient conditions.

Assuming an isotropic expansion behavior of the solid, the density $\rho(T)$ is calculated according to equation 5.13.

$$\frac{V(T)}{V_0} = \frac{\rho_0}{\rho(T)} = \left(1 + \frac{\Delta l(T)}{l_0}\right)^3 \quad (5.13)$$

In figure 5.35 the calculated arithmetic mean value of $V(T)/V_0$ and $\rho(T)/\rho_0$ of the corrected three YSZ samples is depicted. The initial density was evaluated by dimensions and mass of the solid cylinders and yielded $\rho_0 = 5.923$ g cm⁻³ with $\sigma_\rho = 0.033$ g cm⁻³.

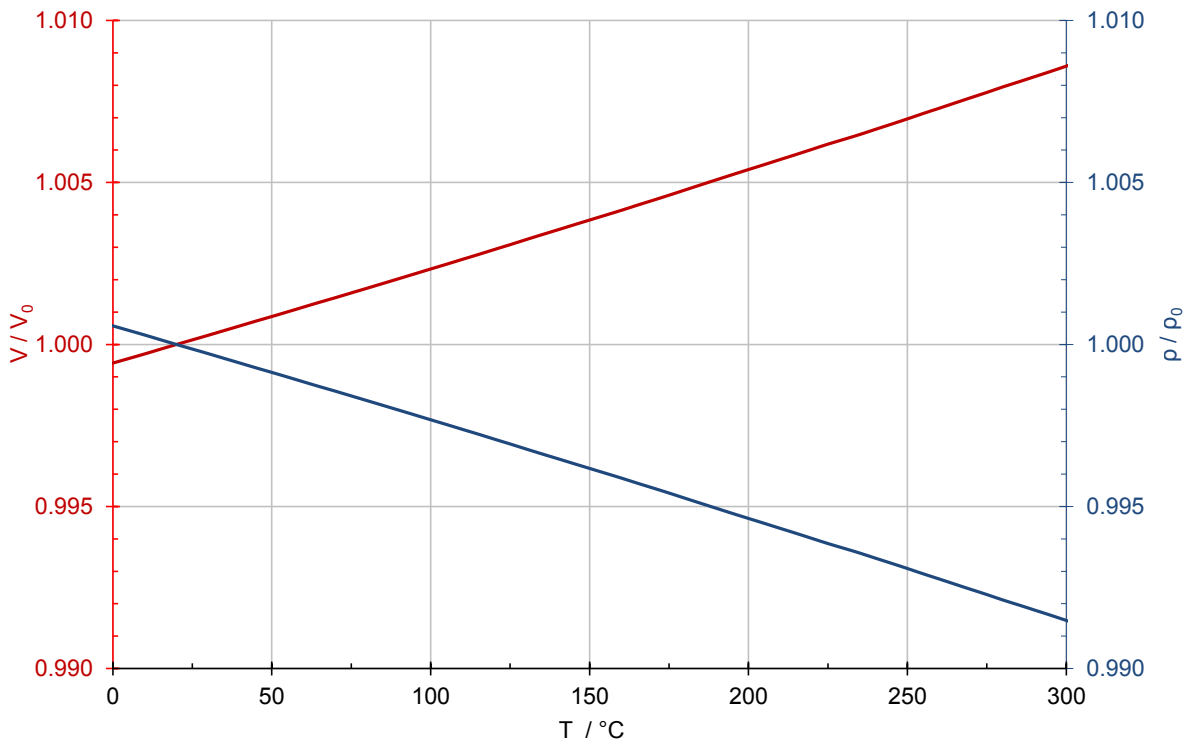


FIGURE 5.35: Density and volume change of YSZ between $T = 0$ to 300 °C; $\rho_0 = 5.923$ g cm⁻³, $\sigma_\rho = 0.033$ g cm⁻³

The results for $\rho(T)$ of the solid YSZ show less than 1% decrease of the density between the reference temperature $T_0 = 20$ °C with an initial density of $\rho_0 = 5.923$ g cm⁻³ and $\rho = 5.873$ g cm⁻³ at a temperature of $T = 300$ °C.

Thermal diffusivity and conductivity of the solid

The thermal diffusivity of the solid YSZ is measured by the LFA technique as shown in section 3.8. The used equipment and setup is already described in section 5.3.3. Again, three samples in total are prepared from the solid YSZ cylinder with a diameter of $d = 12.7$ mm and a height of $l \approx 1$ mm. For a better radiation absorption behavior, the prepared samples

are coated with a graphite layer as described in section 5.3.3. The defined temperature program uses steps with $\Delta T = 50^\circ\text{C}$ between $T = 0$ and 300°C . The pulse and detector settings as well as data analysis and uncertainty calculation for $a(T)$ and $\lambda(T)$ are adopted from the TCM measurement protocol, shown in section 5.3.3.

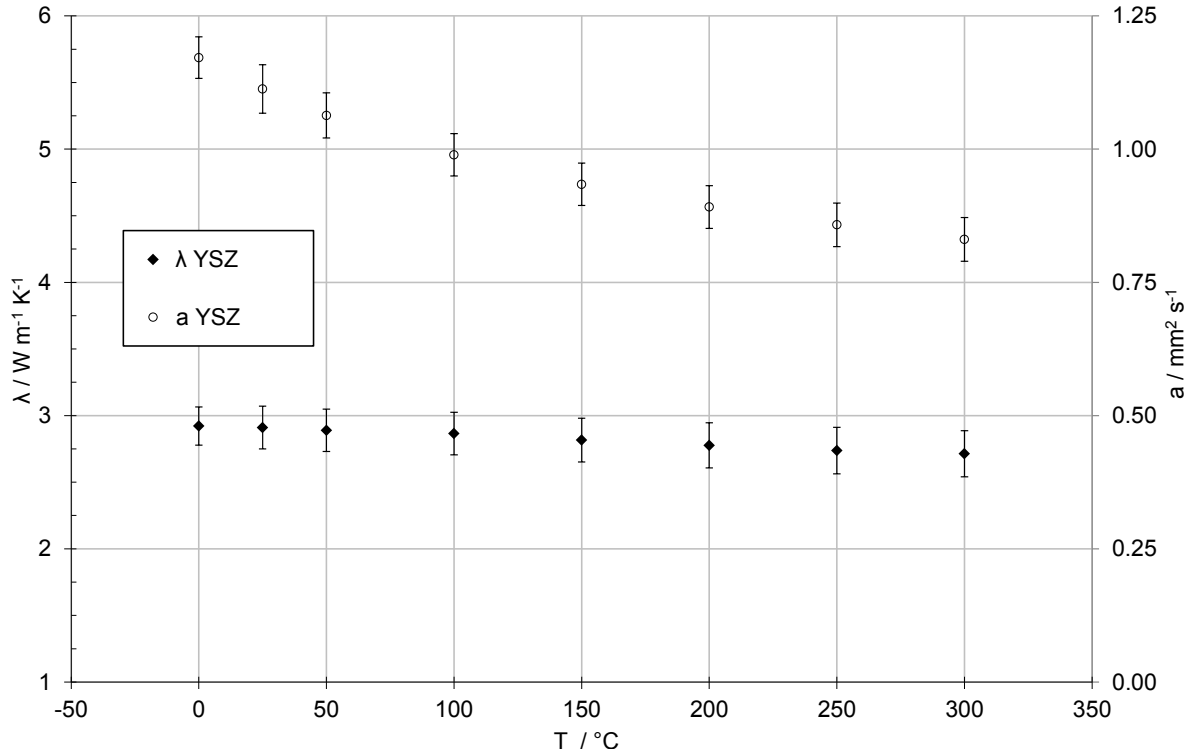


FIGURE 5.36: Thermal diffusivity $a(T)$ and conductivity $\lambda(T)$ of the solid YSZ

The data shown in figure 5.36 represent the measured thermal diffusivity $a(T)$ and the evaluated thermal conductivity $\lambda(T)$ from $\lambda(T) = a(T) \cdot c_p(T) \cdot \rho(T)$ of the solid YSZ material. These results are used for further comparison of the evaluated effective thermal conductivity $\lambda_{eff}(T)$ of the subsequent packed bed measurements.

5.5.3 Effective thermal conductivity measurements of YSZ packed beds

Three different measurement methods are applied to measure λ_{eff} of the YSZ packed beds with three different particle diameters. The first experiments were performed with the LFA method, where also different gases can be used to fill the pores between the measured particles. After that, THB experiments, as already described for TCM in section 5.3.4, were performed by immersing the foil sensor into the packed beds. Finally, the HFM is applied as a complementary method and the measured λ_{eff} of all three methods are compared amongst each other.

LFA experiments

As already shown for PCMs in the liquid phase (s. 4.3.1), a special sample holder system is needed to measure a packed bed of powdery material inside the LFA.

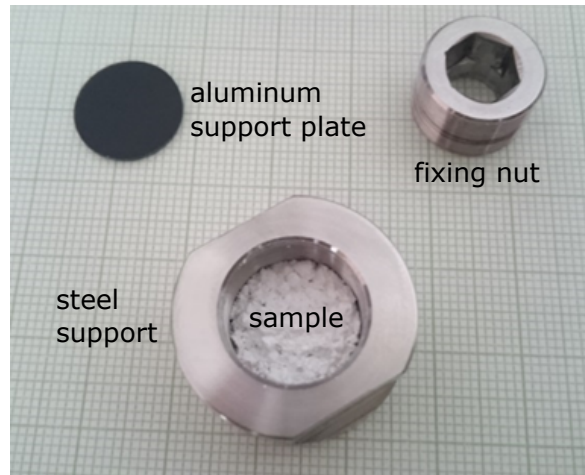


FIGURE 5.37: Sample holder system for LFA powder measurements

The powdery sample is placed between two aluminum support plates with a thickness of $\delta = 1$ mm. This three layer setup is placed inside a hollow cylinder made of stainless steel (steel support) with a thread inside. A defined compression can be achieved by a fixing nut which is screwed into the steel support.

The different powders were filled into the sample holder system. The lower and upper aluminum support plate were coated with a graphite layer to enhance radiation absorption as already described in section 5.3.3. Due to a high heat capacity C of the whole setup, higher pulse energies were applied to the light source with a pulse duration of $t = 600 \mu\text{s}$ and a lamp voltage of $U = 270$ V to get a good SNR of the detector signal. Additionally, the sample thickness was reduced to $\delta \leq 1$ mm to further decrease the heat capacity C as well as the thermal resistance R_{th} of the setup.

One sample per particle size was prepared and measured at room temperature with ambient, low pressure and helium gas conditions. The fixing nut was fixed with a calibrated torque wrench at 0.4 N m for all three samples. The bulk density ρ_B of the sample was evaluated through the inner diameter of the steel support ($d = 14.9$ mm), the thickness of the three layer setup in the middle of the fixing nut by a micrometer gauge, and the mass of the sample by differential weighing using a lab balance.

The applied thermal diffusivity three layer model is based on [74] as already shown for PCM measurements in section 4.3.1. The uncertainties in the data analysis are standard deviations according equation 4.5 of 10 measurements for each sample.

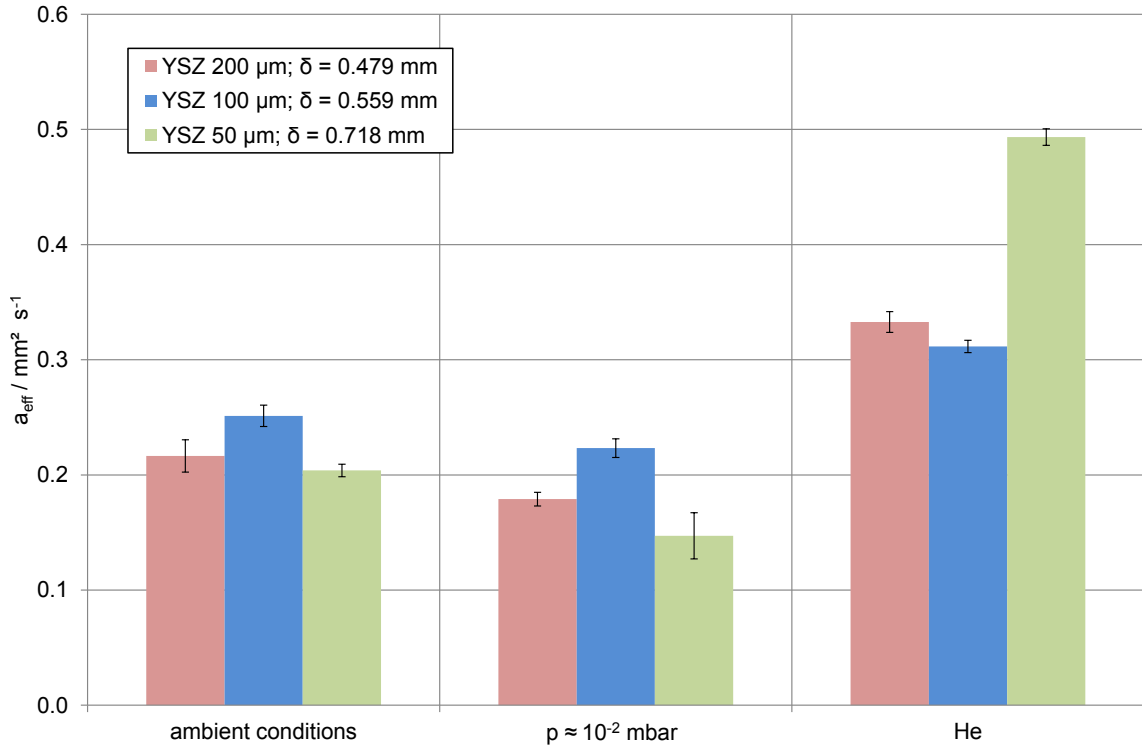


FIGURE 5.38: $a_{eff}(T)$ results for YSZ with particle diameters of $d = 50 \mu\text{m}$, $100 \mu\text{m}$ and $200 \mu\text{m}$ under ambient, low pressure and helium gas conditions

In figure 5.38, $a_{eff}(T)$ for YSZ with the different particle diameters of $d = 50 \mu\text{m}$, $100 \mu\text{m}$ and $200 \mu\text{m}$ under ambient, low pressure and helium gas conditions can be compared. The measured data show a significant relation between $a_{eff}(T)$ and the applied gas conditions. While $a_{eff}(T)$ under ambient gas conditions show values between 0.204 to $0.251 \text{ mm}^2 \text{ s}^{-1}$, measurements under low pressure indicated 0.147 to $0.223 \text{ mm}^2 \text{ s}^{-1}$ and under helium conditions 0.312 to $0.493 \text{ mm}^2 \text{ s}^{-1}$. A connection between the different particle sizes and the gas conditions could not be observed in these experiments.

THB experiments

The performed THB experiments are similar to the measurements done on powdery TCM as shown in section 5.3.4.

The different YSZ powders with the three particle diameters of $d = 50 \mu\text{m}$, $100 \mu\text{m}$ and $200 \mu\text{m}$ were filled into measuring glass beakers with a maximum volume of $V_{max} = 200 \text{ cm}^3$ and shaken under defined conditions until no optical volume change was noticed any more. The bulk density ρ_B was evaluated for each particle size and 5 different volumes in the measuring glass beaker with $V = 50 \text{ cm}^3$, 75 cm^3 , 100 cm^3 , 125 cm^3 and 150 cm^3 to analyze the influence of the different YSZ particle sizes and applied volumes. The uncertainty model of the evaluated ρ_B is based on equation 5.14.

$$u_{c, \rho_B}^2 = 2 \left[\left(\frac{\partial \rho_B}{\partial m} \right)^2 u_m^2 + \left(\frac{\partial \rho_B}{\partial V} \right)^2 u_V^2 \right] \quad (5.14)$$

The uncertainty of weighing with the lab balance was estimated with $u_m = 0.1$ mg and the uncertainty of the volume measurement in the glass beaker was estimated with $u_V = 1$ cm³.

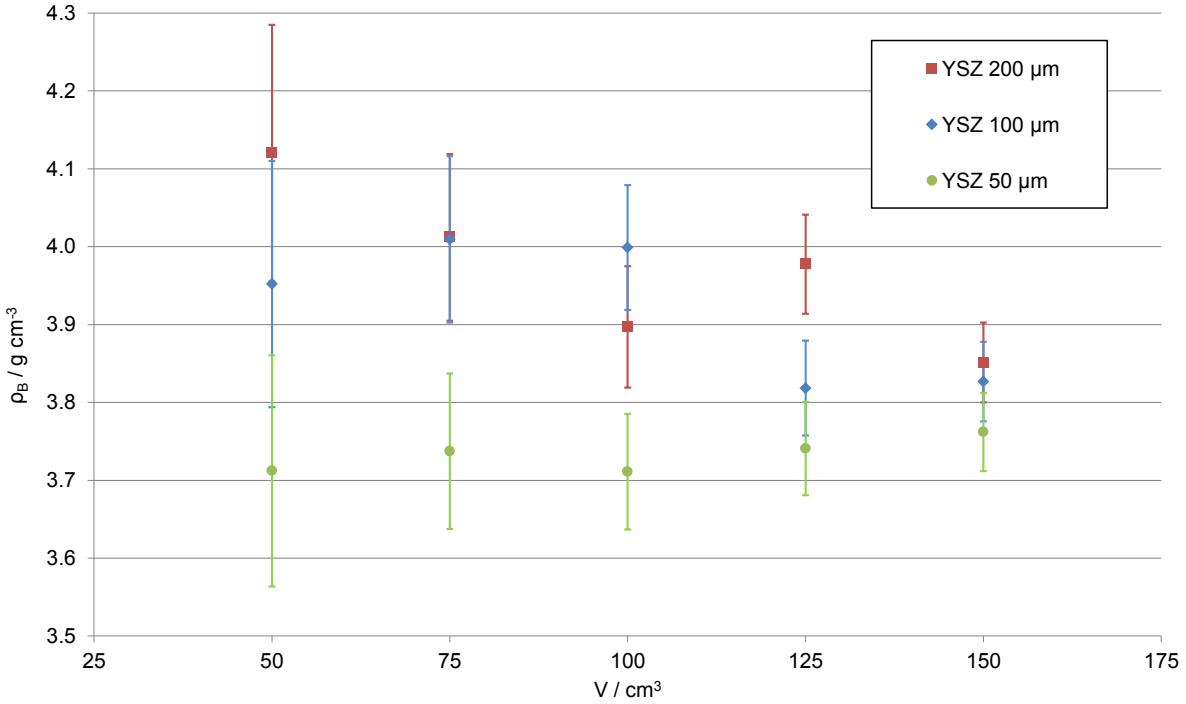


FIGURE 5.39: Bulk density ρ_B evaluation for YSZ particles with $d = 50$ μm , 100 μm and 200 μm for THB measurements

Results of ρ_B show an increasing uncertainty for small volumes as well as lower ρ_B for the small particles with $d = 50$ μm in comparison to the $d = 100$ μm and 200 μm . The subsequent THB measurements are done with a volume of $V = 150$ cm³.

Again, a metal frame kapton foil sensor (42 mm x 22 mm) was calibrated with a water standard and immersed into the packed beds with the three different YSZ particle sizes. For each particle size, the experiment was repeated three times with the same sample but a re-positioned THB sensor in the packed bed. Additionally, five measurement points were recorded for each sensor position and particle size at ambient conditions. All THB experiments are performed with an adjusted heating current of $I = 70$ mA for the current source and a data acquisition time of $t = 15$ s. The uncertainty of λ_{eff} is calculated with the standard deviation σ .

δ μm	T $^{\circ}\text{C}$	λ_{eff} $\text{W m}^{-1} \text{K}^{-1}$	$u_{\lambda_{eff}}$ $\text{W m}^{-1} \text{K}^{-1}$	ρ_B g cm^{-3}	u_{ρ_B} g cm^{-3}
200	26	0.256	0.004	3.851	0.051
100	27	0.222	0.004	3.827	0.051
50	27	0.187	0.003	3.762	0.050

TABLE 5.7: THB results for λ_{eff} of YSZ packed beds with particle diameters of $d = 50$ μm , 100 μm and 200 μm

The results in table 5.7 show a decrease of the measured λ_{eff} with smaller particle diameters. This effect may be connected to the lower ρ_B of the packed beds for smaller particle diameters as shown in figure 5.39.

HFM experiments

Finally, also HFM experiments on the different packed beds of YSZ particles were conducted. A detailed description of the method can be found in section 3.10.



FIGURE 5.40: left: Expanded Polystyrene (EPS) sample holder frame with aluminum foil; middle: sample holder frame filled with YSZ powder, right: sample and sample holder inside the used HFM device

A special sample holder consisting of an EPS frame and an aluminum foil on the bottom side was constructed as containment for the different packed beds of YSZ particles. The external frame dimensions are 200 mm x 200 mm x 10 mm with a cut out of 150 mm x 150 mm. The attached aluminum foil covers the whole frame on the bottom side with a thickness of $\delta = 0.02$ mm. The heat flux transducers of the used *NETZSCH HFM 446* device have a dimension of 100 mm x 100 mm, making sure that the upper transducer is completely covered by the powder while the lower plate contacts the aluminum foil. The aluminum foil has a very small thermal resistance R_{th} due to its high thermal conductivity and small thickness in comparison to the whole setup. The additional attached EPS frame is needed to have a constant thickness over the heat flux transducer area and a uniform contribution of the applied powder as well as a thermal insulation for lateral heat fluxes. Therefore, it can be assumed, that the influence of the sample holder is not affecting the measured λ_{eff} of the packed beds of YSZ particles.

The system was calibrated at $T_{mean} = 25^\circ\text{C}$ and $\Delta T = 10^\circ\text{C}$ with a NIST SRM 1450d insulating material at ambient gas conditions as already shown in section 3.10.2. These experimental conditions were also adapted for the subsequent YSZ packed bed measurements.

The sample holder was filled with the different YSZ particles and the mass of the packed bed was measured by differential weighing using a lab balance. The bulk density ρ_B is evaluated by the cut out area of the frame with $A = 225\text{ cm}^2$, the thickness δ measured by four inclinometers inside the HFM and the evaluated mass. The uncertainty of ρ_B is calculated according to equation 5.14 assuming $u_m = 1\text{ g}$ and $u_V = 1\text{ cm}^3$.

The expanded combined standard uncertainty for λ based on equation 3.33 and the propagation of uncertainty according to [72] is calculated as described in the following equation.

$$u_{c,\lambda}^2 = 2 \left[\left(\frac{\partial \lambda}{\partial N} \right)^2 u_N^2 + \left(\frac{\partial \lambda}{\partial V} \right)^2 u_V^2 + \left(\frac{\partial \lambda}{\partial \delta} \right)^2 u_\delta^2 + \left(\frac{\partial \lambda}{\partial \Delta T} \right)^2 u_{\Delta T}^2 \right] \quad (5.15)$$

The uncertainty u_N is estimated with 1 % of the measured calibration factor N resulting from the NIST SRM 1450d standard measurement. The uncertainty of the voltage at the heat flux transducers u_V is calculated with the standard deviation σ of the measured U of the upper and lower transducers. Further assumptions are $u_\delta = 5 \mu\text{m}$ and $u_{\Delta T} = 0.1 \text{ }^\circ\text{C}$.

δ μm	T $^\circ\text{C}$	λ_{eff} $\text{W m}^{-1} \text{K}^{-1}$	$u_{\lambda_{eff}}$ $\text{W m}^{-1} \text{K}^{-1}$	ρ_B g cm^{-3}	u_{ρ_B} g cm^{-3}
200	25	0.199	0.006	4.021	0.036
100	25	0.183	0.006	3.928	0.035
50	25	0.155	0.006	3.819	0.035

TABLE 5.8: HFM results for λ_{eff} of YSZ packed beds with particle diameters of $d = 50 \mu\text{m}$, $100 \mu\text{m}$ and $200 \mu\text{m}$

The measured data in table 5.8 show also decrease of the measured λ_{eff} and ρ_B with smaller particle diameters. Due to the higher sample volume, a lower uncertainty of the density measurement u_{ρ_B} can be identified.

5.5.4 Comparison of the results

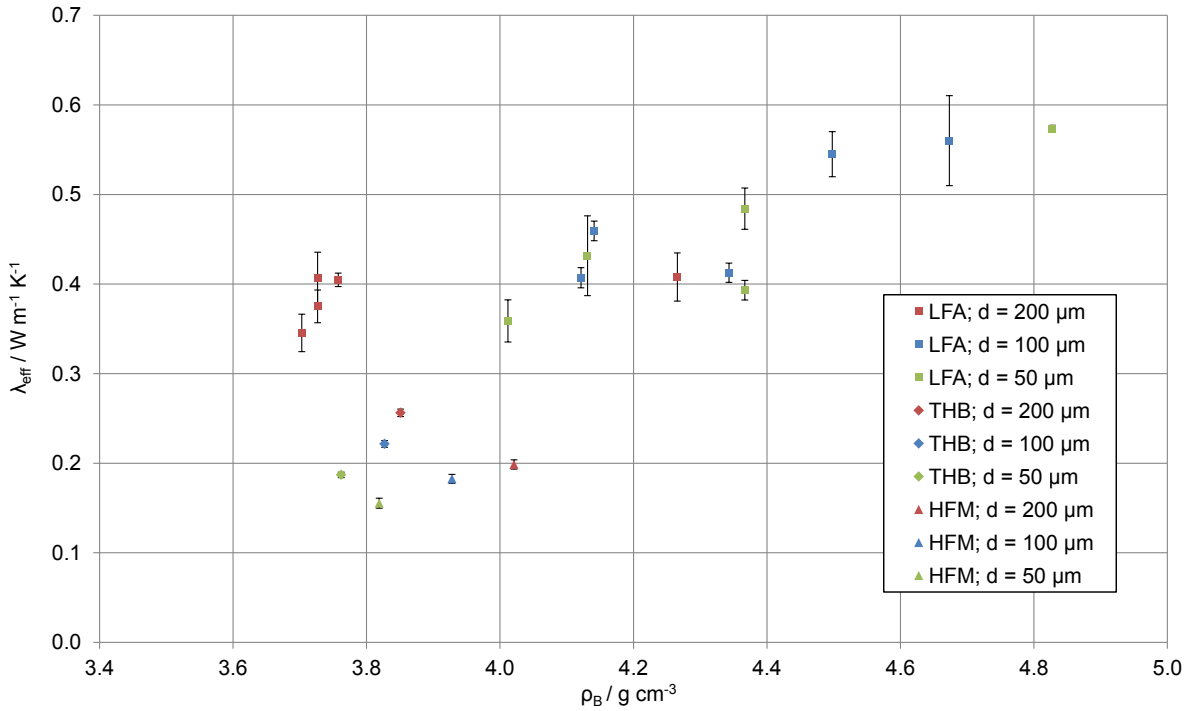


FIGURE 5.41: Comparison of the measured λ_{eff} and ρ_B at room temperature based on LFA, THB and HFM measurements for YSZ with $d = 50 \mu\text{m}$, $100 \mu\text{m}$ and $200 \mu\text{m}$

In figure 5.41, an overview of the obtained λ_{eff} and ρ_B results based on the LFA, THB and HFM for YSZ with $d = 50 \mu\text{m}$, $100 \mu\text{m}$ and $200 \mu\text{m}$ can be seen. The evaluated λ_{eff} data for the depicted LFA measurements are calculated with the product of the thermal diffusivity data shown in figure 5.38 at ambient gas conditions, the measured specific heat capacity of the solid described in section 5.5.2, and the ρ_B measurement according section 5.5.3.

The LFA results show significant higher λ_{eff} data for all measured bulk densities than the THB and HFM method. This effect may be associated with the pressure applied on the upper aluminum support plate by the fixing nut of the sample holder system, leading to better contact conditions between the YSZ particles in the packed bed.

Furthermore, the thickness δ is measured between the centers of the upper and lower aluminum support plate. If no uniform contribution is reached inside the sample holder, the upper and lower aluminum support plate would not be plane-parallel and a variation of the thickness would occur.

This effect also influences the measured ρ_B of the used LFA samples. While the maximum value for ρ_B in the HFM measurement was $\rho_B = 4.021 \text{ g cm}^{-3}$, one LFA sample showed $\rho_B = 4.828 \text{ g cm}^{-3}$.

In the study of [106] a model for thermal conductivity in packed beds based on spherical particles is described and the possible packaging structures are shown. Assuming the tightest packaging of spheres, which is the Face-Centered Cubic (FCC) structure, the maximum bulk density of YSZ is $\rho_B = 4.44 \text{ g cm}^{-3}$ derived from the solid density ρ .

THB and HFM results show slight differences in the evaluated λ_{eff} values. While THB results are between $\lambda_{eff} = 0.187$ and $0.256 \text{ W m}^{-1} \text{ K}^{-1}$, HFM indicate slightly lower values with $\lambda_{eff} = 0.155$ to $0.199 \text{ W m}^{-1} \text{ K}^{-1}$.

5.6 Conclusion

The performed experiments with sorption and composite materials have shown the applicability of the STA experiment to evaluate sorption isotherms, enthalpies as well as sorption rates. A detailed investigation on a natural clinoptilolite and salt-based composites with the applied STA measurement protocol allowed a comparison of the possible water uptakes and associated enthalpy data at specified application conditions. Additional experiments on a synthetic zeolite verified the accuracy of the developed protocol with available literature data.

In case of powdery TCM candidates, measurement protocols have been developed to analyze the specific heat capacity $c_p(T)$, effective thermal diffusivity $a_{eff}(T)$ and effective thermal conductivity $\lambda_{eff}(T)$. While the STA method is used as preliminary experiment to identify reaction free temperature intervals and reaction enthalpies Δh_r , DSC is applied to evaluate $c_p(T)$ of the reactants and products. Furthermore, LFA and THB procedures for compacted powdery samples as well as in packed bed configurations are represented to evaluate the thermal transport properties at different bulk densities ρ_B .

These protocols were applied on four possible TCM candidates, $\text{CaC}_2\text{O}_4 \cdot \text{H}_2\text{O}$, H_3BO_3 , $\text{Ca}(\text{OH})_2$ and $\text{Mg}(\text{OH})_2$. Starting from thermal decomposition experiments to identify reaction free temperature intervals and reaction enthalpies Δh_r , the apparent specific heat capacity $c_p^{app}(T)$ was evaluated and compared to available literature data. These data have shown the difference between $c_p(T)$ of pure substances described in the literature and the actual $c_p^{app}(T)$ of the investigated TCMs. The outcomes for the thermal transport properties $a_{eff}(T)$ and $\lambda_{eff}(T)$ indicated the strong dependency on the actual bulk density ρ_B of the investigated powdery TCM.

Finally, a detailed investigation on $a_{eff}(T)$ and $\lambda_{eff}(T)$ of packed beds consisting of YSZ powder with different particle diameters based on the LFA, THB and HFM method were performed. The LFA results indicate a significant relation between the $a_{eff}(T)$ and the used gas conditions. A comparison of the evaluated λ_{eff} results based on the applied three measurement methods showed diverse results. While HFM and THB indicated comparable λ_{eff} data at related bulk densities ρ_B , LFA showed significant higher values for λ_{eff} . Considerations about a non uniform distribution of the powder inside the sample holder system lead to the assumption, that the evaluated bulk densities ρ_B are not correct and also plane-parallelism is not given which is a requirement for accurate LFA measurements.

Chapter 6

Discussion

This study examined standardized and new methodologies to determine thermophysical properties, focusing on specific heat capacity $c_p(T)$, phase transition enthalpy Δh_t , reaction enthalpy Δh_r , thermal diffusivity $a(T)$, thermal conductivity $\lambda(T)$ and characteristic temperatures of PCM and TCM materials for TES.

A detailed analysis of heat flow DSC experiments have shown, that low heating rates β are necessary to get a higher accuracy in the determination of characteristic temperatures for PCM due to the low thermal conductivity $\lambda(T)$ of the investigated materials. Calibration measurements with phase change and $c_p(T)$ standard reference materials indicate different DSC sensor sensitivities S_{DSC} at the same experimental conditions. This result implicates a connection between the sensor sensitivity S_{DSC} and the occurring heat flow rate ϕ . Due to that, a new DSC measurement protocol was defined and verified by an octadecane paraffin wax round robin test, concentrating on characteristic temperatures and the enthalpy curve $\Delta h(T)$ measurements. This protocol showed its assets in the phase change region but limitations due to high uncertainties for the $c_p(T)$ evaluation before and after the phase change. This was investigated by comparative DSC measurements of an organic PCM at different heating rates β .

Thermal diffusivity $a(T)$ measurements of an organic PCM based on the LFA method indicated a good reproducibility for the solid phase but challenges due to liquid capillary ascension and low viscosity in the liquid phase of the sample. In contrast, thermal conductivity $\lambda(T)$ experiments via the THB method have shown their assets in the liquid phase but on the other hand unsatisfactory results in the solid phase due to varying contact conditions between foil sensor and sample. A numerical investigation of a LFA liquid sample holder system filled with pure water has shown the transient and spatial temperature field distribution inside the sample holder system and the influence on the measured half time $t_{1/2}$ depending on the detector focus.

Moreover, STA experiments to determine sorption isotherms, enthalpy changes Δh and sorption rates of zeolites and salt-based composites were performed at technological relevant conditions. The applicability of the developed protocols was verified by several experiments on a synthetic zeolite and available literature data.

Furthermore, measurement protocols to analyze the specific heat capacity $c_p(T)$, effective thermal diffusivity $a_{eff}(T)$ and effective thermal conductivity $\lambda_{eff}(T)$ of powdery TCM

candidates were developed and applied on four different candidates: $\text{CaC}_2\text{O}_4 \cdot \text{H}_2\text{O}$, H_3BO_3 , $\text{Ca}(\text{OH})_2$ and $\text{Mg}(\text{OH})_2$. These data have shown the difference between $c_p(T)$ of pure substances described in literature and the actual $c_p^{app}(T)$ of the investigated TCMs in the temperature range of interest. The investigated thermal transport properties $a_{eff}(T)$ and $\lambda_{eff}(T)$ represent the strong dependency on the actual bulk density ρ_B of the measured sample.

Finally, a detailed investigation on $a_{eff}(T)$ and $\lambda_{eff}(T)$ of packed beds consisting of a YSZ powder with different particle diameters based on the LFA, THB and HFM method were performed and compared. The LFA results indicate a significant relation between the $a_{eff}(T)$ and the used gas conditions. Under ambient conditions, the HFM and THB method indicate comparable $\lambda_{eff}(T)$ data while LFA showed significant higher values. Considerations about a non uniform distribution of the powder inside the LFA sample holder system lead to the assumption, that the evaluated bulk densities ρ_B are not correct and also plane-parallelism is not given, which is a requirement for accurate LFA measurements.

Further investigations of thermal conductivity measurements in the solid and liquid phase as well as in the packed bed are needed, to verify the applicability of the different methods. This is already started with a new *IEA SHC Task 58* joint with the *ECES Annex 33* about *Material and Component Development for Thermal Energy Storage*. This joint program started in January 2017 and has a focus on material properties and bulk properties of PCM and TCM, developing new characterization and testing protocols under application conditions.

Appendix A

Thermophysical data from literature

A.1 Sensible heat storage materials - SHSM

#	Name	Class	c_p kJ kg ⁻¹ K ⁻¹	λ W m ⁻¹ K ⁻¹	ρ kg m ⁻³	Q/V ($\Delta T = 1$ °C) kJ m ⁻³	Ref
1	Water	Water	4.19	0.58	1000	4190	[2]
2	Ethanol	Organic fluids	2.40	0.17	790	1896	[2]
3	Propanol	Organic fluids	2.50	0.16	800	2000	[2]
4	Butanol	Organic fluids	2.40	0.17	809	1942	[2]
5	Isobutanol	Organic fluids	3.00	0.13	808	2424	[2]
6	Isopentanol	Organic fluids	2.20	0.14	831	1828	[2]
7	Octane	Organic fluids	2.40	0.13	704	1690	[2]
8	Brick	Building materials	0.84	1.20	1600	1344	[2]
9	Concrete	Building materials	1.13	1.10	2240	2531	[2]
10	Cement sheet	Building materials	1.05	0.36	700	735	[2]
11	Gypsum plastering	Building materials	0.84	0.42	1200	1004	[2]
12	Granite	Stones/Minerals	0.90	2.90	2650	2385	[2]
13	Marble	Stones/Minerals	0.88	2.00	2500	2200	[2]
14	Sandstone	Stones/Minerals	0.71	1.83	2200	1566	[2]
15	Clay sheet	Natural products	0.84	0.85	1900	1590	[2]
16	Asphalt sheet	Building materials	1.70	1.20	2300	3910	[2]
17	Steel slab	Metals	0.50	50.00	7800	3916	[2]
18	Corkboard	Natural products	1.89	0.04	160	302	[2]
19	Wood	Natural products	2.09	0.16	800	1674	[2]
20	Plastic board	Polymers	0.84	0.50	1050	879	[2]
21	Rubber board	Polymers	0.20	0.30	1600	320	[2]
22	PVC board	Polymers	1.00	0.16	1379	1385	[2]
23	Asbestos sheet	Natural products	1.05	0.16	2500	2625	[2]
24	Fiberboard	Building materials	1.00	0.06	300	300	[2]
25	Siporex board	Building materials	1.00	0.12	550	552	[2]
26	Polyurethane board	Polymers	0.84	0.03	30	25	[2]
27	Light plaster	Building materials	1.00	0.16	600	600	[2]
28	Dense plaster	Building materials	1.00	0.50	1300	1300	[2]
29	Aluminum	Metals	0.90	204.00	2707	2425	[2]
30	Aluminum oxides	Oxides	0.84	30.00	3900	3276	[2]
31	Cast iron	Metals	0.84	29.30	7900	6612	[2]
32	Pure iron	Metals	0.45	73.00	7897	3569	[2]
33	Copper	Metals	0.38	385.00	8954	3429	[2]
34	Stone. granite	Stones/Minerals	0.82	2.84	2640	2165	[2]
35	Stone. sandstone	Stones/Minerals	0.71	1.83	2200	1562	[2]
36	Alumina (99.5%)	Oxides	0.80	20.00	3960	3168	[4]
37	Cast iron (BSgrade3D)	Metals	0.54	22.00	7800	4212	[4]
38	High alumina concrete	Building materials	0.98	1.30	2400	2352	[4]
39	Graphite	Graphite	0.71	120.00	2230	1583	[4]
40	Magnesia	Oxides	0.94	40.00	3565	3351	[4]
41	Silicon carbide	Carbides	1.04	41.00	3210	3338	[4]

TABLE A.1: Thermophysical literature data for sensible heat storage materials

A.2 Phase Change Materials - PCM

#	Name	Class	T_t °C	Δh_t kJ kg ⁻¹	ρ kg m ⁻³	$\Delta H/V$ MJ m ⁻³	Ref
1	Aluminum nitrate	Salt solution	-30.6	131	1267	166	[6]
2	Sodium chloride	Salt solution	-21.2	222	1137	252	[6]
3	Calcium Chloride	Salt solution	-10.7	283	1116	316	[6]
4	Water	Water	0.0	333	958	319	[6]
5	Lithium chlorate trihydrate	Salt hydrate	8.0	155	1625	252	[6]
6	Potassium fluoride trihydrate	Salt hydrate	18.5	231	1451	335	[6]
7	Calcium chloride hexahydrate	Salt hydrate	29.0	180	1636	294	[6]
8	Sodium sulfate decahydrate	Salt hydrate	32.0	254	743	189	[6]
9	Disodium phosphate dodecahydrate	Salt hydrate	39.5	280	1482	415	[6]
10	Sodium thiosulfate pentahydrate	Salt hydrate	51.5	198	1710	339	[6]
11	Sodium acetate trihydrat	Salt hydrate	58.0	245	1365	334	[6]
12	Barium hydroxide octahydrate	Salt hydrate	78.0	273	2059	561	[6]
13	Magnesium nitrate hexahydrate	Salt hydrate	89.5	156	1607	251	[6]
14	Magnesium chloride hexahydrate	Salt hydrate	117.0	167	1510	252	[6]
15	Lithium nitrate	Salt	254.0	360	1960	706	[6]
16	Sodium nitrate	Salt	307.0	172	2080	358	[6]
17	Potassium nitrate	Salt	333.0	266	1895	504	[6]
18	Magnesium chloride	Salt	714.0	452	2140	967	[6]
19	Sodium chloride	Salt	800.0	492	2160	1063	[6]
20	Sodium carbonate	Salt	854.0	276	2533	699	[6]
21	Potassium fluoride	Salt	857.0	452	2370	1071	[6]
22	Potassium carbonate	Salt	897.0	236	2290	540	[6]
23	n-Tetradecane	Paraffin	6.0	230	760	175	[6]
24	n-Pentadecane	Paraffin	10.0	212	770	163	[6]
25	n-Hexadecane	Paraffin	18.0	224	760	170	[6]
26	n-Heptadecane	Paraffin	19.0	240	776	186	[6]
27	n-Octadecane	Paraffin	28.0	283	794	225	[6]
28	n-Eicosane	Paraffin	38.0	246	779	192	[7]
29	n-Triacontane	Paraffin	66.0	251	775	195	[7]
30	Polyethylene	Polymer	122.5	200	905	181	[6]
31	Caprylic Acid	Fatty acid	16.0	149	941	140	[6]
32	Capric Acid	Fatty acid	32.0	153	945	145	[6]
33	Lauric Acid	Fatty acid	43.0	178	939	167	[6]
34	Myristic Acid	Fatty acid	58.0	195	926	180	[6]
35	Palmitic Acid	Fatty acid	62.5	194	920	178	[6]
36	Xylitol	Sugar alcohol	94.0	263	1500	395	[6]
37	D-Sorbitol	Sugar alcohol	97.0	185	1520	281	[6]
38	Erythritol	Sugar alcohol	120.0	340	1390	473	[6]
39	D-Mannitol	Sugar alcohol	167.0	316	1520	480	[6]
40	Galactitol	Sugar alcohol	188.0	351	1520	534	[6]
41	PEG400	PEG	8.0	100	1177	118	[6]
42	PEG600	PEG	19.5	127	1179	150	[6]
43	PEG6000	PEG	61.0	190	1149	218	[6]
44	Gallium	Metals	29.8	80	5904	472	[33]
45	Indium	Metals	156.6	28	7310	205	[33]
46	Tin	Metals	231.9	61	7265	440	[33]
47	Aluminum	metals	660.3	397	2700	1072	[33]
48	Zinc	Metals	419.5	108	7140	768	[33]

TABLE A.2: Thermophysical literature data for latent heat storage materials

A.3 Thermochemical materials - TCM

#	Name	Class	T_{char} °C	T_{eq} °C	ρ kg m ⁻³	Δh_r MJ kg ⁻¹	$\Delta H_r/V$ GJ m ⁻³	Ref
1	Zeolite type 13X	Physisorption	180		739	0.54	0.40	[14]
2	Zeolite type LiX	Physisorption	180		711	0.81	0.58	[14]
3	Microporous SG-127B	Physisorption	90		710	0.13	0.09	[14]
4	Macroporous SG-LE32	Physisorption	90		620	0.09	0.05	[14]
5	Aluminosilicate/30% CaCl ₂	Composite	180		972	0.64	0.62	[14]
6	Mesoporous SG/33.7% CaCl ₂	Composite	90		646	0.48	0.31	[14]
7	Zeolite 13X / 15 wt.% MgSO ₄	Composite	150		922	0.65	0.60	[14]
8	MgSO ₄ · 7 H ₂ O	Hydrate	150		1330	2.50	3.32	[14]
9	Na ₂ S · 5 H ₂ O	Hydrate	83		928	3.84	3.56	[14]
10	MgCl ₂ · 6 H ₂ O	Hydrate	130		1165	1.72	2.00	[14]
11	CaCl _{2sol} + H ₂ O	Absorption	44.8		469	0.91	0.43	[14]
12	LiCl _{sol} + H ₂ O	Absorption	65.6		328	4.39	1.44	[14]
13	MgH ₂	Hydride		280	1450	2.81	4.07	[103]
14	CaH ₂	Hydride		950	1700	4.28	7.28	[103]
15	Ca(OH) ₂	Hydroxide		479	2240	1.47	3.30	[103]
16	Mg(OH) ₂	Hydroxide		258	2340	1.39	3.26	[103]
17	CaCO ₃	Carbonate		896	2710	1.67	2.49	[103]
18	PbCO ₃	Carbonate	450		6600	0.33	2.17	[19]
19	NH ₄ HSO ₄	Ammonia	927		1062	2.92	3.10	[19]
20	2 C ₃ O ₄	Redox		885	1229	0.86	1.06	[19]

TABLE A.3: T_{ch} correspond to the charging temperatur of the refered used reactor system, T_{eq} the equilibrium temperature of the reaction at $p = 101.325$ kPa. Candidates 11 and 12 were charged in a closed system at a charging pressure of $p = 4.2$ kPa.

List of Figures

2.1	Temperature difference ΔT and stored heat difference ΔQ of two materials with different specific heat capacities c_p	4
2.2	Comparison of the specific heat capacity c_p and energy density Q/V for a temperature difference of $\Delta T = 1$ °C versus thermal conductivity λ of different sensible heat storage candidates from [5] and [4]	6
2.3	Temperature ΔT versus stored heat ΔQ characteristics before, during and after a phase change region	8
2.4	Phase change enthalpy Δh_t related to mass and volume $\Delta H V^{-1}$ versus T_t of different PCM classes	11
2.5	Simplified representation of a physical adsorption process. As shown in [14], the adsorptiv (water vapor) is adsorbed by a solid substrate surface and builds the adsorbate. Heat is released (exotherm) during the adsorption process while heat is consumed (endotherm) during desorption, which is the reverse process	13
2.6	TCM classification based on [14, 21, 19]	16
2.7	Comparison of the reaction enthalpy related to mass Δh_r and related to volume $\Delta H_r V^{-1}$ versus the charging or equilibrium temperature T over several TCM classes. Associated data can be found in table A.3 in Appendix A on page 132.	18
3.1	Activation energy of a forth and back reaction	24
3.2	Morse potential (solid) and harmonic oscillator (dashed)	25
3.3	Schematics of a heat flow DSC with a disk type sensor - heat flow paths . . .	25
3.4	Furnace temperature T_F , reference temperature T_R and sample temperature T_S of a heat flow DSC versus time of a sample material with a first-order phase transition	26
3.5	U_{DSC} versus T during a transition with the characteristic temperatures	27
3.6	DSC signals for ϕ_R and ϕ_0 to evaluate the calibration factor $K(T)$ for $c_p(T)$ measurements according [36]	29
3.7	Schematics of a TGA with a thermocouple at the sample bottom	31
3.8	Characteristic temperatures and mass change evaluation based on the standard DIN 51006 [40]	33
3.9	Principle of a LFA for thermal diffusivity measurements	34
3.10	Heat pulse, theoretical adiabatic trend and IR experimental detector response of the sample back side temperature of a LFA experiment	35
3.11	Equivalent circuit diagram and THB foil sensor	37

3.12	THB sensor calibration setup with PMMA	38
3.13	Sketch of a possible THB signal $U(t)$ and its first derivative	39
3.14	Sketch of a HFM with a symmetrical arrangement and one slab sample	40
3.15	Sketch of a horizontal push rod dilatometer	42
4.1	Extrapolated initial transition temperatures $T_{e,i}$ of adamantane ($C_{10}H_{16}$), indium, tin, bismuth and zinc at $\beta = 2 \text{ K min}^{-1}$, 5 K min^{-1} and 10 K min^{-1}	48
4.2	Evaluated sensitivity $S_{DSC}(T_t)$ of the DSC sensor based on adamantane ($C_{10}H_{16}$), indium, tin, bismuth and zinc transitions at $\beta = 2 \text{ K min}^{-1}$, 5 K min^{-1} and 10 K min^{-1}	49
4.3	Evaluated sensitivity $S_{DSC}(T)$ of the DSC sensor based on standard reference $\alpha\text{-Al}_2\text{O}_3$ sapphire measurements at $\beta = 2 \text{ K min}^{-1}$, 5 K min^{-1} and 10 K min^{-1}	50
4.4	Comparison of the sensitivity $S_{DSC}(T)$ based on heat and heat flow calibrations under the same experimental conditions	51
4.5	Heating rate test on an organic PCM <i>Rubitherm RT70HC</i>	52
4.6	Data representation of the enthalpy change Δh of a paraffin wax PCM from a DSC measurement according [63]	53
4.7	Evaluated $c_p^{app}(T)$ of <i>Rubitherm RT70HC</i> with $\beta = 0.25 \text{ K min}^{-1}$ and 10 K min^{-1}	56
4.8	Detailed view of $c_p^{app}(T)$ before and after the melting process of <i>Rubitherm RT70HC</i> with $\beta = 0.25 \text{ K min}^{-1}$ and 10 K min^{-1}	57
4.9	left: Solid sample in cylindrical shape and graphite coated; middle: Aluminum container for liquids with sample and lid, assembled with graphite coated bottom; right: PEEK ring with sample inside and steel support outside, assembled with two steel plates on the upper and lower side of the PEEK ring with graphite coating	59
4.10	Thermal diffusivity $a(T)$ of an organic PCM <i>Rubitherm RT70HC</i> in solid and liquid phase	61
4.11	left: Preparation of two sample blocks and placed foil sensor between the blocks with a defined contact pressure; right: Melting of the PCM in the lab furnace and placed metal frame foil sensor in the PCM liquid	62
4.12	Thermal conductivity $\lambda(T)$ of an organic PCM <i>Rubitherm RT70HC</i> in solid and liquid phase based on THB measurements	64
4.13	Thermal conductivity $\lambda(T)$ of <i>Rubitherm RT70HC</i> based on LFA, DSC and THB measurements	65
4.14	FEM 2-D model of the LFA experiment with the steel/PEEK containment	66
4.15	Thermal diffusivity of water measured with the steel/PEEK containment in the LFA experiment	69
4.16	Qualitative FEM analysis result of the time and spatial dependent temperature field inside the water sample and the steel/PEEK containment	70
4.17	FEM analysis result of the modeled detector node temperature due to the radiation exchange between center, middle and edge of the upper cover steel plate	71

5.1	STA system <i>NETZSCH STA 449 F1</i> with exchangeable steel and rhodium furnace	75
5.2	Natural clinoptilolite with a particle size between 0.2 and 5 mm	77
5.3	Furnace temperature program $T_F(t)$ and water vapor pressure p_{H_2O} during the clinoptilolite and salt-based composites STA measurements	78
5.4	Clinoptilolite mass change $\Delta m/m_i$ and specific heat flow rate ϕ/m_i at a water vapor pressure $p_{H_2O} = 12.5$ mbar from STA measurements	79
5.5	$\Delta m/m_i$ and Δh between $T = 35$ and 200 °C of clinoptilolite and salt-based composites	79
5.6	Molecular sieve <i>Köstrolith 4A</i> from the company <i>Chemiewerk Bad Köstritz</i> in Germany	80
5.7	Furnace temperature program $T_F(t)$ and water vapor pressure p_{H_2O} during the zeolite 4A STA measurements	81
5.8	Zeolite 4A water uptake and enthalpy change results from STA measurements	82
5.9	Zeolite 4A $\Delta m(t)/m_i$ and $\phi(t)$ at $T = 34$ °C and different water vapor pressures $p_{H_2O} = 6$ mbar, 12 mbar and 24 mbar	83
5.10	B_2O_3 sample in aluminum crucible and cold welded pierced crucible on a STA type S sensor	85
5.11	$CaC_2O_4 \cdot H_2O$ powder material and pressed cylindrical shaped $CaC_2O_4 \cdot H_2O$ DSC sample in aluminum crucible	86
5.12	Time-dependent temperature and heating rate progress for $c_p(T)$ measurements in the heat flow DSC	87
5.13	Plot of DSC raw data files as input for the $c_p(T)$ and uncertainty calculation for $CaC_2O_4 \cdot H_2O$	88
5.14	$c_p(T)$ of the reference sapphire NBS SRM 720 and the applied polynomial model	89
5.15	Plot of the apparent specific heat $c_p^{app}(T)$ and the corresponding uncertainty u_c for $CaC_2O_4 \cdot H_2O$	90
5.16	Light flash analysis system <i>NETZSCH LFA 467 HyperFlash</i>	90
5.17	Carver lab press with a cylinder tool kit for 12.7 mm samples and compacted H_3BO_3 samples	91
5.18	THB sensor calibration with water and immersed into the powdery sample inside the lab furnace	95
5.19	STA result at $\beta = 20$ K min ⁻¹ for $CaC_2O_4 \cdot H_2O$ using two different sample masses	97
5.20	STA result of $CaC_2O_4 \cdot H_2O$ using three different heating rates $\beta = 20$ K min ⁻¹ , 10 K min ⁻¹ and 5 K min ⁻¹	98
5.21	$c_p^{app}(T)$ of $CaC_2O_4 \cdot H_2O$ and CaC_2O_4	99
5.22	λ_{eff} and a_{eff} of $CaC_2O_4 \cdot H_2O$ and CaC_2O_4	100
5.23	STA result for H_3BO_3 using three different heating rates $\beta = 10$ K min ⁻¹ , 5 K min ⁻¹ and 2.5 K min ⁻¹	102
5.24	STA result for B_2O_3 using two subsequent heating cycles	103
5.25	$c_p^{app}(T)$ of H_3BO_3 and B_2O_3	104

5.26	λ_{eff} and a_{eff} of H_3BO_3 and B_2O_3	105
5.27	STA results for $Ca(OH)_2$ and CaO using three different heating rates $\beta = 10\text{ K min}^{-1}$, 5 K min^{-1} and 2.5 K min^{-1}	107
5.28	$c_p^{app}(T)$ of $Ca(OH)_2$ and CaO	109
5.29	λ_{eff} and a_{eff} of $Ca(OH)_2$ and CaO	110
5.30	STA results for $Mg(OH)_2$ using three different heating rates $\beta = 10, 5$ and 2.5 K min^{-1}	112
5.31	$c_p^{app}(T)$ of $Mg(OH)_2$ and MgO	114
5.32	λ_{eff} and a_{eff} of $Mg(OH)_2$	115
5.33	YSZ powder with $d = 50\text{ }\mu\text{m}$, $100\text{ }\mu\text{m}$ and $200\text{ }\mu\text{m}$ and as solid cylinder with $d = 12.7\text{ mm}$ and $l = 10\text{ mm}$	116
5.34	$c_p(T)$ of YSZ and literature values for ZrO_2 from [98]	117
5.35	Density and volume change of YSZ between $T = 0$ to $300\text{ }^\circ\text{C}$; $\rho_0 = 5.923\text{ g cm}^{-3}$, $\sigma_\rho = 0.033\text{ g cm}^{-3}$	118
5.36	Thermal diffusivity $a(T)$ and conductivity $\lambda(T)$ of the solid YSZ	119
5.37	Sample holder system for LFA powder measurements	120
5.38	$a_{eff}(T)$ results for YSZ with particle diameters of $d = 50\text{ }\mu\text{m}$, $100\text{ }\mu\text{m}$ and $200\text{ }\mu\text{m}$ under ambient, low pressure and helium gas conditions	121
5.39	Bulk density ρ_B evaluation for YSZ particles with $d = 50\text{ }\mu\text{m}$, $100\text{ }\mu\text{m}$ and $200\text{ }\mu\text{m}$ for THB measurements	122
5.40	left: EPS sample holder frame with aluminum foil; middle: sample holder frame filled with YSZ powder, right: sample and sample holder inside the used HFM device	123
5.41	Comparison of the measured λ_{eff} and ρ_B at room temperature based on LFA, THB and HFM measurements for YSZ with $d = 50\text{ }\mu\text{m}$, $100\text{ }\mu\text{m}$ and $200\text{ }\mu\text{m}$. .	124

List of Tables

4.1	Material properties T_t , Δh_t and λ of the applied DSC calibration references . . .	49
4.2	Measured characteristic temperatures and transition enthalpies for <i>Rubitherm RT70HC</i> with $\beta = 0.25 \text{ K min}^{-1}$ and 10 K min^{-1}	58
4.3	Evaluated c_p^{app} at $T = 60 \text{ }^\circ\text{C}$ for <i>RT70HC</i> with 0.25 K min^{-1} and 10 K min^{-1} . . .	58
4.4	PCM sample dimensions for the LFA experiments	60
4.5	Thermophysical data of X15CrNiSi25-20 according [76]	68
4.6	Thermophysical data of PEEK supplied by the containment manufacturer . . .	68
4.7	Thermophysical data of water according [3]	68
4.8	Thermal diffusivity $a(T)$ according to [41] of the three layer containment (steel plate / water sample / steel plate) from FEM simulations and measured via LFA experiment	71
5.1	Comparison between the <i>STA 449 F1</i> and <i>STA 449 F5</i> STA systems used . . .	76
5.2	Mass fraction of the three different composite materials based on a clinoptilolite zeolite	76
5.3	Key technical specification for <i>NETZSCH LFA 467</i>	91
5.4	Measurement parameters <i>NETZSCH LFA 467</i>	93
5.5	Measured Ca(OH)_2 dehydration temperatures T and dehydration reaction enthalpies Δh_r for $\beta = 10 \text{ K min}^{-1}$, 5 K min^{-1} and 2 K min^{-1}	108
5.6	Measured Mg(OH)_2 dehydration temperatures T and dehydration reaction enthalpies Δh_r for $\beta = 10 \text{ K min}^{-1}$, 5 K min^{-1} and 2 K min^{-1}	113
5.7	THB results for λ_{eff} of YSZ packed beds with particle diameters of $d = 50 \text{ }\mu\text{m}$, $100 \text{ }\mu\text{m}$ and $200 \text{ }\mu\text{m}$	122
5.8	HFM results for λ_{eff} of YSZ packed beds with particle diameters of $d = 50 \text{ }\mu\text{m}$, $100 \text{ }\mu\text{m}$ and $200 \text{ }\mu\text{m}$	124
A.1	Thermophysical literature data for sensible heat storage materials	130
A.2	Thermophysical literature data for latent heat storage materials	131
A.3	T_{ch} correspond to the charging temperatur of the refered used reactor system, T_{eq} the equilibrium temperature of the reaction at $p = 101.325 \text{ kPa}$. Candidates 11 and 12 were charged in a closed system at a charging pressure of $p = 4.2 \text{ kPa}$	132

Bibliography

- [1] Antoni Gil et al. "State of the art on high temperature thermal energy storage for power generation. Part 1. Concepts, materials and modellization". In: *Renewable and Sustainable Energy Reviews* 14 (1 2010), pp. 31–55. ISSN: 13640321. DOI: 10.1016/j.rser.2009.07.035.
- [2] S. Kalaiselvam and R. Parameshwaran. *Thermal energy storage technologies for sustainability. Systems design, assessment, and applications*. 1st ed. London, U.K: Academic Press, 2014. 1 p. ISBN: 978-0-12-417291-3.
- [3] *CRC handbook of chemistry and physics. A ready-reference book of chemical and physical data*. 85. ed., 2005. Boca Raton, Fla.: CRC Press, 2005. ISBN: 978-1-4822-6096-0.
- [4] S. Khare et al. "Selection of materials for high temperature sensible energy storage". In: *Solar Energy Materials and Solar Cells* 115 (2013), pp. 114–122. ISSN: 09270248. DOI: 10.1016/j.solmat.2013.03.009.
- [5] A. I. Fernandez et al. "Selection of materials with potential in sensible thermal energy storage". In: *Solar Energy Materials and Solar Cells* 94 (10 2010), pp. 1723–1729. ISSN: 09270248. DOI: 10.1016/j.solmat.2010.05.035.
- [6] Harald Mehling and Luisa F. Cabeza. *Heat and cold storage with PCM. An up to date introduction into basics and applications : with 208 figures and 28 tables*. Heat and mass transfer. Heidelberg: Springer, 2008. ISBN: 978-3-642-08807-0.
- [7] Jan Košny. *PCM-enhanced building components. An application of phase change materials in building envelopes and internal structures*. Engineering materials and processes. Cham: Springer, 2015. ISBN: 978-3-319-14285-2.
- [8] Atul Sharma et al. "Review on thermal energy storage with phase change materials and applications". In: *Renewable and Sustainable Energy Reviews* 13 (2 2009), pp. 318–345. ISSN: 13640321. DOI: 10.1016/j.rser.2007.10.005.
- [9] Amir Gholaminejad and Reza Hosseini. "A Study of Water Supercooling". In: *Journal of Electronics Cooling and Thermal Control* 03 (01 2013), pp. 1–6. ISSN: 2162-6162. DOI: 10.4236/jectc.2013.31001.
- [10] P. W. Atkins and Julio de Paula. *Atkins Physical chemistry*. 8th ed. New York: W.H. Freeman, 2006. 1053 pp. ISBN: 0-7167-8759-8.
- [11] Pia Trawiel Gottfried Ehrenstein Gabriela Riedel. *Praxis der thermischen Analyse von Kunststoffen*. 2nd ed. Carl Hanser Verlag, 2003. ISBN: 3-446-22340-1.

- [12] Martin Bonnet. *Kunststoffe in der Ingenieur Anwendung. Verstehen und zuverlässig auswählen*. 1. Aufl. Wiesbaden: Vieweg+Teubner Verlag / GWV Fachverlage GmbH Wiesbaden, 2009. ISBN: 978-3-8348-0349-8.
- [13] Peter Haasen. *Physikalische Metallkunde*. Berlin u.a.: Springer, 1974. 379 S. ISBN: 3-540-06669-1.
- [14] N. Yu, R. Z. Wang, and L. W. Wang. "Sorption thermal storage for solar energy". In: *Progress in Energy and Combustion Science* 39 (5 2013), pp. 489–514. ISSN: 03601285. DOI: 10.1016/j.pecs.2013.05.004.
- [15] Parfait Tatsidjoudoug, Nolwenn Le Pierrès, and Lingai Luo. "A review of potential materials for thermal energy storage in building applications". In: *Renewable and Sustainable Energy Reviews* 18 (2013), pp. 327–349. ISSN: 13640321. DOI: 10.1016/j.rser.2012.10.025.
- [16] Kokouvi Edem N'Tsoukpoe, Nolwenn Le Pierrès, and Lingai Luo. "Experimentation of a LiBr-H₂O absorption process for long term solar thermal storage". In: *Energy Procedia* 30 (2012), pp. 331–341. ISSN: 18766102. DOI: 10.1016/j.egypro.2012.11.039.
- [17] F. Schaubé et al. "A thermodynamic and kinetic study of the de- and rehydration of Ca(OH)₂ at high H₂O partial pressures for thermo-chemical heat storage". In: *Thermochimica Acta* 538 (2012), pp. 9–20. ISSN: 00406031. DOI: 10.1016/j.tca.2012.03.003.
- [18] K. Posern and Ch. Kaps. "Calorimetric studies of thermochemical heat storage materials based on mixtures of MgSO₄ and MgCl₂". In: *Thermochimica Acta* 502 (1-2 2010), pp. 73–76. ISSN: 00406031. DOI: 10.1016/j.tca.2010.02.009.
- [19] P. Pardo et al. "A review on high temperature thermochemical heat energy storage". In: *Renewable and Sustainable Energy Reviews* 32 (2014), pp. 591–610. ISSN: 13640321. DOI: 10.1016/j.rser.2013.12.014.
- [20] Andreas Hauer and Fabian Fischer. "Open Adsorption System for an Energy Efficient Dishwasher". In: *Chemie Ingenieur Technik* 83 (1-2 2011), pp. 61–66. ISSN: 0009286X. DOI: 10.1002/cite.201000197.
- [21] Devrim Aydin, Sean P. Casey, and Saffa Riffat. "The latest advancements on thermochemical heat storage systems". In: *Renewable and Sustainable Energy Reviews* 41 (2015), pp. 356–367. ISSN: 13640321. DOI: 10.1016/j.rser.2014.08.054.
- [22] Ekbert Hering, Rolf Martin, and Martin Stohrer. *Physik für Ingenieure*. 6th ed. Berlin Heidelberg: Springer-Verlag, 1997. ISBN: 3-540-6244-2.
- [23] Helmut Vogel. *Gerthsen Physik*. 20th ed. Berlin Heidelberg: Springer-Verlag, 1995. ISBN: 3-540-65479-8.
- [24] Arno Behr, David W. Agar, and Jakob Jörissen. *Einführung in die Technische Chemie*. Heidelberg: Spektrum Akademischer Verlag, 2010. ISBN: 978-3-8274-2073-2. DOI: 10.1007/978-3-8274-2195-1.

- [25] Terry M. Tritt. *Thermal Conductivity. Theory, Properties, and Applications*. Physics of Solids and Liquids. Boston, MA: Kluwer Academic/Plenum Publishers New York, 2004. ISBN: 978-0-306-48327-1. DOI: 10.1007/b136496.
- [26] Rhena Wulf. "Wärmeleitfähigkeit von hitzebeständigen und feuerfesten Dämmstoffen. Untersuchungen zu Ursachen für unterschiedliche Messergebnisse bei Verwendung verschiedener Messverfahren". Fakultät für Maschinenbau. Dissertation. Freiberg: Technische Universität Bergakademie Freiberg, 2009. URL: <http://nbn-resolving.de/urn:nbn:de:bsz:105-9458830>.
- [27] Cho Yen Ho and Richard Erwin Taylor, eds. *Thermal expansion of solids*. Vol. 4. CINDAS data series on material properties Group 1, Theory, estimation, and measurement of properties. Materials Park, Ohio: ASM International, 1998. 293 pp. ISBN: 0-87170-623-7.
- [28] Robert F. Speyer. *Thermal analysis of materials*. Vol. 5. Materials engineering. New York: Dekker, 1994. 285 pp. ISBN: 0-8247-8963-6.
- [29] Philip M. Morse. "Diatomic Molecules According to the Wave Mechanics. II. Vibrational Levels". In: *Physical Review* 34 (1 1929), pp. 57–64. ISSN: 0031-899X. DOI: 10.1103/PhysRev.34.57.
- [30] G. W. H. Höhne, W. F. Hemminger, and H.-J. Flammersheim. *Differential Scanning Calorimetry*. 2nd revised and enlarged edition. Berlin and Heidelberg: Springer, 2003. 298 pp. ISBN: 978-3-662-06710-9. DOI: 10.1007/978-3-662-06710-9.
- [31] Stefan Mathias Sarge, Günther W. H. Höhne, and Wolfgang Hemminger. *Calorimetry. Fundamentals, instrumentation and applications*. Weinheim, Germany: Wiley-VCH Verlag, 2014. 300 pp. ISBN: 978-3-527-32761-4.
- [32] Burghart Brinkmann. *Internationales Wörterbuch der Metrologie. Grundlegende und allgemeine Begriffe und zugeordnete Benennungen (VIM) Deutsch-Englische Fassung ISO/IEC-Leitfaden 99:2007*. 4. Aufl. Beuth Wissen. s.l.: Beuth Verlag GmbH, 2012. 120 pp. ISBN: 978-3-410-22472-3.
- [33] DIN Deutsches Institut für Normung e. V., ed. *Plastics – Differential scanning calorimetry (DSC) – Part 1: General principles (ISO 11357-1:2016)*. Berlin: Beuth Verlag, Feb. 1, 2017.
- [34] *Die internationale Temperaturskala von 1990. (ITS-90)*. Vol. 87. Vorträge des PTB-Seminars. Braunschweig: Physikal.-Techn. Bundesanst, 1989. 204 pp. ISBN: 3-89429-040-4.
- [35] DIN Deutsches Institut für Normung e. V., ed. *Plastics – Differential scanning calorimetry (DSC) – Part 4: Determination of specific heat capacity*. Berlin: Beuth Verlag, Oct. 1, 2014.
- [36] DIN 51007. *Thermal Analysis, Differential Thermal Analysis, Principles*. Beuth Verlag GmbH, 1994.
- [37] Wolfgang F. Hemminger and Heiko Karl Cammenga. *Methoden der thermischen Analyse*. Vol. 24. Anleitungen für die chemische Laboratoriumspraxis. Berlin: Springer, 1989. 299 pp. ISBN: 3-540-15049-8.

- [38] Joseph D. Menczel and R. Bruce Prime, eds. *Thermal analysis of polymers*. Hoboken, N.J.: John Wiley, 2009. 688 pp. ISBN: 978-0-471-76917-0.
- [39] M. P. Sepe. *Thermal analysis of polymers*. Vol. v. 8, no. 11. Rapra review reports. Shawbury, Shrewsbury, Shropshire, UK: Rapra Technology Ltd, 1997], ©1995. 120 pp. ISBN: 978-1859571071.
- [40] DIN 51006, ed. *Thermal analysis (TA) - Thermogravimetry (TG) - Principles*. Berlin: Beuth Verlag, July 1, 2005.
- [41] W. J. Parker et al. "Flash Method of Determining Thermal Diffusivity, Heat Capacity, and Thermal Conductivity". In: *Journal of applied physics* 32 (9 1961), pp. 1679–1684. DOI: 10.1063/1.1728417.
- [42] DIN Deutsches Institut für Normung e. V., ed. *Plastics - Determination of thermal conductivity and thermal diffusivity – Part 4: Laser flash method*. Berlin: Beuth Verlag GmbH, Oct. 1, 2016.
- [43] Ralph B. Dinwiddie, ed. *Thermal conductivity 26. Thermal expansion 14 ; joint conferences, August 6 - 8, 2001, Cambridge, Massachusetts, USA ; [proceedings of the Twenty-Sixth International Thermal Conductivity Conference ; proceedings of the Fourteenth International Thermal Expansion Symposium]*. Lancaster: DEStech Publications, 2005. 581 pp. ISBN: 1-932078-36-3.
- [44] Robert D. Cowan. "Pulse Method of Measuring Thermal Diffusivity at High Temperatures". In: *Journal of applied physics* 34 (4 1963), pp. 926–927. DOI: 10.1063/1.1729564.
- [45] L. M. Clark III and R. E. Taylor. "Radiation loss in the flash method for thermal diffusivity". In: *Journal of Applied Physics* 46 (2 1975), pp. 714–719. ISSN: 0021-8979. DOI: 10.1063/1.321635.
- [46] J. A. Cape and G. W. Lehman. "Temperature and Finite Pulse–Time Effects in the Flash Method for Measuring Thermal Diffusivity". In: *Journal of Applied Physics* 34 (7 1963), pp. 1909–1913. ISSN: 0021-8979. DOI: 10.1063/1.1729711.
- [47] Tadahiko Azumi and Yoichi Takahashi. "Novel finite pulse–width correction in flash thermal diffusivity measurement". In: *Review of Scientific Instruments* 52 (9 1981), pp. 1411–1413. ISSN: 0034-6748. DOI: 10.1063/1.1136793.
- [48] H. Mehling et al. "Thermal Diffusivity of Semitransparent Materials Determined by the Laser-Flash Method Applying a New Analytical Model". In: *International Journal of Thermophysics* 19 (3 1998), pp. 941–949. ISSN: 0195928X.
- [49] K. Shinzato and T. Baba. "A Laser Flash Apparatus for Thermal Diffusivity and Specific Heat Capacity Measurements". In: *Journal of Thermal Analysis and Calorimetry* 64 (1 2001), pp. 413–422. ISSN: 14182874. DOI: 10.1023/A:1011594609521.

- [50] U. Hammerschmidt and V. Meier. "New Transient Hot-Bridge Sensor to Measure Thermal Conductivity, Thermal Diffusivity, and Volumetric Specific Heat". In: *International Journal of Thermophysics* 27 (3 2006), pp. 840–865. ISSN: 0195-928X. DOI: 10.1007/s10765-006-0061-2.
- [51] S. E. Gustafsson, E. Karawacki, and M. N. Khan. "Transient hot-strip method for simultaneously measuring thermal conductivity and thermal diffusivity of solids and fluids". In: *Journal of Physics D: Applied Physics* 12 (9 1979), pp. 1411–1421. ISSN: 0022-3727. DOI: 10.1088/0022-3727/12/9/003.
- [52] S. Rudtsch and U. Hammerschmidt. "Intercomparison of Measurements of the Thermophysical Properties of Polymethyl Methacrylate". In: *International Journal of Thermophysics* 25 (5 2004), pp. 1475–1482. ISSN: 0195928X. DOI: 10.1007/s10765-004-5752-y.
- [53] M. J. Assael et al. "Thermal Conductivity of Polymethyl Methacrylate (PMMA) and Borosilicate Crown Glass BK7". In: *International Journal of Thermophysics* 26 (5 2005), pp. 1595–1605. ISSN: 0195-928X. DOI: 10.1007/s10765-005-8106-5.
- [54] DIN Deutsches Institut für Normung e.V., ed. *Thermal performance of building materials and products – Determination of thermal resistance by means of guarded hot plate and heat flow meter methods – Dry and moist products of medium and low thermal resistance*. Berlin: Beuth Verlag GmbH.
- [55] DIN Deutsches Institut für Normung e.V., ed. *Thermal performance of building materials and products – Determination of thermal resistance by means of guarded hot plate and heat flow meter methods – Products of high and medium thermal resistance*. Berlin: Beuth Verlag GmbH.
- [56] DIN Deutsches Institut für Normung e.V., ed. *Thermal performance of building materials and products - Determination of thermal resistance by means of guarded hot plate and heat flow meter methods - Thick products of high and medium thermal resistance*. Berlin: Beuth Verlag GmbH.
- [57] Tiina Ruuska, Juha Vinha, and Henna Kivioja. "Measuring thermal conductivity and specific heat capacity values of inhomogeneous materials with a heat flow meter apparatus". In: *Journal of Building Engineering* 9 (2017), pp. 135–141. ISSN: 23527102. DOI: 10.1016/j.jobe.2016.11.011.
- [58] E. Kozeschnik and E. Gamsjäger. "High-speed quenching dilatometer investigation of the austenite-to-ferrite transformation in a low to ultralow carbon steel". In: *Metallurgical and Materials Transactions A* 37 (6 2006), pp. 1791–1797. ISSN: 1073-5623. DOI: 10.1007/s11661-006-0121-z.
- [59] Y.C Liu, F. Sommer, and E.J Mittemeijer. "Calibration of the differential dilatometric measurement signal upon heating and cooling; thermal expansion of pure iron". In: *Thermochimica Acta* 413 (1-2 2004), pp. 215–225. ISSN: 00406031. DOI: 10.1016/j.tca.2003.10.005.

- [60] DIN Deutsches Institut für Normung e.V., ed. *Determination of the thermal expansion of solids- Part 1: Basic rules*. DIN 51045-1. Berlin: Beuth Verlag GmbH.
- [61] DIN Deutsches Institut für Normung e. V., ed. *Thermocouples - Part 1: EMF specifications and tolerances*. Berlin: Beuth Verlag GmbH.
- [62] *Tagungsband: Die 21. Kalorimetrietage. Braunschweig, 27. - 29. Mai 2015*. In collab. with D. Klaus. Kalorimetrietage. Physikalisch-Technische Bundesanstalt, 2015. 116 Seiten. ISBN: 978-3-944659-02-2.
- [63] S. Gschwander, Th. Haussmann, G. Hagelstein, A. Sole, L. F. Cabeza, G. Diarce, W. Hohenauer, D. Lager, A. Ristic, Ch. Rathgeber, P. Hennemann, H. Mehling, C. Peñalosa, Ana Lazaro. *Standardization of PCM Characterization via DSC. A technical report of subtask A2.1 of IEA-SHC 42 / ECES Annex 29*. Ed. by IEA SHC Task 42 / ECES Annex 29. January 2015. URL: <http://task42.iea-shc.org/publications>.
- [64] Daniel Lager. "Thermal analysis on organic phase change materials for heat storage applications". In: (), p. 030001. DOI: 10.1063/1.4955229.
- [65] Christoph Zauner et al. "Experimental characterization and simulation of a fin-tube latent heat storage using high density polyethylene as PCM". In: *Applied Energy* 179 (2016), pp. 237–246. ISSN: 03062619. DOI: 10.1016/j.apenergy.2016.06.138.
- [66] Tilman Barz et al. "Experimental Analysis and Numerical Modeling of a Shell and Tube Heat Storage Unit with Phase Change Materials". In: *Industrial & Engineering Chemistry Research* 55 (29 2016), pp. 8154–8164. ISSN: 0888-5885. DOI: 10.1021/acs.iecr.6b01080.
- [67] Yago Magan Montoto et al. "Sugar Alcohols and Synthetic Derivatives as Phase Change Materials". In: (), pp. 155–164. DOI: 10.18690/978-961-286-052-3.16.
- [68] Ala B. Bazyleva et al. "Thermodynamic properties of adamantane revisited". In: *The journal of physical chemistry. B* 115 (33 2011), pp. 10064–10072. ISSN: 1520-5207. DOI: 10.1021/jp204792b.
- [69] VDI. *VDI Heat Atlas*. 2nd ed. Springer Verlag GmbH, 2010. ISBN: 978-3-540-77876-9.
- [70] Yerman S. Touloukian, ed. *Thermal conductivity. Metallic elements and alloys*. Vol. 1. Thermophysical properties of matter. New York u.a.: IFI/Plenum, 1970. Getr. Zählung. ISBN: 306-67021-6.
- [71] Eugene S. Domalski and Elizabeth D. Hearing. "Heat Capacities and Entropies of Organic Compounds in the Condensed Phase. Volume III". In: *Journal of Physical and Chemical Reference Data* 25 (1 1996), pp. 1–525. ISSN: 0047-2689. DOI: 10.1063/1.555985.
- [72] Joint Committee for Guides in Metrology, ed. *Evaluation of measurement data - Guide to the expression of uncertainty in measurement*. Version Corrected version 2010. URL: www.bipm.org/utils/common/documents/jcgm/JCGM_100_2008_E.pdf.

- [73] D. Maillet, C. Moyne, and Rémy B. "Effect of a thin layer on the measurement of the thermal diffusivity of a material by a flash method". In: *International Journal of Heat and Mass Transfer* 43 (2000), pp. 4057–4060.
- [74] T. Y. R. Lee, A. B. Donaldson, and R. E. Taylor. "Thermal Diffusivity of Layered Composites". In: (), pp. 135–148. DOI: 10.1007/978-1-4615-9083-5_17.
- [75] Clemens Groth and Günter Müller. *FEM für Praktiker*. 5., neu bearb. Aufl. Vol. 45. Edition expertsoft. Renningen: Expert-Verl., 2009. 439 pp. ISBN: 978-3816927143.
- [76] Friedhelm Richter. *Physikalische Eigenschaften von Stählen und ihre Temperaturabhängigkeit. Polynome und graphische Darstellungen; Mitteilung aus dem Forschungsinstitut der Mannesmann AG*. Vol. 10. Stahleisen-Sonderberichte. Düsseldorf: Verl. Stahleisen, 1983. 28 pp. ISBN: 9783514002944.
- [77] Jürgen Blumm and André Lindemann. "Characterization of the thermophysical properties of molten polymers and liquids using the flash technique". In: *High Temperatures-High Pressures* 35/36 (6 2003), pp. 627–632. ISSN: 0018-1544. DOI: 10.1068/htjr144.
- [78] Gerald Englmaier, Bernhard Zettl, and Daniel Lager. "Characterisation of a Rotating Adsorber Designed for Thermochemical Heat Storage Processes". In: *Conference proceedings / EuroSun 2014, International Conference on Solar Energy and Buildings, Aix-les-Bains, France, 16 - 19 September*. Ed. by Elimar Frank and Philippe Papillion. Freiburg: International Solar Energy Society, 2015, pp. 1–8. ISBN: 978-3-9814659-3-8.
- [79] Daniel Lager. *TG/DSC Untersuchungen an neuen Materialien für Sorptionswärmespeicher*. In collab. with Arbeitskreis Thermophysik. Aachen: IWM-RWTH, Mar. 9, 2015. URL: <http://www.ak-thermophysik.de/gefta/gefta2015.html>.
- [80] Daniel Lager. *Thermophysical analysis of sorption materials for thermal energy storage*. In collab. with Sorption Friends. Sicily, Italy, Sept. 14, 2015. URL: <http://www.sorptionfriends.org/>.
- [81] Ch. Reichl et al. "Fluid dynamics simulations for an open-sorption heat storage drum reactor based on thermophysical kinetics and experimental observations". In: *Applied Thermal Engineering* 107 (2016), pp. 994–1007. ISSN: 13594311. DOI: 10.1016/j.applthermaleng.2016.06.119.
- [82] Markus Deutsch et al. "High-Temperature Energy Storage. Kinetic Investigations of the CuO/Cu₂O Reaction Cycle". In: *Energy & Fuels* 31 (3 2017), pp. 2324–2334. ISSN: 0887-0624. DOI: 10.1021/acs.energyfuels.6b02343.
- [83] Daniel Lager. *Experimental approaches to analyse thermophysical properties of thermochemical heat storage materials*. Selb: Arbeitskreis Thermophysik, Apr. 3, 2017. URL: <http://www.ak-thermophysik.de/gefta/gefta\2017.html>.
- [84] Daniel Lager. *Thermal conductivity measurements of calcium oxalate monohydrate as thermochemical heat storage material*. Logan, Utah, USA: Utah State University, May 16, 2017.

- [85] Daniel Lager. *Specific heat capacity determination of metal hydroxides for thermochemical energy storage*. In collab. with Journal of Thermal Analysis and Calorimetry. Budapest, Hungary, June 9, 2017. URL: <https://jtac-jtacc.akcongress.com/>.
- [86] Daniel Lager. "Effective thermal conductivity measurements of packed beds for thermochemical energy storage". In: *ECTP 21st - European Conference on Thermophysical Properties. September 3-8, 2017, Graz University of Technology, Graz, Austria : book of abstracts & program*. Ed. by Gernot Pottlacher. Graz: Verlag der Technischen Universität Graz, 2017, pp. 168–169. ISBN: 978-3-85125-546-1. URL: <https://ectp2017.tugraz.at/>.
- [87] W. Hohenauer and D. Lager. "Flash Techniques to Measure Thermal Diffusivity and Thermal Conductivity of Metal-Foam-Materials". In: *Thermal conductivity 30/thermal expansion 18. Joint conferences ; August 29 - September 2, 2009, Pittsburgh, Pennsylvania, USA ; [proceedings of the Thirtieth International Thermal Conductivity Conference (ITCC) and proceedings of the Eighteenth International Thermal Expansion Symposium (ITES)]*. Ed. by Daniela S. Gaal. Lancaster, Pa.: DEStech Publ, 2010, pp. 513–520. ISBN: 978-1-60595-015-0.
- [88] Bernhard Zettl, Gerald Englmaier, and Gerald Steinmaurer. "Development of a revolving drum reactor for open-sorption heat storage processes". In: *Applied Thermal Engineering* 70 (1 2014), pp. 42–49. ISSN: 13594311. DOI: 10.1016/j.applthermaleng.2014.04.069.
- [89] Bernhard Zettl, Gerald Englmaier, and Walter Somitsch. "An Open Sorption Heat Storage Concept and Materials for Building Heat Supply". In: *Energy Procedia* 73 (2015), pp. 297–304. ISSN: 18766102. DOI: 10.1016/j.egypro.2015.07.692.
- [90] U. R. Fischer. "WHAT IS THE BEST POSSIBLE HEAT STORAGE DENSITY FOR A SEASONAL ADSORPTIVE THERMAL ENERGY STORAGE". In: *Effstock 2009, Thermal Energy Storage for Efficiency and Sustainability. 11th International Conference on Thermal Energy Storage, June 14-17, 2009, Stockholm, Sweden : abstract book & proceedings*. Ed. by Signhild Gehlin. [Stockholm]: [Energi- och Miljötekniska Föreningen / EMTF Förlag], 2009. ISBN: 9789197627139. URL: http://intraweb.stockton.edu/eyos/energy_studies/content/docs/effstock09/Posters/163.pdf.
- [91] Shigetaka Wada. "Thermal Conductivity of Al₂O₃ Ceramics: The Inconsistency between Measured Value and Calculated Value based on Analytical Models for a Composite". In: *The Journal of Scientific Research Chulalongkorn University* 30 (1 2005). URL: www.thaiscience.info/journals/Article/CJSR/10324250.pdf.
- [92] DIN EN ISO 11357-4. *Plastics – Differential scanning calorimetry (DSC) – Part 4: Determination of specific heat capacity (ISO 11357-4:2014)*; Beuth Verlag GmbH, 2014.
- [93] H. Chang ; Pj. Huang. "Thermal Decomposition of CaC₂O₄ · H₂O Studied by Thermo-Raman Spectroscopy with TGA/DTA". In: *Analytical Chemistry* 69 (Apr. 1997). URL: <http://dx.doi.org/10.1021/ac9608811>.

- [94] Benjamin Carroll Eli S. Freeman. "The Application of Thermoanalytical Techniques to Reaction Kinetics: The Thermogravimetric Evaluation of the Kinetics of the Decomposition of Calcium Oxalate Monohydrate". In: *The Journal of Physical Chemistry* 62 (Apr. 1958), pp. 394–397. URL: <http://dx.doi.org/10.1021/j150562a003>.
- [95] Gert Wolf Galina Sádovská. "Enthalpy of dissolution and thermal dehydration of calcium oxalate hydrates". In: *Journal of Thermal Analysis and Calorimetry* 119 (Mar. 2015), pp. 2063–2068. URL: <http://dx.doi.org/10.1007/s10973-014-4350-x>.
- [96] Wendell M. Latimer, Philip W. Schutz, and J. F. G. Hicks. "The Heat Capacity and Entropy of Calcium Oxalate from 19 to 300 Absolute. The Entropy and Free Energy of Oxalate Ion". In: *Journal of the American Chemical Society* 55 (3 1933), pp. 971–975. ISSN: 0002-7863. DOI: 10.1021/ja01330a015.
- [97] Fatih Sevim et al. "Kinetic analysis of thermal decomposition of boric acid from thermogravimetric data". In: *Korean Journal of Chemical Engineering* 23 (5 2006), pp. 736–740. ISSN: 0256-1115. DOI: 10.1007/BF02705920.
- [98] Malcolm W. Chase. *NIST-JANAF thermochemical tables*. 4. ed. Woodbury, NY: American Institute of Physics, 1998. ISBN: 1-56396-831-2.
- [99] Herrick L. Johnston and Eugene C. Kerr. "Low Temperature Heat Capacities of Inorganic Solids. 1 I. The Heat Capacity of Boric Acid from 16 to 296K. Description of The Ohio State University Solid Calorimeters". In: *Journal of the American Chemical Society* 72 (10 1950), pp. 4733–4738. ISSN: 0002-7863. DOI: 10.1021/ja01166a107.
- [100] Jun Kariya, Junichi Ryu, and Yukitaka Kato. "Development of thermal storage material using vermiculite and calcium hydroxide". In: *Applied Thermal Engineering* 94 (2016), pp. 186–192. ISSN: 13594311. DOI: 10.1016/j.applthermaleng.2015.10.090.
- [101] P. Pardo et al. "Ca(OH)₂/CaO reversible reaction in a fluidized bed reactor for thermochemical heat storage". In: *Solar Energy* 107 (2014), pp. 605–616. ISSN: 0038092X. DOI: 10.1016/j.solener.2014.06.010.
- [102] Matthias Schmidt et al. "Experimental results of a 10 kW high temperature thermochemical storage reactor based on calcium hydroxide". In: *Applied Thermal Engineering* 62 (2 2014), pp. 553–559. ISSN: 13594311. DOI: 10.1016/j.applthermaleng.2013.09.020.
- [103] M. Felderhoff, R. Urbanczyk, and S. Peil. "Thermochemical Heat Storage for High Temperature Applications – A Review". In: *Green* 3 (2 2013). ISSN: 1869-8778. DOI: 10.1515/green-2013-0011.
- [104] Zhihao Pan and C. Y. Zhao. "Dehydration/hydration of MgO/H₂O chemical thermal storage system". In: *Energy* 82 (2015), pp. 611–618. ISSN: 03605442. DOI: 10.1016/j.energy.2015.01.070.

- [105] Stephan Parzinger. *Analytische Modellierung der temperatur- und gasdruckabhängigen effektiven Wärmeleitfähigkeit von Pulvern*. 1. Aufl. Energietechnik. München: Verl. Dr. Hut, 2014. XXVIII, 176 S. ISBN: 3843916861.
- [106] A. V. Gusarov and E. P. Kovalev. "Model of thermal conductivity in powder beds". In: *Physical Review B* 80 (2 2009). ISSN: 1098-0121. DOI: 10.1103/PhysRevB.80.024202.

Lebenslauf



ANGABEN ZUR PERSON

Name Dipl.-Ing. (FH) Daniel Lager, MSc
Adresse Schubertgasse 3, A-2491 Steinbrunn
Telefon +43 (0)650 343 62 73
E-Mail lager.daniel@gmail.com
Geburtsdatum 9. Mai 1981
Staatsangehörigkeit Österreich
Zivildienst abgeleistet
Familienstand verheiratet, zwei Kinder (09/2008, 08/2012)

ARBEITSERFAHRUNG

- Zeitraum Oktober 2013 – jetzt
• Arbeitgeber AIT Austrian Institute of Technology GmbH, Donau-City-Straße 1, A-1220 Wien
• Tätigkeitsbereich Center for Energy - Sustainable Thermal Energy Systems
• Funktion Research Engineer
• Wichtigste Tätigkeiten Leitung des Labors für thermische Analyse und Thermophysik, interne Projektleitung, Kundenbetreuung, Mitarbeit in nationalen und internationalen F&E Projekten
- Zeitraum Dezember 2012 – September 2013
• Arbeitgeber Aerospace & Advanced Composites GmbH, Viktor-Kaplan-Straße 2, A-2700 Wr. Neustadt
• Tätigkeitsbereich Material- und Komponentenprüfung
• Funktion Wissenschaftlicher Mitarbeiter - Senior Scientist
• Wichtigste Tätigkeiten Softwareentwicklung eines Steuerungs- und Auswertetools für Schadensdetektionssysteme
- Zeitraum Februar 2012 - November 2012
• Arbeitgeber NETZSCH-Gerätebau GmbH, Harterstraße 1, A-8053 Graz
• Tätigkeitsbereich Geschäftsbereich Analysieren & Prüfen
• Funktion Customer Service Engineer
• Wichtigste Tätigkeiten Internationales Service & Training der NETZSCH Gerätebau Produktpalette
- Zeitraum März 2011 - Jänner 2012
• Arbeitgeber Aerospace & Advanced Composites GmbH, A-2444 Seibersdorf
• Tätigkeitsbereich Material- und Komponentenprüfung
• Funktion Wissenschaftlicher Mitarbeiter - Senior Scientist
• Wichtigste Tätigkeiten Multiphysik Simulationen, Softwareentwicklung eines Steuerungs- und Auswertetools für Schadensdetektionssysteme, Systemadministration
- Zeitraum Oktober 2007 - Februar 2011
• Arbeitgeber AIT Austrian Institute of Technology GmbH, A-2444 Seibersdorf
• Tätigkeitsbereich Materialwissenschaften
• Funktion Wissenschaftlicher Mitarbeiter
• Wichtigste Tätigkeiten Thermische Analyse und thermophysikalische Messtechnik, Multiphysik Simulationen. Kundenbetreuung, Mitarbeit in nationalen und internationalen F&E Projekten
- Zeitraum März 2006 - September 2007
• Arbeitgeber Frequentis AG, Innovationsstraße 1, A-1120 Wien
• Tätigkeitsbereich Kommunikations- und Informationssysteme für sicherheitskritische Applikationen
• Funktion System Ingenieur für Forschungs- und Entwicklungsprojekte im Bereich öffentliche Sicherheit
• Wichtigste Tätigkeiten Requirementsengineering, Systemdesign, Systemintegration, Entwicklungskoordination, Software Configuration und Quality Management, Laborverantwortung

- Zeitraum
- Arbeitgeber
- Tätigkeitsbereich
- Funktion
- Wichtigste Tätigkeiten

Juli 2004 - Februar 2006
 AIT Austrian Institute of Technology GmbH, A-2444 Seibersdorf
 Informationstechnologien / Sichere Mobilkommunikation
 Wissenschaftlicher Mitarbeiter
 Forschungsstudien über die Wirkung elektromagnetischer Felder auf den menschlichen Körper

- Zeitraum
- Arbeitgeber
- Tätigkeitsbereich
- Funktion
- Wichtigste Tätigkeiten

Juli 2003 - August 2003
 Motorola GmbH, Jacquingasse 16-18, A-1030 Wien
 Telekommunikation
 Java Programmierer
 Entwicklung eines Java Programms zur Auswertung von GPRS Daten

- Zeitraum
- Arbeitgeber
- Tätigkeitsbereich
- Funktion
- Wichtigste Tätigkeiten

April 2002 - September 2002
 DIS AG, Floragasse 1, A-1040 Wien
 Informationstechnologien
 IT Trainer
 Trainer im Bereich Netzwerktechnik, HTML, Java Script, PHP und MySQL

- Zeitraum
- Arbeitgeber
- Tätigkeitsbereich
- Funktion
- Wichtigste Tätigkeiten

Oktober 2001 - März 2002
 Create-Mediadesign GmbH, Margaretenstraße 22/3, A-1040 Wien
 Multimedia
 Programmierer
 Programmierung und Design von Web- und CD/DVD Applikationen

- Zeitraum
- Arbeitgeber
- Tätigkeitsbereich
- Funktion
- Wichtigste Tätigkeiten

Oktober 2000 - September 2001
 Arbeiter-Samariter-Bund Österreichs, Hollergasse 2-6, A-1150 Wien
 Rettungswesen
 Zivildienstler
 EDV Support und Netzwerkadministration

SCHUL- UND BERUFSBILDUNG

- Zeitraum
- Ausbildungseinrichtung
- Spezialisierung
- Bezeichnung der Qualifikation

März 2015 – jetzt
 TU Wien, Institut für Energietechnik und Thermodynamik, Getreidemarkt 9/BA, A-1060 Wien
 Thermophysikalische Eigenschaften von neuen Phasenwechsel- und Thermochemischen Materialien für Wärmespeicheranwendungen
 Doktor der technischen Wissenschaften, Dr. techn.

- Zeitraum
- Ausbildungseinrichtung
- Spezialisierung
- Bezeichnung der Qualifikation
- Master Prüfung

September 2006 - Juni 2008
 Fachhochschule Technikum-Wien, Höchstädtplatz 5, A-1200 Wien
 Biomedical Engineering Sciences
 Master of Science in Engineering – MSc
 18. Juni 2008, mit ausgezeichnetem Erfolg bestanden

- Zeitraum
- Ausbildungseinrichtung
- Spezialisierung
- Bezeichnung der Qualifikation
- Diplomprüfung

September 2002 - Juni 2005
 Fachhochschule Technikum-Wien, Höchstädtplatz 5, A-1200 Wien
 Biomedizinische Technik / Computer- und Systemtechnik
 Diplom-Ingenieur für Elektronik (FH)
 15. Juni 2005, mit ausgezeichnetem Erfolg bestanden

- Zeitraum
- Ausbildungseinrichtung
- Spezialisierung
- Bezeichnung der Qualifikation
- Reifeprüfung

September 1995 - Juni 2000
 HTL Technologisches Gewerbe Museum, Wexstraße 19-23, A-1200 Wien
 Elektronik / Nachrichtentechnik
 Reife- und Diplomprüfung
 21. Juni 2000, mit gutem Erfolg bestanden

- Zeitraum
- Ausbildungseinrichtung

September 1991 - Juni 1995
 Bundesrealgymnasium, Kandlgasse 39, A-1070 Wien

WEITERBILDUNG

- Zeitraum
- Ausbildungseinrichtung
- Thema

18. Oktober 2016
WIFI Wien
Seminar Wissenschaftskommunikation

- Zeitraum
- Ausbildungseinrichtung
- Thema

12. - 13. Februar 2015
WIFI Wien
Grundlagen Projektmanagement

- Zeitraum
- Ausbildungseinrichtung
- Thema

5. - 6. November 2009
GEFTA Fortbildungskurs
Methoden der Thermischen Analyse

- Zeitraum
- Ausbildungseinrichtung
- Thema

22. - 26. Juni 2009
European Powder Metallurgy Association
Powder Metallurgy Summer School

- Zeitraum
- Ausbildungseinrichtung
- Thema

1 - 3. April 2009
CADFEM Austria GmbH
Finite Elemente Methode Seminar

- Zeitraum
- Ausbildungseinrichtung
- Thema

19. März 2009
Bruker Optik GmbH
TGA-FT-IR-Kopplungstechniken

- Zeitraum
- Ausbildungseinrichtung
- Thema

26 - 27 Februar 2008
Netzsch Gerätebau GmbH
Kinetik Seminar

PERSÖNLICHE FÄHIGKEITEN UND KOMPETENZEN

Muttersprache

Deutsch

SONSTIGE SPRACHEN

- Sprache
- Lesen
- Schreiben
- Sprechen

Englisch
Ausgezeichnet
Ausgezeichnet
Ausgezeichnet

- Sprache
- Lesen
- Schreiben
- Sprechen

Spanisch
Grundkenntnisse
Grundkenntnisse
Grundkenntnisse

TECHNISCHE FÄHIGKEITEN UND KOMPETENZEN

- Anwendung thermophysikalischer Messverfahren (Dilatometrie, Dynamische Differenzkalorimetrie, Laser Flash Verfahren, Thermogravimetrie)
- Gasanalyse mit Massenspektrometer und Fourier-Transform-Infrarot-Spektrometer
- Anlagensteuerung und Softwareentwicklung mit LabView
- Signalverarbeitung unterschiedlicher Sensormessdaten, Algorithmen Entwicklung und Auswertung mit MATLAB
- Piezosensorik und Messtechnik
- Temperaturfeld- und strukturmechanische Berechnungen mit Finiten Elemente Simulation, Kinetische Analyse und Modellierung
- Requirement Engineering (Rational RequisitePro)
- Hard- und Softwareintegration, Systemtests und Fehleranalyse auf sicherheitskritischen Kommunikationssystemen (Windows 2003 Server, MS SQL, C#)
- Messtechnik von HF-Quellen wie z.B. WLAN, WiMAX, Bluetooth (LabView)
- Simulation diverser HF-Quellen mit optischen Simulationsprogrammen (Wireless Insite)
- Auswertung von Messdaten (MATLAB, Excel, Java)
- Netzwerktechnik (Cisco Networking Academy Program, Windows 2003 Server)
- Programmierung von dynamischen Websites, CDs/DVDs und Datenbanken (HTML, PHP, Java, Lingo, MySQL)
- EDV Support und Netzwerkadministration (Windows NT, Office)

WISSENSCHAFTLICHE TÄTIGKEITEN

- Messung thermophysikalischer Eigenschaften und thermische Analyse von Phasenwechsel- und Thermochemischen Materialien für Wärmespeicheranwendungen (seit 2013)
- Entwicklung und Validierung eines transportablen Schadendetektionsystems (Structural Health Monitoring System) zur Überwachung von Strukturen aus Faserverbundstrukturen (2011)
- Bestimmung und Anwendung formalkinetischer Werkstoffmodelle für den Entbinderungs- und Sinterprozess von PIM Bauteilen in der FE Simulation (2007-2011)
- Simulationsbasierte Verbesserung der Temperaturleitfähigkeitsmessung an inhomogenen Materialien mit dem Laser Flash Verfahren (2009)
- Bestimmung der realen Feldverteilung von hochfrequenten elektromagnetischen Feldern in der Umgebung von Wireless LAN Einrichtungen (WLAN) in innerstädtischen Gebieten, Austrian Research Centers Seibersdorf, November 2006
- Störbeeinflussbarkeit von implantierbaren Herzschrittmachern und Cardioverter Defibrillatoren (ICD) durch elektromagnetische Resonanzsysteme, Austrian Research Centers Seibersdorf, Oktober 2005
- Bestimmung der Exposition bei Verwendung kabelloser Übermittlungsverfahren in Haushalt und Büro, Austrian Research Centers Seibersdorf, Juli 2005
- Diplomarbeit: Messtechnische und numerische Expositionsbeurteilung von WLAN-Komponenten als Quellen elektromagnetischer Felder, Austrian Research Centers Seibersdorf, Mai 2005

PUBLIKATIONEN

- https://www.researchgate.net/profile/Daniel_Lager

FREIZEITBESCHÄFTIGUNGEN

- Familie, Haus und Garten, Gitarre

FÜHRERSCHEIN

- Klasse B